The University of
Nottingham

UNITED KINGDOM · CHINA · MALAYSIA

Development of 4D-Printed Shape Memory Polymer Actuators for Induced-Strain Shape Change

A thesis submitted to the University of Nottingham Malaysia

in fulfilment of the requirements of the award of the degree of

Doctor of Philosophy in Electrical and Electronic Engineering

Author	:	**Yousif Saad Alshebly**
Main Supervisor	:	**Dr. Marwan Nafea**
Internal Co-Supervisor	:	**Prof. Dr. Haider Abbas F. Almurib**
External Co-Supervisor	:	**Ir. Dr. Mohamed Sultan Mohamed Ali**

April 2023

Declaration

I declare that this thesis entitled "*Development of 4D-Printed Shape Memory Polymer Actuators*" is the result of my own research except as cited in the references. The thesis has not been accepted for any degree and is not concurrently submitted in candidature of any other degree.

Signature   : ………*Yousif*………..........

Name   : Yousif Saad Alshebly

Date   : 30th April 2023.

Dedication

Dedicated to those who supported this work from the first day to the last

List of Publications

- **Journal Papers**

1. Y. S. Alshebly, and M. Nafea, "Effects of Printing Parameters on 4D-printed PLA Actuators," *Smart Mater. Struct.*, vol. 32, no. 6, p.064008, 2023. (WoS Q1).

2. Y. S. Alshebly, K. B. Mustapha, A. Zolfagharian, M. Bodaghi, M. S. Mohamed Ali, H. A. Almurib, and M. Nafea, "Bioinspired Pattern-Driven Single-Material 4D Printing for Self-Morphing Actuators," *Sustainability*, vol. 14, no. 16, p. 10141, 2022. (WoS Q2).

3. D. S. Cheah, Y. S. Alshebly, M. S. Mohamed Ali, and M. Nafea, "Development of 4D-Printed Shape Memory Polymer Large-Stroke XY Micropositioning Stages," *J. Micromech. Microeng.*, vol. 32, no. 6, p. 065006, 2022. (WoS Q3).

4. Y. S. Alshebly, M. Nafea, M. S. Mohamed Ali, and H. A. F. Almurib, "Review on Recent Advances in 4D Printing of Shape Memory Polymers," *Eur. Polym. J.*, vol. 159, p. 110708, 2021. (WoS Q1).

5. Y. S. Alshebly, M. Nafea, and M. S. Mohamed Ali, "Development of 4D Printed PLA Actuators," *ELEKTRIKA- J. Electr. Eng.*, vol. 20, no. 2–2, pp. 9–14, 2021. (GS & MCC). *Best Presentation Award (conference proceedings).*

- **Conference Papers**

1. Y. S. Alshebly and M. Nafea, "Control of 4D Printed Actuators Twisting Behavior via Printing Direction," *2022 IEEE 20th Stud. Conf. Res. Dev. (SCOReD)*, Bangi, Malaysia, 2022, pp. 163-167. (Scopus).

2. W. H. Lee, Y. S. Alshebly, M. S. Mohamed Ali and M. Nafea, "Development of a 4D Printed Variable Stiffness Gripper," *2022 IEEE 20th Stud. Conf. Res. Dev. (SCOReD)*, Bangi, Malaysia, 2022, pp. 151-156. (Scopus).

3. W. H. Lee, Y. S. Alshebly, M. S. M. Ali and M. Nafea, "Pattern-Driven 4D Printed PLA Actuators," *2022 IEEE 8th Int.l Conf. Smart Instrum. Meas. Appl. (ICSIMA)*, Melaka, Malaysia, 2022, pp. 116-121. (Scopus).

4. Y. C. Lee, Y. S. Alshebly, and M. Nafea, "Joule Heating Activation of 4D Printed Conductive PLA Actuators," in *2022 IEEE Int. Conf. Autom. Control Intell. Syst. (I2CACIS)*, Shah Alam, Malaysia, 2022. pp. 221–225. (Scopus).

5. Y. S. Alshebly, M. Nafea, H. A. F. Almurib, M. Sultan Mohamed Ali, A. A. Mohd Faudzi and M. T. T. Tan, "Development of 4D Printed PLA Actuators with an Induced Internal Strain Upon Printing," *2021 IEEE Int. Conf. Autom. Control Intell. Syst. (I2CACIS)*, Shah Alam, Malaysia, 2021, pp. 41-45. (Scopus).

6. K. J. Tong, Y. S. Alshebly, and M. Nafea, "Development of a 4D-Printed PLA Microgripper," in *2021 IEEE 19th Stud. Conf. Res. Dev. (SCOReD)*, Kota Kinabalu, Malaysia, 2021, pp. 207–211. (WoS).

- **Book Chapters**

1. Y. S. Alshebly, M. Nafea, K. B. Mustapha, M. S. Mohamed Ali, A. A. Mohd Faudzi, M. T. T. Tien, and H. A. Almurib, "Variable Stiffness 4D Printing," in *Smart Materials in Additive Manufacturing, Volume 2: 4D Printing Mechanics, Modeling, and Advanced Engineering Applications*, M. Bodaghi and A. Zolfagharian, Eds. Elsevier, 2022, pp. 407–433. (Scopus).

- **Copyrights**

1. Y. S. Alshebly, and M. Nafea, "Effects of Printing Parameters on the Bending Angle of 4D Printed PLA Actuators", *Copyright University of Nottingham Malaysia*, LY2022W05131, pending.

Abstract

Four-dimensional (4D) printing is gaining interest in the past few years. The prototyping freedom of three-dimensional printing, coupled with the abilities of smart materials and their properties, gave rise to a new field of active structures. The field is still developing in the freedom of control over the shape programming and design reliability, caused by the lack of mathematical models and simulations of the materials. This thesis presents advancement in the shape programming that allows for control of the actuation in actuators, based on printing parameters, structural manipulation, and Joule heating. Fused deposition modelling is used to print all actuators and structures in this research. Printing parameters consisting of the printing speed, passive-to-active layers ratio of prints, printing temperature, layer height, and thickness are tested to investigate the effect they produce on the PLA actuators. A predictive mathematical model is created for all the printing parameters used to control the internal strain in the actuators, with an accuracy of 98% in predicting the bending angle. The model is linked to the simulation methods, allowing simulations of the effect of the parameters. Variable stiffness of the structures by different patterns is used in the assessment, which provides varying effects on the printed structures. A total of 40 different actuator designs are made with each deforming differently because of the patterns used. Design insights are provided by using certain pattern arrangements for specific behaviour. The bending angles are varied between 6.21° and 30.96°, depending on the pattern arrangement used, with very high repeatability. Furthermore, Joule heating of the actuators is done by variating the activation voltage which enables direct control of local activation and allows measurements of thermal and force to be taken on the actuators while it is deforming. After the testing, thermal simulation of conductive materials, with analysis and deformation is performed for validation. The research is finalized with further explorations of concepts in 4D printing, which induce twisting behaviour with high control and thermal-dependent actuation. The thermal-dependant actuators are designed by printing sandwiched layers of different directions, activated at different temperatures, which allows for isolated deformation of each section of layers. The designs and control concepts of the actuators are used to create proof-of-concept structures, showing high control of the shape programming and activation. The mechanisms and methods developed can be used and implemented to achieve more reliable 4D-printed designs. As a result, many of these designs improve the fundamental understanding of shape programming in 4D printing.

Table of Contents

List of Figures

List of Tables

List of Abbreviations

AM	Additive manufacturing
CNT	Carbon nanotubes
DED	Direct energy deposition
DIW	Direct ink writing
DLP	Digital light printing
DMA	Dynamic mechanical analysis
DSC	Differential scanning calorimetry
FDM	Fused deposition modelling
LOM	Laminated object modelling
MEMS	Micro-electromechanical system
PAC	Printed active components
PLA	Polylactic acid
Rf	Shape fixity
Rr	Recovery rate
SLA	Stereolithography
SLM	Selective laser melting
SLS	Selective laser sintering
SMA	Shape memory alloy
SME	Shape memory effect
SMP	Shape memory polymer
Tg	Transition Temperature
UV	Ultra-violet

List of Appendices

Appendix A – FESEM Report

Appendix B – Figure Reuse Permissions

Chapter 1: Introduction

1.1 Overview

Additive manufacturing (AM), or three-Dimensional (3D) printing, has been advancing at a fast pace due to the degree of freedom and complexity it allows for prototype manufacturing [1], [2]. The rapid prototyping of 3D printing provided many augmentations and much-needed improvements in many fields such as biomedicine [3], construction [4], and rapid complex prototyping [5]. Along with the recent advances in the material science of smart substances, AM gave rise to four-Dimensional (4D) printing, or 3D printing of smart materials [6], [7]. 4D printing is a recent and rapidly changing research field that was first introduced in 2014 [8].

Shape-shifting of structures was demonstrated on printed materials. The concept of printed active components (PACs) was soon realized and printed, and the components were printed using a polyjet printer [9]. Since then there was a huge surge of advances in the field, 4D printing has become closer to industrial applications in robotics engineering [10], strucurtal shape cahgning supports [11], and non-chemically reactive medical grade materials [12].

4D printing depends on the materials used and the printing method, which offered greater advantages to this field than traditional 3D printing such as persoanlaized actuators that adapts [13], photoresponsive materiasls for ligt activation sensors [14], and remotely controlled printed nanarchetecuttres in actuators [15]. Various materials possess smart characteristics that respond to specific stimuli, more specifically materials with shape memory behaviours are used in this field for endovascular support [12], energy absorbing meta-materials [16], and high shape recovery materiasl capable of retaining from damaged shape [17].

Various printing techniques are used for 3D printing and subsequently 4D printing. The printing of polymers, metals and other materials is of endless possibilities. Printing techniques of metals such as powder beds and laminated objects will not be discussed in the thesis [18]. The most popular 4D printing technique is fused deposition modelling (FDM) [19], [20], in which the material is extruded through a heated nozzle one line at a time,

creating a model. FDM is the most popular because of the relatively low cost of printing and the freedom of use in terms of materials, since it uses filaments to print [21].

Smart materials can change their properties under certain conditions, these can be actively applied or environmentally induced [22]. Materials respond to certain stimuli in order to achieve their property change, there are many possible stimuli that affect different materials such as temperature, swelling ability, pH level, and magnetic fields [23].

Smart materials are the heart of 4D printing, since it is the change in characteristics over time, which is the fourth dimension, that gives 4D printed structures their advantages. Most of the literature on the subject focuses on the printing of materials with the shape memory effect (SME). This characteristic is favourable since it provides the ability to the application of force for an unbounded number of applications such as reconfigurable structures for delicate applications [24], tissue repair engineering [25], and highly adaptive medical deivces [26].

Shape memory polymers (SMPs) are the most investigated and applied type of materials used in 4D printing, this is due to their superior characteristics and the prospect of applications [6], [27], [28]. Popular SMPs in this field such as polyurethane-based polymer [21], [29] and polylactic acid (PLA) [13], [20] are of good shape memory characteristics, relatively low cost, and easily augmented by material mixing to form composites [30]. These composites are used widely to change the SME and actuation of the SMPs, some composites are made so to control the transition temperature of the SMPs or to change the type of stimulus that is needed to activate the SME [31], [32].

Most SMPs respond to heat, more specifically they have a certain temperature at which the material changes from its glassy state into its rubbery state, making it easily mendable into many temporary shapes [16]. During the rubbery state of a material, a force is used to bend it, while preserving the new shape, the material is cooled below its transition temperature thus holding its temporary shape with a withheld strain; the original shape is retrieved when the temperature is raised above the transition temperature [33].

Different combinations of materials with different stimulus has allowed complex, programmable, and various shape changes in materials which include spring compression and decompresion [34], origami shape change in surfaces [35], and metamatteriasl hinges with negative poisson's ratio [36]. These shape changes are made as proof of concept of the use of

the SME characteristic of the materials, they are used in more complex designs and applications.

In a general sense, there are four main components involved in 4D printing, these are the printing method, the materials used, the stimulus of the smart material, and the programming of the printed shape.

1.2 Problem Statement

4D printing, an emerging research field, holds significant potential, but it faces numerous gaps that hinder its application-oriented development. These gaps span various domains, from industrial to biomedical applications such as adaptive medical devices [37], peronalzied tissue engineering [38], and body heat energy harvesting actuators [39].

While 4D printing can enable the design and production of medical devices like sensors, wearable adaptive devices, and micro-electromechanical systems (MEMS), its utilization remains limited due to its early-stage development. Researchers require reliable design models to streamline the creation of application-specific designs, particularly when working with specific materials. These models hinge on a deeper, collective comprehension of the control parameters governing 4D printing.

Research into Shape Memory Polymers (SMPs) and shape programming is emerging as a central focus, alongside refining printing method control, albeit still at an early stage not ready for practical applications. Shape programming mechanisms in 4D printed structures offer a foundation for design and activation criteria, crucial for actuator control.

Enhancements to these programming mechanisms encompass parameter control and structural adjustments. Control over induced strain in printed actuators can be achieved by manipulating printing parameters, thereby avoiding post-printing shape changes. While studies on parameter effects exist exploring printing speed [40], temperature [41], recovery force [42], and others [43], [44] these often examine isolated parameters and lack a comprehensive understanding of their collective impact.

Additionally, limitations in printing settings, especially with specific materials, restrict control through printing parameters. In such cases, structural manipulation can compensate for this lack of control without altering the printing parameters. These shape programming techniques can introduce varying stiffness profiles within structures, a concept with tremendous potential but still not well-explored.

Traditional 4D printing activation methods involve subjecting structures to a heated or swelling-inducing environment, limiting the range of shape-change analyses possible. Adopting local activation methods, such as electrical stimuli, offers better observation and evaluation capabilities, particularly when employing thermal and force sensors. Local activation methods show promise for controlled and planned activation in application-driven 4D printing.

Addressing these research gaps in shape programming is imperative for the field's advancement, providing essential tools and methodologies. These fundamental insights, though highly beneficial for 4D printing applications, remain inadequately understood and controlled, slowing progress towards real-world applications.

1.3 Research Objectives

The main aim of this research is to achieve printing-parameters-based shape programming of 4D printed PLA and conductive PLA actuators without requiring manual training. To address this, the following objectives need to be accomplished:

1. To investigate the effect of the printing parameters on the programmed shape of 4D-printed PLA actuators and derive a shape-programming model that predicts the bending angle based on the parameters.
2. To investigate different pattern effects in PLA and develop bioinspired pattern-driven variable stiffness 4D printed actuators for robotics applications, with evaluation of performance by design of grippers.
3. To develop Joule-heating-activated 4D printed conductive PLA actuators for locally controlled robotics applications, by control of activation voltage and evaluating its effect on the performance.
4. To investigate the principles of temperature-dependent multi-shape actuation of 4D printed PLA actuators.

1.4 Scope of the Research

This research covers 4D printing of shape memory polymers, focusing on shape programming of actuators to establish control parameters used in the 4D printing process. This covers topics of strain inducing by the control of printing parameters, structural manipulations, and assessment of local activation by electrical stimulation.

The designs primarily focus on fundamental actuator units employed to measure the variations achievable through different shape programming mechanisms. These actuators are restricted to sizes suitable for the testing requirements. These basic actuator designs serve as the foundation for more intricate proof-of-concept designs, primarily centered around gripping actions, all of which are derived from the same fundamental designs. SolidWorks software is utilized for the design process, while Simplify3D software is employed to slice and program the printing parameters for all the actuators. The finite element analysis (FEA) procedure is conducted using ANSYS software, incorporating static structural, static thermal, transient thermal, and electric toolboxes.

A single-extruder FDM printed is used for all the printing processes in this work. The materials used are limited to thermal SMP filaments, including PLA and carbon black PLA (CB/PLA), which is a conductive PLA. It is important to note that another material is used for preliminary testing of muti-material printing, although this is out of the scope of this research. This material is biodegradable polyethene terephthalate glycol (Bio-PT).

When activate the designs, two primary actuation methods are employed. The first involves immersing the actuators in a heated water environment, either maintaining a constant temperature or gradually increasing it. The second method utilizes electrical stimulation of conductive materials to induce Joule heating in these actuators. The assessment of the material properties in this study relies on thermal and mechanical analysis techniques. These include a Dynamic Mechanical Analysis (DMA) machine, a Differential Scanning Calorimetry (DSC) machine, a Thermogravimetric Analysis (TGA) machine, a Tensile Test machine, a Field Emission Scanning Electron Microscope (FESEM), and an Optical Microscope. Additionally, specific sensors, such as a digital thermometer, an Infrared (IR) thermal camera, and a force sensor, are employed to evaluate the activation mechanisms.

1.5 Research Contribution

This research proposes several contributions that are based on the shape programming of 4D-printed actuators using the printing parameters without manual training. In addition, this research contributes to the implementation of structural changes to induce strain in the actuators. Moreover, this work contributes to the development of activation control of Joule heating of conductive actuators. These main contributions and other minor ones are highlighted as follows:

1. This work is the first that investigates the combined effects of the printing speed, printing temperature, the ratio of passive-to-active layers, layer height, and height of actuators on the internal strain induced in 4D-printed actuators.

2. A mathematical model that predicts the bending angle of actuators is proposed in this work. This is the first model that considers the five aforementioned parameters. In addition, an FEA model that uses the calculations of the effect of the printing parameters is developed, which is the first that includes all the aforementioned printing parameters.

3. This work presents a novel investigation of the effect of five bioinspired printing patterns on the variable stiffness behaviour and actuation performance of 4D printed actuators. These patterns include the *Volvox carteri* (circles), *Haloquadratum walsbyi* (squares), honeycombs (hexagons), *Sapium sebiferum* (rhombuses), and *Oxalis triangularis* (triangles).

4. This work proposes a novel approach of using geometrical patterns to create controllable strain differences between the layers of the actuators. This concept is then used to develop a hand-like-shaped gripper that can grip and pick up delicate objects with uniform and non-uniform cross-sections.

5. In this work, a significant advancement is made with the implementation of Joule-heating-activation control for CB/PLA 4D printed actuators. The research delves into the time-dependent impact of activation power on various electro-thermo-mechanical aspects of the actuators. Expanding on this breakthrough, the concept is further applied to introduce an innovative CB/PLA 4D printed manipulator. This manipulator comprises an upper arm, a lower arm, and two fingers, with each component being independently controlled using Joule heating. This design enables the manipulator to delicately grip and maneuver objects along both the x- and y-axes..

6. This work presents a novel method for temperature-dependent multi-shape actuation in single-material structures. The concept is demonstrated by the development of a layer-sandwiching printing method that isolates the deformations in different directions.

1.6   Potential Impact of the Research

This research is expected to contribute to medical and academic advances, across and within disciplines, including significant advances in theory, understanding, methods, and application of 4D printing of SMP actuators. The study on the effects of controllable printing parameters on the shape memory effect in actuators can provide high and accurate control over the shape change, removing the training step in 4D printing and providing a more

streamlined and precise production technique. The understanding of the effects of these parameters along with developing mathematical predictive models that are linked to the simulation of actuators, can greatly aid in the design process. The use of the material's stiffness to manipulate the deformation and shape change can provide design preferences beyond traditional force inducement in the structures, giving more control when other parameters in 4D printing are limited in their use.

Control over local activation of actuators by Joule heating allows for the use of actuators in a more controlled environment. This enables better observations and analysis to be done on actuators in the process of shape change. In addition, recent studies have shown that the proposed research presents a promising solution for various research problems while showing a growing fundamental influence on the economy and society. These benefits that the field can be used in the contruction industrry [4], biomedical sensors applications [45], medical implants [46], various appplications into soft robotics [47], electromechanical manupliation of structures [48], and many other prospects into field ready applications [49].

1.7   Thesis Outline

The thesis is divided into eight chapters which are, the introduction, literature review, methodology, printing parameters of 4D-printed actuators, 4D-printed variable stiffness actuators, Joule heating of conductive actuators, exploring further concepts in 4D printing, and conclusion and future works. Chapter 1 presents an overview of the topic with research criteria. Then, Chapter 2 discusses material properties, shape memory effect, stimulus, 4D printing techniques, shape programming, application-based 4D printing, and a summary. Following that, Chapter 3 discusses the theoretical study of the topic, the design, and simulations, fabrication and testing of models, and mathematical model developments. Then, Chapter 4 discusses the control provided by the printing speed, passive and active layers ratio, printing temperature, layer height, and thickness on the SME of the prints. Next, Chapter 5 presents the assessment of variable stiffness 4D printing using printing patterns. After that, Chapter 6 presents the local activation of conductive 4D printed actuators, based on voltage and activation time. Next, Chapter 7 introduces two sections, the first is on the twisting behaviour of actuators, and the second section is on thermal-dependant actuation for single material multi-shape change. Lastly, Chapter 8 presents the conclusion and an insight into future works planned for the feild.

Chapter 2: Literature Review

2.1 Introduction

Shape memory polymers in 4D printing are the focus of this research, this is due to the heavy research around SMPs in the past few years, as the applications and printing techniques for these materials are changing rapidly [39], [50] As compared to other popular SME materials used in 4D printing, SMPs are favourable for specific applications. In a general sense, SMPs possess better SME characteristics, such as the difference in the modulus between the glassy and rubbery state which is of a higher ratio than that of SMAs and Hydrogels. SMPs also possess higher control of their transition temperatures, making them more appropriate for customized applications [38]. This section presents a discussion of the material properties of SMPs, SME of printed SMPs, and the stimulus of the 4D printing materials.

This chapter would also serve as a reference for the rest of the research, the areas that this research focuses on are based on the fields of 4D printing that are still in their early stages and in need of improvements in terms of establishing fundamentals.

Figure 2.1 shows a complete basis of 4D printing, with deciding factors on all the choices of the 4 main components a design can be made. Not all the printing methods presented in **Figure 2.1** are commonly used in 4D printing. These are added in the figure because they can be used in the field with further research. The materials included in the figures are based on the ones currently used, there is no limit to the materials that can be used alongside the smart materials, but the ones mentioned are part of the active parts of the designs.

The activation of the Shape Memory Effect (SME) in the printed shapes relies on stimuli utilized in recent papers published since 2015. While other stimuli for SMPs exist, they have not been explored extensively in recent 4D printing research. The programming of the designs follows a broad framework. However, it was observed that the selection among these options is crucial for determining the design specifications and the necessary materials and stimuli.
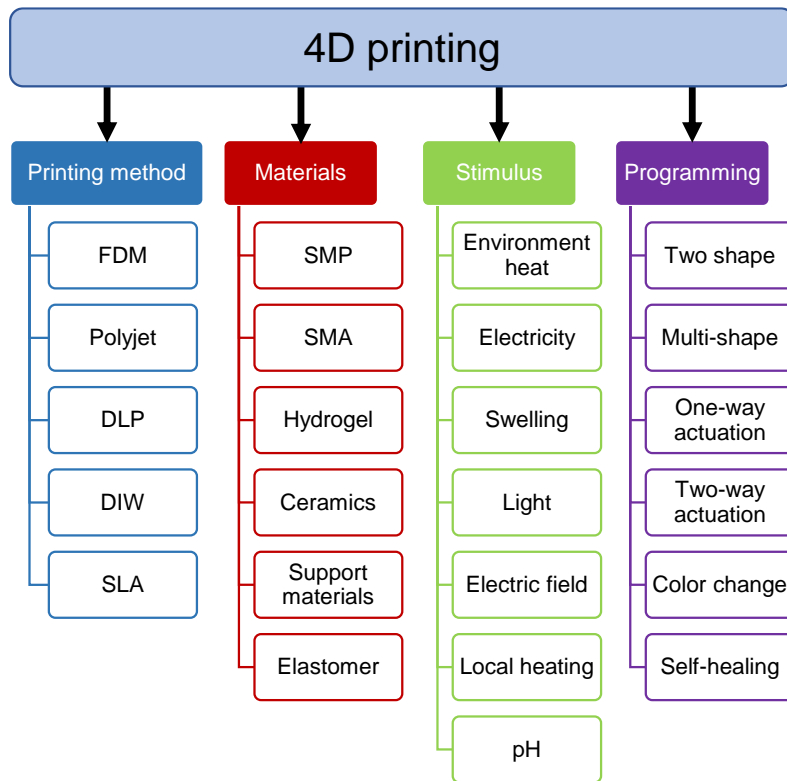
Figure 2.1. The general breakdown of all the steps needed in 4D printing, this figure represents the commonly used 4D printing parts, other less popular methods are not included.

2.2   Shape Memory Polymers

Shape memory polymers in 4D printing are the focus of this study, due to the extensive research around SMPs in the past few years, as the applications and printing techniques for these materials are changing rapidly [39], [50]. As compared to other popular SME materials used in 4D printing, SMPs are favourable for specific applications. In a general sense, amorphous SMPs possess better SME characteristics, such as the difference in the modulus between the glassy and rubbery state, which is of a higher ratio than that of shape memory alloys (SMAs) and Hydrogels. SMPs also possess a higher control of their transition temperatures, making them more appropriate for customized applications [47]. This section discusses the material properties of SMPs, SME of printed SMPs, and the stimulus of the 4D printing materials.

2.3   Material Properties

As compared to other SME materials, SMPs are lightweight, possess a larger elastic modulus, higher flexibility, and a better degree of biodegradability [51]. The SME of materials is assessed by many techniques that are becoming standards of assessment, which is observed in most of the recent literature these are made by bending angle assessment [6], which have been applied to many actuators and methods [31], [52].

Comparisons of SME properties, especially for SMPs, are made using Young's modulus, elastic modulus, shape fixity ratio, and shape recovery ratio. Young's modulus is a measure of how a material can withstand changes in length when under tension [11], and the elastic modulus is a measure of the tensile elasticity. These parameters are used to assess the elastic characteristics of materials, which is the backbone of SMPs in 4D printing [53].

Shape fixity of the material is a measure of the ability of a material to conserve a temporary shape when the programming step is done, while the shape recovery is a measure of how close to the original shape does the deformed material recover upon stimuli [54]. SMPs are easier to program because of their molecular formation, they can take on more strains and possess better shape fixity (R_f) and recovery rates (R_r) [19].

2.4   Shape Memory Effect

Most tested amorphous SMPs and their composites are assessed in a similar fashion. This allows researchers to compare each material to whether it is suitable for their application. Amorphous SMPs' actuation mechanism is characterised by its transition temperature (T_g), which is the temperature at which the polymer will change from its glassy phase to its elastic phase, allowing shape change.

T_g is the temperature that the stimulus is set above to enable the shape memory effect of the materials to be activated. These temperature points are set externally to allow the shape change of prints to take place [55]. Melting temperature (T_m) is the temperature at which the material melts, this temperature is used for printing the materials, when using an extruder. The temperature used is set up higher than T_m to allow a good flow of melted polymer. SME effect is categorized into three sections, the control of SME actuation of recent years, one-way SME, and two-way SME, also known as, reversible actuation.

2.4.1 Control of SME Actuation

Control of SME characteristics has been reported with a high degree of freedom. This is usually done by creating composites of SMPs and other materials. These composites are made for either an improvement of the SME or to change the triggering stimulus of the SMP. There have been many useful and highly-tuneable SMP composites that were made in the past few years, which have been tested and presented in the literature.

Recently, an SMP composite resin was created with high shape fixity and recovery rates, made with DLP printing. The material possessed a very fast shape recovery time of 7 to 13 seconds, which is needed in certain applications. The triggering temperature is also controllable from about 48 to 77 °C, which allows high control of stimulus for more applications [56]. This material has also been tested for cycling endurance where it kept 100% of its shape fixity for 16 cycles of loading and unloading. Development of DLP-suitable SMPs is needed because of the lack of suitable materials that are used in research.

In a different approach, a PLA composite with tuneable recovery triggering temperature was developed. This was done by mixing poly(ethylene glycol), showing much better SME characteristics. Localized actuation of the material was also achieved by printing the material with graded layers, thus allowing different times for the actuation of sections [54]. This technique can be used in different applications that require timed actuation of certain sections of the print by using different temperatures. This is also important since PLA is the most used SMP in research [57].

Similarly, the use of PLA/Fe_3O_4 composite using FDM printing to achieve a very high recovery speed of about 5 seconds is reported, which is significant [58]. The object is triggered by direct heat, but because of the Fe_3O_4, the object can heat up with magnetic fields, while keeping the same recovery speed.

The high-speed shape recovery is favoured in many applications, since some applications need a fast response to environments or stimuli. the composite is also relatively of a low cost because of the use of PLA. The use of magnetically actuated structures can be of great benefit in biomedical research since the shape change can be made remotely in implanted prints.

Table 2.2 The table shows useful composites that can be used for many applications. The materials are described, and the synthesis of these materials can be found in the articles'

references. The properties of the materials provided are not standardized since many researchers prefer certain properties of SMPs to others. Thus, there are variations in the tested and reported properties of the prints.

Table 2.1. Tuneable composites of common and recent SMPs that are tuned to specific characteristics.

Year	SMP	Printed material properties	Proposed application	Reference
2021	UV-curable Thermochromic SMP liquid resin	Tuneable Tg: from 74.2°C to 81.7°C Rf: 96.7%, Rr: 100% Colour-changing patterns as controlled by temperature	Encryption of data, by means of colour change of code.	[59]
2020	Semi-crystalline (PLA)-based	T_g: 70.35°C R_f: 98%, R_r: 99% Storage modulus below and above Tg: 1826.2 MPa and 5.52 MPa	Self-deploymetns of large area surfaces, such as antennas	[60]
2020	PLA and PCL	T_g: 45°C Based on mixing ratios: Tensile strength: 26 MPa to 30 MPa Young's modulus: 165 MPa to 340 MPa Strain at break: 815% to 510% R_f: 99.5% to 97%, R_r: 99.6% to 86%	Patient adaptable treatment options, such as elbow protectors	[61]
2020	FlexPro filaments and PU-SMP	T_g: 60°C Storage modulus at 20°C and 80°C: 1.656 GPa and 3.18 MPa	Reversable energy absorption, such as shock resist	[16]

		Young's modulus: 66.6 MPa (FlexPro) and 1.64 GPa (SMP) Poisson's ratio: 0.42 (FlexPro) and 0.36 (SMP)		
2019	Acrylate-based photosensitive resins	T_g from 48°C to 77°C, depending on mixing ratio R_r: 100% for 16 cycles, R_f: 96% Storage modulus: 1.48 GPa	Photosensitive polymers expanding SLA and DLP materials	[56]
2019	PLA and poly(ethylene glycol) (PEG)	T_g: 41.54°C PLA and 10% 30% PLA/PEG composite T_m: 61.32°C, 166.44°C, Elastic modulus: 844.84 MPa, 652.91 MPa, 119.92 MPa R_f: ~ 100 %	Self-sensing, Changing of mechanical properties based on tempareure	[54]
2019	PLA/Fe$_3$O$_4$ composite	Three samples of different mixing ratio: T_g: 62.7 °C, 64.0 °C and 66.7 °C PLA and three mixing ratios: Storage modulus: above 1600 MPa at 40°C for three composites: R_r: 95.6%, 95.8%, and 96.3% R_f: 96.5%, 96.9%, and 96.9%	Materials with low activation temrpature for medical use, without high heat	[58]

Year	SMP		Remark	Reference
2019	Pristine PLA SMP and MWCNT reinforced PLA SMPC	T$_g$: 80°C For SMP and MWCNT SMPC: Elastic modulus: ~17 GPa Tensile strength: 41 MPa and 28 MPa Compression strength: 35 MPa and 55 MPa Energy absorbance: 0.16 J and 0.22 J	Self-deployable space aircrafts for space saving	[20]

2.4.2 One-Way SME

One-way actuation is the most reported in recent 4D printing advances, since it is simple and provides a good basis for designs and proof of concepts. **Table 2.2** shows a useful and applicable design and prints of one-way actuation with their build method and possible applications, these had been selected based on how useful they can be in other designs because of their wide range of applications and good reported SME.

Table 2.2. Recent advances in 4D printing of materials with one-way actuation with their printing methods and applications.

Year	SMP	Printing method	Remark	Reference
2021	Thermoplastic PU filament	FDM	Using PU of different glass temperatures, the temporary shape can be achieved, and then the prints are still bendable.	[62]
2020	Moisture-cured PU elastomers	FDM	Different gradients of mixing of two polymers to produce shape memory change, by water swelling.	[63]
2020	VeroBlack and TangoPlus	Inkjet	Network design of two materials for tuneable characteristics of SME.	[64]
2019	PU paint, carboxymethyl	Syringe	Simple and inexpensive	[65]

	cellulose (CMC), and silicon oxide nanoparticles (NPs)		fabrication of polymer.	
2019	DiAPLEX MM-4520 and Tecoflex EG-72D	FDM	Change in the characteristics of the materials over recovery cycles.	[66]
2018	DiAPLEX MM-4520 and Carbon black	FDM	Polymer with increased conductivity due to Carbon black.	[67]

The simplest SME is achieved in a one-way actuation of SMPs. In this case, there are two shapes, one is the permanent shape and the other is the temporary shape. This actuation is the most common type of actuation. In other more complex programming techniques, although it is still a one-way actuation, there are more than two shapes. This is demonstrated by the triple-shape memory effect in [68], where the use of three polymers in a single structure is used to allow multiple shape changes. The use of two materials in a structure allows the existence of one permanent shape and two temporary shapes [22]. This has also been done with a great amount of control over the actuation in solvent-driven shape change [69], with a predictable response of the structure based on the solvent and temperature used in the stimuli.

One-way actuation is the most common approach because of the wide range of materials that possess one-way actuation abilities. These materials are highly augmentable, allowing them to possess a wide range of controlled parameters [70]. A composite of PLA infused with CNT is made to enhance its shape memory behaviour, at which faster shape recovery is achieved and better performance. Recovery force was also increased, which is beneficial when the SMP used is needed to produce stronger strain [71].

Another modification to the common PLA material is the use of PLA and thermochromic pigments in 4D printed parts using FDM. Control of actuation and colour of the object is achieved, as each can be activated separately, where The characteristics of the SPM are not affected to a noticeable extent by the addition of the pigments, as shown in **Figure 2.2** [72]. This same characteristic has also been achieved in a more recent study, by using ultraviolet curable SMP [59].
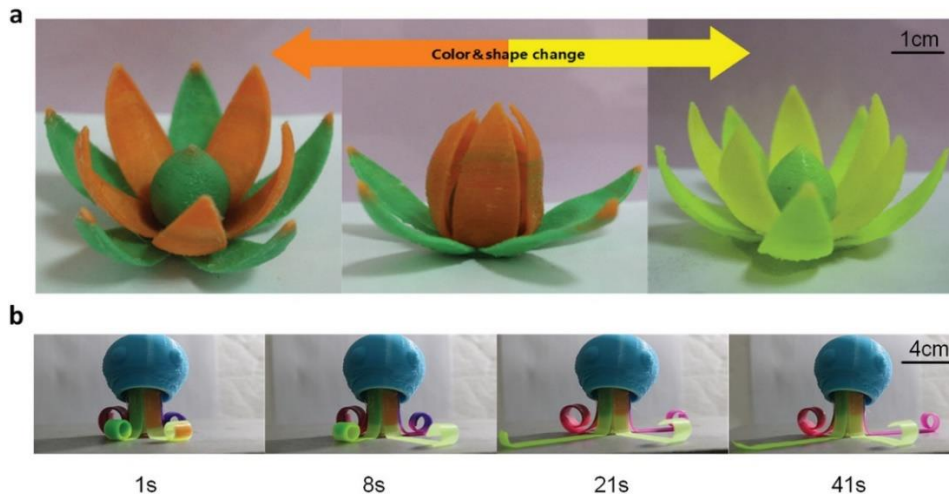
Figure 2.2. (a) Blooming of a flower with sequential shape change, coupled with programmed colour change. (b) sequential octopus legs opening. Reused with permission from [72].

Another use of CNT for SMP composite is reported by the development of an SMP that is heat or light irradiation activated, where the mixture of the SMP is tuneable to control the melting and transition temperature. The use of CNT also allows the structure to be activated via light irradiation, where the design is made of a box with two lids. These two can be actuated separately based on a stimulus [73]. Although these composites are capable of complex shape change and recovery, they are only one-way actuation, with only two shapes.

Multi-shape actuation is also possible when needed in an application, these had been reported in many papers [22], [39] The multi-shape application is achieved by using multi-SME materials structures, by printing them together. Deployable structures, with multi-shape recovery ability at which sequential triggering of materials can be done, are used in order to perform complex applications. The shapes are stable and rigid because of using the bi-stability concepts of materials in specific designs. The structures can change their shape into more than one, allowing multiple applications for a single printer structure. This complexity and multi-use of this design make it a suitable deployable structure in harsh and unreachable environments. A design based on SMP recovery and bi-stability structure is reported in [74].

A triple-shape structure was developed using two different SMP materials, printed using polyjet printing with materials specific to the printer. The triple SME is achieved by having the two materials with different transition temperatures, thus activating each one at a different temperature and thus different time. The strain of the design is programmed by

stretching it, creating a strain difference between the two materials. The three shapes are the original printed shape, the strained stretched shape, and the shape when only one material is triggered [75].

2.5 Stimulus

SMPs in 4D printing recover their original shape by being exposed to a stimulus that ranges from heat, electrical activation, pressure, pH, light, swellability medium, and magnetic fields [49], [76]. SME can be induced by strain difference between two materials, elongation of the structures, electric current via heating, and expansion of prints in part or whole [47], [77]. These changes in the printed structures can provide a large shape change, where different strain between sections of the structure is high. The most popular activation stimuli are environmental heat, electrical activation, photo-activation, swelling, and magnetic activation. There are other stimuli that can be used in smart materials, but these had not been reported by mainstream 4D printing. Thus, they are not included in this study.

The most popular stimulus used in 4D printing is environment heat, since it is the easiest to induce and has the widest range of materials to respond to. A design that responds to the heat that is induced by immersion in hot water is reported. The design is printed in a shape resembling a ball, which is then stretched and cooled down to preserve a temporary shape. Then, the original shape is recovered by the heat in the water [78].

Another popular shape change-inducing stimulus is swelling in a liquid medium. This is generally an easily reversible method, since the swelling is reversible by the removal of the liquid. This method is usually improved by adding an SMP with the swellable materials to preserve the temporary shape while the swelling is reversed. The original shape is retrieved by actuating the SMP to recover its original shape [79].

The heat-induced by an electric current is categorized as independent of heat stimulus. This choice was made as the targeted actuation of electric current and methods of inducing it differ vastly from simple environment heating [80]. Light activation of smart materials is also a popular stimulus that has been explored. The targeted, or general, application of light for actuation is very useful in many situations. Magnetic field activation of SMPs is an important method for stimulus, since it can be activated remotely. This method can be used for the activation of structures that are not accessible via direct heating. Its potential is vast in many areas of biomedicine and others [58].

Joule heating is a method used to activate conductive SMPs, which are a type of SMP that usually have conductive particles mixed in with the filaments [81]. Conductive shape memory polymers are made by incorporating conductive materials into the polymer matrix, such as metals or conductive polymers. Joule heating is a process in which an electric current is passed through the conductive material, generating heat due to the material's resistance [82]. This was used to activate the material and release the induced strain in a printed actuator. This method has several advantages over other methods of activating SMPs since it provides full control over the activation temperature. In addition, this method provides a rapid rise in temperature, which can benefit applications requiring quick shape-change [83].

In addition, Joule heating can be applied selectively to different parts of the conductive SMP, allowing for more complex shape changes to be achieved [84]. In recent studies, silver nanowires were combined with an SMP to achieve local activation, designed to open petals of flowers independently of each other [80].

Conductive materials have also been used in the form of printable ink [85], which allows for the conduction of the current over flexible materials, since the ink does not break at high deformation rates. This concept was implemented in a bi-layer actuator made up of a soft elastomer and a glassy elastomer to enable reversible actuation.

Liquid metal has also been used to print a conductive layer that is sandwich between two silicon elastomer layers [86]. This conductive actuator was able to change its stiffness from rigid to soft by heating up the conductive materials. Similarly, the use of stiffness tunable 4D printed composite allows for control over the deformation of actuators [87]. These actuators were used as pressure sensors and were able to release that pressure when activated. A study presented a design that is activated by an electrical current, which is fed into the structure by electrical wires [80]. The actuation of each separate arm can be controlled, and the gripper created allowed full control in most environments.

Light activation of smart materials is also a popular stimulus that has been explored. The targeted, or general, application of light for actuation is very useful in many situations. Deployment of structures that can be controlled via light, or sunlight timing, can be very useful. Light activation of hinges printed on passive materials is used with dark-coloured material, which can be activated in a sequential manner since targeted light can be used for each hinge [88].

Magnetic field activation of SMPs is an important method for stimulus since it can be activated remotely. This method can be used for the activation of structures that are not accessible via direct heating. The potential of this approach is vast in many areas of biomedicine and others [58].

A printed PU material with different gradients of two materials, one triggered by heat and the other is water-swellable to form a combination of two stimuli, was reported in [63]. The design of the object was tested for different bends and twists, which can be used as a basis for programmed printing for 4D applications.

The use of two different materials enables three shape designs (the original and one for each stimulus). Since the two materials respond to different stimuli, they can be triggered separately, allowing each shape to be triggered in whatever order desired. This is not achievable in multi-material shape-memory composites that respond to the same stimuli at different levels. Swelling of SMPs was also reported in other literature [89], [90].

Swelling in a water medium is an attractive characteristic in biomedical fields since these characteristics can be of benefit in medical uses since their stimuli can be provided passively by the biological systems [91]. The use of swellability in water is also used in multi-stimuli actuation, as reported in [92]. By using two different stimuli, a great range of control is achieved on the shape change.

Most magnetic field stimuli are similar in the function of actuation, since it uses magnetic fields to generate heat in the SMP [58], [93]. The material is made of PLA with Fe_3O_4 nanoparticles, allowing it to heat up with magnetic fields. The printed design is made for tracheal scaffold, which can be triggered after insertion, providing a better fit for the soft tissue shape and might remove the need for an opening operation. The material possessed favourable characteristics, and since it is biodegradable, it does not need to be surgically removed [13].

2.5.1 Two-Way SME

Two-way actuation, or reversible actuation, is a very attractive property of some materials, since the applicable potential of these materials is endless. Some SMPs possess certain reversible shape memory characteristics, although they are weak. There are recent programming methods that allow SMPs to possess substantially reversible actuation, although with relatively smaller strain than that in one-way actuation. This characteristic,

when used in 4D printing, allows for many applications, such as soft robotics and other industry uses, although two-way actuation has not been widely investigated in application-based fields. **Table 2.3** presents the recent advances in 4D printing of two-way, or reversible actuation, of materials. these can be very useful in designs of more complex structures.

Table 2.3. Recent advances in 4D printing of two-way materials, with their potential applications.

Year	SMP	Printing method	Remark	Reference
2021	Graphene polylactic acid (GPLA)	FDM	Voltage-controlled deformation for revisable actuation	[94]
2020	PCL and PU		Programming method of PU material for two-way actuation	[95]
2019	VeroWhitePlus (elastomer) TangoBlackPlus	Polyjet	Reversible actuation via the use of swellable elastomers	[96]
2019	PU prepolymers carrying crystalline polytetrahydrofuran (PTMEG) and poly(ε-caprolactone) (PCL)		Two-way actuation programming	[97]
2018	polycaprolactone	Local photo-irradiation	Revisable two-way actuation on programmed materials for specific actuation.	[98]
2016	Grey60, Tangoblack (TB) and a hydrogel	Polyjet	Reversible and stable actuation	[99]

Two-way actuation is achieved when the material changes its shape without the need for a programming step every time a shape is recovered, without the use of external strain and force to shape it. This type of actuation requires more work when it comes to SMPs, for there

is usually a programming step that is needed in the synthesis of the material. For instance, SMAs have reversible actuation with a specific treatment, which is reported with Nitinol as it is used along with an SMP for improved actuation [19].

As in earlier years of 4D printing, the use of swellable hydrogels is a relatively easy way to achieve reversible actuation, since the gel expands in water or other mediums causing strain against any other material. Good examples of this property are reported in a study on self-expanding and shrinking structures [6], hydration or water sensors [66], and double response of materials by means of swelling and magnetic stimulation [100]. Hydrogels are widely used in two-way actuation, although the reversibility is lengthy and requires a swelling and de-swelling environment [2], [101]. Discussion on these material types is required in more depth, but the scope of this review focuses on SMPs.

Two-way actuation of SMPs has been reported in the past few years, allowing the progress of SMP into the fields of soft robotics and actuators. A programming step for two-way actuation in SMPs, PU and PCL is used and proved to bend and return to the original shape depending on the temperature of the environment. The two states are programmed by heat treatment in the material that allows it to possess two crosslinking networks. The two-way programming is made by specific steps that are reported as being applicable to many materials. The two-way actuation is reported to keep cycling for many trials.

Two-way actuation of SMPs offers a unique characteristic that is highly favourable in many applications [95]. Another programmable reversible actuation is reported, where stress-free actuation is induced by the temperature difference [97]. A flower blooming was made as a proof of concept, where the blooming was controlled between the temperatures of 55 to -5°C. The design of the material is very simple, which was reported to also work with other materials that are still to be tested.

Swelling of elastomers alongside SMPs has been achieved based on a similar approach of having the strain induced by the volume difference of the hydrogel to the SMP, while the SMP holds the new shape in place after the elastomer has been de-swelled. This shape can be held, while the original structure shape is retrieved by heating the SMP, allowing it to recover to its permanent shape, similarly to the actuation of hydrogels [96].

More recently, the design of a reversible actuation unit at which the actuation is made via the swelling of an elastomer is reported, where the shape is held together in a temporary shape via an SMP. As the first layer swells, stress begins to build since the other material

does not swell. The release of the strain of the SMP changes the shape of the PAC into its temporary shape, or permanent if the de-swelling is not allowed [102]. This allows the resetting of the actuator with stimuli instead of manual programming. Another reversible SMP that relies on reversible bonds of the polymer is reported, where the authors designed an SMP that is thermo- and photo-responsive [98]. The structure has two states that can be controlled by changing the temperature from 0 to 80°C. This technique of programming can be used to achieve reversible actuation, which might be used in soft robotics and biomedical applications.

2.6   4D Printing Techniques

4D printing techniques are vital to the nature of the actuation needed for the printed structures, since many functional characteristics of the materials are printer-specific. Each printing method has its advantages and disadvantages; these are application-specific. The most common printing method is FDM, since it is a cost-effective technique that offers freedom in the choice of materials [103]. Another material extrusion method is DIW, which can extrude materials that are heated or in liquid form [65], [79].

Polyjet and SLA printing are favoured by some researchers because of the resolution and accuracy of these printing techniques, although the materials that can be used are limited to resins [46], [104]. DLP printing is a more rapid printing technique than light printing, since it cures a full layer at a time instead of a single point at a time, which has good definition, but may suffer from poor finishing [105]. In this section, the most widely used printing techniques are discussed with their recent uses in 4D printing. FDM, polyjet, DLP, DIW, and SLA printing are discussed.

2.6.1   FDM Printing

Fused deposition modelling is the most common method for 4D printing. This method uses filaments of materials to print light by line, one layer at a time [29], [106]. FDM uses a heated extruder head that melts the material while depositing it onto the print board. The heating of the material not only makes it easily printable in all directions, but also generates enough heat to melt previous layers of the extruded materials, thus melting the newly extruded material into the old one. This method is the cheapest of the printing methods because of the ease of use, but it is favoured by researchers mainly because of the freedom of choice of filament. Due to the nature of the material needed for extrusion, the filaments can easily be made with few complications [107].

Any suitable material can be shredded and extruded with simple heated extruders to make filaments, allowing endless easily-made composites for variations of applications. Because of the popularity of this printing method, many predictive models for design are made. This is done with the aim of providing faster fabrication time for untested designs. A recently developed concept model for SMP behaviour, which can be used in designing SMP actuators, is made for the predicted behaviour of the print. The model can be used for pure SMP and SMP-based composites [108].

PLA, which is the most common 4D FDM print material, is used as a base material for printing using FDM in another study, in which a wide control of printing temperature and speed is available [42]. By varying the printing nozzle temperature, the recovery time is varied. Thus, by using different printing temperatures for different sections of the print, the authors managed to have a multistage actuation of the object, as is presented in **Figure 2.3**. By controlling the filling angle of the nozzle, the shape memory force of the object was controlled, thus controlling different sections of the print. These parameters provide a great guide for the printing of PLA with pre-determined programming [42].
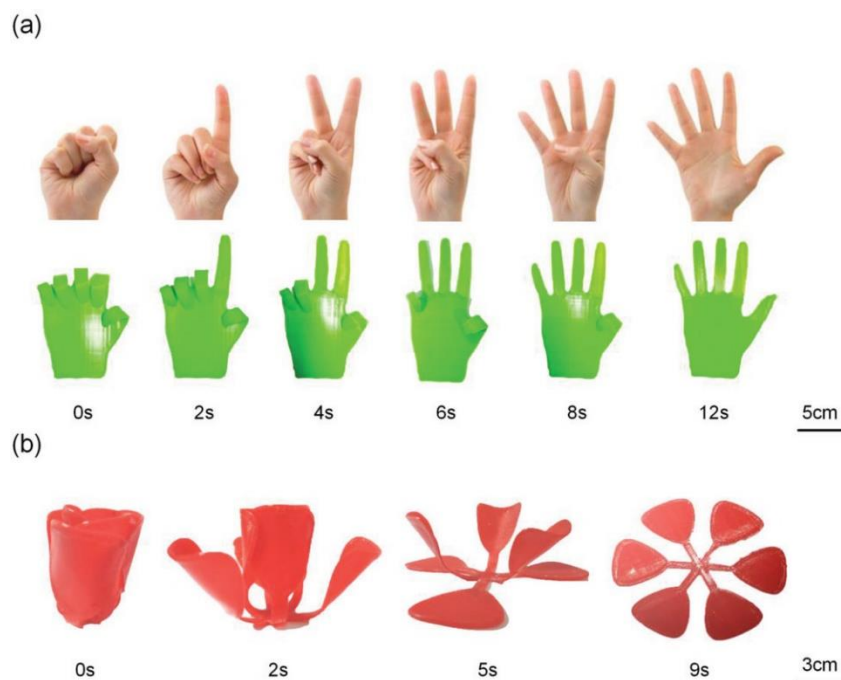
Figure 2.3. Printing of PLA with different thickness values to produce a sequential shape change. Reused with permission from [42].

2.6.2   Polyjet Printing

Polyjet printing is another popular printing method that is used because of the accuracy and resolution of printing. This method provides many advantages over other printing methods although it is relatively expensive. Polyjet printing is a non-contact print, in which droplets of ink or polymer are deposited on the printing tray, which is usually then cured by UV light [45], [109]. Such an approach provides high printing freedom, which is mostly favoured when printing multi-material structures. Polyjet printing is an AM method where the mechanism allows easy use of multi-material in the print [110], [111].

Grading of material changes the SME response of that material based on the width. A graded SMP that can have sequential shape recovery is printed using a polyjet, allowing it to form relatively complex recovery shapes. The shape recovery is triggered by heat, and thus the placement in hot water was used as a stimulus.

Polyjet-printed structures can also be tailored for rapid shape recovery and shape recovery by sections [112]. The sequential triggering can also be programmed in a way to induce better bending of materials. Hinges with a 90° bending angle of sequential triggering were created, where the bending sequence depends on temperature. The folding of the object can lock itself by making use of the time each section moves. This is shown by the bending of a flat design to make a locked box in **Figure 2.4**. The full bending of the design is achieved in a very short time of less than 20 seconds [113].
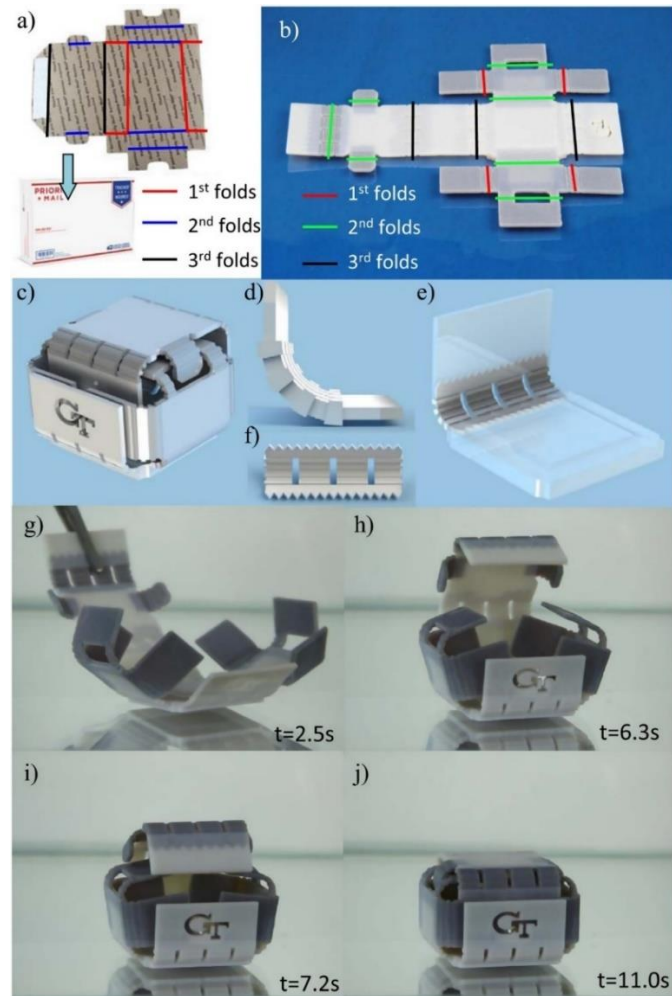
Figure 2.4. Polyjet printing of multi-material box that is made up of active and passive materials, allowing sequential and locking SME. Reused with permission from [113].

2.6.3 DLP Printing

DLP printing is a rapid method of printing that is very similar to SLA printing, but uses a projector to polymerise a full layer of a design. Any projector with UV light can be used, as the resin will react to UV light, thus it is an affordable printer that can be made using a UV projector and a screen [114]. The print is made by pixels of light onto the resin, which causes the finishing of the smooth object to be rough, since no smooth movement of light is required [115]. where the layers are printed and lifted one at a time, while the other layer is being cured.

Polymer enhancements are made by fixing the resin used in printing and incorporating ureido-pyrimidinone units into PCL to obtain a polymer with good shape memory properties

and self-healing ability. Therefore, the actuators created are soft actuators with favourable properties [30]. Printed using DLP, the designs are low-cost and applicable in human-machine interactions [116]. An SMP with tuneable properties upon fabrication was developed using DLP. The material's agreement shape is reconfigurable allowing the reuse of the material. Various uses of the same printed object can be done if it is to be reconfigured, presenting a wide range of applications [117].

Printable ink with very high mechanical strength and good shape memory properties is also reported, with a high transition temperature, allowing industrial use. Since the material is ink printable, it can have a very high resolution with DLP [118]. Studies had also been made on creating photo-curable materials with better SME characteristics for applications in DLP [119]. This allows for the creation of mechanically robust prints that can stand excessive loading onto the structure, which is demonstrated in **Figure 2.5** by printing mechanically robust hinges that are used in robotics.
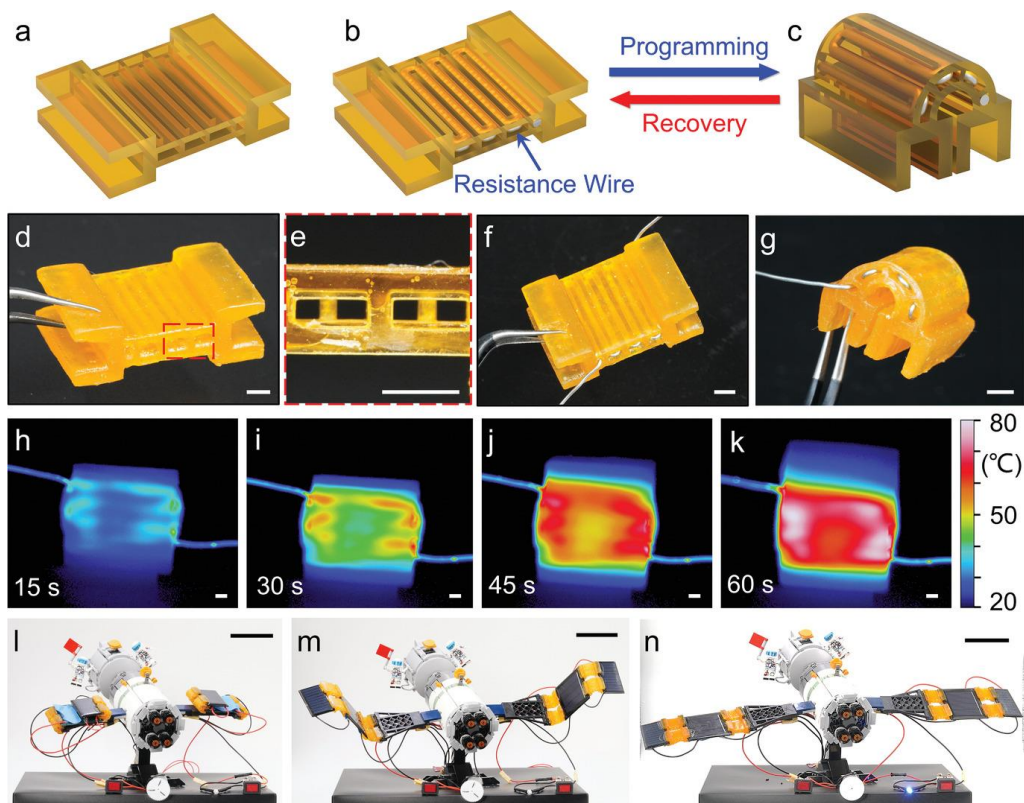
Figure 2.5. Highly complex designs printed using DLP with mechanically superior characteristics. Reused with permission from [119].

2.6.4 DIW Printing

DIW printing is not much different from FDM or DLP, as it dispenses polymeric ink onto the print bed, which is then cured one layer at a time [120]. DIW is known for the high resolution of prints, although it is not as popular as other printing methods due to the curing step that is involved after the print of every layer [121]. This printing method is highly customizable, since the curing of the ink can be made to cure right after print, allowing for the complexity of design without the loss of structures [122]. A highly-stretchable, self-healing material using different resins in direct-ink-writing printing is reported. The combination of the shape memory and self-healing materials provides advantages to this material, making it of versatile use, especially in biomedical applications. The material is soft and is capable of maintaining high-complexity shapes [123].

DIW, also commonly known as syringe printing, is used for special prints. Usually, the two names are based on the apparatus used for the printing. Since most syringe printing is done with semi-liquid materials that are either ready or need to be cured after deposition, a syringe that is piston or pneumatically engaged is used and thus the naming distinction is used [124]. A major advantage of this printing method is that it can be printed in a support medium, allowing delicate and sensitive designs to be constructed without the need to print supporting structures [125]. As heat is not always needed for the print, a lot of freedom is allowed in this method of printing. This method is favoured in biomedical applications because of the freedom of printing, and the relatively low effect it applies to the materials.

As reported in [126], there are multiple ways in which a syringe can dispense materials, depending on the material needed. The use of this printing method allows easy mixing of materials with the SMP, thus providing a test bench for many mixtures of improved and re-enforced SMPs. The syringe is used to print an object with active and passive regions, a technique widely used for 4D hinges. The material used responds to water and acetone for swelling and de-swelling, as the objects close in acetone and can return to their original shape in water [79]. To demonstrate the versatility of this method, PU composites with nanoparticles were mixed into a syringe extruder to explore the properties of PU 4D printing capabilities and improve them [65]. The material shows favourable characteristics with the potential for higher-resolution printing. Various objects were printed with high fixity and recovery rate, while still being cost-effective. The printed designs that were tested are shown in **Figure 2.6**.
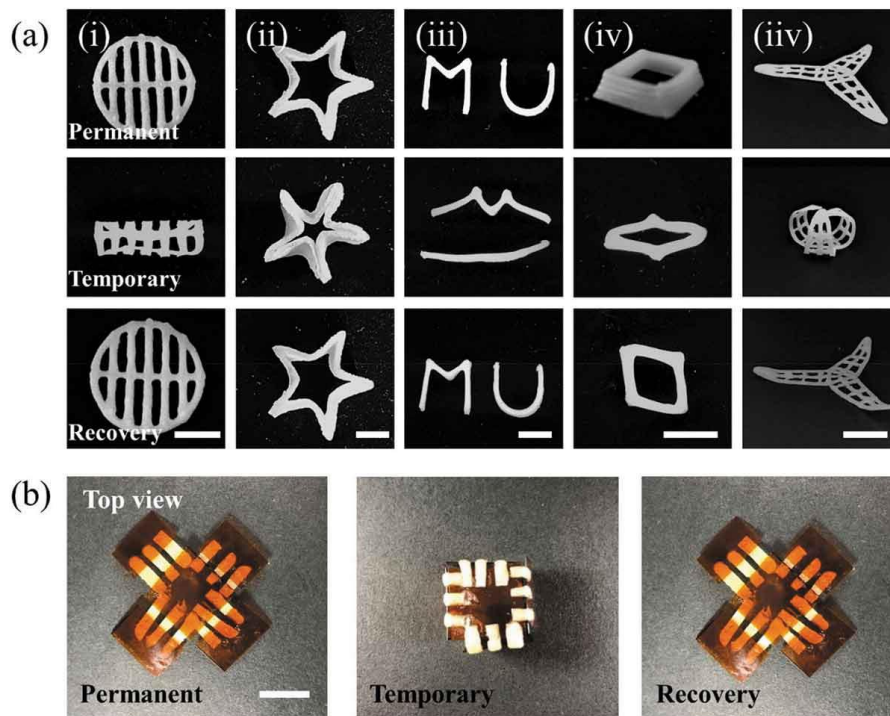
Figure 2.6. Printing of PU composite with nanoparticles for favourable SME characteristics. Reused with permission from [65].

2.6.5 SLA Printing

SLA printing uses a laser-emitting diode to polymerise a resin mixture. This technique does not require support for the structure because of the moving base of the resin [127], [128]. SLA printing has a very fine finish on the printed materials since it uses a continuous light source for printing, removing any trace of pixelation in the structure [109].

SLA is one of the fastest-growing printing methods in 4D printing because of how accurate and precise its prints are, and the smoothness of the print that is caused by the laser movement [128]. The printouts of SLA are favourite in sensitive applications in which high precisions and finish are vital for the success of the design. The control of the parameters is also used in order to develop specific characteristics.

To improve the resins used, Nanosilica was infused into the SMP for better curing. The nanosilica has altered the light scattering of the printing irradiation. The curing time for each layer of the resin has been extremely reduced from 4 seconds to 0.7 seconds. The SME properties had also been enhanced with the nanosilica, where high shape fixity and recovery, along with a longer cycle life, had been achieved [129].

The design of grippers is one of the most popular proofs of concept designs in 4D printing, since it not only tests the flexibility of the material, but also requires timing of recovery and strain induced by the gripper to grab objects, as shown in **Figure 2.7**. The design of highly-customizable SMP structures is printed using SLA, at which the stimuli temperature can be controlled. The use of projection micro-stereolithography allows much higher resolution than typical 3D printing techniques [130].
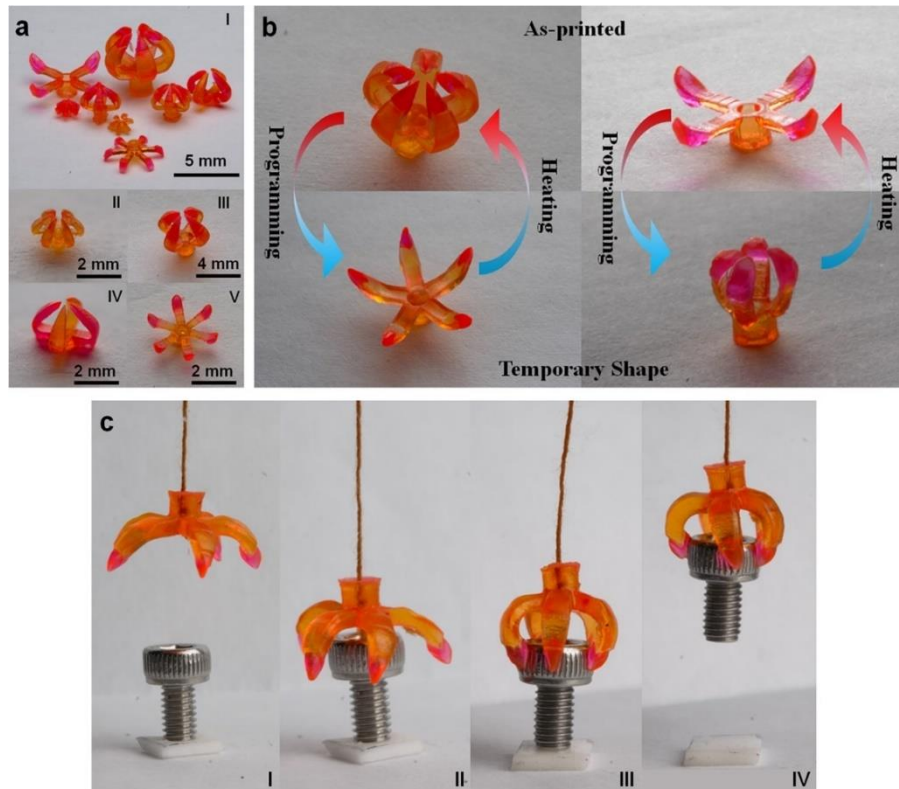
Figure 2.7. SLA-printed gripper with 5 arms. The gripper is small but with enough strain to hold a bolt. Reused with permission from [130].

2.6.6   Other 3D Printing Techniques

There are many 3D printing techniques that are not considered in this review since they will not be of benefit to this review. Although that is the case, there are some 3D printing techniques that are not used commonly for 4D printing but have the potential to be used in such applications, SLS, SLM and DED are a few of those methods. The use of these methods is predicted to be incorporated into 4D printing in a more inclusive manner in the years to come.

2.7   Shape Programming

The programming of both the permanent shape and temporary shapes of a printed structure can be achieved in several ways, most commonly is inducing strain on the material post-printing and heating beyond the transition temperature [38]. This type of programming is the easiest to predict and repeat since the force used and strain-induced are measured and applied in a precise manner, but this, of course, dictates that the printed structure is in a permanent structure. This does not need to be the case since there are other ways of programming SMP materials pre- and post-printing. Strain-induced in the printing process (called pre-strain) [131], if measured and used accurately, can be used to program precise shape changes in the structure so that the structure is printed in its temporary state [42]. This type of shape programming is commonly referred to as non-manual programming, which is normally found in all reversible actuation where a certain stimuli-activated actuation can reset another strain in the structure [102], [132].

For one-way or non-reversible actuation, certain printing parameters, such as speed, temperature, and printing patterns, can affect the shape change of the structure. These techniques of printing that dictate the shape change when the SME is activated are called shape programming of 4D printed structures. This section discusses the shape programming of SMP-printed materials, whether it is manual, non-manual, or post-printing. The programming is categorised by the nature of the shape programmed into the structure. Shape programming is different when using a single material or multiple materials in a PAC. This section discusses programming approaches, including single-material prints, multi-material prints, and origami approaches to shape programming.

2.7.1   Single Material

Shape programming of single-printed materials is made using either controlled printing parameters, post-print strain-inducing above the transition temperature, or changes in material thickness. Bending of materials as recovery is the most commonly reported actuation, since it is the most basic and provides a good ground for proof of concept [21], [31]. Most proofs of concept prints are either printed in a dumbbell shape for parameters testing, or long actuators for SME testing [71], [133].

Other methods of recovery involve twisting of the structure, but this is induced by strain force [130], where the twisting can be forward or reverse. The material is printed in its permanent shape whether twisted or straight, while the actuation is usually the change

between these two states. **Table 2.4** presents recent studies done on shape programming for single-material prints, which can be used as a reference for shape programming for applicable structures. The mentioned methods in the table are presented visually by their actuating mechanism in **Figure 2.8**.

Table 2.4. Shape programming for single-material prints.

Shape change programming	Method	Advantage	Reference
Bending	Recovery from permanent shape after a strain-inducing bend.	The simplest form of shape change	[21], [31], [58], [71], [133]
Twisting	Recovery to printed spring structure after strain-inducing straightening.	Used in non-linear movements	[130]
Unfolding	Recovery to shape after edges are folded.	Sharp bending angles	[32], [52], [72], [133], [138]
Sequential shape change	Activation of sequential hinges using different thicknesses of sections.	Timed activation	[42], [73], [134]
Elevation	Printing of auxetic patterns that elevate when activated.	Mechanical application	[20], [135]
Local bending	Activation of certain sections of the structure using light-induced heating.	Controlled actuation of different parts	[15]
Concave	Concentric printing pattern of SMP, varying print temperature to control induce printing strain.	Surface manipulation	[136]
Expand to fit a mould	Hexagonal patterns recover full expansion shape.	Medical applications, such as stents	[139]
Helix	Recovery to printed helix pattern.	Mechanical applications and energy absorption	[140]
Contract	Strain is induced in the printing process, and the original shape is recovered after activation.	Robotic applications, and linear manipulators	[141]
Non-uniform	Cross-linking of polymer control through grayscale values.	Used for non-confined shape change	[137]
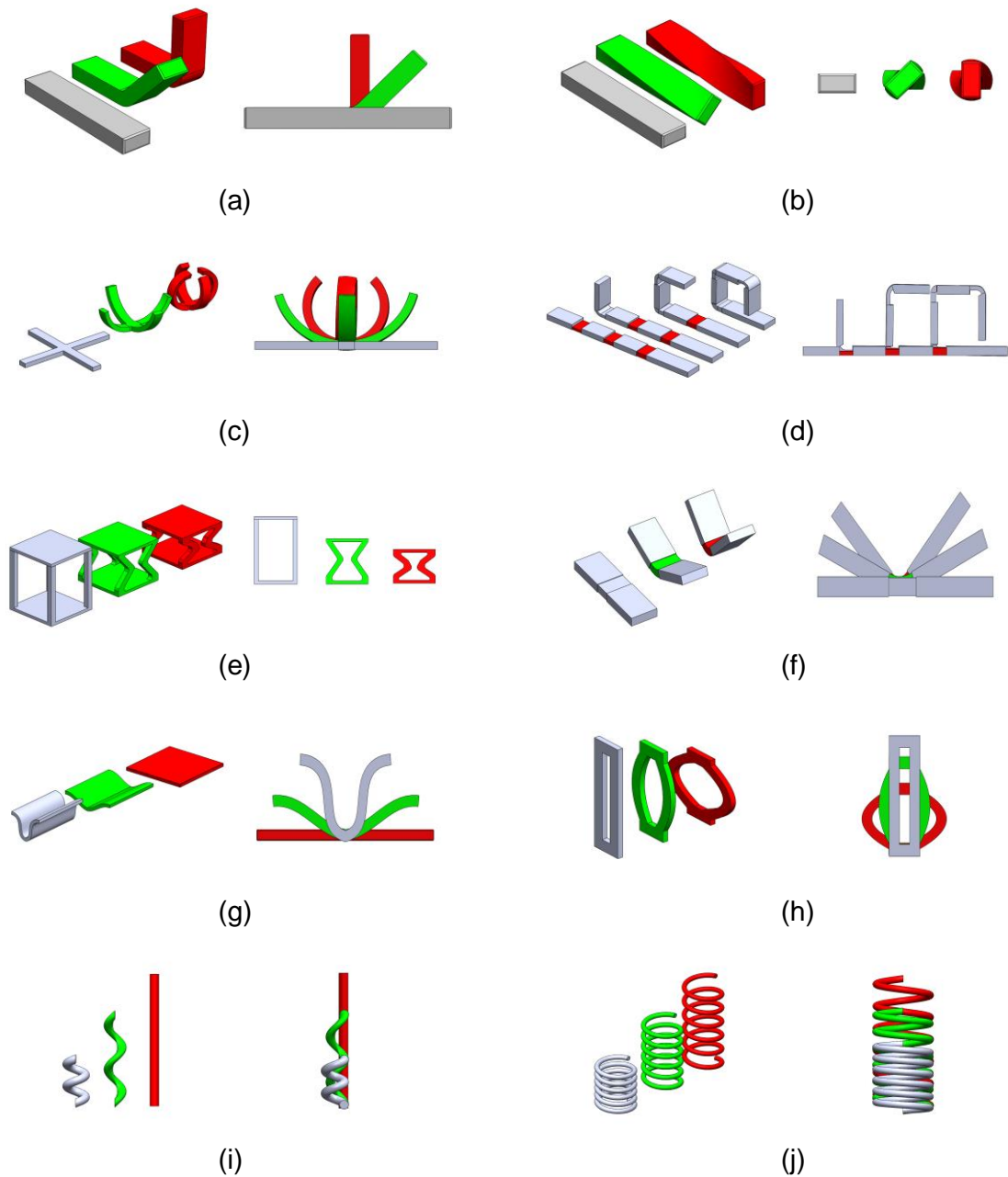
Figure 2.8. 3D and frontal views of shape programming methods for single material prints. (a) Bending. (b) Twisting. (c) Unfolding. (d) Sequential shape change. (e) Elevation. (f) Local bending. (g) concave. (h) Expansion. (i) helix. (j) contraction.

For more complex designs, and not necessarily complex programming, unfolding of the object is used as proof of concept [32], [52]. The designs are usually centrically printed with edges of lower thickness for easier SME, which is activated by the bending of the edges for either programming or actuation [72], [133]. A more applicable design of printed

structures is sequential actuation, whether it is by actuation timing or actuation temperature [134].

Sequential actuation of a single material is a highly-beneficial design since it provides multi-material abilities for a print of a single material, saving time and cost [42], [73]. The actuation is highly controlled with precise timing, which is done by the layer number of each section of the structure. The use of multiple SME prints for elevation is achieved by printing auxetic structures, allowing recovery in a vertical manner [20], [135]. Printing patterns are also used to influence the actuation of the materials into a specific shape. For instance, a centric printing of a flat shape can cause a concave shape to form upon actuation [136]. The curing of materials at different scales can also induce a controlled actuation. This is reported by the use of UV curing of resin at a different rate, allowing non-uniform actuation [137].

2.7.2 Multi-Material

The use of multiple materials in a single printed structure can provide advantages to complex designs that are of superior characteristics to those of a single material. Most commonly, the use of multiple materials provides a better strain, larger angles of actuation, faster shape recovery, better shape fixity, and higher possible complexity of the design.

The use of different strain values between two materials is usually utilised to induce bending in a printed structure [6], [75]. This approach is commonly used for hinges and basic designs for many 4D-printed actuators [11], [108]. The bending is achieved by the use of one or more SMPs, usually an SMP and an elastomer, thus improving the elasticity of the structures. Folding of structures is the base for PAC hinges [79], [88], which is done by either a multi-material hinge with a single material edge for straight folding, or with single materials for both hinge and edge but the bending is induced by strain force [35], [142].

Swelling of a material that is held by another material also causes strain difference, since the volume change of one of the materials bends the other inwards [63]. Sequential shape change is of higher control and strain force when using multiple materials, the use of multi-materials also provides separate actuation requirements for each section, thus allowing a highly complex sequence of SME [112], [113].

Twisting and other non-angled actuations are usually achieved by printing two materials with different printing patterns, thus allowing for twisting in a very controlled direction. This is different from the single material twisting since the material twists by itself

upon activation instead of being manually programmed into a shape [11]. A unique design is reported where controlled rotation is achieved in 4D printing, which opens the way for many applications [143]. Surface expansion using origami is also of superior benefits to single material actuation, which is done in certain applications to save space before deploying any structure [60]. **Table 2.5** presents recent studies done on shape programming for multi-material prints, which can be used as a reference for shape programming for applicable structures. The mentioned methods in the table are presented visually by their actuating mechanism in **Figure 2.9**.

Table 2.5. Shape programming for multi-material prints.

Shape change programming	Method	Advantage	Reference
Bending	Strain difference between two materials when one of the material's SME is activated.	Superior shape change due to strain difference	[6], [11], [64], [75], [108], [144]
Folding	Bending of hinge section to induce folding of the rest of the structure.	Passive sections unaffected by the shape change	[35], [36], [79], [88], [142]
Sequential shape change	Activation of sequential hinges using graded mixing.	Timed actuation of certain parts of structures	[112], [113]
Helix	Printing pattern of one of the materials in a diagonal pattern.	Non-manual shape change	[75]
Twisting	Printing of SMP around support in a helix pattern.	Control of bending polymer by printing means	[11]
Rotation	Printing of centred base with connectors using bi-stable design of rigid and rubbery materials.	Complex mechanical movements	[143]
Uniform	Recovery of SMP patterns	Surface expansion	[145]

patterns	printed on textile.		
Elevation	Multiple hinges used to lift a base when activated.	Mechanical applications	[36]
Gripper	Bending of multiple sections into the centre.	High-strain grippers for better manipulation of objects	[80], [146]
Surface expansion	Origami patterns with active materials.	Used in self-deployment	[60]
Non-uniform	Non-uniform graded shape changes based on different ratios of two materials for swelling in water.	Used on non-confined shape change	[63]
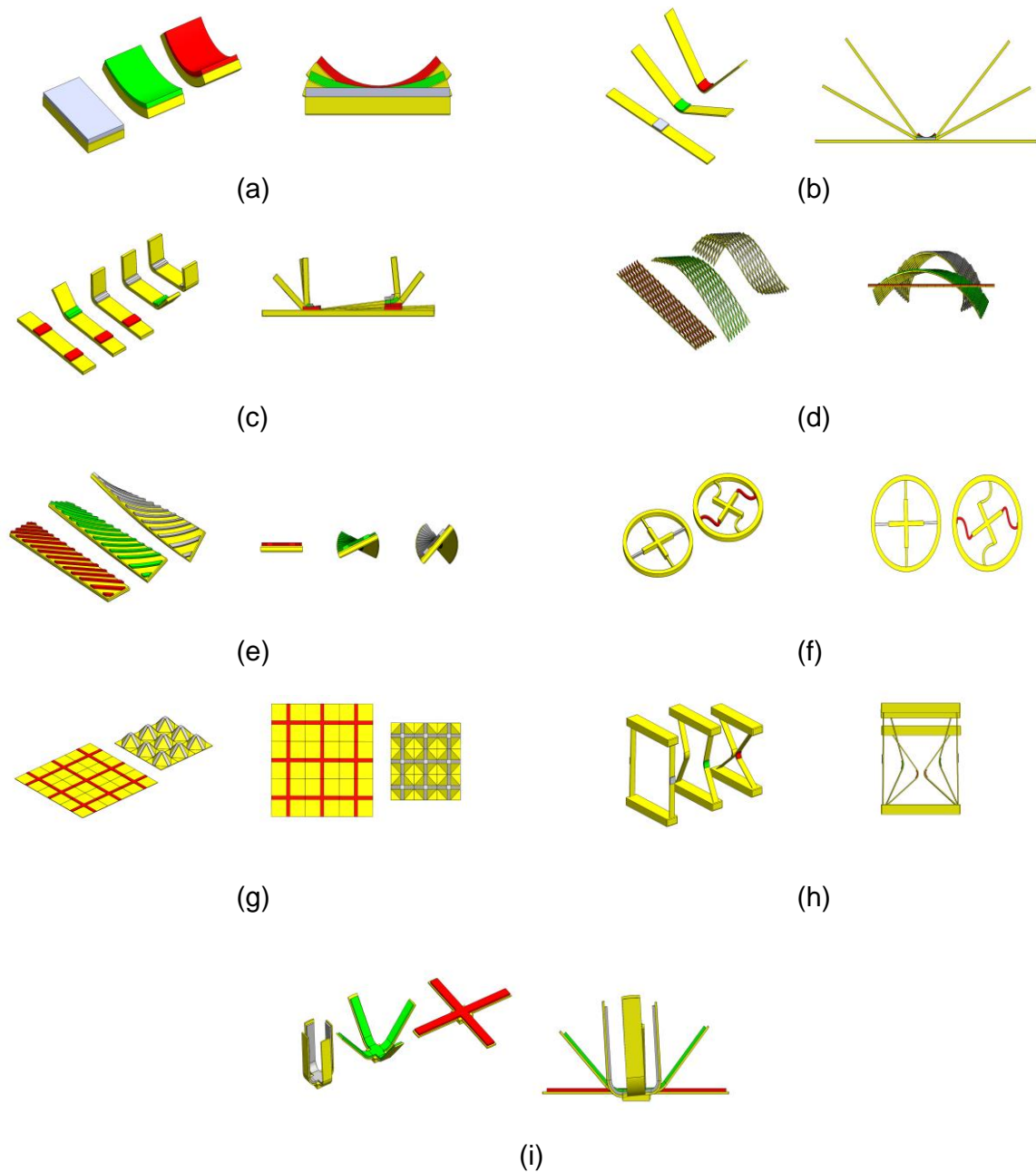
Figure 2.9. 3D and frontal views of shape programming methods for multi-material prints. (a) Bending. (b) folding. (c) Sequential shape change. (d) Helix. (e) Twisting. (f) Rotation. (g) Uniform patterns. (h) Elevation. (i) Gripping.

2.7.3 Origami and Patterns Approach

4D printing and origami design go hand in hand, since the complex yet controlled folding of origami can be achieved via 4D printing. Certain characteristics of SMPs, which are highly tuneable as discussed, can be controlled for either sequential or separate actuation [147]. The knowledge of origami will allow the design of self-assembled highly-complex

structures. These structures can be printed into a flat sheet that will sequentially fold to a specific structure [148], allowed by either hinge on the design of strain difference.

Reversible origami has been reported by using hydrogels and photolithography. The design is complex, yet the printed material followed the specification with reversibility. 4D printed scaffolds that unfold using origami patterns are presented in **Figure 2.10**, where the scaffolds are tested by deformation in hot water [149]. The use of origami patterns in the prints allows for uniform deformation along the whole scaffold. The uniformity in deformation is vital for application in medical implants since the force of deformation is equal along the scaffold, reducing injury risk and size of the implant upon insertion.

Hydrogels allow a wide range of actuation since they are easily designed to bend at certain hinges [150]. These structures are printed flat and can go between the origami structure to a flat sheet. Hydrogels are used alongside SMPs since they cannot hold their shape in certain environments, unlike SMPs. PAC active hinges have been used in polymer origami, which allowed a wide range of structures to be constructed [35], [142]. PAC hinges are developed and designed to specific angles that are sometimes controllable in their angle, recovery speed, and time. Other types of shape change, although without overlapping in the sections, are based on origami designs which produced cross folding structures of times and well-coordinated shape change [151], Miura-origami structures capable of delicate and complex shape change [152], and circuit application [153].
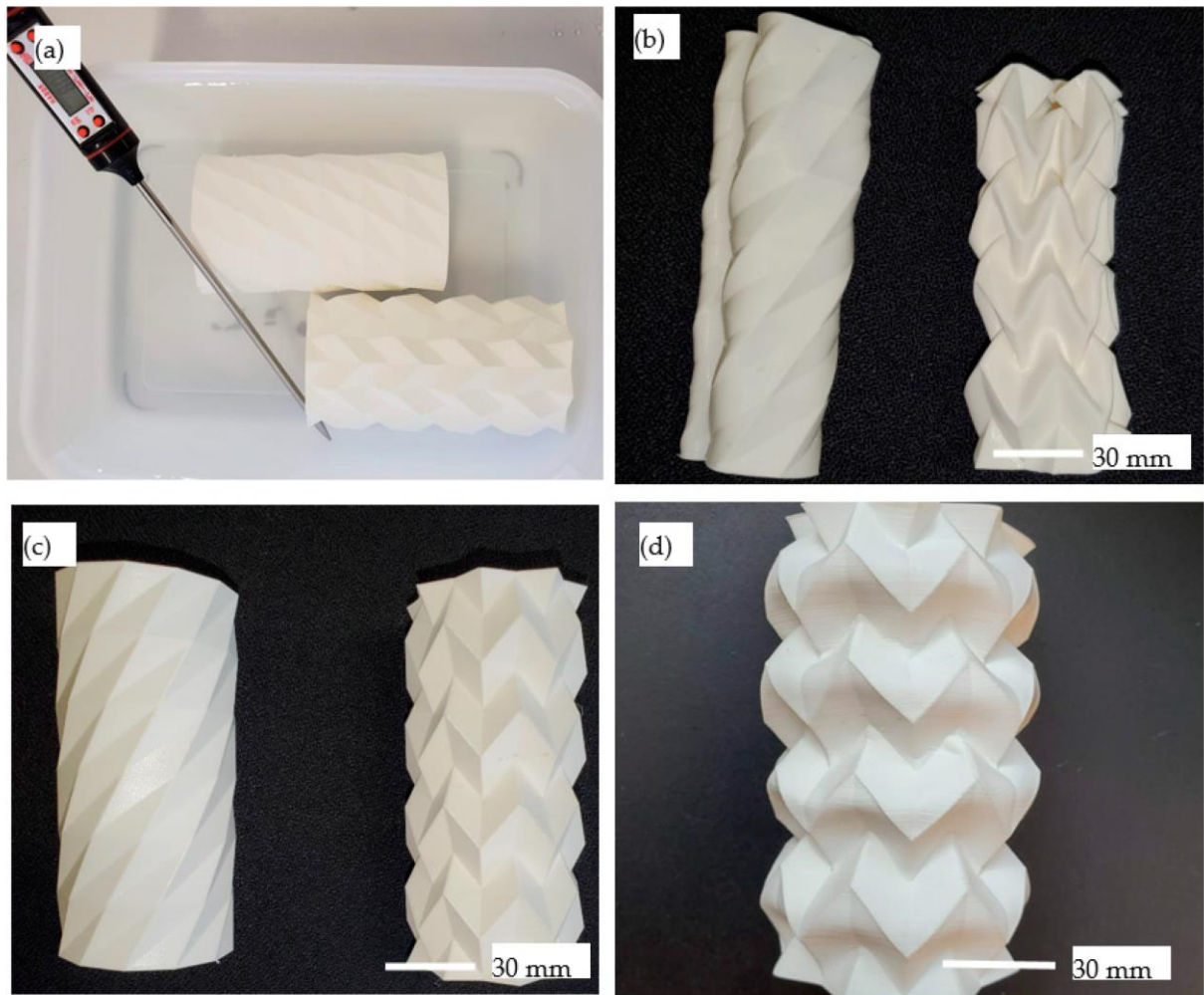
Figure 2.10. Origami-inspired design of scaffold prototypes tested through cycles of deformation. Reused with permission from [149]. A) Heating b) Manual programming c) Different patterns d) Activation

4D-printed origami-based designs rely on the more complex programming mechanisms of 4D printing. Most proofs of concept designs that use origami are based on surface shape change, buckling, folding, or changing the volume of the structure. This is because of the precision needed in forming complicated shapes by origami. Biomimetic 4D printing is widely based on origami designs because of the complicated folding patterns that occur in nature. Although biomimetic designs may seem limited in applications, the same concept can be applied to a plethora of applications that require complicated actuation of materials, because the designs are ready in nature. An origami opening of a wing is reported with a high volume change [154].

Origami provides easier design once the nature of the actuation is understood. The use of origami can be of a very high complexity that is reduced by understanding the printing patterns needed to be done on a flat sheet. Once the hinges of the design are made, the designs can be personalised freely in non-uniform bending [155], [156].

Other designs are made with reversible hinges that can be activated via electrical current. The use of hinges can be implemented in multiple ways that can go to and from 3D structures designs to flat shapes, with high control over the timing because of the stimulus [157]. Two-way SMP actuation in origami designs still faces many challenges that limit its practical implementation. This is most probably due to the complexity needed in designing reversible origami, as well as the finding the suitable materials that can be both reversible and of biomedically appropriate characteristics.

In a similar manner, many researchers are looking toward nature for improved designs, where these designs are bio-inspired 4D printed structures. This concept has been a big part of multiple leading technological advancements because of the freedom it allows in the formation of structures, providing the ability to make agile mechanical movements in a rigid body [158]. In addition, bioinspired designs topology optimisation, enable energy-efficient actuation, embodied intelligence, and allow flexible robots to exhibit different behaviour than traditional structures [159], [160].

Bioinspired 4D printing has been applied in many fields due to its ability to control many characteristics in the structure that may be uncontrollable by materials preference or too complex and non-compliant for traditional mechanisms. The structures of various living organisms have been mimicked by many researchers to develop 4D-printed bioinspired flexible and adaptable devices [161]. For instance, Faber *et al.* utilised programmable folding based on the wing of the *Forficula auricularia* to 4D print a structure using PLA and thermoplastic polyurethane [154]. In another work, Liu *et al.* developed 4D-printed hydrogel tubes that were inspired by the structure of the coral polyp [162].

Bioinspired designs were also investigated by McCracken *et al.*, who used ionic hydrogels to 4D print biomimetic aquatic organisms [163], and Gladman *et al.*, who developed biomimicking plants for complex planar to 3D morphology [164]. Another research team developed leaves-like structures that were inspired by the reversible shape-changes of *Pinus wallichiana*, which were 4D printed using wood-polymer composite and acrylonitrile butadiene styrene (ABS) [165]. Peng *et al.* developed biomimetic leaf, snail shell, and worm-like structures that were 4D printed using PLA [166]. Other researchers

utilised the tensioning of the stem helix of the *Dioscorea bulbifera* to develop a 4D-printed self-tightening splint [167]. The structure was printed using a combination of wood-polymer composite and ABS. In another research, Zeng *et al.* proposed bioinspired 4D printed actuators based on the adductor muscle and hinge of the muscle-shell using PLA [168].

Despite the promising advancement achieved in bioinspired 4D printing, there are still many areas that require investigation and improvement. The possibilities of living organisms that can be used as inspiration for biomimetics are unlimited. In addition, the effect of printing patterns on the performance of 4D-printed actuators has not been explored well so far.

2.8   Application-Based 4D Printing

4D printing has the potential to be implemented in many applications because of the prototyping freedom and the use of smart materials, specifically SME materials [169], [170] Although it is a relatively new field of study, there is a great interest in using 4D printing in many fields, such as biomedicine, industrial unit, sensors and soft-actuators of robotics, and electronics [70]. The categorisations of the recent applications are made by seeing the directions in which the majority of researchers were heading in the past few years which includes going into medical application-oriented designs [38], [51] and soft robotics [103]. Other fields that have risen in the literature include the use of 4D printing in the food sector [171], energy harvesting [172], and the use of fibres in the materials [173].

In this review, a section presents the applications, which are appropriately divided into four categories, namely, biomedical, engineering, bio-mimetic, and electronics applications, as demonstrated in **Figure 2.11**. Furthermore, recent advanced applicable 4D printed structures are presented. Application-based 4D printing is the next step in the advancement of this field. This is where the materials and printing methods are chosen according to the application that is needed, instead of the other way around. There is still a limited number of reported studies on the applications of 4D printing. However, in recent years, there have been advancements in the nature of applications of printed designs.
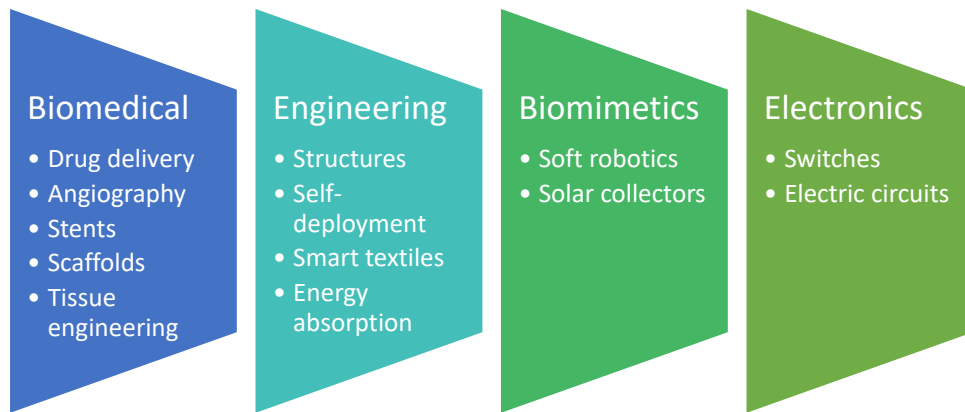
Figure 2.11. Application fields that are popular in 4D printing.

The field of applications that seems to benefit the most from 4D printing is biomedicine [174], [175]. This is because of the ability of the SME to allow never-before-possible applications in the medical field. Biomedical applications need a certain type of materials in order to be safe to be used in the human's body, since they may need to be non-reactive or possess a certain lifetime. In certain biomedical applications, the need for devices for structures that can be used with minimally invasive surgeries can be achieved and enhanced by the use of 4D-printed structures [176]. The applications in this field could benefit greatly from better triggering or actuation mechanisms so that 4D-printed structures can be used in more difficult and harder-to-reach bio-life structures [105].

Radiopaque and porous materials are developed for biomedical use, since they are not reactive [12]. The synthesised materials for 4D printing are vital for certain applications because the structures and printed need to pass many regulations on health and safety thus they are needed to be applied to other designs. The development of tissue-replacing support structures [177] is made with certain materials that support the tissue while it heals. These structures are made with materials that can be integrated into the body without causing any harm.

Deployable antennas with a small surface area that expand upon activation [60] are an important development in deployable structure studies, since they can be used to save space in vehicles or space applications, where the reduction of mechanical hinges and space is needed. Various activation mechanisms can also be used in bio-life applications, where heat is not the most suitable stimulus, such as in cases that benefit from solvent-driven actuation [178].

Structural supports for surgical replacement of heart problems have been reported in [179], in proof of concept of absorbable appendages that can change their shape to allow muscle movement. Early prototypes of other supporting scaffolds that make use of the benefits of 4D printing have also been made [180].

A similar approach is made using origami principles [150]. These types of prototypes are the basis for applicable and medically viable devices. The development of a printed SMP that is enzymatically activated is reported for drug delivery mechanisms as well in [27], [140]. Drug delivery systems of similar effects have been reported using piezoelectric valves in the past [181] and pneumatic micro-actuators [182], the same mechanism can be replicated for an appropriate 4D printing application.

Engineering applications are categorized as those that involve structural designs for non-medical applications, support systems, and self-deployed structures. Structures that make use of the ease of complexity of AM have benefited from 4D printings since not only these prototypes can be rapidly printed, but they also benefit from the characteristics that are added by the smart materials. The SME of SMPs allows for timed and selectively-activated reactions, making these materials suitable for self-deployed structures.

Many self-deployed structures and smart textiles can benefit from 4D printing, which can range from antennas that open without any mechanical parts, to expanding robotics. This will allow not only for smaller space for storage, but also it will allow multi-functions for the objects.

One of the most interesting emerging applications of 4D printing is energy-absorbing structures, which are usually made up of patterned structures that have a negative Poisson's ratio. These characteristics of SMPs are suitable for such applications, making them great materials for energy retention and absorption [38], [51].

Designs based on materials that can be printed on the nano-scale have been achieved [183]. This sort of prints can be applied as ink for surfaces. Energy-absorbing of a 4D-printed structure has been developed for shock absorption without permanent deformation, as it can be reset by actuation, as reported in [20], [135]. These structures can be used for shock absorption on structures and on small devices.

VSA is widely observed in natural biological systems. It has been mimicked to provide flexible and adaptable manipulators that are bio-inspired. For these applications and

many others, VSA provides agile motion and facilitates safer robot-human interactions by minimizing the effect of impact on human operators. In addition, VSA enhances energy-efficient actuation, enables embodied intelligence, and allows flexible robots to exhibit different behaviour than traditional structures that are designed exclusively with rigid members [184].

VSA has been applied in many fields due to its ability to control many characteristics in the structure that may be uncontrollable by materials preference or too complex and non-compliant for traditional mechanisms. On this premise, VSA has emerged to address the need to overcome the aforementioned weaknesses and the continuous demand for adjustable compliance for shock absorption, delicate material handling [185], fast and safe motion control [186], bipedal robots [187], artificial muscles [188], adaptable grippers [189], and underwater robots [190], among others.

Biomimetic applications in 4D printing are different since not only they are printed with the same complexity, but also these printed objects can adapt to the changing environment. This makes them more suitable than most previous attempts at bio-mimicking. The ability of 4D-printed structures to act in certain ways that will imitate biological structures is great, providing much help in medical applications. Biomimetics have also been explored in renewable energy and solar collectors, by studying the movements of plants and flowers. A better energy-absorption ratio is achieved by using SME materials. The response of the materials to either heat or light makes them perfect for use in solar energy applications, allowing the change of the panel shape depending on sunlight.

Soft robotics is one of the first potential applications of 4D printing because of how the replacement of mechanical parts was finally made possible. The printing of grippers and moving objects inspired by plants' movements and shapes are still a major part of 4D printing, although these are still in the very early development process these use metamaterial printing designs [30], and many others such as locally controlled medical grippers [38], [103].

A biomimetic application for solar energy enhancement was reported, which was based on flower petal blooming. This approach was followed because these flowers can maximize the amount of sunlight absorbed by changing their shape [191]. Biomedical implants, such as trachea fixation stents and vascular stents were developed for similar applications [13], as reported in [139]. This stent is designed with PLA material to be tough,

yet soft so that it does not damage the tissues around it. A trachea fixation that is made in a similar manner is shown in **Figure 2.12**. This is based on the study of trachea structure and the needed strain applied so that it stays fixed in place without causing damage. These structures are vastly tuneable and personalized to use.
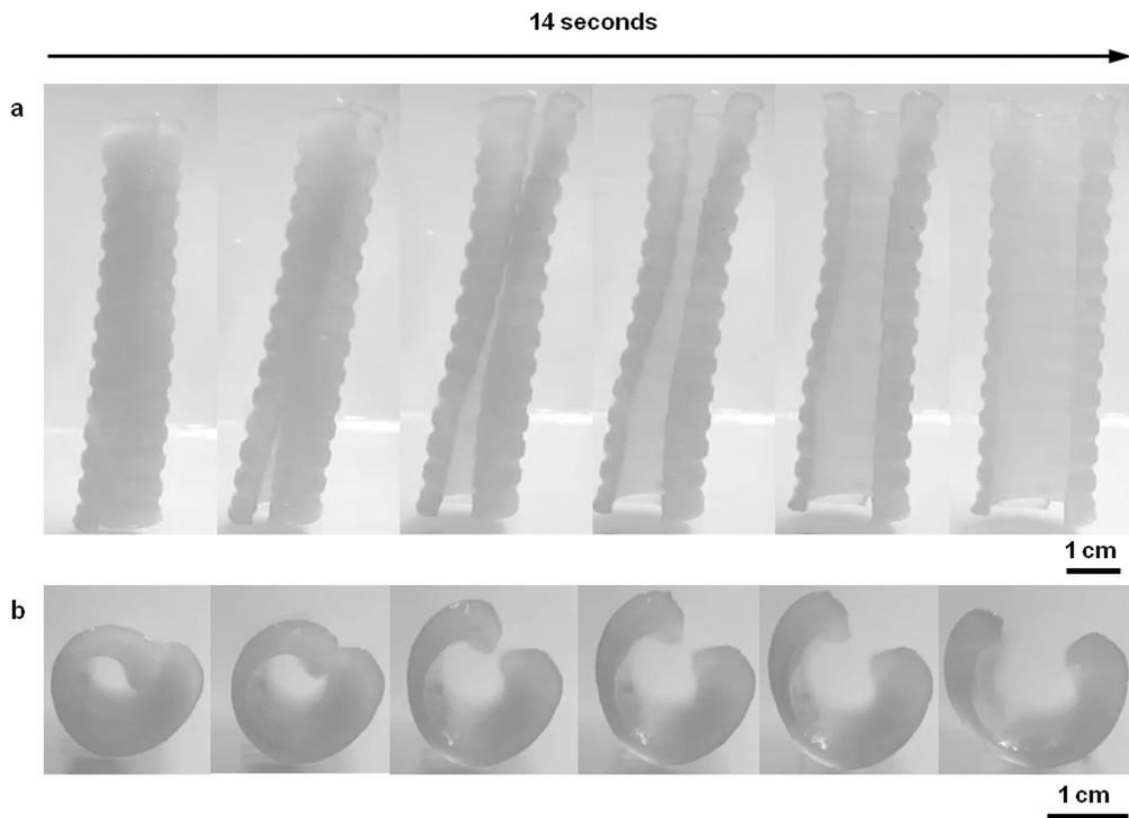
Figure 2.12. Trachea fixation that is designed to be put into the trachea and then expands when needed to be fixed in place. Reduced with permission from [32].

Electronics in 4D printing are a widely-explored application field, since the use of electrical components, whether printed or placed, is suitable in 4D printing. Micro- and soft actuators are improved by the addition of the fourth dimension of printing. The stimuli response of the materials, which can be stimulated electrically, adds a new set of abilities to these actuators that will allow them to be more target-specific and with higher control.

Circuits can be controlled by sensing the environments, making the applications not only act as switches, but also as sensors without the need for an electrical component at an added cost [38], [49]. The incorporation of conductive ink onto printed-SMP is designed for active electric switches is presented in [28], which allows the printing of ready-to-use circuits. Circuits designed for local heating can also aid in the applications of 4D printing, since it allows more control and timing preferences in the stimulation [192].

2.9   Modelling for 4D Printed Structures

Modelling for 4D printed structures or actuators is a challenging task since the effect of strain retainment and release is not integrated into simulation models yet. Researchers started replicating the effects of the activation of SME printed actuators by using the expansion of sections of the structures to cause a change in size thus bending in one direction. This method is popular in the literature since it is easy to replicate and provides good results when used in relatively simple designs, mostly used in beam-like structures. More recently, a thermo-visco-hyperelastic model is being used, this model uses the strain in the material to replicate the effects of the SME. Although this model is closer to the simulation of the material, it is still in the early stages with limitations, although improvements are being made.

For the use of coefficients of thermal expansion for the FEA simulations, a study is made by dividing the CAD structures into horizontal sections, representing the layers of the print. This model is widely used and has a high accuracy [131]. By estimating the compression or expansion of sections of the actuators, a specific coefficient of thermal expansion is assigned to each layer, thus each would expand at a different rate as temperature rises. In the study, COMSOL Multiphysics FE modelling is used, with coefficients that are mathematically modelled from experimental data. The results that are produced can represent the SME of beams and small actuators very efficiently with a very low error rate. This method might not suit more complex designs but can be used when the required shape change is known and can be represented by a single-direction shape change. in another study, the same method is used for replicating the effects of SME on the recovery of actuators [193].

The coefficient of thermal expansion was used to represent the deformation that is caused by printing the actuators at different speeds, this effect is directly related to the deformation. This test of activated beams is then analysed on a composite structure, the beams are used to shape a sheet by varying the bending in different beams on the sheet. The strain caused by the deformation of the 4D printed structures is also explored in another study using COMSOL, which provided a stress distribution in the structure as a result [63]. With this design, a hinge that was printed and tested is simulated by this method, since it was manually programmed. This demonstrates that the simulation can account for a manual programming step, and thus might not require numerous testing and assessment of internal strain as a result of changing the structure into its temporary shape. This method of replicating the behaviour of actuators to assess deformation is popular in the literature

because of its simplicity and high accuracy in estimating the bending that is caused by the SME with changes to the methods that vary from the introduction of artificial intelligence into the algorithms [194], Timushenko beam strain calculations [195], and alteration of that method for visco-elastic simulation [196]. In a study of 4D printed beams that used polylactic acid, a thermo-visco-hyperelastic model by ABAQUS, which is a software that is gaining popularity among the 4D printing modelling researchers [41].

Classic regression models are foundational in machine learning and statistics. They are used for predicting continuous target variables based on one or more independent variables. These models include Linear Regression, which assumes a linear relationship between variables, and Polynomial Regression, which extends this to include polynomial relationships [197]. However, they come with inherent limitations. One significant drawback is their assumption of a linear relationship between variables, which can result in poor performance when the actual relationships are nonlinear. [198].

The MLP is a type of artificial neural network. In this case, it is a three-layer MLP, typically consisting of an input layer, one or more hidden layers for feature transformation, and an output layer for producing predictions. MLPs are versatile and can be used for various supervised learning tasks, including regression and classification, especially when dealing with complex, non-linear data [199]. However, their strength is accompanied by complexity. Training MLPs can be computationally intensive and often requires careful hyperparameter tuning to prevent overfitting, especially with small datasets. Additionally, MLPs are not easily interpretable due to their complex architecture, which can pose challenges in applications requiring model transparency [200].

Linear SVM is a supervised learning model used for classification and regression tasks. It works by finding the optimal hyperplane that best separates data points in a high-dimensional space. Linear SVMs are particularly effective when the data is linearly separable. The RBF SVM is another variant of the Support Vector Machine that utilizes radial basis functions as kernel functions. This allows it to capture complex non-linear relationships in data, making it suitable for tasks where linear separation is not effective [201]. However, their primary limitation lies in their linear assumption. They may struggle when confronted with nonlinear data and require the use of kernel functions or other techniques to handle such cases. Furthermore, linear SVMs do not naturally provide probability estimates, which can be a drawback in probabilistic modelling. Selecting suitable

values for parameters like the regularization parameter (C) can also be a non-trivial task [202].

Non-linear regression models are crucial when the relationship between independent and dependent variables is not linear. The "Through the Origin" aspect signifies that this model does not include a constant term (intercept) in its equation. It is used when there's a strong theoretical or practical reason to believe that the regression line should pass through the origin, making it a specialized choice in regression analysis [203]. However, they come with their own complexities. They can be computationally demanding, especially with large datasets or high-dimensional feature spaces. Moreover, interpreting RBF SVMs can be challenging due to the transformations induced by kernel functions, and selecting appropriate kernel parameters requires careful consideration and experimentation [204].

In this study, they analysed the effects of printing parameters such as layer height, print speed and nozzle diameter on the pre-strain that is generated by the printing process. This method uses a two-plate model with different pre-strain values to simulate the effects of the release of strain. The results of the simulation are close to those of the experimental, with a good representation of the activation final shape. In a similar FEA study, which used ABAQUS, stress and strain loading is done through the FEA, by applying force to the structure. The structure used is a stent that can close to a small size and then expand when heated [139]. The FEA followed three different stages, where the first has the force onto the structure to load it under heat with strain and close the stent. Following that, a cooling period to hold the stent, then a timely release as the temperature increased again. This result validated the use of these stents, since they had a large strain and a slow recovery process, which is a characteristic needed in stents. This software is being used by a larger number of researchers [205].

In another work, the simulation method is divided into two sections, one for pre-strain estimation and the other for the deformation of actuators based on the release of strain [206]. Much like a thermo-visco-hyperelastic the pre-strain is estimated and is the main contributor to the final shape deformation. Making this type neither time nor thermal dependant, it is a model for the final shape of the actuators after stimuli. The activation temperature is assumed to be constant, and the results of the beams tested are acquired after the full release of strain. The error rate is very small when compared with the experimental data, which is a good indicator of the pre-strain estimation. The stress and strain relationship is also explored in simulation in another study, this one aims at the ability of 4D printed grids in energy

absorption [16]. The use of the ANSYS elastoplastic model for estimating the loading and unloading of the deformation caused by straining is accurate, and proves to be a useful tool in energy absorption and release by SME.

In a more detailed and technical manner, there are several methods for modelling that are involved in 4D printing, these are represented very elegantly in a literature review named "Laws of 4D Printing" reported in 2020 [207], which the summary of which is included in **Table 2.6** below, with references for the sources of these models.

Table 2.6. Summary of the major modelling methods that are used to represent the governing formulas and their perspective studies.

Based on	Formula	Used in	Notes	Ref.
Trigonometry	$$c = \frac{1}{r}$$ C: bending/unbending r: bending radius of a circle enclosing the actuator	Multi-responsive hydrogel actuators	Simple representation of the bending by geometry	[208]
Sheet materials strain	$$r = \frac{\left[\frac{1}{\varepsilon_R} - 1\right]t}{2}, \varepsilon_R = \frac{L_R - L_0}{L_0}, L_R$$ $$= R \times \theta$$ r: bend radius ε_R: strain at the outer surface t: thickness θ: bending angle L_0: original length L_R: bending length at the outer surface R: outer radius	Self-morphing structures	Representation of the bending using the radius of a circle, relating the bending to the strain in the outer surface of actuators	[209]
Calculating strain based on length changes	$$\varepsilon = \frac{l_0 - l_c}{l_c} = \frac{(R + y_b)\theta - R\theta}{R\theta} = \frac{y_b}{R}$$ $$= Ky_b$$ ε: bending strain l_0: swelled length l_c: free length R: curvature radius θ: bending angle	Self-folding origami structures	Represents the strain of the bending using geometry, including distances between a reference layer	[210]

Based on	Formula	Used in	Notes	Ref.
	K: bending curvature y_b: distance between the swelled layer and reference plane		and a layer that swells for deformation	
Estimation based on initial and final alignments	$$\alpha \approx \frac{Nd}{r}, l \approx \alpha\left(r + \frac{1}{2}D\right)$$ $$\approx \alpha\left(\frac{Nd}{\alpha} + \frac{1}{2}D\right)$$ $$= Md + \frac{1}{2}D$$ α: folding angle r: folding radius N: number of disks d: disk thickness D: disk diameter l: total length	Structures reactive to environment for self-evolving function	Represents the folding angle of a joint based on geometry, customizable for specific application	[211]
Based on the contraction of the materials model	$$\alpha = K\sqrt{\frac{L^2 h}{d^3}}, k = \sqrt{\frac{24 \times (1 - v^2)\mu\rho q}{E^T}}$$ α: bending angle K: coefficient related to the temperature and material properties h: the thickness of the active layer d: the thickness of the passive layer L: length of the bilayer ρ: density of the active material q: unit releasing energy of the active layer μ: mass shrinking ratio of the active layer v: Poisson ratio of the passive layer E^T: flexural modulus of the passive layer cured under temperature T	Finite element analysis of 4D printing	Represents the bending angle of the actuator by assuming that energy caused by the contraction of layers causes the deformation of the actuator	[212]
Euler-Bernoulli	$$\varepsilon(Z) = \varepsilon^0 + KZ$$ $$M = \int_A^- \sigma z dA = \int_A^- zE(\varepsilon^0 + KZ)dA$$ $$= E\varepsilon^0 \int_A^- z dA + KE \int_A^- z^2 dA$$	Design of 4D printed springs	Determines the strain in the actuators in an Euler-Bernoulli beam theory	[34]

Based on	Formula	Used in	Notes	Ref.
	$$\gg M = KEl = \frac{EL}{r} = \frac{0El}{L} \ll\gg \theta = \frac{ML}{EL}$$ ε: strain ε^0: strain at the mid-axis σ: stress z: third axis in the Cartesian coordinate system A: cross-sectional area of the beam K: curvature θ: bending angle r: curvature radius E: Young's modulus I: second moment of area M: moment L: length			50
Timoshenko method	$$\frac{1}{\rho}$$ $$= \frac{6(\varepsilon_2 - \varepsilon_1)(1 + m^2)}{h\left[3 \times (1 + m^3) + (1 + mn)\left(m^2 + \frac{1}{m}\right)\right]}$$ ρ: radius of the curvature $\varepsilon_1; \varepsilon_2$: thermal expansion coefficients of the two layers m: ratio of the thicknesses of the two layers n: ratio of Young's moduli of the two layers h: thickness of the bilayer	Self-morphing structures	Determines the radius of the curvature for deformation by using the classical Timoshenko bimetal model	[79]
Timoshenko method	$$\theta(x, t')$$ $$= \frac{6\varepsilon_r\left(1 - e^{\frac{t'}{\tau_r}}\right)E'_{pm}h_{pm}b_{pm}(h_{pm} + 1)}{(E'_{pm}h_{pm} + 1)(E'_{pm}b_{pm}h^3_{pm} + 1)h_r}$$ θ: bending angle $h_{pm} = h_p / h_m$: thicknesses ratio of the two layers $b_{pm} = b_p / b_m$: widths ratio of the two	Deformation of thin composite sheets	An extension to the Timoshenko bimetal model, determines the bending angles of actuators	[213]

Based on	Formula	Used in	Notes	Ref.
	layers $E'_{pm} = E_{pe}/E_m$: Young's (elastic) moduli ratio of the two layers x: any value between zero and l l: length of the composite strip t': time starting from the point of the glass transition temperature t: total time t_0: time at the glass transition temperature T_R: relaxation time ε_r: stored internal strain p: printed polymer (active layer) m: membrane of paper (passive layer)			
Timoshenko method	$$H = c_1 \frac{\alpha_l - \alpha_1}{h} \frac{\sin^2(\theta)}{c_2 - c_3\cos(2\theta) + m^4\cos(4\theta)}$$ $$= -c_4 \frac{(\alpha_l - \alpha_1)^2}{h^2} \frac{\sin^2(\theta)}{c_5 - c_6\cos(2\theta) + m^4 c\cdots}$$ H: mean curvature; $H = (\frac{1}{2})$ trace (k) k: curvature tensor K: Gaussian curvature; $K = \det(k)$ α_l, α_1: longitudinal and transverse swelling (expansion) strains θ: angle between the two layers in the bilayer h: sum of the layer thicknesses m: ratio of the layer thicknesses c_i: functions of m and the elastic moduli	Biomimetic 4D printing	Determines the mean curvature form by the actuators, using an extension of the Timoshenko bimetal model in 2D space	[214]

It is noteworthy to state that the existing models are not time-dependent, neither are they temperature-dependent. These are not general models since they are based on strain and release of strain. These models mostly act in a linear fashion with time, and that doesn't reflect how the deformation actually happens in the actuators. SMP materials act differently in time of activation, and the method of heating. Nevertheless, these models are very accurate

in replicating the final deformation of the actuators, and mostly can be applied to complex structures.

2.10 Summary

4D printing is a rapidly changing research field because of the possibilities and volume of this new manufacturing method, with huge areas that are still to be explored. The recent advancements in AM have allowed high-precision prototyping at a high complexity and speed, giving way for further advancements.

Recently, in 4D printing, researchers have been discovering more properties of the tested materials and composites, which is the driving force behind the large interest. Until a few years ago, most literature about 4D printing involved testing of materials and printing methods for proof of concept, providing strong basic parameters for further research on applicable designs. Energy retention and absorption of 4D-printed structures have been one of the new sub-fields of 4D prating that are gaining momentum, along with biomedical actuators, and soft robotics.

The creation and testing of new composites and material combinations are allowing for more precise programming of actuation, giving new concepts a wide range of properties to choose from. The research on SMPs and the control of their characteristics although available, along with the control that is allowed in the printing methods, is still largely unexplored with many possibilities and potential breakthroughs. Other niche areas are emerging as a potential application of 4D printing, such as textile manipulation, and large hinge-like movements such as those in spaceships and others.

2.11 Research Gaps

4D printing is a field that is still expanding and finding many uses in other fields. The possibilities are massive with connections to many other domains allowing for a huge amount of research opportunities. The field is simply too fresh and wide that all areas of research regarding 4D printing are largely viable. Although this is the case, some specific fields require more attention to keep up with this evolving field.

In the realm of 4D printing, with a specific focus on the fused deposition modelling (FDM) method, several research avenues can be categorized into three key domains. Firstly, material development and selection pose a critical gap. This entails the quest for novel

materials exhibiting precise responsiveness to environmental stimuli, to trigger desired shape transformations. Composite materials are also being explored to augment mechanical and functional properties. Secondly, optimizing the FDM printing process represents another essential aspect. Researchers aim to fine-tune printing parameters like layer height, nozzle temperature, and printing speed to ensure precise control over transformation rates and reliability.

Lastly, specific application-driven research is gaining prominence, spanning fields like medicine, aerospace, architecture, and fashion. Tailoring 4D-printed objects to meet the mechanical, thermal, and chemical requirements of diverse applications requires a dedicated focus. One noteworthy gap within this landscape is the pursuit of reliable and scalable 4D printing materials tailored for healthcare applications, a field that holds significant promise but demands interdisciplinary research to navigate complex physiological conditions, regulatory challenges, and scalability issues. These are presented in the order of how they contribute to the applications in Figure 2.13.
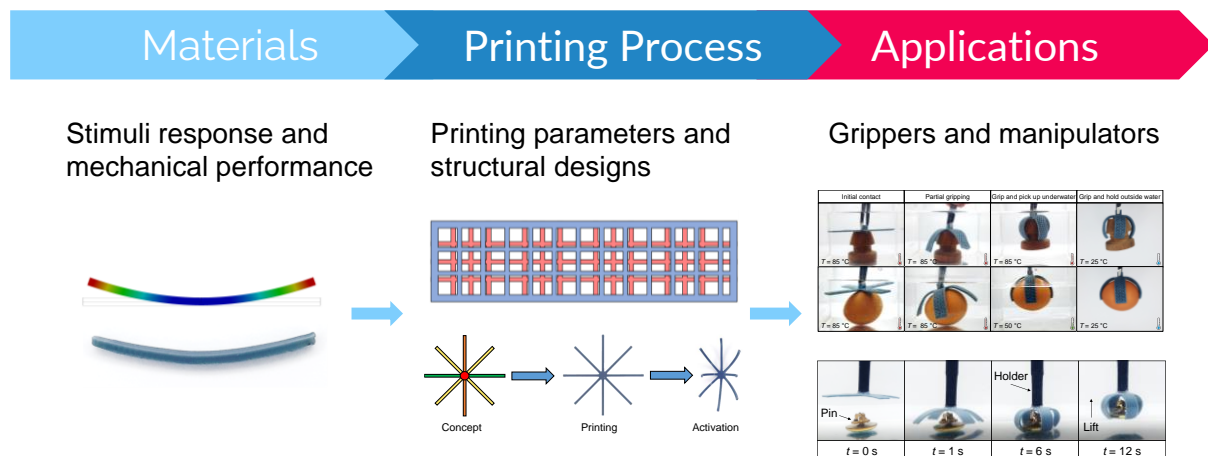
Figure 2.13. Graphical representation of research gap fields.

Through the literature, more research should be made into SMP material properties and their characteristics which can be beneficial in designing applicable structures. Traditional strain-inducing by forcing the temporary shape is widespread, but the control of the SME in the structures by the printing process is more promising since it can provide better accuracy and no training is required. There is a lack of studies into the effects of printing parameters on the shape change and strain-induced onto the structures, the control of which is very beneficial.

Testing multiple parameters and their effects on the strain in the materials can fill some of the gaps in the shape programming area. The testing should be done on multiple parameters, for their individual and combined effects. These parameters and their effects can be supported better by creating predictive models for the shape change based on their results, as that is lacking in the field too.

Manipulating the shape change by changing the structures is not studied well, as most of the literature uses one design and augments it, instead of a comparative study on changes in designs. The effects of simple changes in the structures need to be explored, as these can provide fundamental information about how the lines in the print can affect the structure, in terms of shape change and functionality. This change in design can be made not only by changing the size of the structures, but also by changing the internal filling of the structures. As long as areas of contact remain the same, changes in the infill of 3D prints can be used to manipulate the shape change. These changes can produce different stiffness in the actuators allowing for the control of the SME by structural means.

Other activation methods other than heating environment are emerging with good local activation, such as electrical stimulation, but these are still in the early stages without much control over the activation. These activation methods can allow for better testing methods and analysis to be done on the printed structure since the activation is local to the prints.

By filling these gaps in the literature, the possibility of producing real-life applications using 4D printing is greater and will aid researchers in designing better actuators. There are many fields which can benefit from 4D printing, most promisingly are robotics and biomedical applications. Studies into multiple shapes, or bi-directional actuations, can help with more complex designs, which are sometimes needed to bring the field to real-life applications.

Chapter 3: Experimental Setup and Method of Testing

3.1   Introduction

This section served as a brief overview of the methodology process, as each chapter expanded on the specific methodology used in the study. The proposed research could be divided into the following main streams, namely, materials and characterization, design and experimental setup, fabrication and testing of SMP actuators, results and discussions, and modeling and simulations of the 4D-printed SMP actuators. This order of section was followed roughly in each chapter of results.

The following approach was carried out to achieve the research objectives: Theoretical study of 4D printing of SMP actuators and their shape-programming mechanism, as well as the material properties assessment for analysis and the simulation criteria, were also implemented. This research focused on the effects of the printing parameters on the structures to establish a programming model upon printing.

The characteristics of the structures were also used to develop predictive models using simulations. Following this, the effects of patterns in the actuators on the SME were studied; these patterns were found in nature and were simplified for printing. Different stimuli on the actuators were carried out as well, by using conductive filaments for the prints. The conductive actuators were activated via Joule heating at different settings. Lastly, certain concepts were explored for further control of 4D printing, such as twisting behavior based on printing direction and thermal-dependent controlled actuation.

3.2   Materials and Characterization

The materials that were used in this research were PLA, Conductive PLA, and Bio-PETG. To understand the materials that were used in each section of the study, they were tested with analytical machines. The machines used in this research included dynamic mechanical analysis (DMA), differential scanning calorimeter (DSC), thermogravimetric analyzer (TGA), microscope, field emission scanning electron microscopy (FE-SEM), and a tensile tester. Other characterizations of the materials were acquired from the literature, as PLA is widely used and studied. This ensured better results and a higher confidence in the measurements. These characterization criteria might not have all been used directly in the

results sections of this thesis, but they were acquired for the purposes of better simulations and data analysis.

3.3   Design and Experimental Setup

Initially, the design process focused on the dimensions of the SMP actuators and their effect on the actuation mechanism. Then, shape-programming methods were implemented in the simulation process, which was performed to determine the optimum dimensions and folding sections of the actuators. Moreover, printing parameters were tested to find their effect on the SME induced in the materials upon printing. This was done to allow for 4D prints that did not require a programming step since they had an internal strain that was sufficient to fulfill their application criteria upon printing.

Following this, structural changes and their effect on the SME were tested and analyzed. This was done in the form of printing actuators with patterns made up of repeated geometric shapes. The printing direction of the FDM lines was also used to induce twisting behavior in actuators, which was assessed by comparing the spiral angles formed after actuation with the printing line angles. Furthermore, for non-water-based stimuli, Joule heating was performed and analyzed on conductive materials. This not only allowed for local and controllable actuation but also enabled better observation of the materials during activation.

Finally, gradual heating was used to activate actuators that responded to different temperatures, allowing for different activation temperatures for deformation. These actuators could achieve sequential deformation based on the temperature they reached.

3.4   Fabrication and Testing of the SMP Actuators

In this stage, the fabrication process of the actuators (with different designs) was carried out. The printing of the SMP preliminary structures was done using the Ender 3 v2 printer (Creality, Shenzhen Creality 3D Technology Co., Ltd.). Subsequently, the fabricated actuators were characterized in terms of their temporal and thermal responses, as well as their ability to achieve the desired programmed shapes. Then, the design and performance were evaluated. These could be controlled by the SME-printed controlled characteristics.

The experimental setup for printing and testing is presented in **Figure 3.1**, where the designed actuators were made using a CAD software. The designs were then transferred to the slicer software to prepare the print settings. Following this, the printer used the filament to print according to the settings in printing the designs. The actuator is removed and either

activated in water at a temperature above the glass transition temperature or Joule heated to a desired deformation. The actuator was then removed, and measurements were taken to record the deformation angle that each actuator achieved. In some cases, video tracking was used to assess the deformation. This not only provided a timestamp for actuation and full deformation but also enabled further analysis of the actuation.
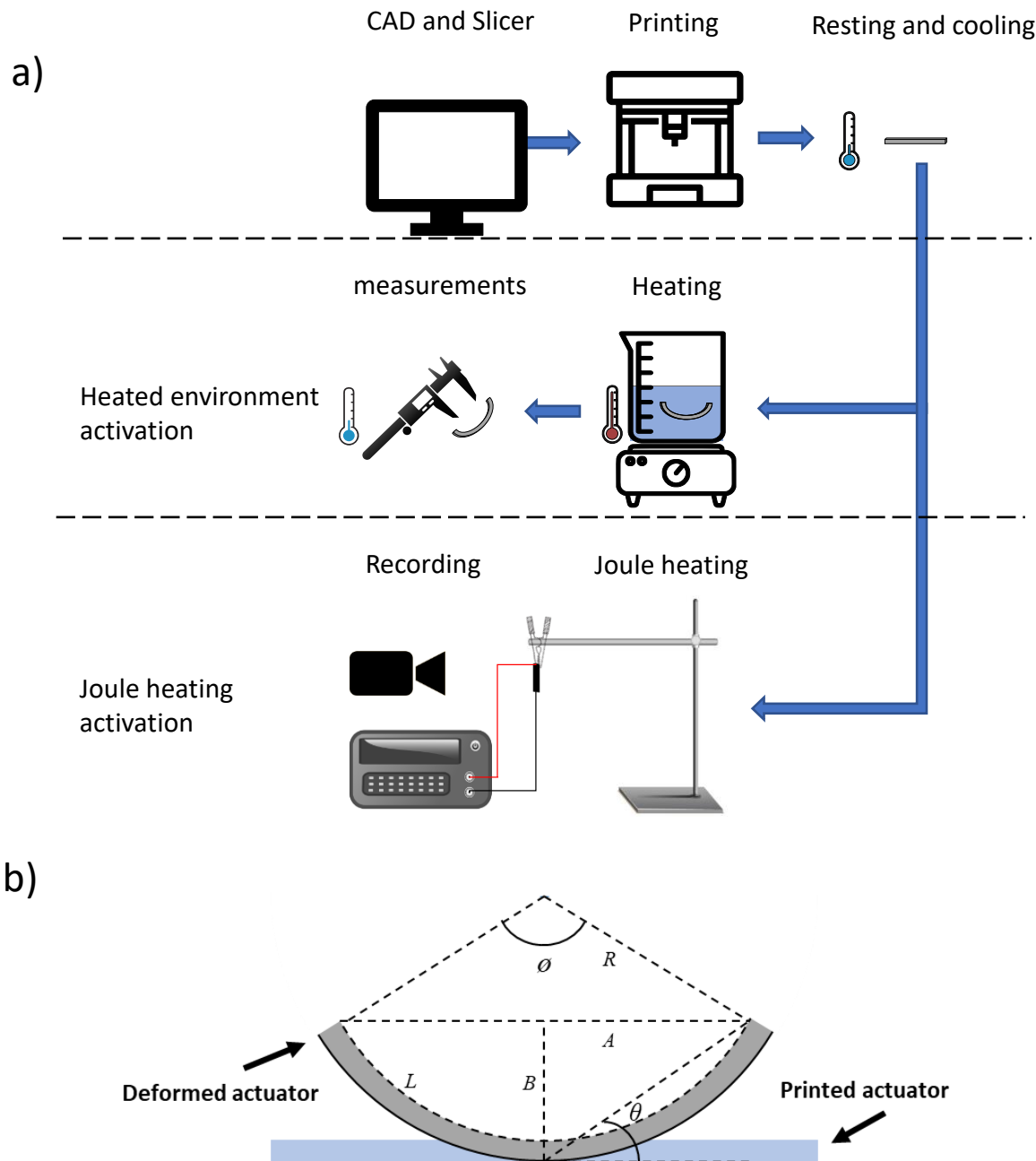
Figure 3.1. (a) Experimental setup of the printing and testing of the actuators. (b) The measurement method of the deformed actuators.

3.5 Assessment of Designs

The results of the experimental tests were recorded in a manner that allowed for a simple and clear understanding of the analysis. The first results chapter was dedicated to testing the effects of varying the printing parameters in the slicer software. The printing of structures for the chapter on printing parameters was standardized, as all changes to the printing parameters were applied to the same structure with a set of dimensions. Standard actuators of SMP were printed with dimensions of 30 mm × 1.6 mm in length and width, respectively.

The prints were carried out by changing one parameter at a time for four different heights of the actuators: 0.6 mm, 0.8 mm, 1.0 mm, and 1.2 mm. The material used for SMP printing was PLA, chosen because it was the most widely used and available SMP in the literature. Additionally, PLA was selected for its cost-effectiveness and ease of work. The parameters are summarised in **Table 3.1**.

Table 3.1. Printing parameters that were tested for their effect on the induced strain in the prints, upon printing.

Parameter	Criteria
PRINTING SPEED	10 mm/s to 80 mm/s
PASSIVE-TO-ACTIVE RATIO	0% to 100%
PRINTING TEMPERATURE	180°C to 230°C
LAYER HEIGHT	0.05 mm to 0.3 mm
THICKNESS	0.6 mm to 1.2 mm

In the first stage of printing, each actuator was printed with only one parameter varied, while the rest were kept the same. This approach was taken to gain a comprehensive understanding of how each parameter individually affected the SME. In the second stage of printing, the parameters were randomized to provide more comprehensive data on how changing multiple parameters simultaneously affected the SME.

For the chapter on the effects of patterns on the SME, the actuators were designed with dimensions of 51.6 mm × 13.6 mm × 2 mm, representing length, width, and height, respectively. These dimensions encompassed geometrical shapes enclosed by a perimeter. The shapes were represented by patterns of circles, squares, hexagons, rhombuses, and triangles, while all other printing parameters remained the same. Three different types of prints were created:

1. Simple patterns.
2. Two horizontal sections with different sizes of the same pattern in each section.
3. A mix of patterns in each horizontal section.

These variations were used to assess the effects of different stiffness caused by the parameters on the SME or shape change.

In the section on Joule heating, there was only one setting for the samples printed, as the actuators were designed with high SME, allowing their release to be controlled by the applied voltage. Joule heating actuators were printed with dimensions of 30 mm × 3.2 mm × 1 mm for length, width, and height, respectively. Different voltages were tested for activations, and their effects on deformation, speed, temperature, and force generated in the actuators were examined.

The last results chapter consisted of two explorations of 4D printing concepts. The first focused on inducing twisting in the printed actuators by varying the printing angles. Standard actuator dimensions were 30 mm × 8 mm × 1 mm for length, width, and height, respectively.

For the second section, plates made up of layers of horizontal or vertical lines were printed with dimensions of 30 mm × 30 mm × 1.6 mm for length, width, and height, respectively. Different printing parameters were used for these printed plate actuators to enhance the results, as some of the forces in certain actuators were too weak to be well analyzed.

Following the testing, the analysis would be carried out for each of the results sections. Each section would have its own discussion and summary, with results demonstrated graphically and visually to aid in the discussion and conclusions.

3.6   Modelling and Simulations

The studies were extended to the derivation of the mathematical model of the 4D-printed SMP actuators. The model included various parameters of the actuators, such as their dimensions and material properties. The model was then validated by comparing its results with the experimental values. These models were mainly for the prediction of bending angles of the actuators based on the printing parameters. Beyond this, if no model was necessary, a behavioural understanding of the effects of certain changes in the printing or actuators was documented and presented in easily formed graphs.

The simulation of the SME material was based on the testing of the printed actuators. This was done using ANSYS static structure by making use of the thermal expansion of the material to replicate the SME effect. This could be achieved by locating a thermal expansion coefficient for each printing parameter, resulting in the same shape change effects.

SME in the simulation required many material properties that needed to be measured on printed material. The testing of the parameters was done after the preliminary simulations, and these parameters were acquired using DMA, force sensors, and thermal imagery. These provided adequate parameters to simulate actual SMEs for more complex and accurate designs. Furthermore, data from the literature was used to further enhance the simulations and ensure more accurate results.

As for the simulation of Joule heating actuators, thermal FEA was performed, and the results were compared with the thermal recordings made experimentally. The thermal characteristics used for the simulations were taken directly from the characterization of the materials and the literature.

3.7   Research flow

The research flow that was planned for this thesis was carried out as follows, as presented in **Figure 3.2**. The research began with a review of the available literature on the subject, followed by the testing of printing parameters on the SME as proposed. Simulation work was conducted and enhanced based on the tested parameters. Following the simulation, thermal and mechanical analyses were performed. For more structural control beyond the

printing parameters, pattern-driven actuation was analyzed using geometrical shapes. This section also included preliminary work on multi-material actuators.

Beyond the testing of actuators in a heated environment, a different stimulus was needed for further tests. The use of conductive filaments was done, using information acquired from previous sections. Joule heating of conductive materials provided the ability to test actuators outside a heated environment and could offer more local and controlled actuation.

Furthermore, additional concepts were explored for improvements in the field. The twisting of the actuator proved to be a useful tool, and control of twisting was achieved by varying the printing angle. Secondly, the actuators were observed to respond differently to gradual heating, which comprised the final results section of this work. Thermal-dependent actuation was explored through a control method used to acquire different shapes of the actuator at different temperatures.

```
                                          ┌─────────────────────────────┐
                                          │  Adjustment and re-assessments│◄──┐
                         ┌────────┐        └──────────────┬──────────────┘   │
                         │ start  │                       ▼                  │
                         └───┬────┘        ┌─────────────────────────────┐   │
                             ▼             │   Simulation of parameter    │   │
                   ┌──────────────────┐    │     controlled Actuators     │   │
                   │ Literature review│    └──────────────┬──────────────┘   │
                   └────────┬─────────┘                   ▼                  │
                            ▼                         ◇ Similar      No      │
          ┌──────────────────────────┐              results ?  ──────────────┘
          │ Testing of SMP printed    │                  │
          │       samples             │                 Yes
          └────────────┬─────────────┘                   ▼
                       ▼                    ┌─────────────────────────────┐
          ┌──────────────────────────┐      │    Parameter controlled      │
       ┌──│ Printing parameters       │      │        grippers              │
       │  │        analysis           │      └──────────────┬──────────────┘
       │  └──────────────────────────┘       End of                ▼
       │                               chapter 4  ─ ─ ─ ─ ─ ─ ─ ─ ─ ─ ─ ─ ─
       │  ┌──────────────────────────┐─┐     ┌─────────────────────────────┐
       ├─►│    Printing speed         │ │     │  Thermal and mechanical      │
       │  └──────────────────────────┘ │     │   analysis of materials      │
       │  ┌──────────────────────────┐ │     └──────────────┬──────────────┘
       ├─►│  Printing temperature     │ │                   ▼
       │  └──────────────────────────┘ │  ┌──│  Pattern driven Actuation    │
       │  ┌──────────────────────────┐ │  │  └──────────────────────────────┘
       ├─►│ Passive-to-active layers  │ │  │  ┌──────────────────────────────┐
       │  │        ratio              │ │  ├─►│   Single shape patterns       │
       │  └──────────────────────────┘ │  │  └──────────────────────────────┘
       │  ┌──────────────────────────┐ │  │  ┌──────────────────────────────┐
       ├─►│     Layer height          │ │  ├─►│   Variable pattern size       │
       │  └──────────────────────────┘ │  │  └──────────────────────────────┘
       │  ┌──────────────────────────┐ │  │  ┌──────────────────────────────┐
       └─►│    Actuator height        │ │  └─►│     Mixed patterns            │
          └──────────────────────────┘ │     └──────────────┬───────────────┘
          ┌──────────────────────────┐◄┘     ┌──────────────────────────────┐
          │  Mathematical modeling    │      │  Variable stiffness profiles  │◄
          └────────────┬─────────────┘       └──────────────┬───────────────┘
                       ▼                                    ▼
       ┌─►┌──────────────────────────┐      ┌──────────────────────────────┐
       │  │ Testing model accuracy    │◄─┐   │   Pattern controlled gripper  │
       │  │ against printed samples   │  │   └──────────────┬───────────────┘
       │  └──────────────────────────┘  │                  ▼
       │  ┌──────────────────────────┐  │   │  Multi-material actuator testing│
       ├─►│    Single parameter       │  │   └──────────────┬───────────────┘
       │  └──────────────────────────┘  │    End of                ▼
       │  ┌──────────────────────────┐  │  chapter 5 ┌──────────────────────┐
       ├─►│   Multiple parameters     │  │           │  Multi-material        │
       │  └──────────────────────────┘  │           │     actuators          │
       │  ┌──────────────────────────┐  │  ─ ─ ─ ─ ─ └──────────┬───────────┘
       └─►│    Random parameters      │  │                      ▼
          └────────────┬─────────────┘  │   ┌──────────────────────────────┐
                       ▼                 │   │  Acquire conductive materials │
                   ◇ Similar    No       │   └──────────────┬───────────────┘
                  results ? ──────────────┘                 ▼
                       │                     ┌──────────────────────────────┐
                      Yes                    │  Thermal and mechanical       │
                       ▼                     │   analysis of materials       │
          ┌──────────────────────────┐       └──────────────┬───────────────┘
          │ Link model of bending to  │                     ▼
          │ two-plate shrinkage model │       │  Design of Joule heating      │
          └────────────┬─────────────┘       │        actuators              │
                       ▼                      └──────────────────────────────┘
          ┌──────────────────────────┐                      ▼
          │  Simulations of model     │              Continued....
          └──────────────────────────┘                      ▼
```
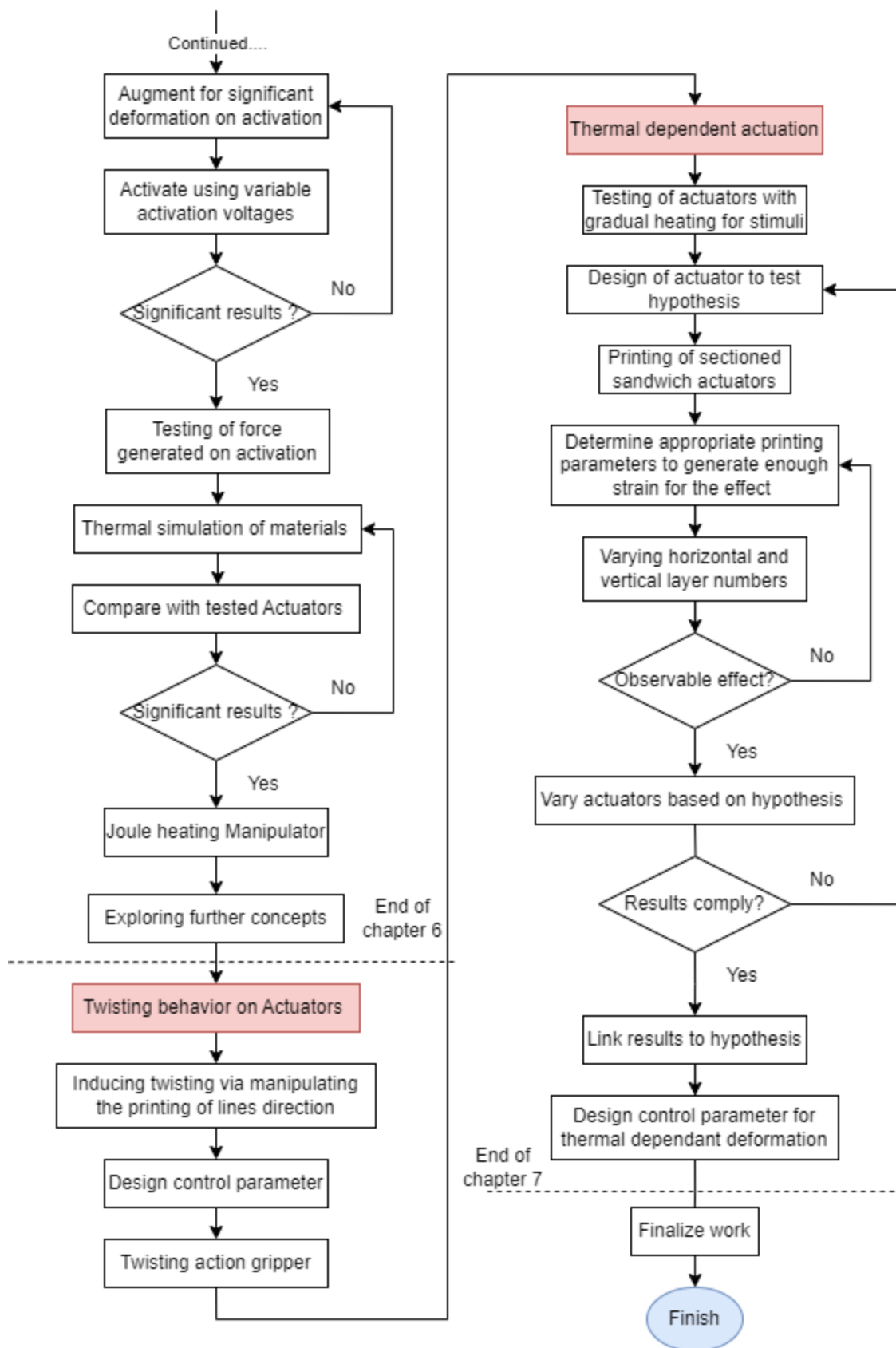
Figure 3.2. Flowchart of the research. Some of the steps are carried out simultaneously.

3.8 Summary

The flow of this thesis was designed to explore the effects of augmentations in the shape programming of actuators. The materials were tested and analyzed to assess their activation criteria and properties. The results of the material analysis were then used to assess the thermal and mechanical performance, which played a crucial role in the printing process and simulations. Following this, an experimental setup was created specifically for each chapter, depending on the criteria required for the results. Experimentations were conducted on the printed actuators by activating them, and the results and recordings were noted and documented for analysis. This process involved the use of sensors in certain chapters, which ranged from thermal analysis to force sensing and deformation assessments.

The effects of varying the printing parameters were assessed by first isolating each parameter and testing its individual effect. Subsequently, the collective effect of combining the parameters to manipulate the internal strain was investigated to understand the overall impact of the parameters on the shape memory effect (SME). Furthermore, the effects of using different patterns in the printing of the actuators were tested for their impact on the SME, introducing an exploratory approach to pattern-driven actuation. Joule heating was employed as a variation of stimuli by varying the activation voltage of the actuators and assessing its effect on shape change. This is to establish new methods of local activation, to allow better testing of the actuators' performance. Finally, thermal-dependent actuation was achieved by varying certain structural layers in actuators to control the timing of actuation in specific directions.

The evaluation of the outcomes predominantly centered on the alteration in shape experienced during and post-actuation. This parameter served as the basis for assessing the strain release resulting from shape programming. The actuators were subject to meticulous modeling and simulations, encompassing static deformation, electrical, and thermal analyses. Employing simulations as predictive tools for intricate designs was deemed essential in the realm of 4D printing. However, it was observed that simulating shape memory polymers (SMPs) posed challenges due to the absence of robust algorithms replicating their distinct shape memory behavior. Consequently, this made the simulation process more intricate compared to simulating other materials

Chapter 4: Printing Parameters of 4D-Printed Actuators

4.1   Introduction

In this chapter, the printing speed, printing temperature, ratio of passive-to-active layers, layer height, and Actuator height of actuators are varied to assess their influence on the stored internal strain in the actuators. A mathematical model of each parameter is developed to evaluate its effect and the degree of control it offers. Following this, a complete mathematical model is formulated by combining the effects of all the parameters on the actuators.

A total of 534 actuators were designed and tested to realise and evaluate the model. The model is tested against actuators printed with random FDM parameters. This is then used to develop an FEA model to replicate the SME in beam-like actuators, which can also be used to test more complex structures. The main contributions of this chapter compared to the existing literature, to the best knowledge of the authors, are:

- This chapter presents the first work that investigates the combined effects of the printing speed, printing temperature, the ratio of passive-to-active layers, layer height, and height of actuators on the internal strain induced in 4D-printed actuators using a mathematical model. The investigation is carried out using polylactic acid (PLA) actuators, where the shape programming is achieved using the printing parameters instead of manual training.
- A mathematical model that predicts the bending angle of actuators is proposed, This is the first model that considers the five aforementioned parameters.
- An FEA model that uses the calculations of the effect of the printing parameters is developed, and the induced strain into the actuators is used to predict the shape change undergone when the actuators are activated above T_g.

4.2   Materials and Methods

This section presents the material properties of PLA that are used in this chapter, acquired by analytical tools. It also presents the experimental setup, with the testing and measurements recording method.

4.2.1 Material Properties

The material used in this chapter was PLA (1.75 mm, 1.0 kg Gray, Flashforge, Flashforge 3D Technology, Co., Ltd., Zhejiang, China). PLA is the most commonly used SMP in 4D printing since it is recyclable, cheap, and easy to print with [170], [215].
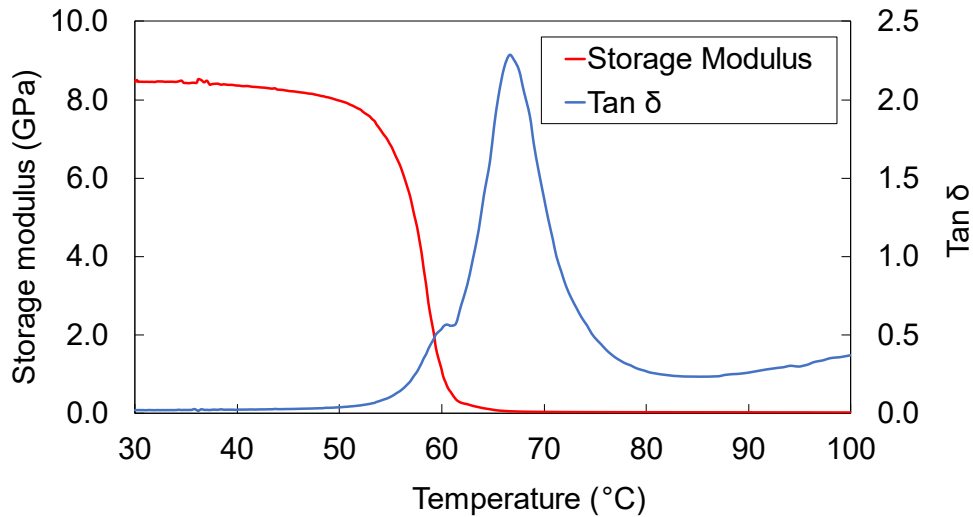
The thermal properties of the PLA used in this chapter were tested using differential scanning calorimetry (DSC), and dynamic mechanical analysis (DMA), as shown in **Figure 4.1**. These tests were respectively performed using a DSC machine (DSC Q2000, Texas Instrument, Dallas, TX, USA), and a DMA machine (DMA 8000, Perkin Elmer, Waltham, MA, USA).

DSC measures the heat required to increase the temperature of the material, as shown in **Figure 4.1** (a). The DSC heating and cooling processes showed negative peaks at two points during the heating process at about 53 °C and 151 °C, which are the glass transition temperature and melting temperature of the PLA, respectively. DMA is used to measure the viscoelastic behaviour of the polymer and is the most vital analysis done on SMPs. The result displayed in **Figure 4.1** (b) showed two different graphs, including tan δ, and the storage modulus. Tan δ is used in determining the T_g of the material, which is centred at the peak of the graph.

The T_g peaked at around 65 °C, but it can be seen that tan δ is relatively high when the temperature is between 55 °C to 80 °C. Thus, for full deformation, the material needs to be heated to a temperature of 80 °C or slightly higher. The storage modulus indicates the ability of the material to store energy elastically. As can be seen, the storage modulus is very high at low temperatures, thus the material is rigid. Around T_g, the storage modulus reduces greatly as the material becomes mendable and rubbery.
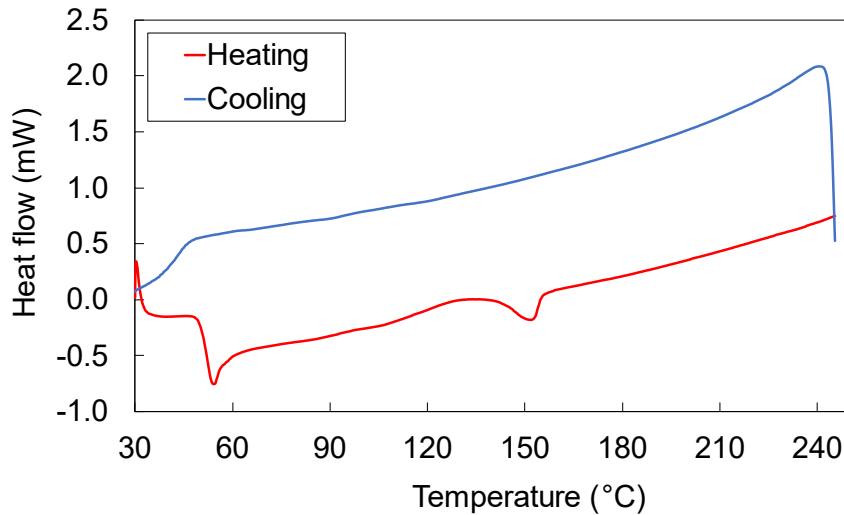
(a)

(b)

Figure 4.1. PLA thermal properties. (a) DSC results of a sample heated from 30 °C to 250 °C, then cooled back down to 30 °C. (b) DMA results of a sample heated from 30 °C to 100 °C.

4.2.2 Printing Process and Experimental Setup

The FDM printer used in this chapter is the Ender 3 V2 (Creality, Shenzhen Creality 3D Technology Co., Ltd.) with a 0.4 mm nozzle. The experimental setup used in this chapter is presented in **Figure 3.1** (a) in the methodology chapter. The designs were developed using a CAD software and exported as STL files, which were then converted into G-code for the 3D printer via a slicer software (Simplify3D).

The printing parameters were controlled using the slicer to test their effect on the bending angle of the actuators. Then, each actuator was printed and removed from the print

bed after it was cooled down to room temperature. Next, each actuator was submerged into a beaker of 85 °C water that was heated up using a hot plate. The heating rate of the actuators affects the recovery shape [216].

In this study, the activation was done immediately at full temperature (85 °C). The actuator was left in water until full deformation was observed. After that, the actuator was removed from the water and allowed to cool down to room temperature so that measurements can be taken to assess the deformation behaviour.

Lastly, measurements were taken using a digital calliper to find the distance between the two endpoints of the arc (*A*) and the bending height of the actuator (*B*). The length of the arc formed by the bending of the actuator is represented by (*L*) while the angle formed by the arc at the centre of the section of the circle is represented by *φ*, as depicted in **Figure 3.1** (b).

calculating the radius of bending for an arc involves understanding the geometry of the curve and applying relevant mathematical formulas. The radius of bending, often denoted as R, represents the distance between the center of the circle from which the arc is derived and the midpoint of the chord (a straight line connecting the arc's endpoints).

To calculate this radius, one can use equation 4.1 This can accurately determine the radius of bending for the given arc, which is crucial in various fields such as engineering, architecture, and design for creating precise and symmetrical curved structures. *R* can be calculated from the measured values of *A* and *B* using the following equation [96]:

$$R = \frac{B}{2} + \frac{A^2}{8B} \qquad\qquad (4.1)$$

The bending angle (*θ*) can be calculated using simple trigonometry. The measurements taken from the deformed actuators were compared with arc calculations to confirm that the arc formed is of a circle. This angle was used for the assessment of the induced strain and bending behaviour of the actuators in the rest of this work. This method of assessing the deformation of actuators is used in literature for uniform actuators [96], [131].

4.2.3   Printing Parameters

The printing process heats and stretches the filament as it is extruded through the nozzle, which stores strain in the printed lines when they are cooled down. This internal strain loading is possible because the printed filament is holding to the build plate and other

printed lines, thus not releasing the strain by itself. This process of inducing strain into the actuator acts like a training step in 4D printing, which can be controlled by setting the printing parameters.

The PLA actuators were fabricated with dimensions of 30 mm × 1.6 mm for length and width, with varying heights from 0.6 mm to 1.2 mm. A 100% infill ratio was employed, ensuring the actuators were printed as solid structures as specified in the slicer settings. Printing occurred in straight lines across the actuators at a 0° raster angle, and a constant 100% cooling fan speed was maintained throughout, limited by the FDM fan speed. This angle ensured uniform strain direction without twisting the actuators. Additionally, the bed temperature was set at 27 °C to prevent induced strain release from the bottom layers, and no adhesion substances were applied during the printing process.

Table 4.1. Calculated coefficient of thermal expansion values for different layers at different printing speeds.

Test	Parameter	Values
S_P vs. H_A	S_P	10 – 80 mm/s
	T_P	200 °C
	R_{PA}	50%
	H_L	0.1 mm
	H_A	0.6 – 1.2 mm
T_P vs. H_A	S_P	60 mm/s
	T_P	180 – 230 °C
	R_{PA}	50%
	H_L	0.1 mm
	H_A	0.6 – 1.2 mm
R_{PA} vs. H_A	S_P	60 mm/s
	T_P	200 °C
	R_{PA}	0 – 100%
	H_L	0.1 mm
	H_A	0.6 – 1.2 mm
H_A vs. H_A	S_P	60 mm/s
	T_P	200 °C
	R_{PA}	50%
	H_L	0.05 – 0.3 mm
	H_A	0.6 – 1.2 mm

The influence of various printing parameters on the internal strain within the PLA actuators was examined through four distinct parameters, with a focus on varying the

actuator's height (H_A). These parameters included the printing speed of the active layers (S_P), printing temperature (T_P), passive-to-active layers ratio (R_{PA}), and the actuator's layer height (H_L).

Each parameter was analyzed individually and then collectively. Regarding the passive-to-active layers, which represent low-strain to high-strain layers, every passive layer was printed at a very slow speed (10 mm/s), inducing minimal strain within these layers. A summary of the printing settings used in each test is presented in **Table 4.1** These values have been determined to compare it by performance in literature [131]. Actuators were fabricated with dimensions of 30 mm × 1.6 mm for length and width, with varying heights from 0.6 mm to 1.2 mm. A 100% infill ratio was employed, ensuring the actuators were printed as solid structures as specified in the slicer settings. Printing occurred in straight lines across the actuators at a 0° raster angle, and a constant 100% cooling fan speed was maintained throughout, limited by the FDM fan speed. The angle ensured uniform strain direction without twisting the actuators.

Additionally, the bed temperature was set at 27 °C to prevent induced strain release from the bottom layers, and no adhesion substances were applied during the printing process. A total of 178 printing settings were tested in this work. Each printing setting was used to print three samples of actuators, making the total actuators tested 534 actuators. Then, the average bending angle of the actuators was used in the predictive model results. Using the printing settings presented in **Table 4.1** actuators were fabricated with dimensions of 30 mm × 1.6 mm for length and width, with varying heights from 0.6 mm to 1.2 mm. A 100% infill ratio was employed, ensuring the actuators were printed as solid structures as specified in the slicer settings.

The effect of each parameter was represented mathematically to understand the effect it has individually. Following this, a predictive model was formulated based on the collective effects of all the printing parameters. Then, 189 actuators were printed using a series of randomized printing parameters (within the ranges in **Table 4.1**) to provide better calibration for the model.

All the tested actuators were used to create the predictive model for the PLA actuators, providing very accurate predictive properties at extremes of the parameters and good predictive properties when using all the parameters to control the internal strain. Then, an FEA model was created by replicating the behaviour of the SME using shrinking to create bending. This model was then used to develop multiple grippers with eight and four fingers.

The bending angles of the fingers were controlled individually based on the developed models, which serve as proofs-of-concept of the proposed approach in this work.

4.3   Results and Discussion

This section presents the results acquired from the tests of each parameter, each represented visually and with mathematical equations. The results are discussed by the effects of these parameters on the bending caused in the actuators after activation. Following that, each parameter is discussed.

4.3.1   Printing Speed

The first parameter tested in this chapter is the printing speed of the active layers, which was varied in the range of 10 mm/s to 80 mm/s at an interval of 10 mm/s. At printing speeds beyond 80 mm/s, the actuators started to get overstretched and delaminated, making those speeds unsuitable for the printing of stable structures on basic FDM printers. Four different actuator heights were printed in the range of 0.6 mm to 1.2 mm at a 0.2 mm interval to investigate the dependency of the results on the height of the actuator.

When using a printing speed of 10 mm/s for the active layers, the actuator consists of passive layers completely. This causes the ratio of passive-to-active layers ratio to be 100%, which is an exception to the ratio presented in **Table 4.1**. The bending angle of the actuators increases in a linear manner as the printing speed increases, as shown in **Figure 4.2** (a). This is due to the stretching of the filament, causing a higher potential for the lines to shrink after activation. This behaviour can be seen across all heights of actuators while increasing the height of the actuators caused the bending angle to decrease.

Furthermore, there is a slight reduction in the length of the actuators, the larger the bending is. This is accompanied by a slight expansion in the width of the actuators, which is due to the shrinkage of the PLA [41].

To further illustrate this concept, a square plate with side lengths and height of 30 mm × 30 mm and 1.2 mm, respectively, was printed. The plate was printed with increasing printing speeds ranging from 10 to 80 mm/s so that each part in **Figure 4.2** (b) was printed using the same speed. Upon activation of the plate, it can be seen that the bending increases gradually according to the printing speed. This provides a good visual representation of the effect of changing the printing speed and a proof-of-concept of how to use it to achieve complex shape programming.
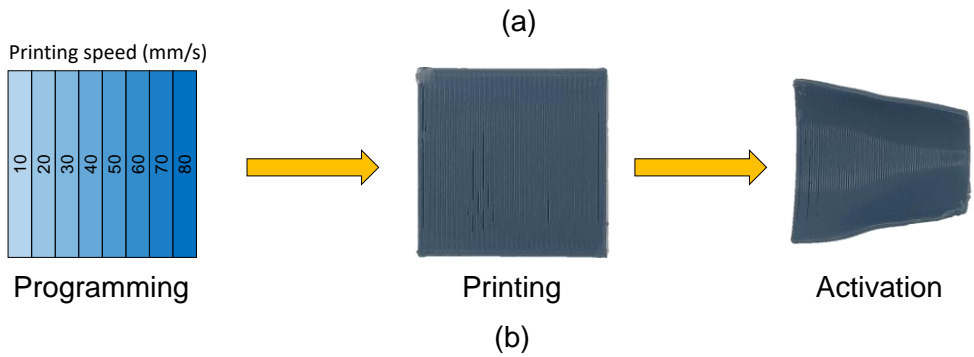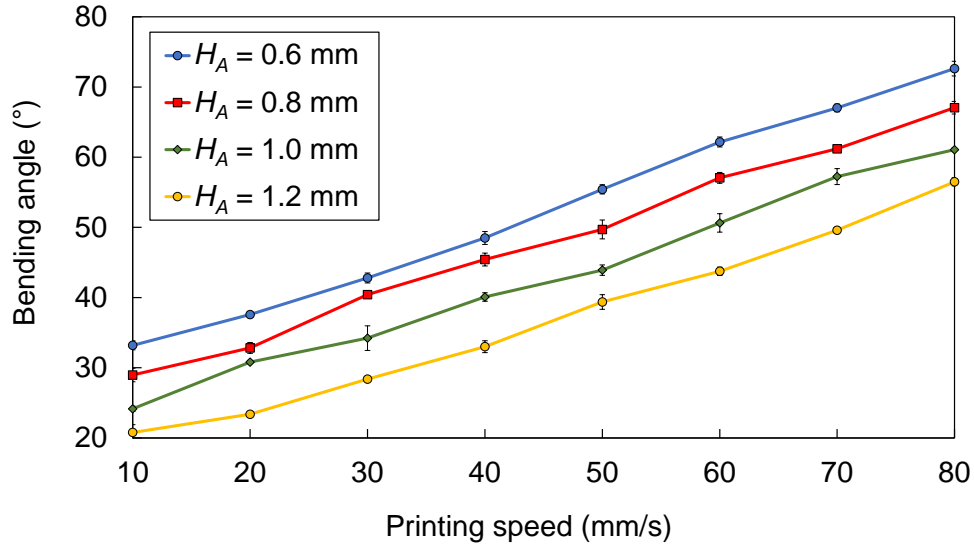
Figure 4.2. The effect of the printing speed on the bending angle. (a) Printing speed (b) Illustrative example showing top views of the shape-programming concept, printed shape, and activated shape.

The relationship between the bending angle and the printing speed can be set in a linear model with an R-squared value of 0.99. A linear regression model was used to formulate the relationship between the bending angle (in degrees), the printing speed, and the actuator height, yielding the following equation:

$$\theta = 0.54S_P - 25.88H_A + 43.77 \qquad (4.2)$$

4.3.2   Printing Temperature

The second printing parameter under examination was the printing temperature, which ranged from 180 °C to 230 °C, with a 10 °C increment, as shown in **Figure 4.3**. When printing the actuators at temperatures exceeding 230 °C, it results in excessively melted lines

that tend to leak outwards. To address this problem, higher-powered cooling fans can be employed, but this approach establishes the constraints for standard FDM printers, at which modifications are needed to change for a powerful fan. Similar to the previous evaluation, four different actuator heights were assessed.
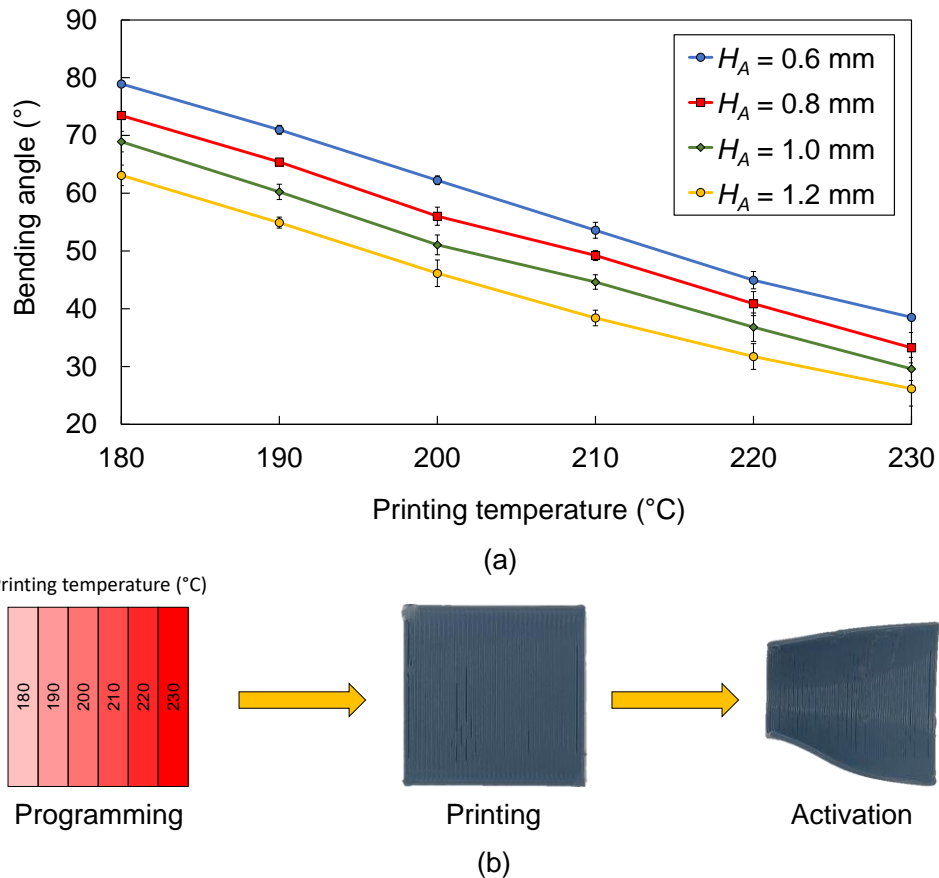

(a)

(b)

Figure 4.3. The effect of the printing temperature on the bending. (a) Printing (b) Illustrative example showing top views of the shape-programming concept, printed shape, and activated shape.

The results shown in (a) demonstrate that the bending angles of all actuator height values decrease when increasing the printing temperature. The strain in the structure decreases as the PLA is heated up since it becomes more viscous, causing less stretching to be applied to the PLA when being extruded. As previously designed, **Figure 4.3** (b) shows a printed plate with increasing printing temperature for each part of the plate. In this case, the behaviour is opposite to the one observed when varying the printing speed. It can be seen that increasing the printing temperature has a negative effect on the bending angle.

All the actuators with different heights seem to respond in an almost inverse linear relationship. The relationship between the bending angle and the printing temperature can be set linearly. A linear regression model with an R-squared value of 0.99 was formulated to present the relationship between the bending angle (in degrees) and the printing temperature at different actuator heights, as follows:

$$\theta = -0.79T_P - 24.44H_A + 234.67 \tag{4.3}$$

4.3.3 Passive to Active Layer Ratio

The third parameter that was tested is the ratio of the passive-to-active layers, meaning layers printed at a slow speed to layers printed at faster speeds. The ratio was varied in the range of $0 - 100\%$ using four different actuator heights. Since four different heights are used and all of them use a layer height of 0.1 mm, the ratios cannot be the same for all heights. The 0.6 mm actuators have only six layers meaning that the R_{PA} is using an interval of 16.7%, while the 1.0 mm actuators have ten layers and use an R_{PA} interval of 10%. Nevertheless, this does not cause problems in the comparisons since all actuators have a ratio from 0% to 100%.

The results of the printed actuators are presented in **Figure 4.4** (a), with all heights following similar responses to the R_{PA}. The relationship between the bending angle and the R_{PA} seems to be a negative parabolic one. The bending angle is the highest when the R_{PA} is at about 50% (when the number of passive and active layers is equal). This behaviour can be explained as a result of the strain difference between the layers.

The presence of a passive layer, a layer that does not shrink as much as an active one, created a larger size difference between the active and passive layers causing a larger bending angle. The parabolic behaviour can be seen in **Figure 4.4** (b), where the square plate was 4D-printed using an R_{PA} that varies from 0% to 100%. The figure shows a bowtie-like shape with the maximum bending angle at its centre, which proves the previous observations.

The bending angle of the actuators (in degrees) as related to the R_{PA} can be modelled using a second-order polynomial or higher (the higher the order the more accurate it is). A third-order polynomial can be fit into the model with an R-squared value of 0.92, as follows:

$$\begin{aligned} \theta = -1.36 \times 10^{-4}R_{PA}{}^3 + 2.12 \times 10^{-3}R_{PA}{}^2 \\ +1.01R_{PA} - 34.53H_A + 50.78 \end{aligned} \tag{4.4}$$
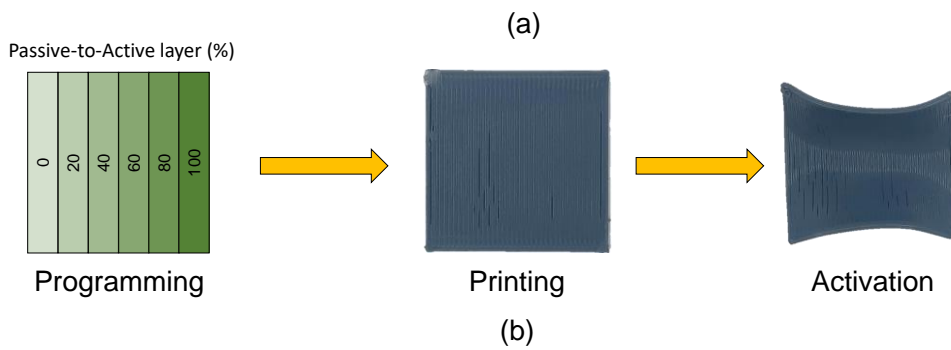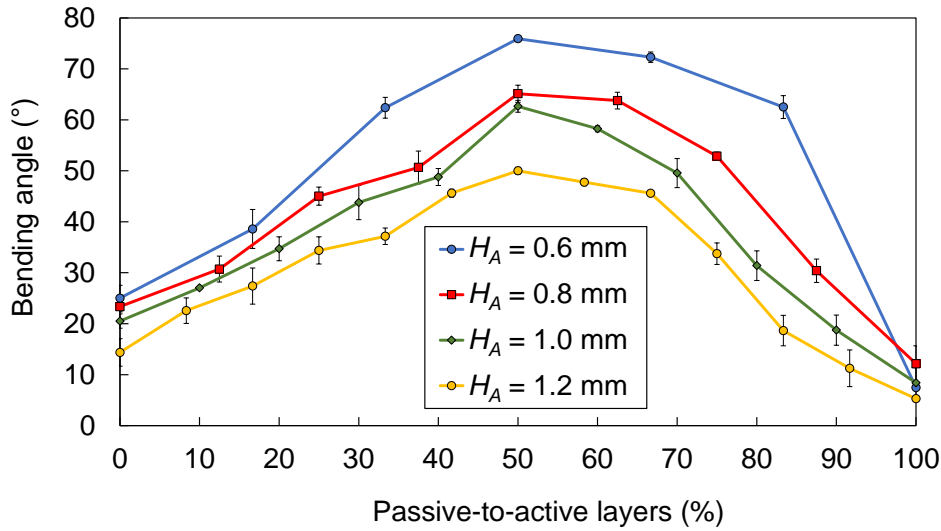
Figure 4.4. The effect of the ratio of passive-to-active layers on the bending. (a) Passive-to-active ratio (b) Illustrative example showing top views of the shape-programming concept, printed shape, and activated shape.

4.3.4 Layer Height

The fourth parameter that was tested is the layer height of the printed PLA, which ranged from 0.05 mm to 0.30 mm, at an interval of 0.05 mm. Since the R_{PA} of all actuators needs to be 50%, then not all layer heights can be used for all actuators due to the difference in the actuators' height. All the layers' heights seem to follow a similar behaviour, which can be modelled using the same approach.

The bending angle of the actuators decreases as the layer height increases, as shown in **Figure 4.5** (a). This effect can be explained by a decrease in the pressure in the heated nozzle when the layer height increases. As the pressure decreases, less strain is stored in the lines since there is more space for the polymer to settle into. **Figure 4.5** (b) shows the printed plate with varying layer heights ranging from 0.05 mm (where the bending angle was at its maximum value) to 0.3 mm (where the bending angle was at its minimum value).
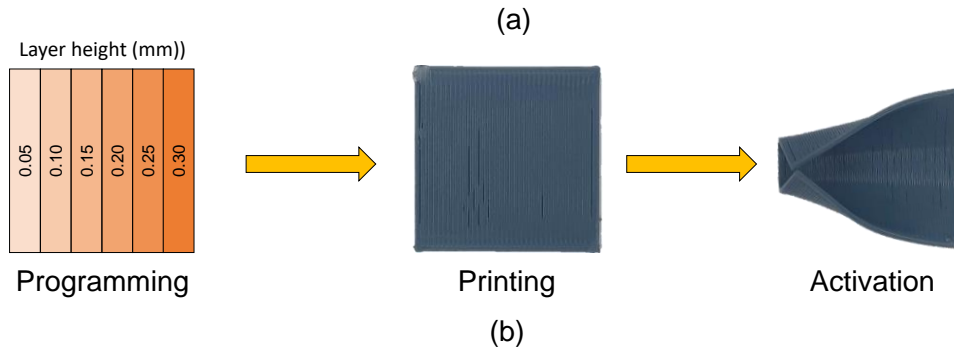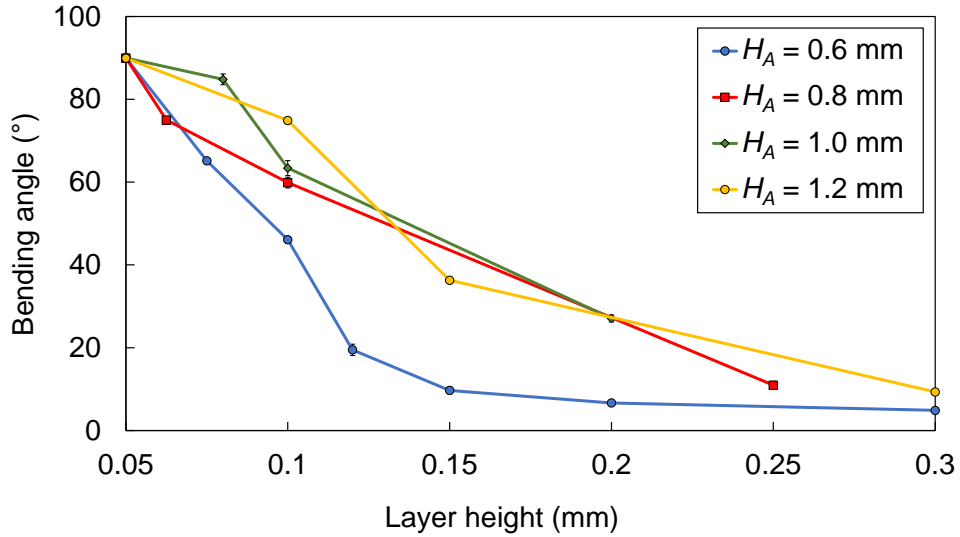
Figure 4.5. The effect of the layer height on the bending. (a) Layer (b) Illustrative example showing top views of the shape-programming concept, printed shape, and activated shape.

The relationship is nonlinear and can be represented by a negative logarithmic model with an R-squared value of 0.93. The relationship between the bending angle (in degrees) and the layer height can be represented using the following equation:

$$\theta = 106.86 H_L - 64.07\, ln(H_L) - 32.32 H_A - 74.85 \tag{4.5}$$

4.4 Model's Formulation

The model is formulated by using all the tested actuators using multiple linear regression, this model is presented in this section. The same model is used to predict the thermal expansion coefficient needed for the simulation of the bending of the actuators.

4.4.1 Predictive Model

Using all the results from the actuators, a predictive model can be formulated to encase all the effects of the parameters into a single predictive equation. For this purpose,

many different methods were used to construct this predictive model. These models are presented in Table 4.2, in which a classic regression model, a Multi-Layer perception (MLP) based on three layers, a linear support vector machine (SVM), a radial basis function (RBF) SVM, and finally a non-linear regression through the origin (RTO) model. R2 is error square of the results, Adjusted R2 is the fixed according to the number of predictors used, while MSE is the means squared error.

Table 4.2. The results from the different modelling methods tested for this algorithm.

Model	*R2*	*Adjusted R2*	*MSE*
Linear Regression	0.910	0.905	40.928
MLP-Layer=3	0.942	0.939	26.362
MLP-Layer=2	0.952	0.949	22.098
MLP-Layer=1	0.949	0.946	23.316
SVM-Linear	0.903	0.897	44.360
SVM-RBF	0.970	0.968	13.688
RTO	0.979	0.972	6.873

As can be seen in Table 4.2, the RTO regression model has the best R-square value, along with being the most easily understood and adjusted model. A nonlinear RTO (Real-Time Optimization) model was formulated for all five variable settings. Among these variables, the printing speed, printing temperature, and actuator height parameters exhibit linear effects on the bending of the actuators. Consequently, each of these variables can be represented by a single parameter. However, in the case of the passive-to-active ratio, the relationship is best captured by a third-order polynomial, necessitating three parameters for an accurate representation.

The layer height followed a negative logarithmic pattern, requiring two parameters. A total of 534 actuators were used to develop the model. To investigate the accuracy of the model, 189 actuators designed using randomly chosen parameters were used to validate the accuracy of the model. The model is a regression through the origin (RTO) model, which is decided based on the regression intercept statistical significance. RTO is applicable under the assumption that the model passes through the origin [203], which can be explained by the physical characteristics of the actuators. This is based on the lack of bending when printing with minimal strain-inducing parameters, which do not produce bending in the actuators [131], [196]. The results show that the model is a reliable predictor for the bending angle of the actuators since it offers an R-squared value of 0.98. The mathematical predictive model for the bending angle based on the printing parameters is presented as follows:

$$\theta = -7.42 \times 10^{-5} R_{PA}{}^3 - 5.14 \times 10^{-3} R_{PA}{}^2 + 1.12 R_{PA} + 176.62 H_L$$
$$-67.72 \ln(H_L) + 0.60 S_P - 0.81 T_P - 29.27 H_A \qquad (4.6)$$

This model represented the control allowed within the actuators by parameter control. Through the equation, we could design actuators with the desired bending angle which ranges from 0° to 90°.

4.4.2   FEA Model

The FEA model was created by replicating the behaviour of the SME using shrinking to create bending. The use of the difference in the coefficient of thermal expansion (CTE) to shrink some parts of a design to replicate SME is popular in 4D printing since it can reproduce the same shape change that is undergone by the SME in the actuators [217]. The effect of bending can be replicated by modelling the actuators as two parts with different CTEs, allowing different shrinking in the parts, which causes bending. It is worth mentioning that the FEA process can be carried out using other approaches, such as the one presented in [41], which relies on the thermo-visco-hyperelastic model.

The results from the predictive model can be used by converting the bending angle into an arc length difference between the top and bottom surfaces of the actuator. Thus, the CTE of each of the top and bottom parts can be estimated and translated into the models. This same CTE can be used for various other models regardless of the size, as long as they use the same parameters as the ones tested in this work. This approach is demonstrated in **Figure 4.6** (a), which presents an FEA simulation using ANSYS software by dividing an actuator into two parts (top and bottom) to simulate the bending and shrinking behaviour. This FEA example mimics the behaviour of the actuator shown in **Figure 4.6** (b), which was printed using S_P, T_P, R_{PA}, H_L, and H_A of 20 mm/s, 200 °C, 20%, 0.1 mm, and 1 mm, respectively.

In terms of boundary conditions, a uniform thermal condition is imposed on all sides of the beam, gradually raising the temperature from the initial room temperature of 24°C to 85°C. To maintain structural integrity and prevent sections of the beam from interpenetrating or sliding apart during the simulation, a bonded contact type is established between the faces of each beam section. Lastly, to ensure stability and constrain the beam appropriately, a fixed support is applied at the bottom center of the beam. This fixed support serves as an anchor

point, preventing the beam from translating or rotating at that location and providing a stable foundation for the simulation.
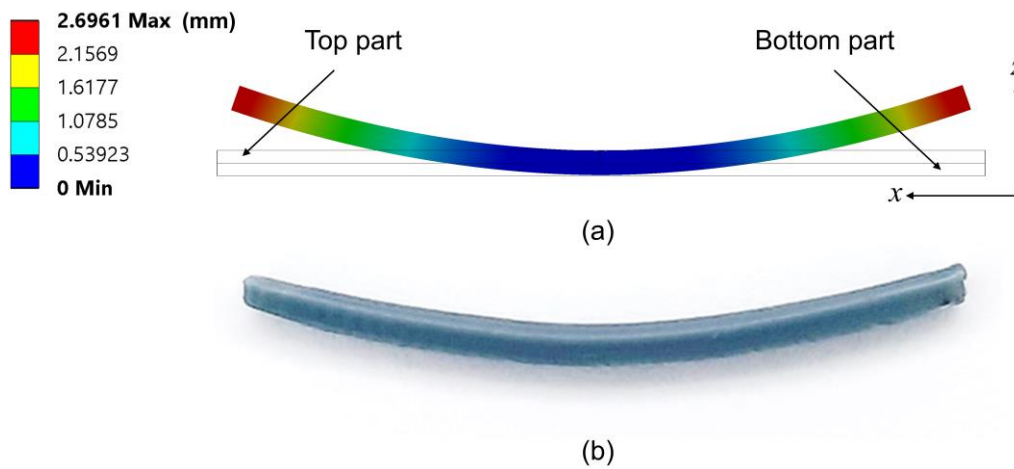

Figure 4.6. FEA vs. fabrications results. (a) An FEA model that uses a two-part approach to mimic the actuation performance of the 4D-printed actuator in (b).

The FEA process played a pivotal role in the study, and the capabilities of the ANSYS software were harnessed to carry out this intricate analysis. Within the ANSYS environment, the static structural analysis module was specifically employed to comprehensively address the influence of the Coefficient of Thermal Expansion (CTE) on the system. The CTE effect was a critical aspect of the investigation as it pertains to the response of the structure to temperature changes. In the simulation, a foundational assumption was made that all parts of the body experienced heating at an identical rate, with no heat loss to the environment. This assumption allowed for the creation of a controlled and simplified environment within the simulation, enabling a more precise examination of the CTE effect without the complexities of varying heat distribution or dissipation.

The thermal aspect of the analysis involved gradually heating the structure, starting from the standard room temperature of 23 °C. The heating process continued until reaching a temperature of 85 °C. It is at this specific temperature that the PLA material, a commonly used thermoplastic, undergoes a phase change and becomes activated. This activation point was of particular interest in the study, as it marks a critical transition in the behavior of the material and can have significant implications for its performance in various applications. The heating process in ANSYS was carried out by convection, according to the following formula:

$$\dot{Q} = hA(T_2 - T_1) \tag{4.7}$$

where h is the coefficient of heat transfer, A represents the area of the surface where the heat transfer takes place, T_1 is the PLA temperature, and T_2 is the temperature of the water environment. The original location of a particle can be represented by X. At a certain time (t), when a new location is generated from the movement of the particle to $x = x(X,t)$. Therefore, the displacement vector, $u = u(X,t)$, is the one pointing from the original location of the particle to its new location. Thus, the deformation gradient (F) can be defined as:

$$F = \frac{\partial x}{\partial X} = I + \frac{\partial u}{\partial X} \tag{4.8}$$

where I is the identity tensor. The displacement, the second Piola-Kirchhoff stress tensor (S), and the elastic strain tensor (ε_{el}) can be related by a linear momentum balance equation and a stress-strain equation, as follows:

$$\rho \frac{d^2 u}{dt^2} = \nabla \cdot (FS) + f_v \tag{4.9}$$

$$S = C : \varepsilon_{el} \tag{4.10}$$

where ρ is the density, ∇ is the divergence, f_v is the volumetric force, and C is the elasticity tensor. Changes in volume happen as a result of the changing temperature, which is denoted by (ε_{th}) that is given as:

$$\varepsilon_{th} = \alpha \left(T - T_{ref} \right) \tag{4.11}$$

where T and T_{ref} are the current and reference temperatures, respectively [218]. The FEA model using CTE is based on the shrinking of objects to represent the shape change in materials. The CTE of the material is implemented in the simulation based on the following equation:

$$\alpha_n = \frac{\Delta L_n}{L_0 \Delta T} \tag{4.12}$$

where n represents the current part of the actuator (top or bottom), α_n is the coefficient of thermal expansion of the nth part, L_0 is the initial length of the actuator, ΔL_n is the change in length of the nth part, and ΔT is the change in the temperature. In this model, a two-part design was developed, where the top part is treated as the active component in the actuator. The CTE can be calculated by the difference in the arc lengths of the actuator. Since the actuator is divided into two parts in the simulations, the arc length at the centre of each part is needed to replicate the bending. These lengths can be calculated from the radius of bending, the angle formed by the arc (in radians), and the height of the actuator as follows:

$$\begin{cases} L_t = (R + 0.25 H_A)\varphi \\ L_b = (R + 0.75 H_A)\varphi \end{cases} \tag{4.13}$$

where L_t and L_b are respectively the lengths of the top and bottom parts after deformation. The use of 0.25 and 0.75 as manipulation for the height allows for the arc length to be calculated at half the height of each of the parts of the actuator (25% and 75% of the actuator height) for the top and bottom parts, respectively. Using Equation (4.13), two CTE values can be found for every bending angle, with one for the bottom part (α_b) and another one for the top part (α_t), by solving Equation (4.12).

These CTE values will not only replicate the bending of the actuator but the shrinking value as well. It is worth mentioning that the model can be developed using more parts, which might produce more accurate results. Theoretically, the more parts used in the model, the more accurate the results. Thus, it is possible to increase the number of parts used to formulate Equations (4.12) and (4.13) so that the number of the parts is equal to the number of layers used to print the actuator. However, such an approach increases the complexity and time required to perform the simulation.

To demonstrate the accuracy of the developed FEA model, eight actuators with 30 mm × 1.6 mm × 1 mm for respectively the length, width, and height were printed. Each actuator was printed with a printing temperature of 200 °C, a passive-to-active layers ratio of 50%, and a layer height of 0.1 mm. Meanwhile, the printing speed of the active layers was different in each actuator, which varied between 10 to 80 mm/s. These actuators were then activated to measure the experimental bending angle (θ_{Exp}). Then, ANSYS software was used

to find the FEA bending angle (θ_{FEA}) of each actuator based on the calculated values of α_t and α_b. This was followed by finding the estimation error (E) of the bending angle.

Table 4.3 shows the CTE values used in the FEA process, as well as a comparison between the FEA and experimental results. Even though only two parts were used for each actuator, the results presented in Table 4.3 show that the error is very low. In addition, the same approach was used to compare the bending angle values of all of the actuators developed in this chapter with their corresponding FEA models.

The results showed that the FEA model provided a good fit with an R-squared value of 0.98 and an R-squared value of >0.99 when compared with the values of the predictive model. The comparison is also displayed graphically in Figure 4.7. Thus, the two-part model is sufficient to represent the behaviour of the actuators developed in this work. This allows the model to be used to simplify the development process of more complex designs, which can be carried out based on the control of the printing parameters to control the induced strain.

Table 4.3. Comparison between FEA and experimental results of actuators printed at different printing speeds.

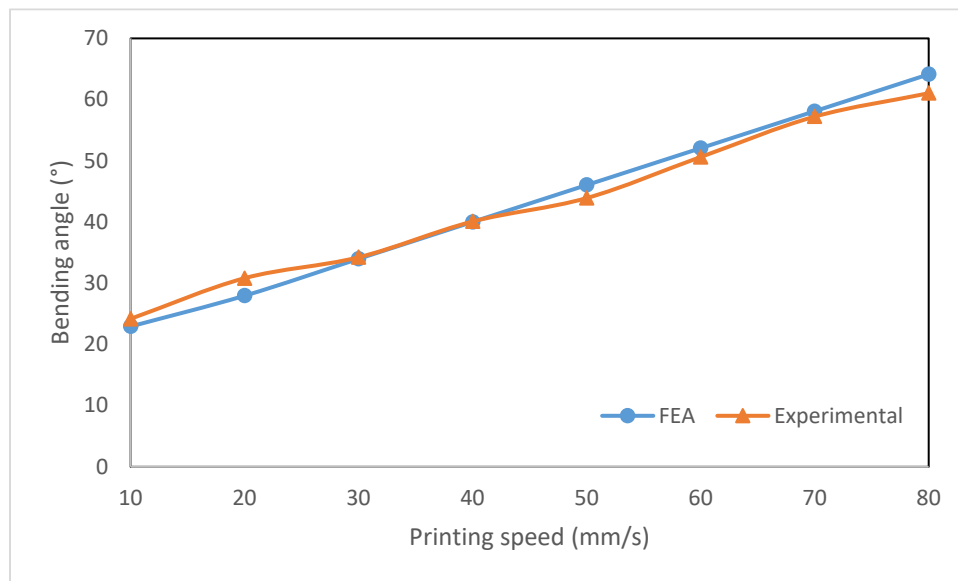| S_P (mm/s)	α_t (°C^{-1})	α_b (°C^{-1})	θ_{FEA} (°)	θ_{Exp} (°)	E (°)
10	-2.43E-03	-2.89E-03	22.92	24.15	1.23
20	-2.88E-03	-3.42E-03	27.95	30.80	2.85
30	-3.21E-03	-3.84E-03	33.98	34.22	0.24
40	-3.39E-03	-4.12E-03	40.01	40.08	0.07
50	-4.31E-03	-5.08E-03	46.04	43.91	2.13
60	-6.86E-03	-7.53E-03	52.07	50.63	1.44
70	-8.86E-03	-9.42E-03	58.11	57.24	0.87
80	-1.05E-02	-1.09E-02	64.14	61.07	3.07

Figure 4.7. Comparison between the results achieved by the experiments and FEA.

4.5 Structures Control

The FEA model served as a valuable tool for creating multiple grippers featuring both eight and four fingers. These fingers were individually manipulated in terms of their bending angles, utilizing the models developed as a proof-of-concept for the innovative approach presented in this work. The process of designing these grippers consisted of segmenting the structures into four distinct parts, each corresponding to specific strain levels determined by the printing parameters. These segments encompassed passive (P) with a bending angle of about 0°, low-strain (LS) with a bending angle of about 9°, medium-strain (MS) with a bending angle of about 24°, and high-strain (HS) sections with a bending angle of about 45°, effectively guiding the development of the grippers based on the induced strain profiles. These are programmed based on the predictive model parameters. The printing parameters used to fabricate and simulate these segments are summarised in **Table 4.4**.

**Table 4.4.** Printing parameters and strain levels used to develop the grippers.

Parameter	P	LS	MS	HS
H_A (mm)	1	1	1	1
H_L (mm)	0.1	0.2	0.1	0.1
R_{PA} (%)	10	20	40	40
S_P (mm/s)	10	40	40	60
T_P (°C)	200	200	210	200
α_t (°C^{-1})	-2.28E-05	-8.12E-04	-6.36E-04	-2.58E-03
α_b (°C^{-1})	-2.04E-05	-7.75E-04	-1.22E-04	-1.82E-03
θ_{FEA} (°)	0.32	8.68	24.06	45.15

The first gripper that was developed in this section included eight fingers, where the centre of the gripper was a passive segment, while the fingers included one pair of low-strain segments, one pair of high-strain segments, and two pairs of medium-strain segments. The developed gripper is presented in **Figure 4.8** (a), where the red colour represents the passive segment, while the orange, yellow, and green colours represent the low, medium, and high strain segments, respectively.

The dimensions of each finger were respectively 30 mm × 1.6 mm × 1 mm for the length, width, and height, while the radius of the circle was 3.75 mm. **Figure 4.8** (a) also shows the printed and activated gripper, where the bending angles of the fingers' pairs varied based on the induced strain. This concept was then verified using ANSYS, where α_t and α_b of each pair were set according to **Table 4.4**. **Figure 4.8** (b) shows the FEA results of the complete gripper, proving that the FEA results agree well with the experimental results and the concept presented in **Table 4.4**. These results agree well with the results of the simulated single actuators and are comparable with the model used to compute the CTE with an R-squared value of 0.98. These results provide the same accuracy in representing the experimental results as the mathematical model of the actuators.
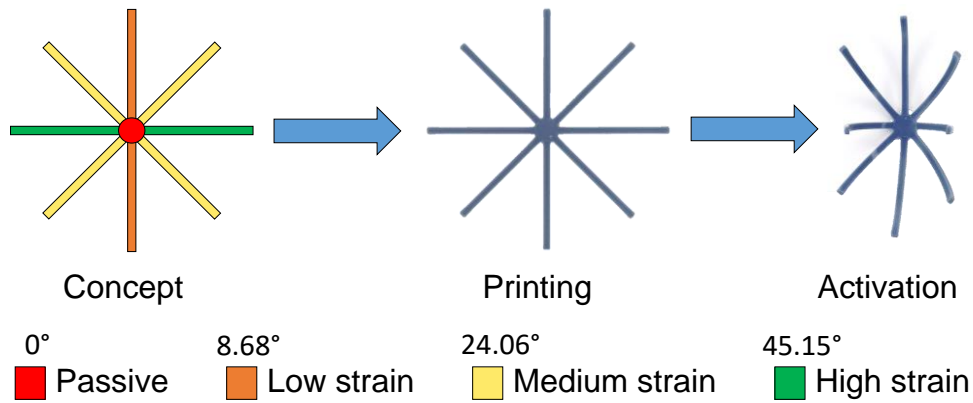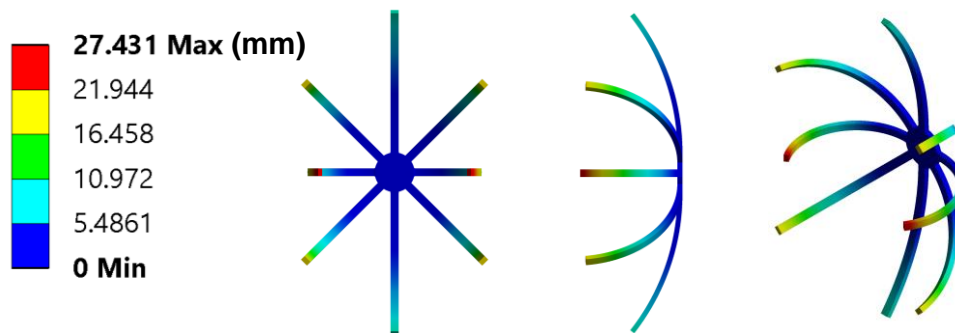
Figure 4.8. Gripper with eight fingers. (a) Top views of the design, and 4D-printed gripper before and after activation. (b) FEA results of the top, side, and isometric views of the gripper after activation.

To prove that the proposed concept is valid for structures with different dimensions, a four-fingers gripper was developed. Each finger is 22 mm long, 8 mm wide, and 1 mm high, as shown in **Figure 4.9** (a). The degree of bending in each finger can be controlled independently. The strain level in each finger is controlled using the printing parameters, which produce the desired shape changes in the structure when activated.

The use of multiple parameters to control the strain can be very helpful when there are certain restrictions on the changes that can be made to the structure. For instance, certain designs might require using adaptive layer height to optimise the printing time while maintaining acceptable quality. When it is such a case, there are other parameters that can be manipulated to achieve the desired bending in the structure, allowing the preservation of other characteristics of the design.
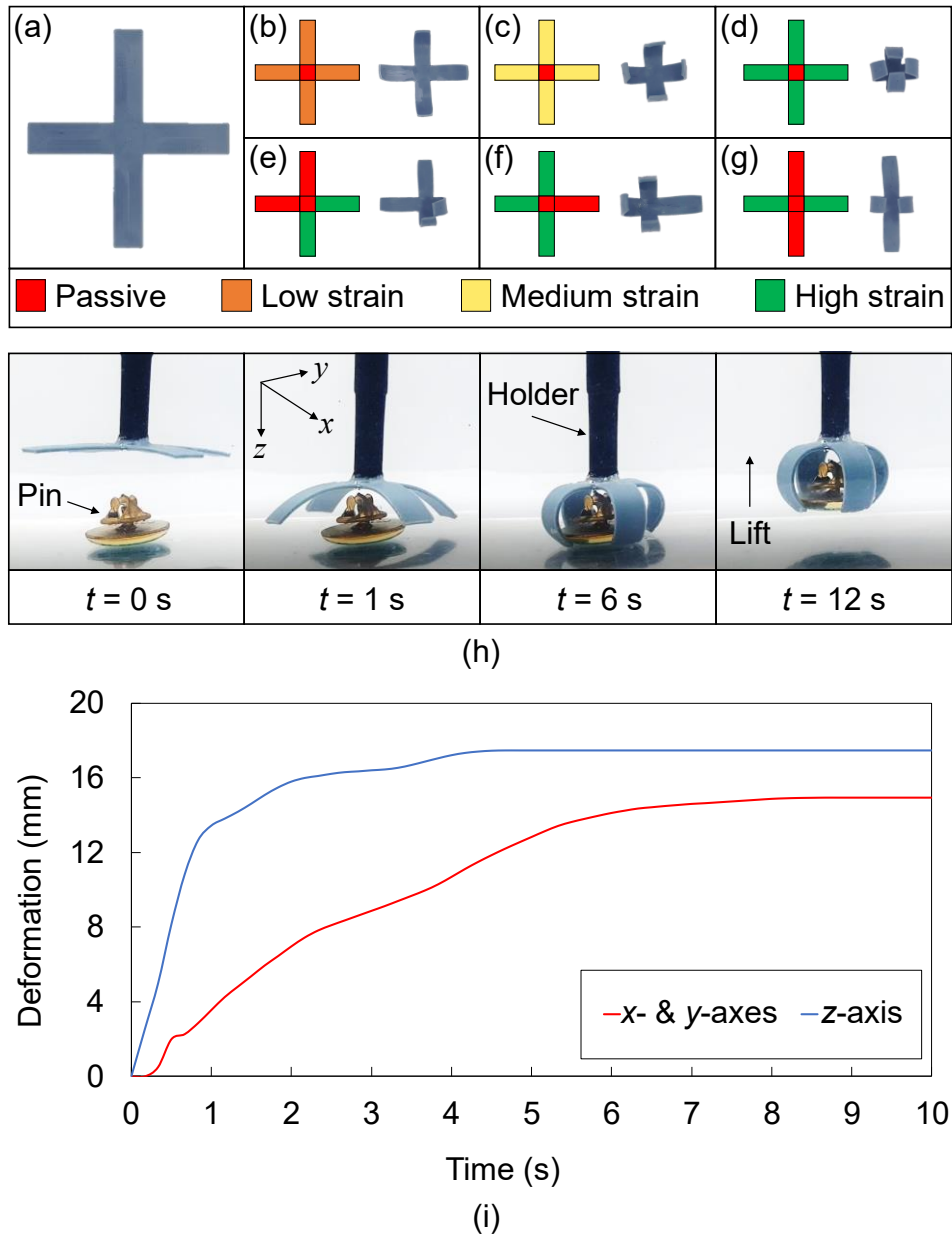
Figure 4.9. Gripper with four fingers. (a) Top view of the 4D-printed gripper before activation. (b-g) Top views showing design concepts. (h) Gripper with four high-strain level fingers gripping and picking a pin underwater at different timestamps. (i) Deformation values of the gripper's fingers.

This concept is demonstrated in **Figure 4.9** (b-d), where the printing parameters presented in **Table 4.4** were used to achieve bending angles of about 15° to 40° to 60° in the grippers, respectively. Meanwhile, the grippers presented in **Figure 4.9** (e-g) achieved bending angles of about 60° in each high-strain level finger. Then, the gripper presented in **Figure 10** (d) was used to pick a pin that is immersed in water at a temperature of 85 °C, as presented in **Figure 10** (h). In this case, the gripper was attached to a holder and flipped so

that the deformation direction is towards the bottom to simplify the gripping process. The deformations of the fingers along the x-, y-, and z-axes were recorded and then analysed using a video-analysis tool (Tracker software), as shown in **Figure 4.9** (i).

It is worth noting that the deformation values along the x- and y-axes are almost identical. Thus, both axes are represented by a single graph. The results show that the deformation values of the fingers across all axes reached steady-state values after around 8 seconds, where the deformation along the x- and y-axes was 14.94 mm while the deformation along the z-axis was 17.47 mm. The results presented in this chapter demonstrate clearly the ability of the proposed approach to accurately control certain parts of 4D-printed structures to achieve different bending levels according to the induced strain during the printing process without the need for manual training.

4.6   Development of 4D-Printed PLA Microgripper

4.6.1   Design and Fabrication

Figure 4.10 presents the envisioned microgripper design, complete with slots to accommodate the microactuator holders. The gripper itself remains passive, devoid of any internal strain during the printing process. As a result, when activated, it experiences no shape change but maintains a rubbery, mendable state. The microactuators serve as the active components of the design, responsible for inducing deformation in the structure. This deformation arises from the internal strain intentionally incorporated into them during the printing process, which is precisely controlled by specific printing parameters. These parameters allow for a high level of regulation over the internal strain, facilitating a wide range of deformation possibilities in the actuators. By examining the ratio of deformation between the holders and the actuators, effective control over the gripping distance can be achieved.
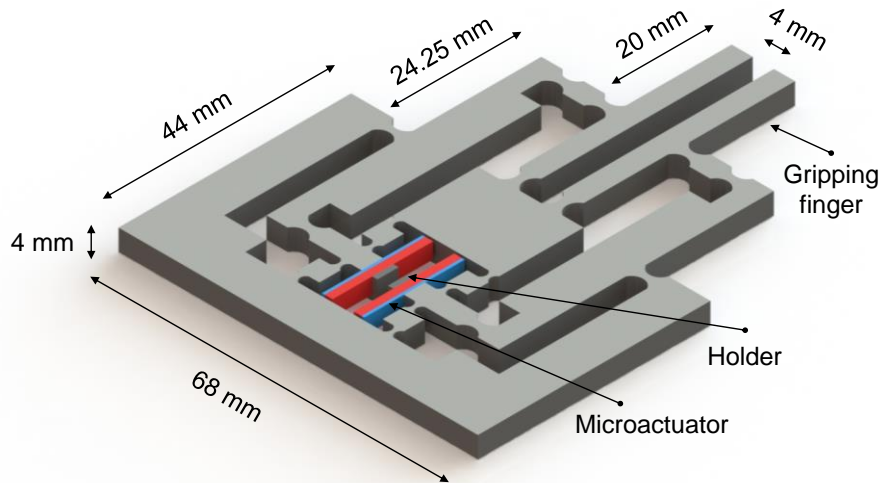
Figure 4.10. A 3D view of the microgripper design. The blue and red parts represent the passive and active layers of the actuators, respectively.

The microactuators consist of passive and active layers, each with a height of 1 mm, resulting in a total thickness of 2 mm for each actuator. These actuators are oriented horizontally and inserted into the holders in an opposing configuration, ensuring symmetrical deformations. The SME within the actuators operates in opposite directions, causing them to exert outward pressure on each other. This reciprocal motion leads to the holders moving apart from each other, resulting in the gripper fingers closing proportionally to the deformation of the actuators. Throughout the printing process, careful control of internal strain is achieved through specific printing parameters. This allows for a wide range of deformation possibilities in the actuators. A simulation was conducted to determine the necessary displacement of the holders needed to achieve the desired gripper closure distance, aiding in the design of an appropriate actuator.

In this work, the FEA was carried out using ANSYS software (ANSYS, Inc., PA, USA), using a static structural system available on the software. Force was exerted on the holder segment of the design to assess the gripper's response. A simulation of the motion mechanism was conducted to illustrate the gripping procedure, aiming to establish the relationship between the displacement of the gripper arms and the displacement of the holders. This measurement of displacement was employed to define the configurations and parameters of the actuators used in the fabrication of the entire structure.

Additionally, the actuators played a role in the simulation to predict the extent of deformation. This is demonstrated in **Figure 4.11**, with the gripper before and after being heated, where the deformed structure is reacting to the force applied by the actuators' bending.

At room temperature, the gripper arms distance is 4 mm while the distance between the actuators is the same, this is the shape that the structures are printed in. As the structure gets heated above T_g the actuators start to deform and bend, but since the gripper body is passive, no deformations are undergone until the two actuators are in contact as seen in **Figure 4.11** (b). The gripper with the deformed actuators and closure of the gripper is shown in **Figure 4.11** (c) the closure of the gripper hand is caused by the force generated by the contacts of the actuators pushing against each other, with the deformation of the gripper body causing the closure of the arms till only 1 mm distance is left between them.
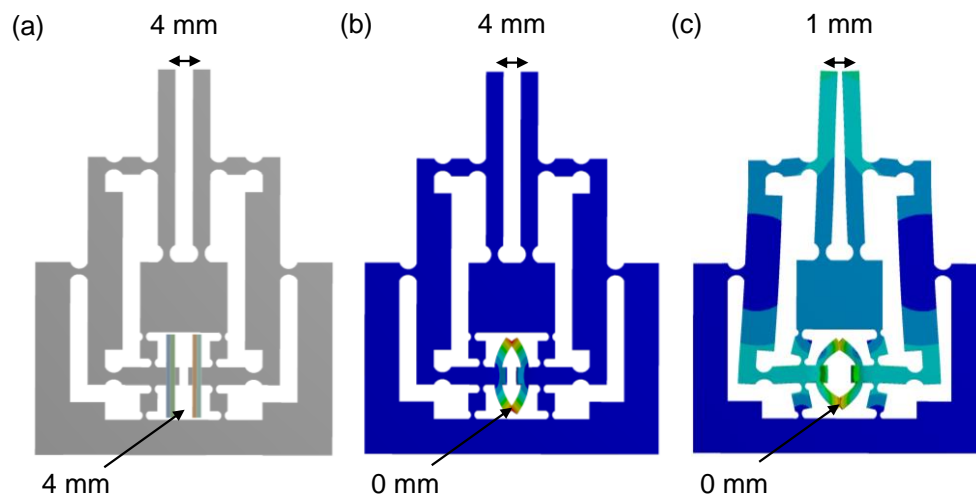

Figure 4.11. Simulation results of the microgripper. (a) The undeformed gripper at room temperature (b) The structures when the actuators are first in contact (c) The fully deformed structure.

The gripper was treated as PLA in a rubbery state to allow the deformation of the arms since PLA is hard to bend in the glassy state. The simulation was run ensuring a deformation measurement of 3.85 mm at the holder translating to 3 mm in the fingers of the gripper, which is to be replicated in the printed actuators to produce the same results in the printed gripper. The height allowed in the gripper for the actuator is limited to 19 mm in length. Thus, to produce a displacement of about 3 mm in the gripper the actuators need to bend to form an arch with a distance between them of 3.85 mm in addition to the distance needed between the two holders of the actuators (4 mm), which would have a total distance of 7.85 mm. as there are two actuators, each actuator needs a displacement of 3.925 mm.

As depicted in the simulation results, a greater degree of deformation is required in the holders compared to the arms. This heightened deformation requirement enhances the gripper's precision by affording greater flexibility for deformation within the holder.

Conversely, this augmentation results in increased force generation at the fingers because a reduced amplification ratio leads to a larger output force, specifically at the gripper fingers. This decreased necessary force is particularly advantageous in the context of 4D printing with PLA, as the force required for deformation in microactuators is relatively small and may not achieve the desired alteration in shape.

The simulation of the active parts was carried out using a static structural system available on the software that allows for thermal expansion and deformation of materials. The SME was replicated by adjusting the thermal expansion of each layer used in the actuators. PLA in 4D printing usually shrinks as it is activated due to the stretching of the material by the FDM printing process. Thus, for both the passive and the active parts of the actuator, the CTE has to be negative of values (-0.0062 and -0.004, respectively).

For the printing, the design of beam structures with dimensions of 19 mm × 3 mm × 2 mm for length, width, and height, respectively, were 4D printed with a different printing parameter to control the bending degree and maximize it. The actuators that are slotted were printed in two sections, which are the bottom passive layer and the top active layers to create a strain difference between the layers. For the bottom layer, the printing resolution was set at 0.3 mm per layer. The temperature values of the liquefier, print bed, and the environment were respectively set at 230, 25, and 25 °C and a printing speed of 10 mm/s. As for the top layer (active layers), the printing resolution was set at 0.05 mm per layer.

The temperature of the liquefier, print bed, and chamber were respectively set at 190, 25, and 25 °C and a printing speed of 70 mm/s. The top layer is made to have a higher strain stored in the lines of printing, thus forcing the actuator to bend toward the top. As for the body of the gripper, the same set of parameters were used as the ones for the bottom layers of the actuators. This is to ensure that no shape memory effect is added to the gripper or the passive parts of the design. This was tested by submerging the gripper in a bath of hot water to test if there is pre-strain stored in it. No shape change was observed in the passive parts, meaning that gripping happens because of the active beams in the holder of the grippers.

4.6.2   Results and Discussion

After the microgripper was manufactured, the initial phase entailed evaluating the microactuators independently to measure the extent of bending and the distance of deformation they would induce in the gripper. This is demonstrated in **Figure 4.12**, where the

beams before and after deformation are shown. The distance of deformation, extending from the actuator ends to the center of the arch, measures 3.925 mm. This aligns with the required simulation distance for the beams. At this specified distance, the deformation proves sufficient to displace the gripper holders adequately, resulting in the closure of the gripper's fingers.

Notably, the passive section (the bottom layer during printing) of the actuators is marginally wider than the active portion (the top layer during printing). This occurs when the layer height is notably elevated, allowing the molten PLA to spread towards the sides due to reduced pressure between the preceding layer and the nozzle. The elevated temperature and slower printing speed mean that the PLA remains in a rubbery state for a longer duration compared to typical printing, enabling it to adhere to the sides more effectively. While this phenomenon can be mitigated during regular printing, it must be intentionally incorporated due to the actuators' dimensions to reinforce the SME.
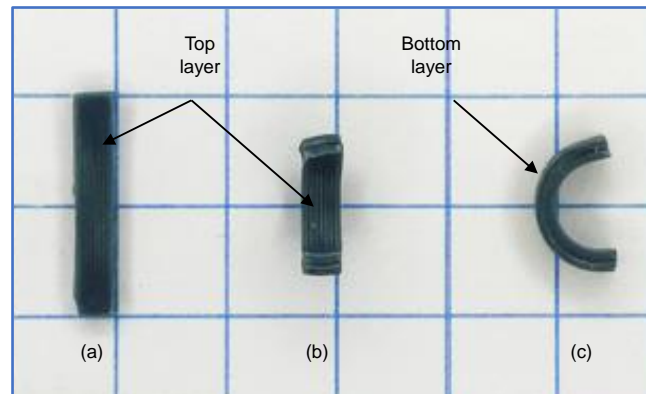

Figure 4.12 The microactuators used in the microgripper. (a) The top view of the actuator before deformation, (b) The top view of the actuator after deformation. (c) The side view of the actuator after deformation.

The actuators are slotted in the gripper, as demonstrated in **Figure 4.13**. In Figure, the gripper is presented before and after a 30-second immersion in a hot bath to ensure complete deformation. The gripper's closure progresses steadily up to the point demonstrated in the figure. To prevent any potential structural bending induced by the deformation of the actuators, the gripper is securely anchored at its right and left edges. This setup channels the entire deformation towards the holders and the microgripper's fingers, facilitating precise control over the gripping degree. This level of precision is particularly advantageous in delicate operations where smooth and controlled gripping is essential. These microgrippers find valuable applications in fields such as biomedicine, where controlled, non-electric actuation is highly beneficial
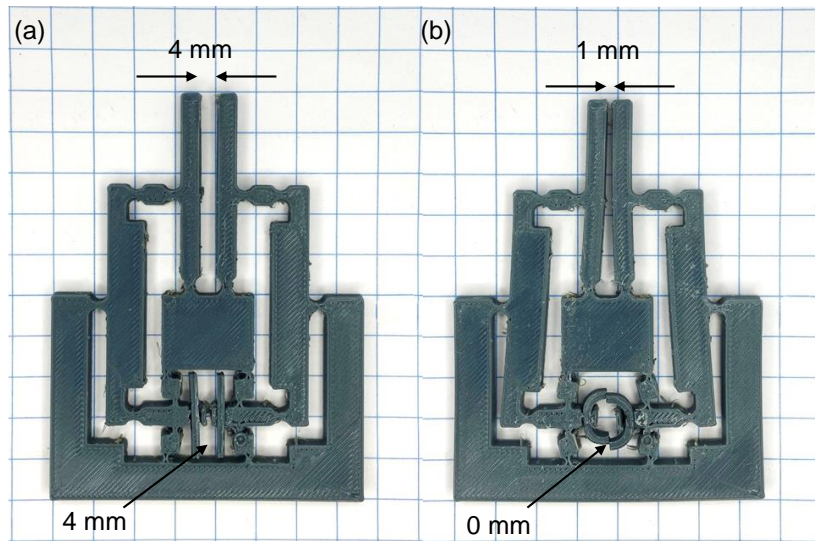
Figure 4.13 The microgripper with the actuators slotted in the holders. (a) The microgripper at room temperature (b) The microgripper after being activated at a temperature above T_g,

Measurements were conducted both before and after the microgripper underwent deformation. Prior to deformation, the distance between the gripper arms measured 4 mm, which was subsequently reduced to 1 mm after deformation. Likewise, the distance between the holders measured 7.5 mm before deformation, which increased to 11.35 mm after deformation. This variance in distances is utilized to regulate gripper closure by employing actuators with varying bending degrees for different gripping distances. The control of the gripper is configured based on the necessary gripping distance, achieved by adjusting the gripper distance to the required length and calculating the requisite holder displacements and, consequently, actuator deformations.

4.7   Development of 4D-Printed Micropositioning Stage

4.7.1   Micropositioning stages designs

In this study, we present two micropositioning stages with distinct designs. Each design incorporates a microstage measuring 10 mm × 10 mm × 2 mm. The position of this microstage is controlled by the previously discussed actuators, which have dimensions of 30 mm × 1.6 mm × 1 mm. **Figure 4.14** showcases the two designs put forth in this study, with the grey and red segments representing the passive and active components (microactuators), respectively. Both designs were entirely manufactured using PLA material, with the color differentiation serving to illustrate the working principle. The passive components were printed at a speed of 10 mm/s, while the actuators were printed at varying speeds of either 40,

50, 60, 70, or 80 mm/s. Consequently, each design was produced using five distinct printing configurations to investigate the impact of microactuator printing speed on the performance of the designs. Based on the aforementioned observations, it is anticipated that designs featuring microactuators printed at higher speeds will exhibit expanded actuation ranges.
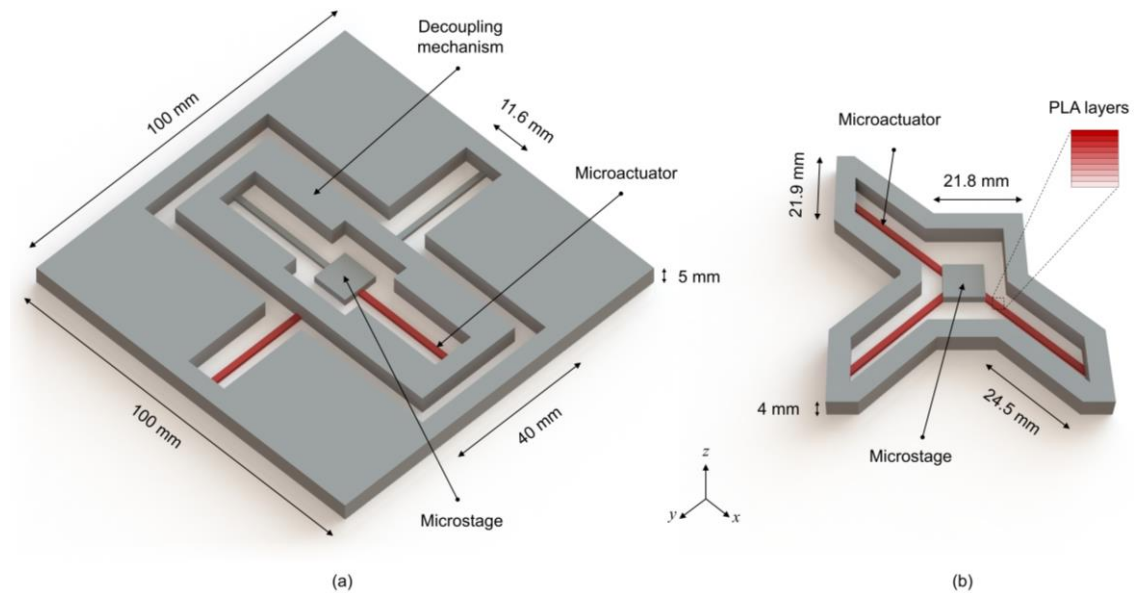

Figure 4.14. 3D views of (a) Stage 1, and (b) Stage 2. The red parts represent the microactuators, while the grey parts represent the passive elements.

Stage 1 employs two identical microactuators to control the microstage's position along both the x and y directions. The x-axis microactuator's two ends are securely fixed between the decoupling mechanism's frame and the microstage. Additionally, a passive supporting beam is affixed in the same manner on the opposing side of the x-axis microactuator. This configuration effectively prevents the microactuator from bending towards the z-axis, a movement that would otherwise cause it to contract and shift the microstage along the x-axis. Simultaneously, the beam on the opposite side ensures that the microstage remains stable and does not rotate around the y-axis.

The same principle applies to the y-axis microactuator, firmly attached between the external frame of the device and the frame of the decoupling mechanism. The primary purpose of the decoupling mechanism is to eliminate any rotation of the microstage around the z-axis, a phenomenon observed in an initial prototype lacking this mechanism. Such unintended rotation may arise from imperfections in the printing process. While this mechanism does increase the overall size of the device, it also underscores the microactuators' ability to manipulate objects with greater mass. To overcome the

aforementioned issues, Design 2 utilizes an asymmetrical star-like shape that has three identical microactuators that are connected to the microstage at angles of 135°, 225°, and 315°, causing the microactuators to form two isosceles right triangles.

4.7.2   Finite element analysis

The simulation process started by analyzing the thermomechanical performance of the microactuators using different printing speeds. Then, Stage 1 and Stage 2 were analyzed and optimized based on the same process followed in the previous step. **Figure 4.15** shows selected FEA results of the microactuator, Stage 1, and Stage 2 when using a printing speed of 80 mm/s for the actuators, while the passive parts were printed at a speed of 10 mm/s. Figure D.3(a) shows a side view of the deformation behavior of the microactuator when its two ends are free to deform. It can be seen that the maximum defamation towards that z-axis was around 6.96 mm.
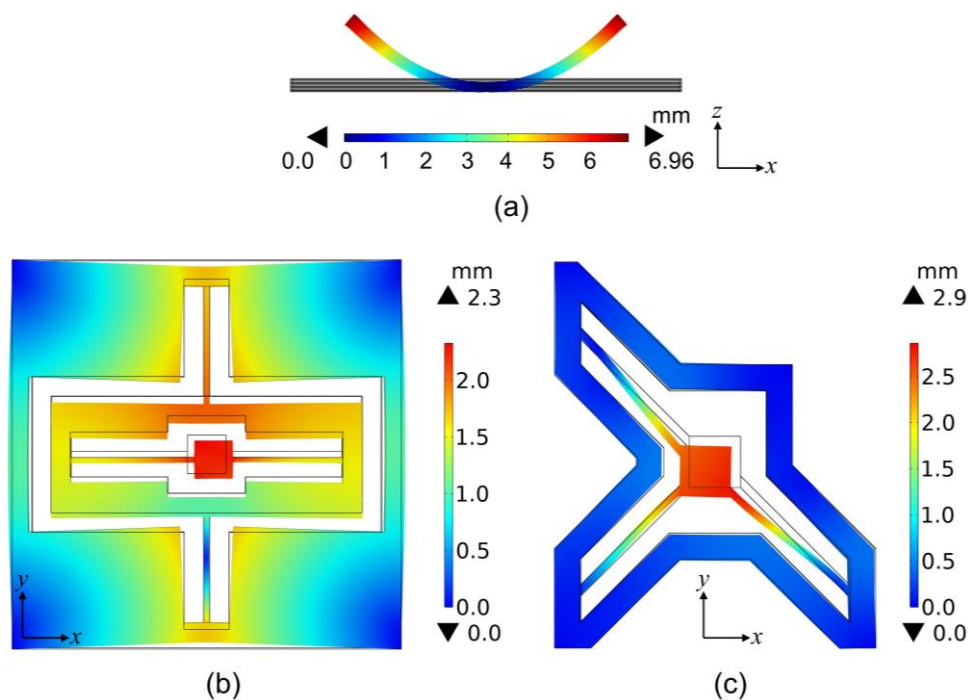

Figure 4.15. FEA results of (a) side view of the microactuator, (b) top view of Stage 1, and (c) top view of Stage 2.

Figure 4.15 (b) and (c) show the top views of Stage 1 and Stage 2, respectively. It can be seen that the two designs were able to move the microstage along the x- and y-axes. The microstage in Stage 1 moves towards the positive sides of the x- and y-axes while it moves

towards the negative sides in Stage 2. To simplify the comparisons between the two designs, we will consider the absolute values of the displacements. The maximum displacement values in the *x*- and *y*-directions were respectively 1.99 mm and 1.41 mm for Stage 1, and 1.89 mm and 2.37 mm for Stage 2. It should be noted that the maximum values shown in **Figure 4.15** (b) and (c), which are 2.3 and 2.9 mm, represent the total magnitude of the *x*- and *y*-components of the displacement.

In Stage 1, the displacement along the x-direction surpasses that in the y-direction because actuating the latter necessitates the pulling of the decoupling mechanism, x-axis microactuator, supporting beams, and microstage. Furthermore, it is noteworthy that the internal frame exhibits undesired deformation towards the center, measuring 1.37 mm.

On the other hand, in Stage 2, as previously discussed, the asymmetrical shape of the design can influence the displacement along both the x- and y-axes. In this scenario, the outer frame experiences slight deformation along both axes, with a maximum deformation of 0.27 mm. However, this deformation is not uniform in magnitude or direction. Certain regions of the frame deform inward, while others deform outward. This non-uniform deformation leads to varying stress levels on the ends of the microactuators, causing them to actuate differently despite being identical. This discrepancy accounts for the differences in actuation values along the x- and y-axes in Stage 2.

4.7.3   Results and discussion

The study's results support the feasibility of integrating our proposed approach into the micropositioning stage design. Passive components were printed at 10 mm/s, while the actuators used higher speeds. Managing internal strain and deformation in active components is crucial for effective micropositioning, as demonstrated visually in the study's figures. In this analysis, we will continue presenting the results and comparisons based on the printing speeds presented in **Table 4.5**.

Table 4.5. Comparisons between the experimental and simulated recovered-shape parameters at different printing speeds.

Shape parameters		Printing speed (mm/s)				
		40	**50**	**60**	**70**	**80**
A_1 (mm)	Exp.	28.39	28.44	27.36	27.20	26.86
	Sim.	28.40	28.36	27.46	27.32	26.82
A_2 (mm)	Exp.	25.88	25.16	23.47	22.37	21.30
	Sim.	25.84	25.03	23.54	22.39	21.17
A_3 (mm)	Exp.	5.01	5.67	6.09	6.57	6.92
	Sim.	5.04	5.70	6.03	6.64	6.96

Stages 1 and 2 were fabricated using the aforementioned printing speeds for the microactuators. **Figure 4.16** presents the fabrication results of Stage 1 when using different printing speeds for the microactuators. **Figure 4.16** (a) shows the initially printed shape of Stage 1, which is the same initial shape when using any printing speed for the microactuators. **Figure 4.16** (b)-(f) show the maximum actuation results after activating Stage 1 for 60 seconds in water with a temperature of 85 °C, where the printing speeds of the microactuators were 40, 50, 60, 70, and 80 mm/s, respectively.

In all cases, the microstages were consistently actuated along the positive segments of the x- and y-axes. The shape recovery of each microactuator impels the microstage to move in the direction corresponding to that microactuator. However, during the shape recovery of the microactuator, the supporting beam that holds both the microactuator and microstage undergoes softening, which affects the microstage's performance. To counteract this, the supporting beam is printed with a 30% infill density and a standard raster angle of 45° and -45° to minimize deformation. This configuration ensures that the microstage exhibits smooth linear movement during the activation process.
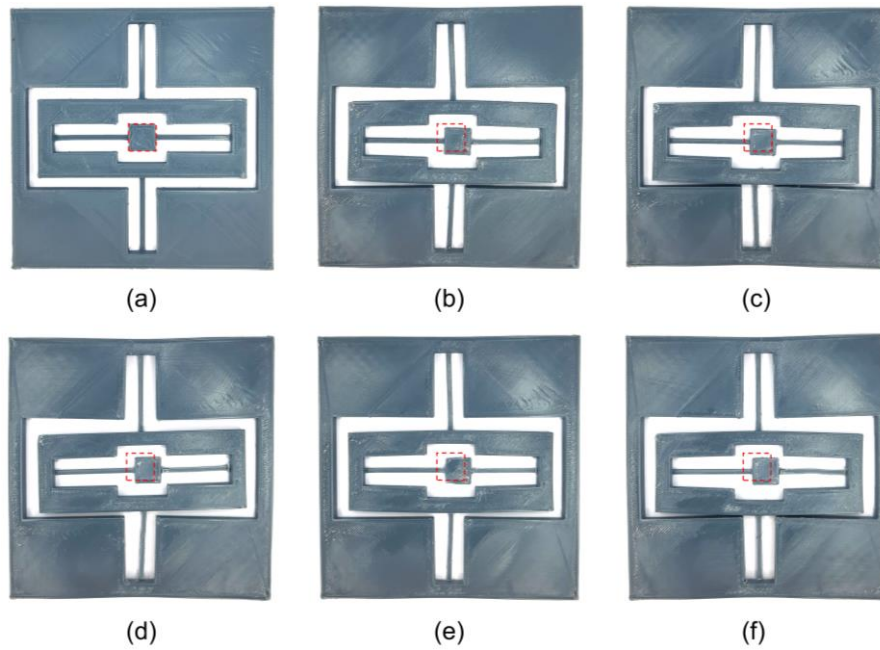
Figure 4.16. Printed samples of Stage 1 showing (a) the initial structure before activation, and after activation when printing the microactuators at a speed of (b) 40, (c) 50, (d) 60, (e) 70, and (f) 80 mm/s.

It is noteworthy that the x- and y-actuation values exhibit a gradual increase with higher printing speeds for the microactuators. This effect is also evident when observing the position of the decoupling mechanism, which comes into close proximity to the design's frame, with a distance of approximately 0.1 mm when a printing speed of 80 mm/s is employed. Furthermore, we observe unwanted deformations occurring at various parts of the design, particularly in the lower regions. These deformations are not uniform in specific locations, and they are likely attributed to imperfections in the printing process. These issues arise due to the microactuators' shrinking, which pulls the structure toward the center.

To address these challenges, we propose two potential solutions. First, localized heating of the microactuators using a hot air gun can be applied, ensuring that minimal heat transfer affects the rest of the structure. Second, an alternative approach often used in micropositioning stages involves the use of screws to secure the frame of the design. However, this approach may not be suitable for applications requiring swift batch-processing or in environments lacking adequate support for the microstage design. Therefore, this work introduces the idea of optimizing the design to minimize undesired deformations without the need for additional components, offering a practical solution to this challenge.
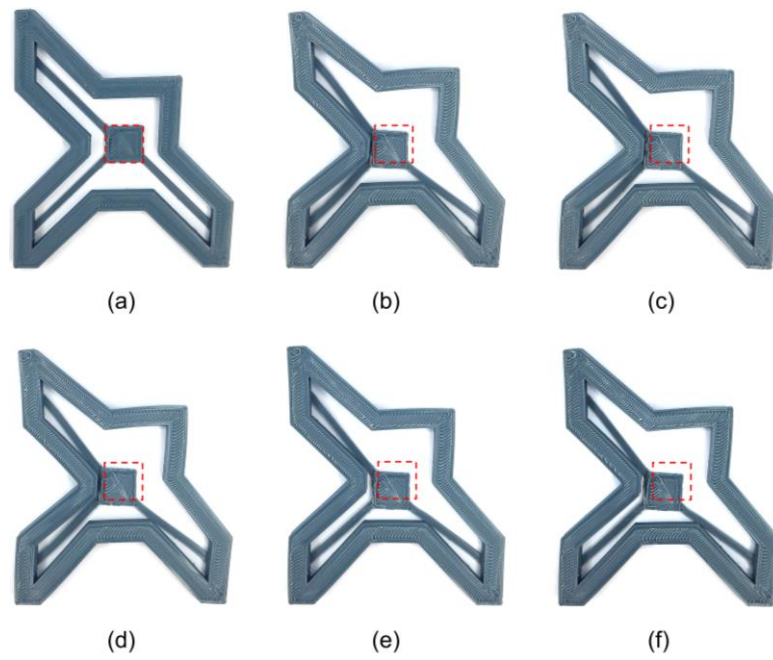
Figure 4.17. Printed samples of Stage 2 showing (a) the initial structure before activation, and after activation when printing the microactuators at a speed of (b) 40, (c) 50, (d) 60, (e) 70, and (f) 80 mm/s.

Stage 2 offers a solution for the aforementioned issues by greatly reducing the value of the unwanted structure deformation while using a smaller structure that achieves higher actuation values. **Figure 4.17** (a) shows the initially printed shape of Stage 2, which is the same initial shape when using any printing speed for the microactuators. **Figure 4.17** (b)-(f) show the maximum actuation results after activating Design 2 for 60 seconds in water with a temperature of 85 °C, where the printing speeds used to print the microactuators were respectively 40, 50, 60, 70, and 80 mm/s. It can be seen that the actuation occurs along the negative parts of the *x*- and *y*-axes. Stage 2 has an asymmetrical star-like shape that utilizes three identical microactuators connected to the microstage at angles of 135°, 225°, and 315°, causing the microactuators to form two isosceles right triangles. This design does not utilize supporting beams like the ones used in Stage 1. On the contrary, Stage 2 utilizes the special arrangement of the microactuators to pull the microstage along the *x*- and *y*-axes while preventing it from rotating around the *z*-axis.

In Stage 2, similar to what was observed in Stage 1, the x- and y-actuations increase with higher printing speeds for the microactuators. However, the deformation of the frame exhibits a contrasting behavior. While the x- and y-actuations occur towards the negative sides of the respective axes, the deformation of the frame takes place towards both the positive and negative sides. Moreover, it is notable that the undesirable deformation tends to

decrease at higher printing speeds. This trend becomes particularly pronounced when examining the frame's edge at the 180° mark. It is important to note that the complete elimination of deformation is challenging due to the inherent shrinking behavior of the material.

However, higher printing speeds accentuate the microactuators' shrinking, which exerts tension on the frame from three points located at 135°, 225°, and 315°. This inward-pulling effect causes other sections of the frame, especially at 180°, to deform outward. Consequently, the drawback of deformation can be mitigated by employing higher printing speeds for the microactuators. Nevertheless, it is essential to acknowledge that the design's performance may be constrained by the limitations imposed by the frame's shape. Notably, the microactuators come into contact with the frame at maximum actuation. Addressing this issue might involve modifying the frame's shape, although there exists a trade-off between altering the frame's configuration to increase actuation range and the potential for undesired frame deformation.

4.8   Summary

Controlling the SME of 4D-printed actuators by setting the printing parameters allows for accurate control of the SME to a degree higher than that of traditional printing. There are many printing parameters that affect the internal strain in 4D-printed actuators. This chapter investigated the effect of the printing speed, printing temperature, ratio of passive-to-active layers, layers height, and actuator height on the bending angle of 4D-printed PLA actuators.

The results showed that increasing the printing speed improved the bending of the actuators linearly while increasing the printing temperature has the opposite effect. The results also showed that using different passive-to-active layer ratios affects the bending too, with a maximum bending angle at a ratio of 50%. Moreover, increasing the height of the printed layer reduced the bending angle, as does the height of the actuator itself.

A prediction model of the bending in the actuators has been created based on linear and nonlinear regression of all the printing parameters with an R-square value of 0.98. A total of 534 actuators were designed and tested for developing the model, which was to predict the bending in the actuator and to develop the FEA model. The FEA model was created based on a two-part actuator model that replicates the SME in the 4D-printed actuator. This was done using CTE values for each part, which can be obtained from the predictive model of the printing parameters. These parameters were used to simulate the behaviour of the actuators with an R-square value of 0.98 of the bending angle based on the printing parameters used.

This CTE simulation method was then used to predict the behaviour of an eight-arm gripper and a four-arm gripper as proofs-of-concept of the accuracy of the proposed approach. Beyond the manipulation of the printing parameters to control the bending angle, other methods can be used to do so. In certain applications, there are limitations to the changes in the parameters, such as temperature and structure integrity, other structural manipulations can be used instead. Printing the actuators with certain patterns can influence the shape change, without changing the printing parameters.

Chapter 5: 4D-Printed Variable Stiffness Actuators

5.1 Introduction

This chapter presents pattern-driven actuation by variable stiffness. Motivated by the features of bioinspired 4D printed structures and the limitations that need to be addressed in this area, this chapter presents single-material bioinspired actuators that offer different actuation performances based on the printing patterns used. This chapter uses the induced strain that is achievable in the three-dimensional (3D) printing method of FDM and controls it using the printing patterns. The stiffness of materials can be manipulated in AM by printing the materials in patterns, giving different stiffness profiles to the structures. The main contributions of this chapter when compared to the reported literature are:

- This chapter investigates the effect of five bioinspired printing patterns on the actuation performance of 4D printed actuators, which are shown in **Figure 5.1** (a) – (e). These shapes are inspired by *Volvox carteri* (circles), *Haloquadratum walsbyi* (squares), honeycombs (hexagons), *Sapium sebiferum* (rhombuses), and *Oxalis triangularis* (triangles).

- This chapter presents a novel approach of using geometrical patterns to create controllable strain differences between the layers of prints while assessing the effects of geometrical shape patterns on the actuation of 4D-printed actuators.

- The proposed concept is used to develop a hand-like-shaped gripper that can grip and pick up delicate objects with uniform and non-uniform cross-sections. This is achieved by utilising the different actuation angles caused by the printing patterns, where the effects of full-structure patterns are not reported, to the best knowledge of the authors.

5.2 Design and Working Principle

Variable stiffness actuation (VSA) has emerged as a desired feature in many application-oriented systems. The concept of variability in stiffness centres around the ability of a structure to exhibit a change in compliance within certain spatial-temporal states. Variable stiffness has been a big part of multiple leading technological advancements because of the freedom it allows in the formation of structures, providing the ability to make mechanical movements in a rigid body.

The patterns developed in this chapter have different stiffness in different directions. A direction stiffness profile can aid in the understanding of the SME caused by each pattern since the SME acts in the direction of printing, which is expanded and discussed in the next section. Different stiffness in certain directions will cause the SME to shape the structure in a certain way. This being the case, the mixing of patterns of different sizes and patterns will produce a different SME in the structure because of the difference in the stiffness of the two patterns. This variable stiffness can be useful in many SME programs through the use of patterns.

5.2.1 Patterns Functionality

This section presents the main patterns used in this chapter along with their profiles. The five bioinspired shapes used can be found in *Volvox carteri* (circles), *Haloquadratum walsbyi* (squares), honeycombs (hexagons), *Sapium sebiferum* (rhombuses), and O*xalis triangularis* (triangles), as shown in **Figure 5.1** (a – e). All the patterns are made by repeating a single shape for each pattern. In 3D printing, geometrical shapes are used in the infill, sometimes referred to as internal structures, and each changes the characteristics of the print in a certain way [219], [220], in which basic geometrical shapes are used to create the infill patterns. Although there are many mechanical preferences in choosing these shapes, their effect on the SME is not explored.

Each pattern has a different profile, referred to as a stiffness profile in this work. This profile plays a big role in the shape change experienced by the printed patterns when activated. The profiles of each pattern used are demonstrated in **Figure 5.1** (f – j). The deformation of the actuators can be realized by understanding the shape change in each geometrical formation used in the patterns. The printing of these patterns is done one shape at a time, which makes the SME work along the lines of each shape. The SME of each shape acts in a shrinking manner along the printing direction.
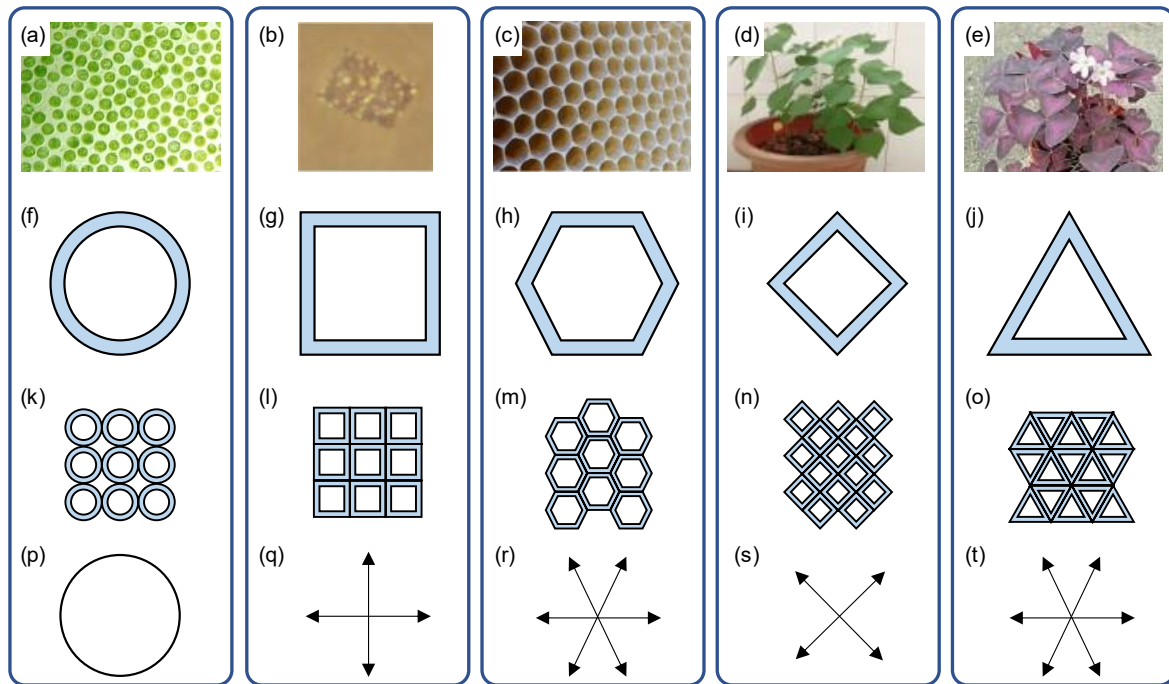
Figure 5.1. Bioinspired designs' concepts. (a) *Volvox carteri* [221]. (b) *Haloquadratum walsbyi* [222]. (c) Honeycomb [223]. (d) *Sapium sebiferum* [224]. (e) *Oxalis triangularis* [225]. (f – j) Bioinspired shapes used to create the patterns of the actuators. (k – o) Bioinspired patterns created with each shape. (p – t) Overall pre-stress profiles of the printed patterns.

The main patterns have simple geometric shapes, where their SME can be analysed by their perimeters. **Figure 5.1** (k) – (o) show the patterns made by using each shape. To understand the shape change, a reverse directional motion of the actuation is represented in **Figure 5.1** (p) – (t). This directional motion represents the pre-stress directions that are achieved during the printing process of the complete pattern. This can also be explained as the force that would have been applied to the patterns if it was done in the traditional programming way in order to achieve the induced-strain shape change. They are presented in the opposite direction of the shape change, acting along each side of the geometric shape.

In this study, the printing process induces the strain, but the pre-stress profiles help explaining the directions of the overall pre-stress. The force is parallel to the sides of the shapes of the patterns since SME acts along with the perimeters in a shrinking manner. This shape profile is introduced in this chapter as an easier way to understand the deformations of the shapes since it has a centre and direction. Although the profiles in **Figure 5.1** (r) and (t) are the same, when placed in their patterns, they act differently since the shapes are in different relative positions to each other, meaning that each pattern will have a different force

profile. Each circle shape in **Figure 5.1** (k) is pre-stressed equally in all directions across the print bed. Thus, there is no linear direction of pre-stress in **Figure 5.1** (p).

With a more complex approach, further differences in the stiffness or force profiles in the patterns can be made. This can be done by having two different layers of the patterns, a bottom layer and a top layer. By using variations of the pattern for the bottom and top sections, different profiles can be created. In this study, there are three configurations of pattern profiles:

- The first configuration is simple patterns with a single shape for each pattern.
- The second configuration is made by dividing the actuators into two layers, where both layers use the same pattern, but the size and number of shapes used in each layer are different, creating a stronger profile difference between the two.
- The third configuration is made of actuators with two layers of mixed patterns, where each layer uses a different pattern.

5.2.2 Single Shape Patterns

The first set of actuators is the simplest one, since the actuators are made of basic geometrical shapes next to each other, as demonstrated in **Figure 5.1**. These actuators are the baseline ones, and the SME in them is small, since their stiffness profiles are the same. Any shape change is mainly caused by the printing parameters. All actuators are printed with standard dimensions of 51.6 mm × 13.6 mm × 2 mm, representing length, width, and height, respectively. These dimensions make up the geometrical shapes that are enclosed by a perimeter. The sizing of the actuators without the perimeter was chosen at 12 mm, since it can hold 3 large shapes (4 mm each) or 4 small shapes (3 mm each), where a perimeter of 0.8 mm thickness is then added to the sides. The length was determined by repeating the shapes until they reached a standard length of 50 mm, while a 0.8 mm perimeter was added on each side. The height is set so that when dividing the actuators into two layers, each layer has a 1 mm height. All the actuators were printed with the same printing parameters, these are based on the previous section with the standards parameters presented in **Table 4.1**.

5.2.3 Variable Pattern Sizes

The use of patterns of the same shape and different sizes for each layer of the actuators creates a bigger difference between the two layers, causing variable stiffness, especially at the boundary between the two different layers. Since the standard pattern uses shapes that are at a width of 4 mm for a total of 12 mm, the smaller patterns are made of 3

mm shapes, using 4 shapes for the width, for a total of 12 mm as well. The difference between the shape size of the bottom and top sections of the actuator generates a higher strain difference due to the variable stiffness in the actuator. The smaller shapes are not only smaller in height, since the size change was made to keep the same formulation of the shape, creating a difference between the shapes in all directions. This difference changes the stiffness profile dramatically since the forces have different directions and centres, as demonstrated by the stiffness profile in **Figure 5.2**.
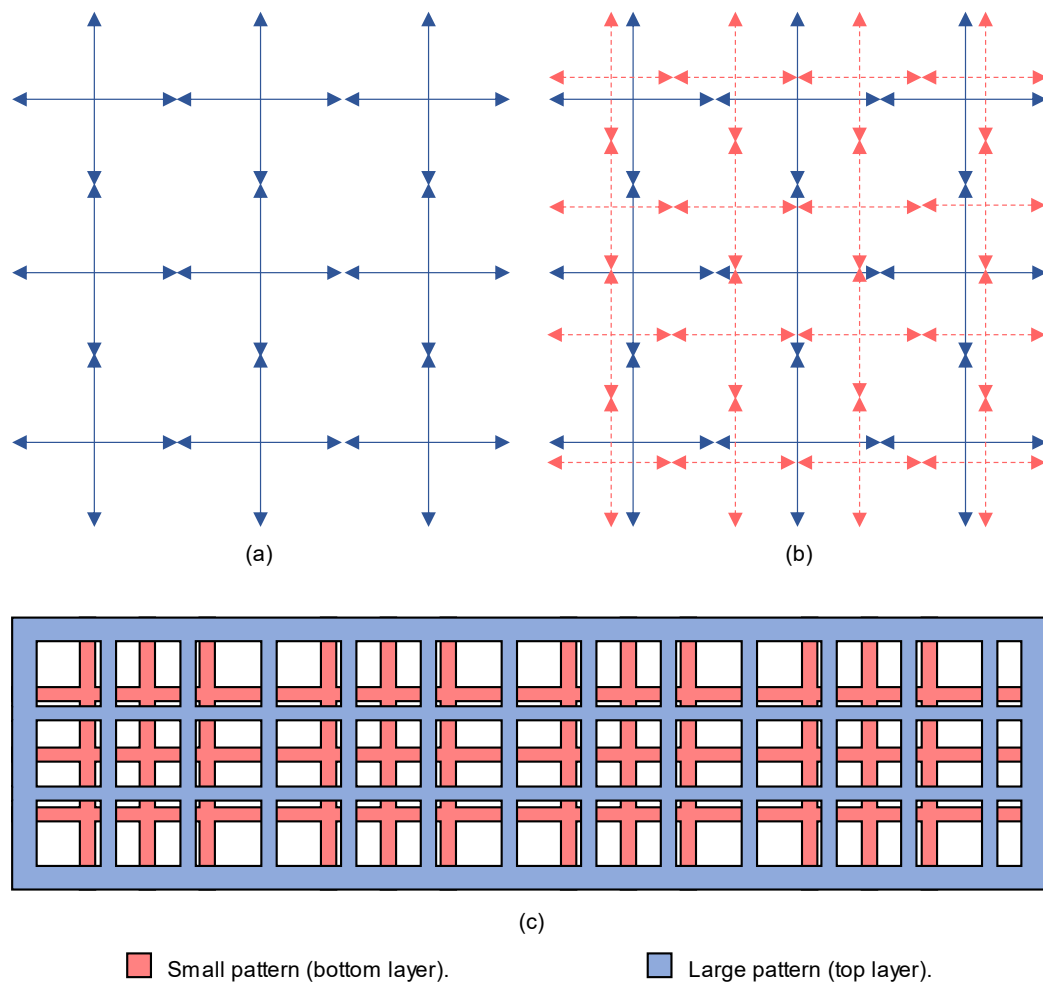

(a)   (b)

(c)

Small pattern (bottom layer).   Large pattern (top layer).

Figure 5.2. The difference in the stiffness in the variable shape and size patterns. (a) The pre-strain profile of a square-pattern actuator with a single shape size. (b) The pre-strain profile of a square-pattern actuator with a variable shape size. (c) Top view of a square-pattern actuator with two layers of variable square sizes.

The shape presented in **Figure 5.2** (a) is the stiffness profile that is created in the pattern made by squares of the 4 mm size, which was described earlier. On the other hand,

the shape presented in **Figure 5.2** (b) is the stiffness profile of an actuator that is made with small and large square patterns, placed one above the other. The blue colour arrows represent the profile of the large-size square pattern, while the pink arrows represent the profile of the smaller square pattern. Square patterns have been chosen since they are the easiest to understand and have only two force vectors.

As can be seen in the figure, the centres of the forces are not at the same spot, which is assumed to be where the shrinking is centred, thus creating a large strain difference. **Figure 5.2** (c) presents the top view of the model of the actuator, which is made of a bottom layer of small squares and a top layer of larger squares for a variable pattern size sample. This concept of the difference in the strain profile is the driving force for the actuation in this study. Ten actuators are characterized in this section, five are in the larger patterns on the top, and vice-versa.

5.2.4 Mixed Patterns

The final set of actuators is printed with all the variations that are possible by mixing two different patterns into one actuator, each one with its own layer. This section explores the SME of patterns of completely different profiles. This does not necessarily show a stronger SME than the previous action, but it gives a lot of information about the combination of the different stiffness patterns to find certain patterns that act better in certain positions. Since there are five different patterns, by testing all possible combinations, a total of 20 different actuators are needed. The size of the shapes is the same as the shapes of the first set, since this section does not aim to maximize the SME, but to assist in understanding the difference in the stiffness profiles of each pattern.

5.2.5 Patterns-Driven Gripper

A four-armed gripper is developed for the testing of the patterns as a proof-of-concept design. The gripper uses two different patterns to allow controlling the final deformation of the gripper. The use of the patterns allows the gripper to hold non-uniform objects by having different deformations in the arms. This is a favoured behaviour when the force exerted by the gripper on the held object should be low enough to not damage a delicate object. This characteristic of controllable force in soft grippers gives them an advantage over uniform deformation grippers.

5.3 Fabrication Process and Experimental Setup

The 3D computer-aided design (CAD) models were created using SolidWorks software. The designs consisted of creating the basic shapes and replicating them to reach the desired pattern size. The arrangement of the shapes in the patterns is made to optimize the number of shapes to be used while keeping optimal contact between the shapes to aid the printing. SolidWorks is then used to generate STL files that the 3D printing software uses, with a total of 40 actuators.

The slicer software used in this chapter is the Simplify3D slicer, which is favourably used because of the degree of control it allows and the lack of automatic software control. In the slicer, all parameters of the print can be controlled, along with simple edits and orientations of the models used.

The actuators are printed using PLA filament as a construction material, via FDM printing. All actuators are set to the same printing settings to ensure that the only difference noticed in the SME is caused by the patterns. The printing temperature (nozzle temperature), bed temperature, and print environment temperature were set to 190 °C, 45 °C, and 25 °C, respectively. The layer thickness is set to 0.1 mm, amounting to a total of 20 layers per sample, and the printing speed was 60 mm/s. These parameters are based on the parameters used in the previous section for the standard settings.

The design, fabrication, and testing are shown graphically in **Figure 3.1** (a). The material used alongside PLA in section 5.6 is biodegradable polyethene terephthalate glycol (Bio-PT) (1.75 mm Bio-PT Filament 1.0 Kg, Fabbxible Technology, Penang, Malaysia).

The testing of the SME of the actuators is done by placing the actuator in a beaker of hot water. The water in the beaker is monitored and constantly heated to keep it at a temperature of about 80 °C, which is higher than the T_g of PLA (~65°C). This is done to ensure that a full release of the internal strain is accomplished.

The dimensions of the actuator are then measured using a digital calliper in order to find the bending angle. The testing of the effect of the internal strain is done by measuring the angle (θ) made by the actuators from the centre of the actuator to the endpoint, as shown in **Figure 3.1** (b), where A is the length of the line between the two endpoints of the actuator, and B is the length of the line from line A to the bottom of the actuator. The angle of bending is found using the following equation:

$$\theta = \text{acrtan}\left(\frac{2B}{A}\right) \tag{5.1}$$

The angle θ is used as the measurement for the strength of the internal strain difference, as clearly, the larger angle means there is a larger internal strain difference between the layers. The radius of curvature, which is the radius of the circle formed by the actuators is represented by R, while the length of the arc formed by the actuators after deformation is represented by L. The angle that is formed by the arc as a section of the circle is represented by φ (measured in radians). Thus, R, φ, and L can be found using Equations (5.2) – (5.4):

$$R = \frac{A^2 + 4B^2}{8B} \tag{5.2}$$

$$\varphi = 2\sin^{-1}\left(\frac{A}{2R}\right) \tag{5.3}$$

$$L = R \times \varphi \tag{5.4}$$

5.4   Results and Analysis

The material properties that are tested in this section are those that are needed for material stimuli, mainly the melting temperature (T_m) of the polymer and the T_g, where the state of the polymer changes from glassy to rubbery, are needed for the actuators. Although PLA is a widely used material with many characterizations being done, the results are slightly different from one filament to another. The differences in the properties of PLA in the test are due to the nature of the filament, since the polymers have slightly different additives and impurities that can change the material properties. Differential scanning calorimetry (DSC) and dynamic mechanical analysis (DMA) tests have been performed on the printed filament to characterize its material properties. The following sections discuss the characterization results of the material properties of PLA, as well as the deformation results of the single pattern, variable pattern size, and different pattern actuators.

5.4.1   Material Properties

The results from the DSC test can be observed in **Figure 4.1** (a). As is demonstrated in the figure, the DSC is carried out for heating and cooling cycles. From the heating graph,

there seem to be two distinct dips in the heat flow, which are marked by the two arrows at temperatures of 53.5 °C and 151.5 °C. The first dip represents the T_g of the material, which is slightly different from the literature T_g of PLA (about 60 °C to 65 °C) [226], [227]. The variance might be because of the impurities in the materials, but mainly, it is because T_g is usually recorded using a DMA machine, which measures a slightly different value. This is also shown in the DMA results in **Figure 4.1** (b), with the peak of the tan δ.

The second dip in the DSC test represents T_m of PLA, which is expected to be below 180 °C, based on the literature. As long as the nozzle temperature stays above this point, the print can be done. The heat flow graph seems to have no other significant characteristics along the rest of the temperature range. The same can be seen in the cooling of the materials, as there is no significant characteristic along the curve. There does not seem to be any irregularities in the change in the heat flow, indicating a regular decrease in the heat capacity.

Figure 4.1 (b) shows the effect of the material temperature over the storage modulus, which reflects the elasticity of the material, and the tan δ. The storage modulus beyond T_g is more than 100 times smaller than that above T_g. This reflects the elasticity of PLA at rubbery temperatures, making it not only extremely mendable, but with a high capacity for storing shape memory.

The point at which the storage modulus starts to stabilize is the same point at the peak of the tan δ graph, which represents T_g. The T_g in the DMA test was found to be around 67.3 °C, which is higher than that measured using the DSC, as expected. From the results, it can be confirmed that the material is to be activated at an environment temperature higher than 67.3 °C, a temperature of 85 °C will be used for the activation.

5.4.2   Single Patterns

This section presents the actuation results of the bioinspired single-pattern actuators using different dimensions of the aforementioned shapes. The actuation as observed in the results is due to the printing parameters acting on each layer differently, thus creating a small strain difference. The testing of this section is conducted to assess the effect that the shapes have on the actuation of the pattern as a whole. The circular-pattern actuators are presented in **Figure 5.3** (1) for the large circles and (2) for the small circles. The larger shapes have a larger bending than the smaller ones because of the length of the sides of the geometrical shape printed in one movement, since larger lengths of lines would have a larger difference in the length after actuation and larger shrinking. Both actuators are bent downwards implying

that if the SME is shrinking, the bottom layers shrink more than the top, causing movement in the downward direction.

The squared-pattern actuators are shown in **Figure 5.3** (3) and (4), with the large squares in (3) and small ones in (4). The bending direction of both actuators is downward, which is a good indicator of the replicability of the actuation in new prints, because the nature of the printing methods causes the bottom layers to shrink larger than the top layers in both circles and squares.
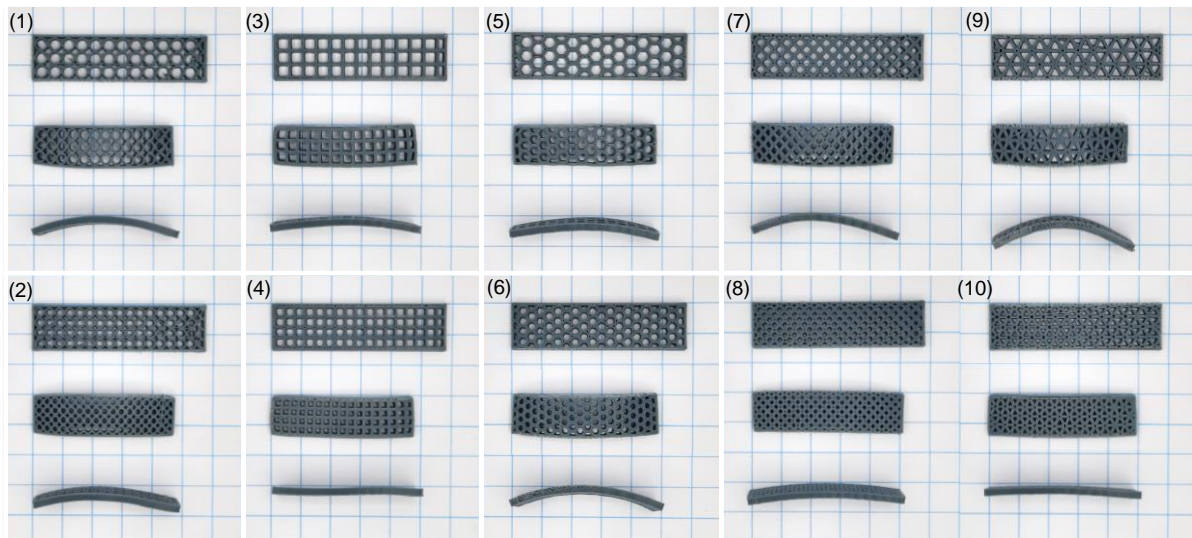

Figure 5.3. Single pattern actuators (1) Large circles. (2) Small circles. (3) Large squares. (4) Small squares. (5) Large hexagons. (6) Small hexagons. (7) Large rhombuses. (8) Small rhombuses. (9) Large triangles. (10) Small triangles.

The hexagon-pattern actuators are shown in **Figure 5.3** (5) and (6). The uneven shape change on a certain side can be caused by the print itself due to impurities and mixtures. Moreover, the difference in the deformed shape occurs due to the imperfections of the printing process, which requires each line of the actuator to be printed perfectly at the same speed and temperature regardless of the environmental effects [217].

In addition, in some cases, the air gets trapped in the prints, whether because of the feeder or bubbles between the layers. The fourth shape that is used is the rhombus, as shown in **Figure 5.3** (7) and (8). The bending behaviour is similar to the previous shapes, but shows different bending angles. The last shape used in this chapter is the triangle, as shown in **Figure 5.3** (9) and (10). Although the deformation follows the trend of larger shapes causing a larger SME, in these actuators, the bending angle difference between the larger and smaller triangles is large.

The actuation performance of the single pattern actuators tests is summarised in **Table 5.1**, where BD represents the bending direction. The table provides a classification of the actuators based on their top and bottom patterns, with measurements A and B representing the length and height of the actuators after deformation, respectively. These are referenced in **Figure 3.1** b. A consistent trend in the table is the downward bending and shrinking of all actuators after deformation, a consequence of the printing process and the uniform stiffness profiles across the actuators. Notably, there's a pattern where larger shapes correspond to larger bending angles, a trend observed in four out of the five patterns, except for the hexagon patterns.

Table 5.1. A summary of the actuation performance of the single pattern actuators.

Design	Bottom pattern	Top pattern	BD	Weight (g)	A (mm)	B (mm)	L (mm)	R (mm)	θ (°)
1	4 mm circles	4 mm circles	Down	0.68	41.58±0.33	5.95±0.30	43.81	39.37	15.96±0.66
2	3 mm circles	3 mm circles	Down	0.80	42.00±0.15	5.14±0.05	43.56	45.44	13.76±0.16
3	4 mm squares	4 mm squares	Down	0.79	43.07±0.04	4.27±0.04	44.18	56.48	11.21±0.11
4	3 mm squares	3 mm squares	Down	0.94	43.33±0.25	2.35±0.04	43.33	101.08	6.19±0.09
5	4 mm hexagons	4 mm hexagons	Down	0.79	42.36±0.23	5.12±0.08	44.29	46.38	13.59±0.23
6	3 mm hexagons	3 mm hexagons	Down	0.94	43.59±0.45	6.75±0.18	46.28	38.59	17.22±0.60
7	4 mm rhombuses	4 mm rhombuses	Down	0.98	42.57±0.61	7.23±0.23	45.64	35.01	18.77±0.74
8	3 mm rhombuses	3 mm rhombuses	Down	1.17	45.47±0.94	6.89±0.25	47.97	41.01	16.87±0.72
9	4 mm triangles	4 mm triangles	Down	1.02	41.43±0.22	8.67±0.29	46.09	29.11	22.71±0.65
10	3 mm triangles	3 mm triangles	Down	1.22	44.95±0.34	3.51±0.36	45.41	74.43	8.86±0.84

Calculation of the arc length (denoted as *L* in the table) reveals that the actuators shrink as they deform, with a shrinkage rate of approximately 12%. This behavior is primarily attributed to the specific printing settings, causing the actuators to bend in a downward direction, a phenomenon evident across all patterns. The table further highlights that the most significant shape change occurs in the larger triangles pattern, while the smallest bending angle is observed in the smaller square patterns. Interestingly, there is no discernible relationship between the weight of the actuators and their degree of deformation. This observation underscores that the deformation value is primarily associated with the printing patterns when all actuators are produced using the same settings.

5.4.3 Variable Pattern Sizes

This section presents the actuation results of the bioinspired actuators printed with two pattern sizes, one at the bottom and one at the top. The first set of actuators is printed with circular-shaped patterns in two different shape sizes, as presented in **Figure 5.4** (11) and (12). As is seen in the actuators, the flipping of the pattern sizes has flipped the actuation direction, which is a good indication of the effect of the action each pattern has.
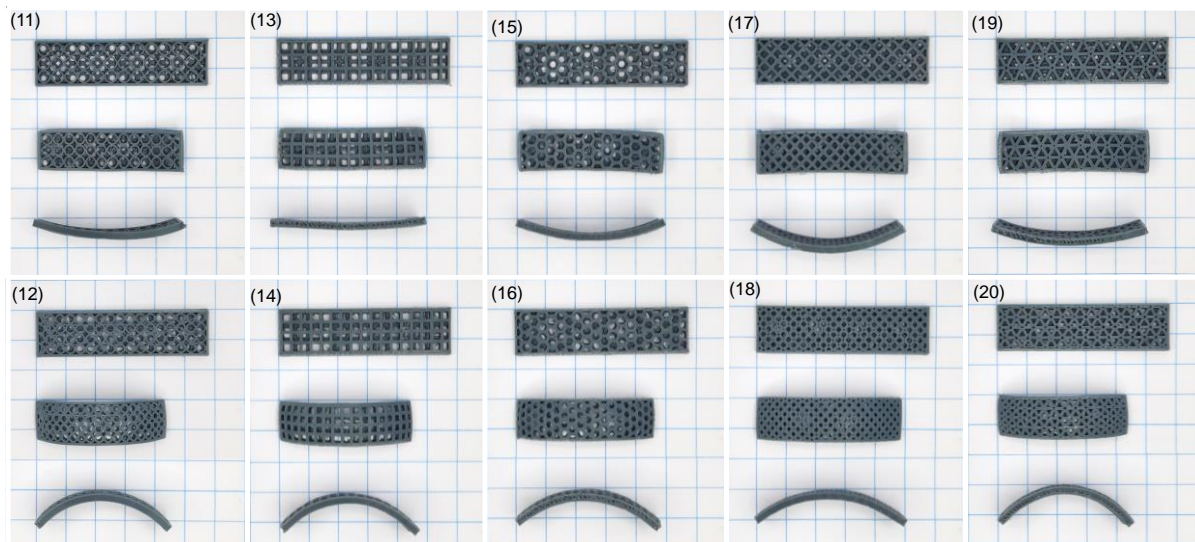

Figure 5.4. Variable pattern size actuators (11) Large-small circles. (12) Small-large circles. (13) Large-small squares. (14) Small-large squares. (15) Large-small hexagons. (16) Small-large hexagons. (17) Large-small rhombuses. (18) Small-large rhombuses. (19) Large-small triangles. (20) Small-large triangles.

The bending angle of the pattern with the smaller shapes at the bottom is 15.31° upwards, while the reverse has a bending angle of 28.70° downwards, which means the difference is great. When observing **Figure 5.4** The actuator with smaller patterns at the bottom exhibits a higher bending angle compared to those with a single pattern. This indicates a greater strain along the border where the two patterns meet. As was demonstrated, the printing of one size of shape before another does not produce the same results as flipping the actuator. This is because the printing method has the tendency to make the actuators bend downwards, as was explained in the previous section. This effect makes the bending in the upwards direction at a smaller angle than that in the downwards direction.

The second tested shapes are the squares, which are presented in **Figure 5.4** (13) and (14). The bending in the actuators follows the same trend as the previous shapes, with the actuator with the smaller shapes bending upwards and the other bending downwards at a much higher angle. The bending angle of the first actuator is 8.25° and the second is 28.54°. As compared to the actuators with different circle sizes, the square actuators have the same bending angle, which might be some evidence that the amount of strain between the two shape sizes is the same.

However, this does not hold when comparing the actuators with the smaller shapes on the bottom, since the bending angle is less in the square than it is in the circle. This behaviour shows a direct effect of the use of the shapes, and not just the strain difference or the induced stress. Although the SME in the circles and squares is similar and is shown to cause the same bending angle in one of the actuators, the effect of the stiffness profile seems to influence the SME as well.

The third set of actuators includes those using the hexagon shapes, presented in **Figure 5.4** (15) and (16). As compared to the hexagon actuators from the previous section, this print has a much higher bending angle. The actuators demonstrated in **Figure 5.4** (17) and (18) are in rhombuses shape patterns. As with the last three actuator patterns, these follow the same bending trend. The bending angles of the two actuators are similar with values of 20.41° and 22.88°. Since switching the position of the smaller and larger shapes has a similar effect to simply flipping the actuators, it has been demonstrated that the strain or stiffness difference between the two sizes of the shapes is the major contributor to the bending in these patterns.

The last set of variable pattern size actuators in this chapter is the triangle. The triangle shape pattern actuators are shown in **Figure 5.4** (19) and (20). The bending angles of the actuators are 15.58° and 30.96°, for the smaller triangles at the bottom and the larger

triangles at the bottom, respectively. The triangles, provide the best combination of directional force, combined with the large strain difference between the smaller and larger triangles. **Table 5.2** presents a summary of all the variable pattern size actuators in this work, allowing for a general overview of the effect of the shape sizes.

Table 5.2. A summary of the actuation results of the variable pattern size actuators.

Design	Bottom pattern	Top pattern	BD	Weight (g)	A (mm)	B (mm)	L (mm)	R (mm)	θ (°)
11	3 mm circles	4 mm circles	Up	0.74	42.61±0.91	6.17±0.17	44.94	39.94	16.16±0.71
12	4 mm circles	3 mm circles	Down	0.74	38.94±0.40	11.37±0.53	47.21	22.39	30.27±1.16
13	3 mm squares	4 mm squares	Up	0.87	44.78±0.79	3.61±0.28	45.54	71.54	9.17±0.65
14	4 mm squares	3 mm squares	Down	0.87	40.51±0.10	10.51±0.94	47.28	24.94	27.39±2.16
15	3 mm hexagons	4 mm hexagons	Up	0.87	43.04±0.71	7.09±0.55	46.04	36.48	18.24±1.59
16	4 mm hexagons	3 mm hexagons	Down	0.87	42.23±0.92	10.20±0.10	48.50	26.97	25.79±0.52
17	3 mm rhombuses	4 mm rhombuses	Up	1.08	45.46±0.96	8.26±0.30	49.35	35.42	19.98±0.59
18	4 mm rhombuses	3 mm rhombuses	Down	1.08	44.37±0.53	9.85±0.45	49.97	29.94	23.93±0.77
19	3 mm triangles	4 mm triangles	Up	1.12	44.49±1.21	6.53±0.82	46.88	42.01	16.40±2.39
20	4 mm triangles	3 mm triangles	Down	1.12	41.30±3.29	12.30±0.44	50.40	23.53	30.86±1.27

From the table, it can be noted that when the smaller patterns are printed at the bottom and the larger patterns are printed on top of them, the bending is in the upwards direction. The exact opposite is observed, which indicates the effect of the variable stiffness profile on the bending direction and force, since the strain difference is always strong enough to change the direction of the bend. It was also observed that there is no relationship between the weight of the actuators and their deformation, similar to Designs 1 – 10.

5.4.4 Mixed Patterns

This section presents the actuation results of the mixed bioinspired pattern actuators. The experiments were carried out to investigate the strain difference generated between each of the patterns. Only the large patterns are used so that the effect of the smaller patterns does not influence the bending, as the aim of this section is not to maximize the bending, but to explore the effect of the patterns on the SME. A total of 20 actuators with all the possible variations that can be made by combining two different patterns and their reversed order were characterized. The variable stiffness profiles created by the different combinations are much different from those in the previous sections, as they are of different shapes.

Designs 21 – 24 consist of all the combinations allowed with the circles at the bottom, as shown in **Figure 5.5** (21) – (24) and are identified by the name of the patterns as bottom-top. The patterns used are circles-squares, circles-hexagons, circles-rhombus, and circles-triangles, respectively, where all actuators are bent downwards. Naturally, the direction of bending is downwards, unless the strain of the boundary is large enough in the upwards direction to reverse it. A similar approach was used to fabricate Designs 25 – 28, Designs 29 – 32, Designs 33 – 36, and Designs 37 – 40, where the bottom layers of these groups of designs use squares-patterns, hexagons-patterns, rhombuses-patterns, and triangles-patterns, respectively. Meanwhile, the top layers of these groups of designs use the other patterns that are not used in their bottom layers, as shown in **Figure 5.5** (25) – (40). From the figures, it can be seen that most of the actuators bend downwards, except for five designs. For of these designs are Designs 33 – 36, which use rhombuses-patterns in their bottom layers. This can be explained as the result of the effect of the force profiles presented in **Figure 5.1**.
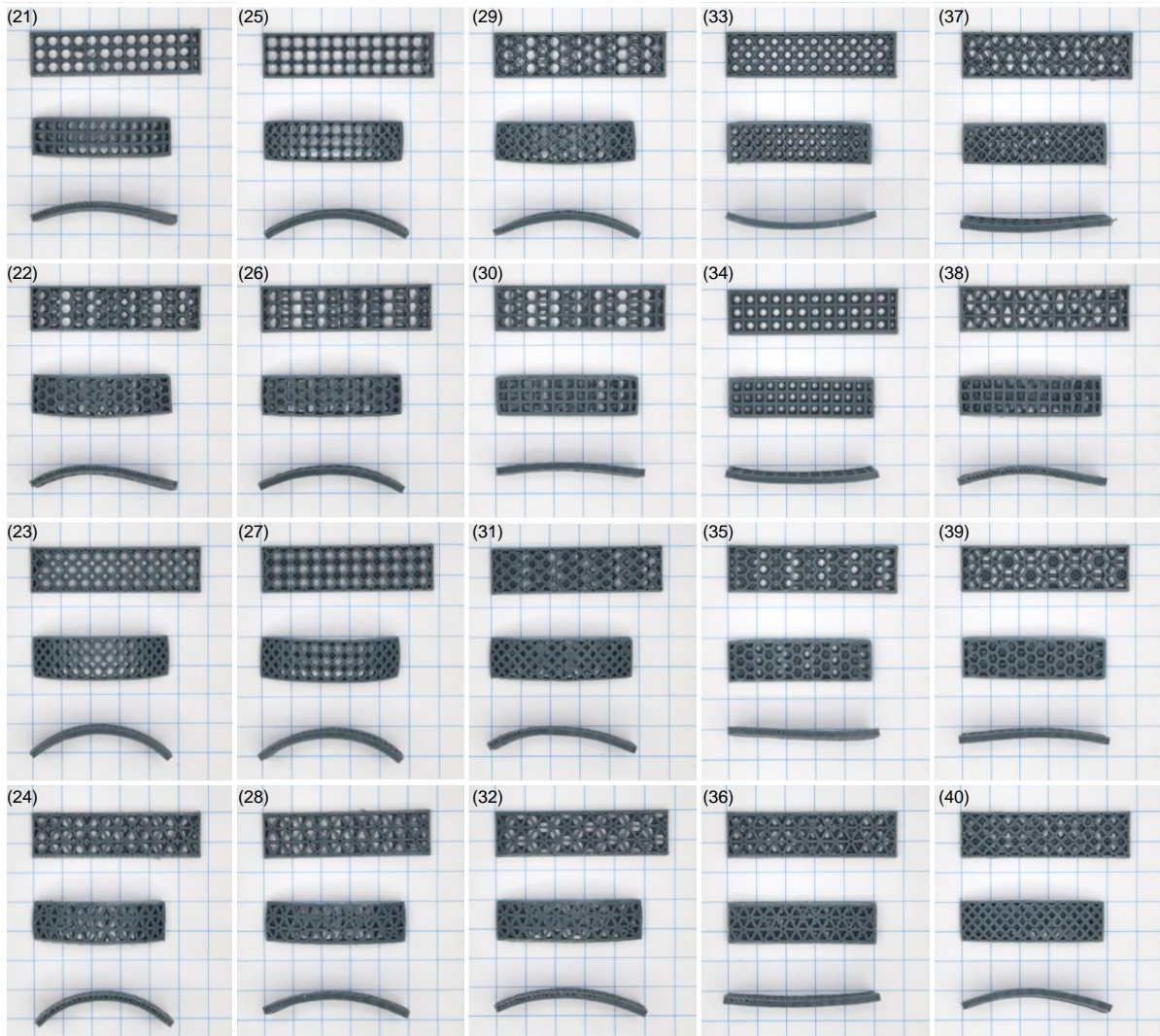
Figure 5.5. Mixed pattern actuators (21) Circles-squares. (22) Circles-hexagons. (23) Circles-rhombuses. (24) Circles-triangles. (25) Squares-circles. (26) Squares-hexagons. (27) Squares-rhombuses. (28) Squares-triangles. (29) Hexagons-circles. (30) Hexagons-squares. (31) Hexagons-rhombuses. (32) Hexagons-triangles. (33) Rhombuses-circles. (34) Rhombuses-squares. (35) Rhombuses-hexagons. (36) Rhombuses-triangles. (37) Triangles-circles. (38) Triangles-squares. (39) Triangles-hexagons. (40) Triangles-rhombuses.

Since the rhombuses patterns do not have force profiles that are parallel to the lengths of the actuators, then the induced strain values are not maximum along the lengths of the actuators. Thus, these actuators will be more affected by the patterns of their top layers, making them bend upwards. The last actuator that bends upwards is the one that uses the triangles-circles structure (Design 37). The reason behind this behaviour might be caused by the way the patterns of the top and bottom layers align on each other, affecting the overall

force profile along the actuator. The effect of the force profiles can also be seen when observing the deformation angles of the designs. A summary of the tested actuators in the final section of this chapter is presented in **Table 5.3**. The bending angels of the mixed pattern actuators are relatively smaller than those of the different shape-sizes actuators and appear to have a weaker strain at the boundary, as indicated by the direction of bending, which is mostly downwards. The shrinkage in this case is about the same, at about 10%, with little variance. It can be seen that there is no relationship between the weight of the actuators and their deformation, similar to Designs 1 – 20.

Table 5.3. A summary of the actuation results of the mixed patterns actuators.

Design	Bottom pattern	Top pattern	BD	Weight (g)	A (mm)	B (mm)	L (mm)	R (mm)	θ (°)
21	4 mm circles	4 mm squares	Down	0.74	42.76±0.57	6.47±0.19	44.75	38.56	16.85±0.42
22	4 mm circles	4 mm hexagons	Down	0.74	42.81±0.09	6.53±0.08	45.39	38.37	16.96±0.23
23	4 mm circles	4 mm rhombuses	Down	0.83	41.35±0.09	9.49±0.78	47.22	27.42	24.63±1.76
24	4 mm circles	4 mm triangles	Down	0.85	41.35±0.43	10.17±0.54	46.84	26.16	26.17±1.11
25	4 mm squares	4 mm circles	Down	0.79	42.60±0.26	7.23±0.46	46.50	35.10	18.74±1.03
26	4 mm squares	4 mm hexagons	Down	0.89	43.62±1.21	9.94±0.49	46.19	28.96	24.49±1.01
27	4 mm squares	4 mm rhombuses	Down	0.91	43.70±0.54	7.43±0.15	47.53	35.86	18.77±0.16
28	4 mm squares	4 mm triangles	Down	0.89	43.81±0.98	7.89±0.60	46.62	34.44	19.78±0.98
29	4 mm hexagons	4 mm circles	Down	0.91	42.58±0.93	6.70±0.28	46.07	37.24	17.46±0.66
30	4 mm hexagons	4 mm squares	Down	1.00	45.86±0.56	3.55±0.27	44.26	76.44	8.81±0.75
31	4 mm hexagons	4 mm rhombuses	Down	0.74	42.26±0.55	9.58±0.86	46.23	28.27	24.36±1.86
32	4 mm hexagons	4 mm triangles	Down	0.74	43.22±0.95	8.19±0.25	46.60	32.59	20.76±0.20

Design	Bottom pattern	Top pattern	BD	Weight (g)	A (mm)	B (mm)	L (mm)	R (mm)	θ (°)
33	4 mm rhombuses	4 mm circles	Up	0.83	44.69±0.65	5.68±0.33	45.56	46.93	14.25±0.73
34	4 mm rhombuses	4 mm squares	Up	0.85	44.01±0.61	3.44±0.27	45.63	72.41	8.89±0.66
35	4 mm rhombuses	4 mm hexagons	Up	0.79	43.12±1.51	4.08±0.41	44.97	59.32	10.69±0.73
36	4 mm rhombuses	4 mm triangles	Up	0.89	43.62±0.96	4.47±0.39	46.42	56.13	11.60±1.24
37	4 mm triangles	4 mm circles	Up	0.91	44.62±1.00	5.97±0.62	44.94	45.18	14.97±1.58
38	4 mm triangles	4 mm squares	Down	0.89	44.92±0.41	2.90±0.53	45.47	91.87	7.36±1.33
39	4 mm triangles	4 mm hexagons	Down	0.91	45.29±0.75	3.90±0.66	45.30	70.09	9.78±1.69
40	4 mm triangles	4 mm rhombuses	Down	1.00	44.04±0.53	6.86±0.38	46.65	38.85	17.30±0.79

5.4.5 Discussion

Among all the developed designs, five designs provided notable performance compared to the rest of the designs. These designs were selected because they either provided the best or worst performance criteria among the other designs. For instance, in terms of θ, Design 20 was the highest, with a bending angle of 30.96°. This also caused the length of B to be the highest since it is proportional to θ, while the opposite was observed when it comes to the length of R since it is inversely proportional to θ. The values of B and R in Design 20 were 11.81 and 22.32 mm, respectively. The design was printed using the bottom and top layers of 4 mm triangles and 3 mm triangles, respectively. On the other hand, Design 4 showed the poorest performance among the rest of the designs. This design was printed using the bottom and top layers of 3 mm squares. The bending angle was 6.21°, causing the lengths of B, L, and R to be the poorest, at values of 2.34, 43.33, and 99.90 mm, respectively.
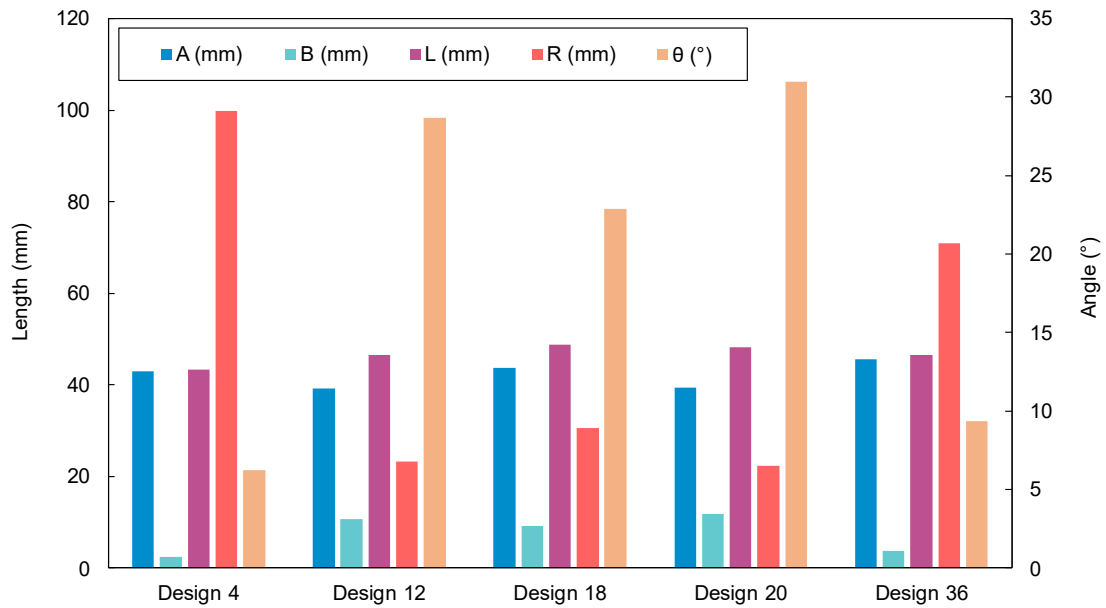
Figure 5.6. Comparison between Designs 4, 12, 18, 20, and 36 based on different performance criteria.

Designs 18 and 36 showed promising results in terms of providing the highest length values of *L* (48.71 mm) and *A* (45.60 mm), respectively. However, when it comes to their bending performance, Design 18 achieved a medium bending performance of 22.88°, while Design 36 bending angle was 9.36°, which is within the low range. Design 18 was printed using rhombus patterns of 4 and 3 mm for the bottom and top layers, respectively, while Design 36 was printed using 4 mm rhombus and triangle patterns for the bottom and top layers, respectively. On the contrary, Design 12 showed the lowest longitudinal length, where the length of *A* was 39.16 mm. However, the resultant banding angle (28.70°) was within the high range. This design was printed using circle patterns of 4 and 3 mm for the bottom and top layers, respectively. The aforementioned observations are essential when selecting the printing patterns based on the desired performance requirements. A comparison among the selected designs is summarised in **Figure 5.6**.

5.5   Proposed Implementation

To demonstrate the feasibility of utilizing the proposed designs in practical applications, a hand-like-shaped gripper was developed, as shown in **Figure 5.7**. The gripper consists of 4 fingers with a length of 41.60 mm, where Fingers 1 and 3 are based on Design 16 (big and small hexagons), while Fingers 2 and 4 are based on Design 20 (big and small triangles), as shown in **Figure 5.7** (a).
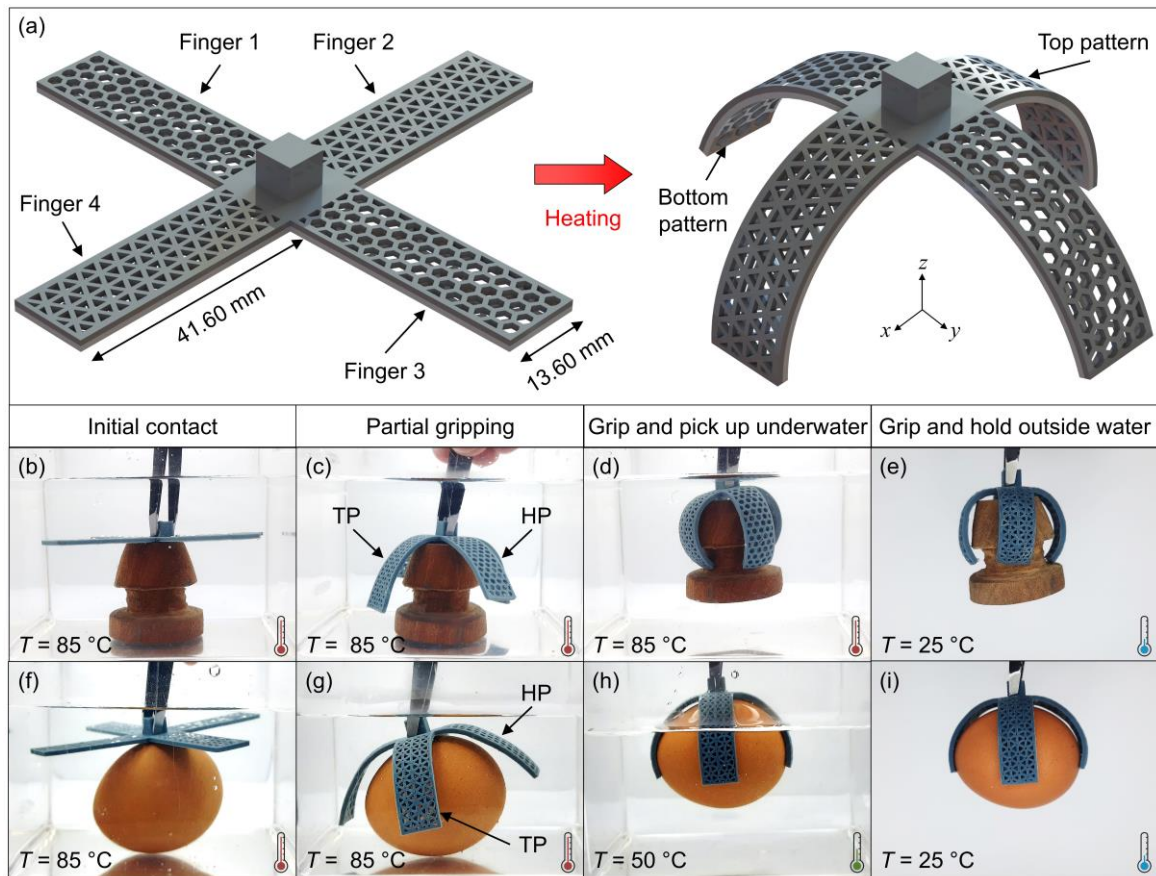
Figure 5.7. Proposed gripper based on the bioinspired patterns. (a) 3D designs of the gripper before and after activation. (b – e) Different stages of gripping a rubber cap. (f – i) Different stages of gripping an egg.

The use of different patterns allows each pair of fingers to achieve different bending angles despite being printed using the same printing parameters. In addition, these patterns allow reducing the weight of the gripper to 3.58 g, making it suitable for mass prototyping of light-weight grippers. To test the gripping performance, the gripper was used to pick objects in two different scenarios.

In the first scenario, the gripper was used to pick a rubber cap with a uniform cross-section (circle) at the gripping pints, as shown in **Figure 5.7** (b) – (e). After 3 seconds, the gripper's fingers reached almost half of their final deformation values (**Figure 5.7** (c)), while the complete deformation required around 11 seconds (**Figure 5.7** (d)). The gripping force was strong enough to hold the 21.15 g cap and lift it outside the water environment even at high temperatures when the gripper was still in a rubbery state.

The temperature of the water was 85 °C throughout the whole process. In the second scenario, the gripper was used to pick an object of a nonuniform cross-section at the gripping

points, which is a 49.82 g egg with an oval cross-section and smooth surfaces, making it harder to be picked up. The process started by immersing the gripper in hot water with a temperature of 85 °C to activate the gripper and allow it to enclose the egg. After 3 seconds (**Figure 5.7** (g)), it can be seen that the triangle patterns are almost touching the surface of the egg, while the hexagon patterns show slower deformation. Then, the gripper was allowed to cool down to a temperature below the start of the transition temperature, which is about 50 °C. The gripper was then in a glassy state and was able to pick up the egg. These steps are presented in **Figure 5.7** (f – e).

Since the length of the egg is larger than the width, thus the fingers that grip the width must have a higher bending ratio compared to the ones gripping the length, as can be seen in **Figure 5.7** (g). After taking the objects out of the water, as shown in **Figure 5.7** (e) and (i), it can be seen that the objects were gripped firmly despite the difference in the bending angles of the two pairs of fingers. This is due to the fact that gripping took place during the rubbery state, where slight force values were applied to the objects [220]. Then, at room temperature, PLA was in a glassy state that allowed the fingers of the grippers to hold the objects without damaging them. Such behaviour proves that the proposed gripper is suitable for delicate gripping applications.

The temporal deformation performance of the fingers of the gripper when gripping the rubber cap and egg was observed using Kinovea software. The hexagon patterns (Fingers 1 and 3) deform along the *y*-axis, while the triangle patterns (Fingers 2 and 4) deform along the *x*-axis, as shown in **Figure 5.8**. In both scenarios, it can be noticed that the triangle patterns deform faster than the hexagon patterns, which confirms the observed performance in **Figure 5.7** (c and g). However, when gripping the rubber cap, the hexagon patterns reached a steady-state value that is equal to the one achieved by the triangle patterns. On the other hand, when gripping the egg, the deformation of the hexagon patterns was lower than that of the triangle patterns since both deformations are restricted by the shape of the egg. This also explains the shorter settling time when gripping the egg.
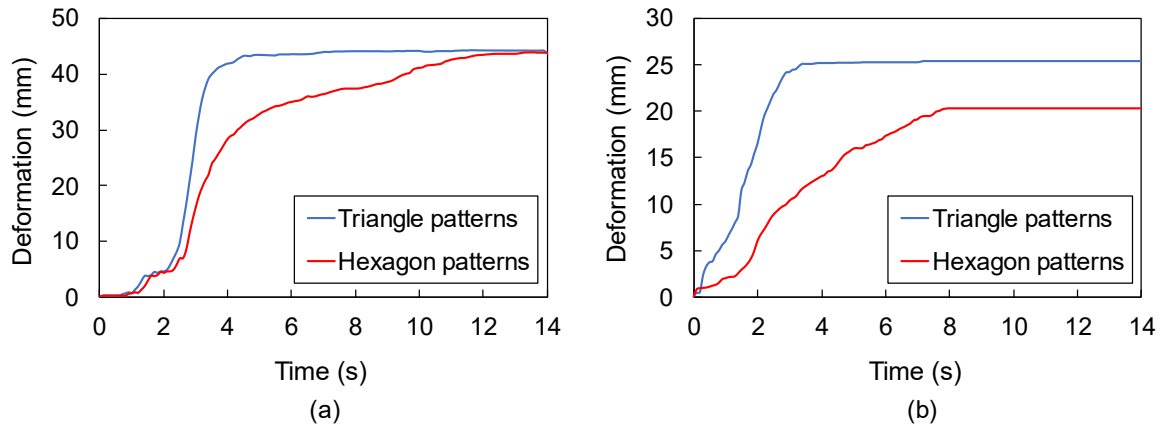
Figure 5.8. Temporal deformation of the fingers of the gripper at 85 °C when gripping: (a) the rubber cap, and (b) the egg.

5.6 Development of Pattern driven Actuators

5.6.1 Actuators Designs and Printing

This work focuses on developing a 4D-printed gripper, with the actuators' performance serving as the foundation. Specifically, chosen actuators will be employed to construct the entire gripper structure. Consequently, the gripper's design process commences with the creation of the actuators and an in-depth analysis of their performance.

These actuators utilize various pattern combinations, primarily drawing from grid, honeycomb, triangular, and rectilinear patterns, as shown in **Figure 5.9** Each actuator consists of two parts (top and bottom), where each part uses one of the patterns presented in **Figure 5.9** Thus, it is possible to create 12 different designs using these patterns, as presented in **Table 5.4**. The actuators were designed using SolidWorks with a length, width, and height of 30 mm, 9.60 mm, and 2 mm, respectively. Each pattern was printed using 10 layers of PLA with a height of 0.10 mm for each layer, giving the pattern a height of 1 mm. The width of the lines of every pattern and the width of the border of the actuators are identical, which are 0.80 mm. Each actuator was designed so that the bottom part is printed at a slower speed (15 mm/s) compared to the top pattern (60 mm/s).
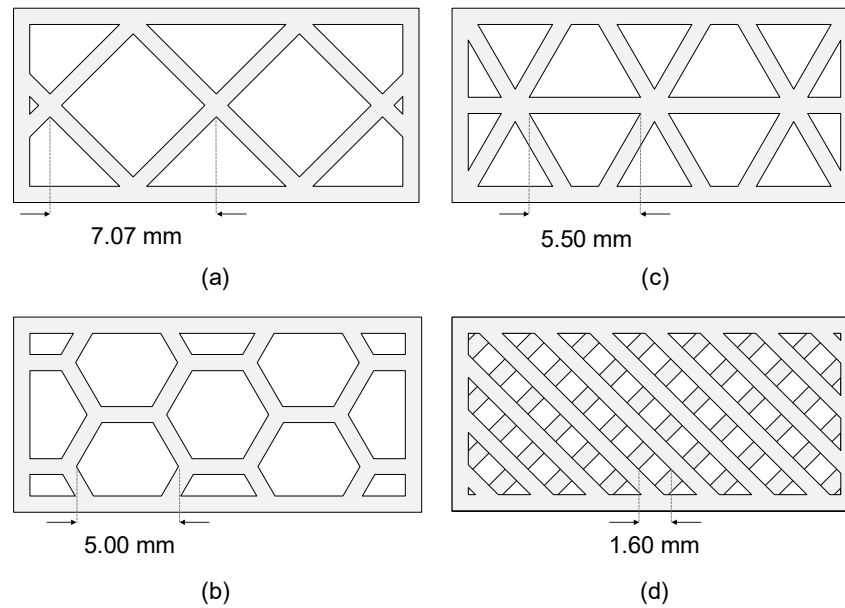
Figure 5.9. Basic printing patterns used in this work. (a) Grid. (b) Honeycomb. (c) Triangular. (d) Rectilinear

Table 5.4. Patterns combinations used in this work

Design	Bottom pattern	Top pattern
P.1	Grid	Honeycomb
P.2	Grid	Rectilinear
P.3	Grid	Triangular
P.4	Honeycomb	Grid
P.5	Honeycomb	Rectilinear
P.6	Honeycomb	Triangular
P.7	Triangular	Grid
P.8	Triangular	Honeycomb
P.9	Triangular	Rectilinear
P.10	Rectilinear	Grid
P.11	Rectilinear	Honeycomb
P.12	Rectilinear	Triangular

This approach results in varying levels of induced strain within the layers of each pattern, with higher printing speeds leading to greater induced strain. Consequently, the top pattern, often referred to as the active pattern, experiences more pronounced shrinkage compared to the bottom pattern, known as the passive pattern, when subjected to temperature changes. Moreover, beyond the difference in strain between the patterns, these pattern variations introduce differing stiffness values between the bottom and top patterns in each

actuator, effectively creating variable stiffness actuators. This innovative concept is further elaborated upon in the paper to develop a gripper with variable stiffness properties.

Table 5.5. Summary of the printing parameters used in this work

Parameter	Value
Nozzle diameter	0.40 mm
Extruder temperature	190 °C
Heated bed temperature	45 (°C)
Printing speed of the bottom pattern	15 mm/s
Printing speed of the top pattern	60 mm/s
Layer height	0.10 mm

Then, each actuator was printed based on the parameters stated in **Table 5.5**. The actuator underwent a sequential process for testing. Initially, it was allowed to cool down to room temperature. Subsequently, it was immersed in hot water at 85 °C to trigger its activation. Afterward, the actuator was removed from the water and left to cool naturally, during which deformation measurements were taken. Following this, the actuator was once again immersed in hot water, all the while subject to an external force to bring it back to its original printed shape. This force was maintained as the actuator was taken out of the water. This cycle was repeated until the actuator had cooled down to room temperature, enabling the measurement of the actuator's shrinking percentage. The shrinking percentage, which is the change in the area of the top pattern, was measured as follows:

$$SP = \frac{A_0 - A_1}{A_0} \times 100\% \tag{5.5}$$

where SP is the shrinking percentage, A_0 is the initial area of the top pattern (192 mm^2), and A_1 is the new area of the top pattern after the activation process.

5.6.2   Actuation Results

The fabricated actuators before and after the activation process are presented in **Figure 5.10**. The figure displays both top and side views of Shapes P.1 through P.12. It is evident that the actuators exhibit bending in different directions, either towards the top or bottom pattern, and the bending angle (θ) varies considerably across all designs. Additionally, there is a

noticeable reduction in the length of the actuators following the activation process, as observed when comparing the two states of the actuators. Consequently, this results in a decrease in the area and volume of the actuators. For the purpose of simplifying the analysis, this work focuses solely on calculating the shrinking percentage in the area.
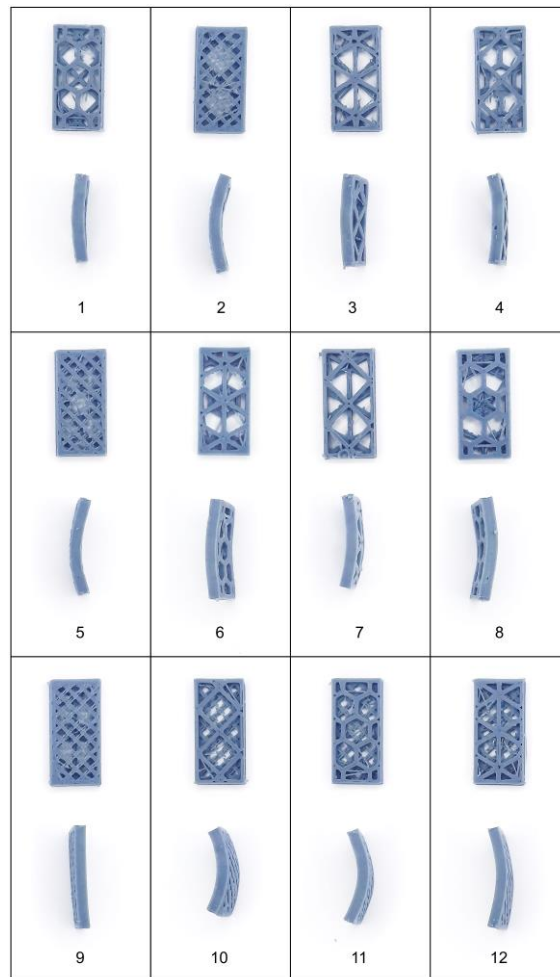

Figure 5.10. 4D printed Designs P.1 – P.12. Top: Top view of the printed design before actuation. Bottom: Side view of the design after actuation.

The actuation results are summarized in **Table 5.6**, where *BP*, *TP*, and *BD* respectively represent the bottom pattern, top pattern, and bending direction. The results reveal variations in the bending angle, ranging from 1.00° for Design 9 to 12.00° for Shape P.11. Notably, Shape P.11 also exhibited the maximum shrinking percentage, approximately 52.60%. Conversely, several other designs, including Designs P.5, P.6, and P.8, displayed the lowest shrinking percentage values, at approximately 45.30%. It is worth highlighting that the bending angle is not solely determined by the shrinking percentage. Instead, it is significantly influenced by the disparity in shrinking between the top and bottom patterns. A greater

difference in shrinking results in a higher bending angle. For instance, Designs P.5, P.6, and P.8, despite having distinct bending angles of 10.00°, 2.00°, and 7.50° respectively, all share a similar shrinking percentage due to the notable difference in shrinking between their top and bottom patterns.

Table 5.6. Actuation results of Designs P.1 – P.12

Design	*BP*	*TP*	*BD*	*θ (°)*	*SP (%)*
P.1	Grid	Honeycomb	Down	4.30	48.96
P.2	Grid	Rectilinear	Down	10.00	47.10
P.3	Grid	Triangular	Down	2.80	48.96
P.4	Honeycomb	Grid	Up	6.17	48.96
P.5	Honeycomb	Rectilinear	Down	10.00	45.30
P.6	Honeycomb	Triangular	Down	2.00	45.30
P.7	Triangular	Grid	Up	7.80	50.00
P.8	Triangular	Honeycomb	Up	7.50	45.30
P.9	Triangular	Rectilinear	Down	1.00	48.96
P.10	Rectilinear	Grid	Up	11.00	49.00
P.11	Rectilinear	Honeycomb	Up	12.00	52.60
P.12	Rectilinear	Triangular	Up	8.00	47.10

The results consistently demonstrate that the bending toward the top pattern is consistently greater than the bending toward the bottom pattern when comparing the same pattern combinations. For example, let's consider Shapes 1 and 4, both incorporating a combination of grid and honeycomb patterns. It is evident that the upward bending in Shape 4 exceeds the downward bending in Shape 1. This pattern holds true when comparing Shapes 2 and 10, Shapes 3 and 7, Shapes 5 and 11, Shapes 6 and 8, as well as Shapes 9 and 12.

This behavior arises from the printing process itself, wherein the upper layers tend to retain higher levels of stored strains in comparison to the lower layers. The variance in stored strain occurs because the lower layers undergo reheating during the printing process, resulting in reduced stored strains. Consequently, this generates an inherent upward bending force for each actuator. In contrast, the bending induced by the shrinking of the patterns, known as patterns bending, can occur either upwards or downwards, contingent upon the difference in the shrinking percentage between the two patterns. Since the total bending is a combination of the

default bending and patterns bending, the upwards bending will always be higher, as observed in **Table 5.6**.

It can also be observed that the patterns can be ranked from stronger to weaker. In other words, based on **Table 5.6**, it can be seen that some patterns have the ability to direct the bending towards them in all or some cases. For instance, the grid pattern consistently exhibits the greatest strength because the bending direction invariably points toward it, regardless of whether it is positioned at the bottom or top of the actuator. Building upon this concept, it can be deduced that the rectilinear pattern is the least robust, while the honeycomb and triangular patterns rank second and third, respectively, in terms of strength. This principle can be further extrapolated to design more intricate structures, including grippers, as elaborated in the subsequent section.

5.6.3 Variable Stiffness Gripper

The actuators developed in this study can serve as the functional fingers of a gripper. In many robotics applications, there is a need to create grippers with finger structures that mimic those found in humans or animals. Such structures often incorporate elements that can alter their stiffness in response to external stimuli. Stiffness, in these cases, refers to the material's ability to revert to its original shape after being subjected to an external force. Examining the actuators created based on Designs 1 through 12, it is evident that each actuator possesses distinct stiffness levels and profiles depending on the shape and location (top or bottom) of the pattern.

Furthermore, the stiffness values of each design can be adjusted by altering the ambient temperature until the material approaches its glass transition temperature. This variation in stiffness is unique to each design, resulting in two distinct sources of variable stiffness behavior. This variable stiffness concept can be utilized to develop a gripper with four fingers, where each finger includes three segments ($S_1 - S_3$) and two joints to mimic the human fingers, as shown in **Figure 5.11** (a). The figure shows a 3D design of the gripper when it is facing up, which is the same printing orientation.
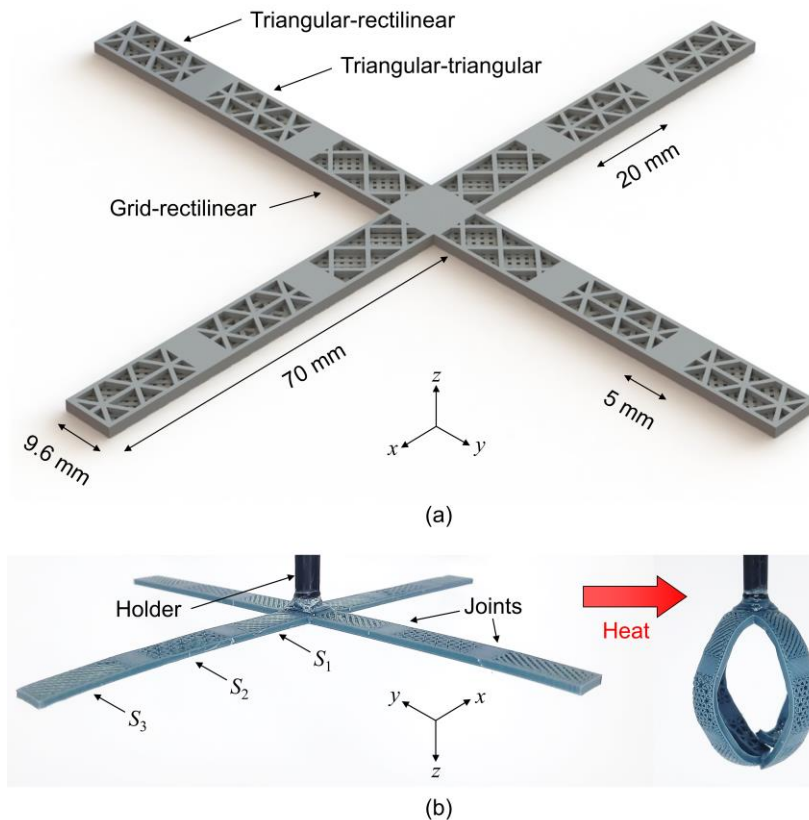
Figure 5.11. Variable stiffness gripper. (a) 3D design of the gripper facing up (as printed). (b) 4D printed gripper facing down before and after activation using hot water

The segment and joint dimensions are standardized at 70 mm for segments and 20 mm for joints. To enable the observation of segment deformation without interference from the joints, the joints were printed with a 100% infill ratio. Segments 1 and 3 were derived from Designs P.2 and P.9, respectively, with their lengths extended to 70 mm. Design P.9, characterized by its minimal bending angle of 1.00°, was chosen for the tip of the finger, as it is well-suited for this purpose. In contrast, Design P.2 was selected for Segment 1 due to its capacity to provide a substantial bending angle of 10.00°, making it suitable for the finger's base. It is noteworthy that other designs offering greater bending angles were not chosen, as they would exceed the design requirements, causing the fingers to interfere with each other.

Segment 2, on the other hand, was created using two triangular patterns of differing sizes. One pattern featured triangles with side lengths of 5.50 mm, while the other consisted of triangles with side lengths of 1.70 mm. This choice was made to demonstrate that bending is also influenced by the percentage of PLA utilized for pattern printing, commonly referred to as the infill ratio. In this case, the deformation direction was directed toward the pattern with the lower infill ratio (the larger triangles). The resulting deformation angle for this segment

was approximately 9.50°, making it suitable for the middle portion of the finger. The 4D-printed gripper before and after activation is presented in **Figure 5.11** (b), which shows the gripper facing down after being attached to a holder. The activation process was done by immersing the gripper in hot water at 85 °C.

The findings demonstrate that the suggested gripper is well-suited for robotics applications as an end-effector, particularly in scenarios demanding variable stiffness gripping. This concept can be further enhanced through the utilization of conductive materials, like graphene-PLA. Such materials enable controlled activation of specific segments of the gripper according to the desired performance, paving the way for self-sensing applications.

5.7   Preliminary Multi-Material Actuators

The first actuator in this section (Design 41) was printed entirely out of PLA while the second (Design 42) of BIO-PT, which were used as comparison actuators with the multi-material structures. The PLA actuator is shown in **Figure 5.12** (a) and (b) while the BIO-PT is in **Figure 5.12** (c) and (d). As can be seen in the figure, the bending of the PLA is moderate, which is expected of an actuator of this size and thickness, and the bending angle is about 20°. While the BIO-PT is small, which is expected too of an actuator of this size and thickness of an elastomer, which is not an SMP, thus not holding a lot of strain upon printing, with a bending angle of about 4°.
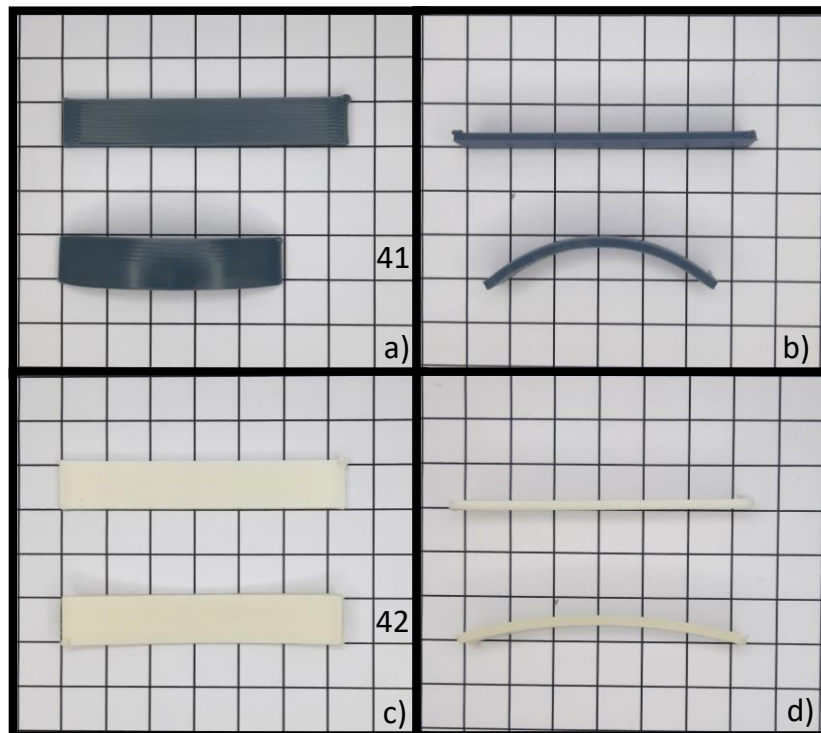
Figure 5.12. (a) and (b) Top and side views of the PLA actuator (Design 41), (c) and (d) Top and side views of the BIO-PT actuator (Design 42).

Design 43 was printed out of a bottom section of PLA and a top section of BIO-PT. The combination of the two materials causes the strain between the two layers to be different due to variations in the stiffness. The two-section actuator is shown in **Figure 5.13** (a) and (b). As can be seen in the figure, the bending of the material is very high (the bending angle is about 88°), which is nowhere compared to the other actuators. The degree of bending of the actuator proves that the difference in stiffness between two materials can create a huge SME. Design 44 was printed out of a bottom section of PLA and a top section of BIO-PT embedded between two sections of PLA and is presented in **Figure 5.13** (c) and (d). As can be seen in the figure, the bending at the part where the BIO-PT is the layer above the PLA is very high, causing a folding effect on the parts of the PLA without BIO-PT. The actuator had a bending angle of about 82°. This actuator is a good indicator of the different SME shapes that can be achieved by multi-material variable stiffness prints when designed properly. A folding effect can be made as the one made by the hinges of variable stiffness patterns. The measurements of the printed and tested actuators above are summarized in **Table 5.7**.
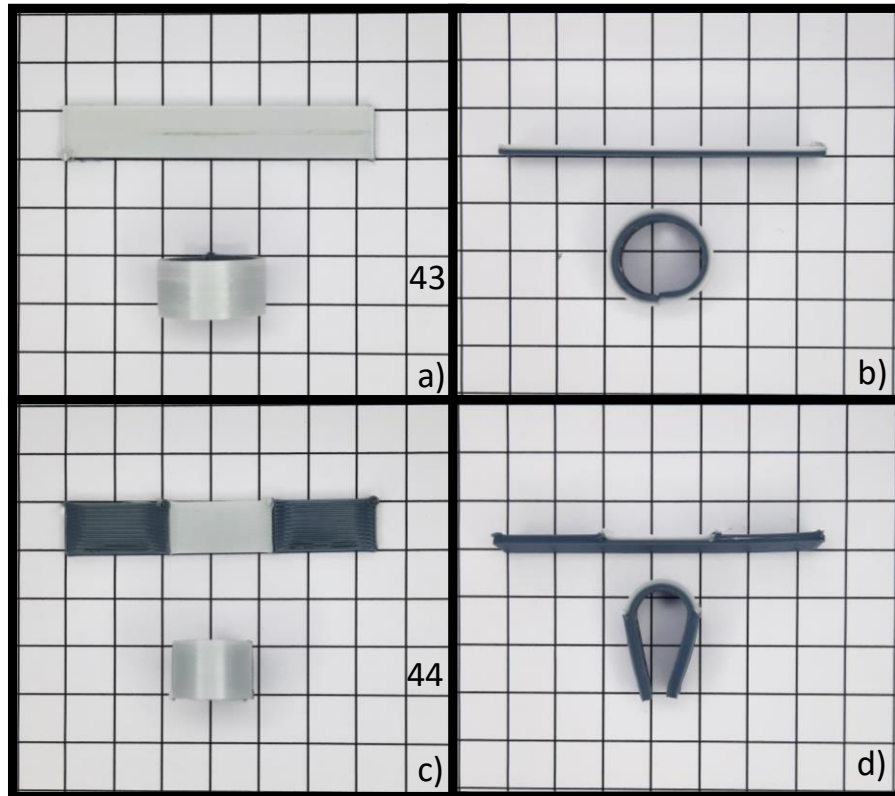
Figure 5.13. (a) and (b) Top and side views of a structure of a bottom section of PLA and a top section of BIO-PT (Design 43), (c) and (d) Top and side views of a structure of a bottom section of PLA and a top section of BIO-PT embedded between PLA (Design 44).

Table 5.7. Summary of the bending results of Designs 41 – 44.

Design	Material	Length A (mm)	Length B (m)	Bending angle (°)	Bending direction
41	PLA strip	46.89	10.42	20.04	Downwards
42	BIO-PT strip	58.24	6.29	4.31	Downwards
43	PLA and BIO-PT strip	0.50	18.26	88.25	Downwards
44	Embedded BIO-PT in PLA	2.88	22.36	81.99	Downwards

From **Table 5.7**, it can be seen that all the actuators bend downwards, which is expected in the printing of non-patterned structures. Since the structure is smooth and straight, the printing is done in straight lines across the whole structure for all the layers. This causes a strain that bends in the only direction which is vertical along the direction of the print. This effect is explained in the infill percentage section.

5.8   Summary

The principle of using the printing parameters to induce internal strain into the actuators in 4D printing can be a useful tool, not only for eliminating the need for manual programming, but also for having a precise SME effect in the actuators. The use of patterns of variable stiffness can be used to control the degree of bending in the actuators. The use of patterns with shapes of different sizes causes the internal strain between the layers to generate large deformations in the actuators, and it is controllable to a very high degree in terms of the degree and direction of bending. Five bioinspired shapes were tested with their variations for a total of 40 different designs, of which some were of different pattern sizes and some were mixed patterns. The shapes used are circles, squares, hexagons, rhombuses, and triangles. The effect of the patterns on the bending performance can be summarized as follows:

- The triangle patterns with different sizes in each layer had the greatest deformation angle, which was $30.96°$.

- The rhombus shape patterns seem to reduce the effects of printing parameters on the direction of the bending, allowing most control.

- Shrinking in all the actuators ranged from 8% to 12% as measured using the arc length.

- Changing the size of the shapes used was highly useful in determining the direction of the bending in the actuators.

These patterns were also used to design a gripper with fingers that bend at different rates and angles, allowing it to pick up uneven objects. More research can be done on pattern variations and their effects, as well as integrating the patterns into larger, more complex structures. Testing on the force caused by the shape change and thermomechanical characterizations of the prints can be done to enhance the understanding of the SME of the patterns in practical applications.

Controlling the actuators by means of non-manual programming such as printing parameters and structural manipulations provided immense advantages for the designs. These actuators have been activated by means of environmental heat, which although it is very quick and achieves full deformation, it limits the testing capabilities of the actuators. the activation of the actuators can be done via local means, this allows better observations of the activation process. This can be made by electrically activating actuators, allowing for sensors and cameras to observe the deformation process.

Chapter 6: Joule-Heating Activation of 4D Printed Conductive Actuators

6.1   Introduction

This chapter presents the control of Joule heating in conductive PLA actuators, by varying the activation voltage. Considering the advances that are made in the field of conductive 4D printing, the control of 4D printed conductive actuators is not well understood. There is still a plethora of conditions of activation, under which the actuators might act differently. The aim of this study is to help in the understanding of some of these characteristics. The contributions of this study are summarized as follows:

- This chapter presents Joule-heating-activation control of CB/PLA 4D printed actuators. The research investigates the time-dependent effect of the activation power on the electro-thermo-mechanical performance of the actuators, including the temperature distribution profiles, deformation behaviour, bending angle, and the generated force.

- This chapter proposes a novel CB/PLA 4D printed manipulator that consists of an upper arm, a lower arm, and two fingers, where each part is controlled individually using Joule heating. The design allows the manipulator to grip and move an object along the *x*- and *y*-axes.

6.2   Materials and Methods

The filament used in this study was a conductive carbon black PLA (CB/PLA) (Protopasta, 1.75 mm, 500 g, Protoplant, Vancouver, Washington, USA). PLA is widely used in 3D printing because of its usability, affordability, and ease of mixing with other additives, such as the CB nano-powder in this work. This makes the filament conductive and thus can be heated by applying a voltage across its terminals.

Thermal analysis of the filament was carried out using a dynamic mechanical analysis (DMA) machine (DMA 8000, Perkin Elmer, Waltham, MA, USA). The DMA was used to measure the viscoelasticity of the filament material, as shown in **Figure 6.1** (a). The storage modulus and tan δ were measured to investigate the ability of the material to store elastic energy and determine glass transition temperature (T_g), respectively.

The DMA results show that T_g of the CB/PLA ranges from about 50 °C to 85 °C, and peaks at about 70 °C. following this, as presented in **Figure 6.1**, a tensile test was performed

to assess the stress that the printed materials can take along the printing lines. The print that was tested had a maximum stress of 26 MPa, which is relatively high and can withstand heavy-duty applications.
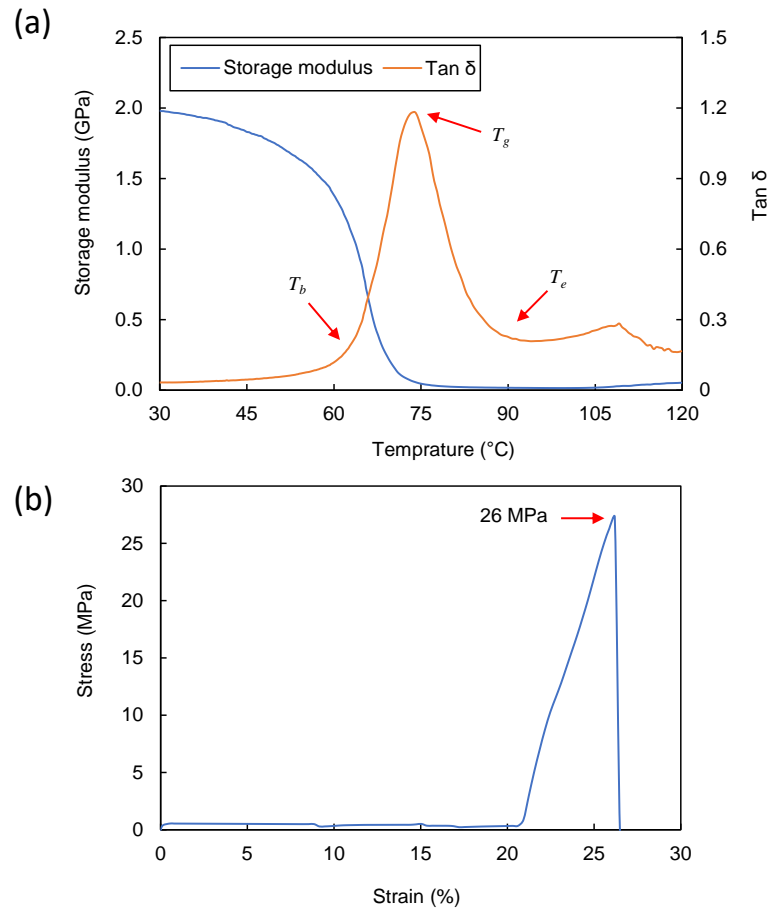

Figure 6.1. CB/PLA material characterization results. (a) DMA results. (b) Tensile test results.

The experimental setup that was used in this study is shown in **Figure 6.2** (a), which is in accordance with the one presented earlier in **Figure 3.1** (a). The 3D designs were transferred to a slicer software (Simplify3D) to generate a G-code that can be used by the FDM printer. After the printing process, each actuator was left to cool down on the print bed. Then, a 0.1 mm enamelled copper wire was attached to one tip of the actuator using a 3D printing pen (3D Pen V2 Shenzhen Hugesmoke Technology Co., Ltd., Shenzhen, Guangdong, China).

The 3D printing pen used the same CB/PLA filament to form a soldering-like contact point between the copper wire and the actuator. The other tip of the actuator was held using an alligator clip that is fixed vertically on a test rig. The copper wire and the alligator clip

were connected to a direct current (DC) power supply (GPS-3303, GW Instek, Taipei, Taiwan). This setup ensures that the actuator can deform freely while being suspended vertically since the effect of the weight of the copper wire is minimal.
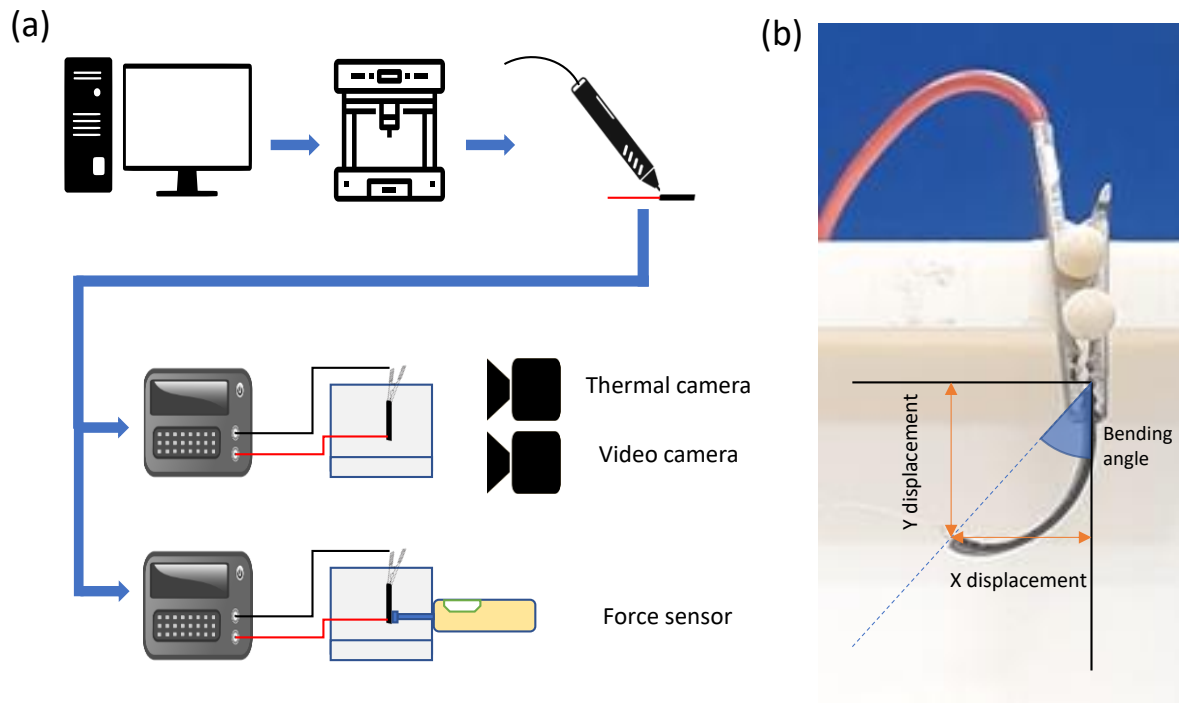
Figure 6.2. Preliminary settings of the experiment. (a) The printing process and experimental setups that are used to characterize the electro-thermo-mechanical performance of the actuators. (b) Deformation characterization method of a sample actuator.

A digital camera and thermal camera (FLIR ONE Pro LT Thermal Imaging Camera, Teledyne FLIR LLC, Wilsonville, Oregon, USA) were used to capture the changes in the actuator's deformation and temperature during activation. The bending angle and the deformation of the actuator along the x- and y-axes were measured, as shown in **Figure 6.2** b). This was done by postprocessing the recorded video using a video analysis tool (Tracker).

During the activation, the supplied voltage and current were recorded to investigate the effect of the power on the generated temperature and deformation angle. An identical actuator was then used in the force characterization experiment, as shown in **Figure 6.2**. A different setup was required since the force measurement requires the actuator to be in contact with a force sensor, which prevents observing the deformation. The force generated by each actuator was measured using a force sensor (ZTA-5N, IMADA Co., Ltd., Toyohashi, Aichi, Japan).

6.2.1 Actuator Testing

Actuators with length, width, and height of 30 mm × 3.2 mm × 1 mm were printed using the printing parameters presented in **Table 6.1**. Each actuator consisted of an active part (top) and a passive part (bottom) with equal heights (0.5 mm). However, the layers of the passive part were printed using a lower printing speed and a higher layer height compared to the layers of the active part. Reducing the printing speed causes less stretching in the printed lines, leading to lower induced strain values in the printed layers. Meanwhile, increasing the layer height decreases the pressure in the nozzle, which causes less induced strain in the printed layers. Thus, the printing parameters were selected to induce lower strain values in the passive layers compared to the active layers. The higher the difference in the strain between the active and passive parts, the higher the bending angle of the actuator. In addition, the bending angle can be maximized when the passive and active parts have equal heights, or when the passive-to-active ratio is 1:1.

Table 6.1. Printing parameters used in this study.

Parameter	Value
Active layers printing speed	80 mm/s
Passive layers printing speed	10 mm/s
Active layer height	0.05 mm
Passive layer height	0.25 mm
Number of active layers	10
Number of passive layers	2
Passive-to-active ratio	1:1
Printing temperature	190 °C
Bed temperature	45 °C

6.3 Modelling and Simulation

This section presents the method used to simulate the effects of Joule heating on the actuators by using different voltages. The first part presents the mathematical modelling behind the simulation, which takes into account the losses of the process in the energy

exchange. The second part is a simulation of Joule heating of the actuator using ANSYS software.

6.3.1 Mathematical Modelling of Joule Energy

In this work, each actuator was activated by means of Joule heating, which is controlled by setting the voltage value across the actuator. It is assumed that the heat loss is only caused by the energy of the heat change of the filament material (E_{SMP}) and the convection losses (E_{con}) from the actuator to the surrounding air. Other losses, such as the copper wire loss are considered negligible. Thus, the energy that is supplied from the electrical current through the wires (E_{in}) can be defined using the following equation [228]:

$$E_{in} = E_{SMP} + E_{con} \qquad (6.1)$$

This energy is expressed as Joule heating as follows:

$$E_{in} = i^2 \sigma \frac{l}{hw} t \qquad (6.2)$$

where i is the supplied current, which is dependent on the voltage, σ is the electrical resistivity of the material, while l, w, and h are the length, width, and height of the actuator, respectively. The energy of the heat change of the filament material can be found as follows [228]:

$$E_{SMP} = \int_{T_0}^{T_f} \rho_{SMP} c_{SMP} lwh \, dT(t) \qquad (6.3)$$

where T_f and T_0 are respectively the final and initial temperatures of the actuator during the heating process. ρ_{SMP} and c_{SMP} are the density and thermal capacity of the SMP respectively. Meanwhile, the convection losses can be represented as follows:

$$E_{con} = = \int_{t_0}^{t_f} h_h (2lh + 2lw + 2wh)(T_0 - T_f) dt \qquad (6.4)$$

where t_f and t_0 are respectively the time instants at the final and initial temperatures of the heating process, while h_h is the convective heat transfer coefficient of the heating process. These equations represent an approximation of the energy exchange in the process. Beyond this, FEA simulations are conducted to calculate the Joule heating, current, and heat generation of the actuators under the stimulus.

6.3.2 FEA

This section includes the FEA of the actuators for the Joule heating process, to assess the temperature generated by the current passing through. The FEA was carried out using ANSYS to verify the mathematical model, where both electrical and thermal analyses were done. Furthermore, the FEA investigates the current distribution, Joule heating, and heat generated in the actuators at different voltages. The material properties used in the simulation were measured using the DMA and tensile tests, as well as measurements reported in the literature[229], [230], [231], [232], [233], as presented in **Table 6.2**.

Table 6.2. Material properties of the Protopasta filament that are used in the simulation process.

Property	Value
Density	1240 kg/m^3
Poisson's ratio	0.42
Isotropic thermal conductivity	0.25 W/(m.K)
Specific heat capacity	1800 J/(kg.K)
Resistivity at 22 °C - 150°C	0.46 - 0.30 Ω.m

The simulation was carried out by assigning a voltage at one end of the actuator and a zero voltage at the other end to present the voltage drop across the actuator. In addition, it was assumed that the material is homogeneous, thus the voltage drop is consistent through the actuator. This meant that each actuator experienced the maximum voltage at one end, and it dropped completely at the other end. It was also assumed that copper wires resistance is considered negligible.

The FEA results are shown in **Figure 6.3**, where the figure is divided into three columns representing each activation voltage used in this work. The current density results of the actuators are presented in **Figure 6.3** (a), where the highest density was observed at the point of contact of the actuators with the copper wires. Due to the homogeneousness of the materials, the current distribution is consistent throughout the body of the actuators.
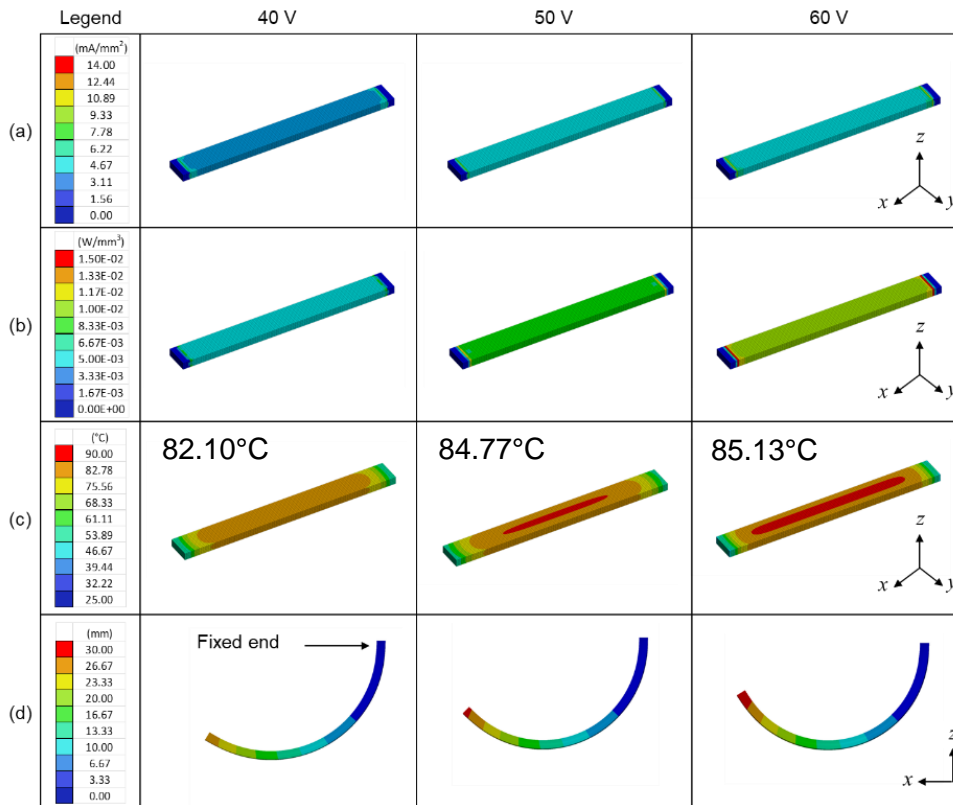
Figure 6.3. FEA results of the actuators using activation voltages of 40, 50, and 60 V. (a) The current density (b) The Joule heating effect. (c) The temperature distribution (d) Maximum deformation.

As for the Joule heating effect, the same behaviour is observed as the current distribution, where it is the highest at the contact point of the copper wires with the actuators, as displayed in **Figure 6.3** (b). The temperature distributions of the actuators are displayed in **Figure 6.3** (c), which demonstrates that the cores of the actuators have the highest temperatures. The assessment of the thermal effect is based on the highest temperature reached in the body of the actuators, which is around the centre of the actuators. This behaviour is compared with the results of the thermal imaging in the practical section, which show similar temperature distribution.

The deformation of the actuators is based on the estimation of the coefficient of thermal expansion, which is used to replicate the effects of stimuli activation [217]. When using 40 V to activate the actuator, the heating was carried out for 80 s, which is the duration when the actuator achieved the highest bending as referred to in **Figure 6.3** (d). Beyond this point, the actuator's temperature stabilizes and reaches a steady state both in the simulation and the experiments, as presented later in the experimental section.

Meanwhile, when activating the actuators using 50 V and 60 V, the activation was carried out for 28 s and 18 s, respectively. The temperatures reached by the actuators at 40 V, 50 V, and 60 V, were 82.10°C, 84.77 °C, and 85.13 °C, respectively.
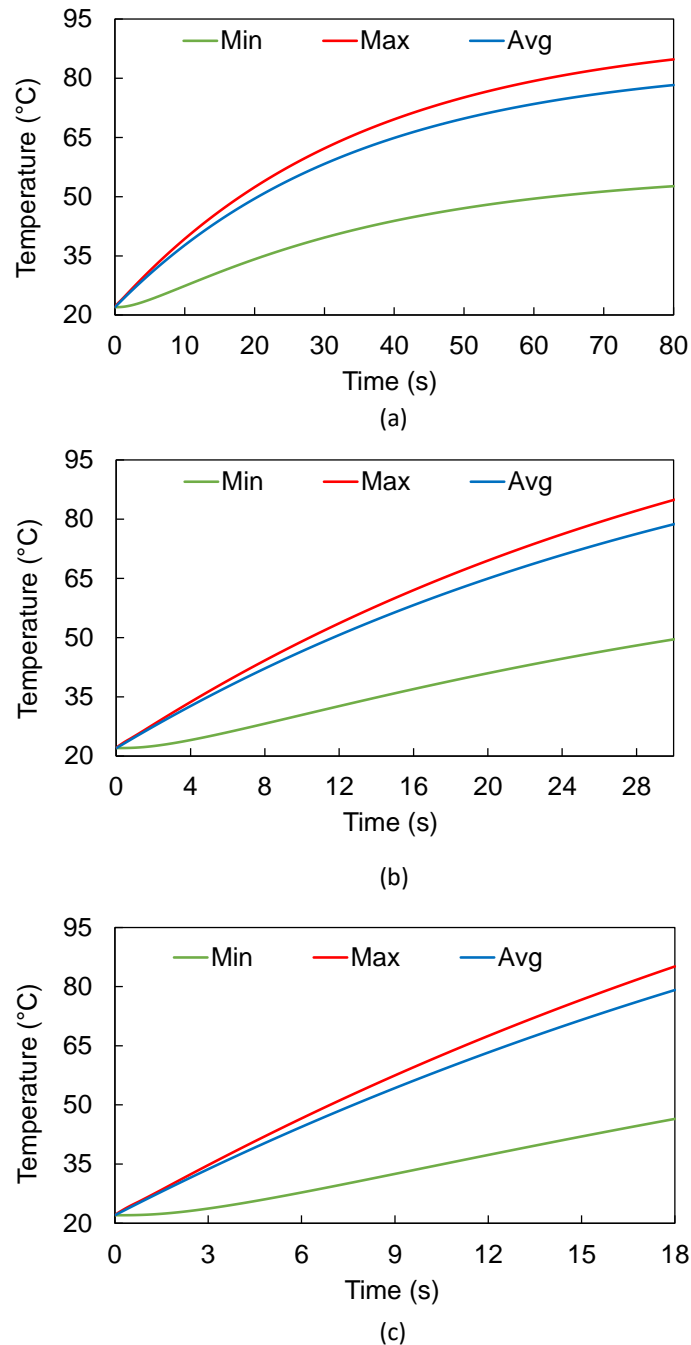
Figure 6.4. FEA results of the time-dependent thermal response of the actuators using activation voltages of (a) 40 V, (b) 50 V, and (c) 60 V.

The previous results can be further understood when analyzing the transient thermal results of the actuators' temperature, as shown in **Figure 6.4**. The temperature values of the actuators are non-linear, where the rate decreases as they reach higher temperature values.

This effect is seen very clearly in the 40 V results, with the temperature reaching a plateau that stabilizes at around 80 s. This is the case for all actuators at different temperatures, but the plateau temperatures are much higher than the melting temperature of the material, which was used as a condition to stop the simulation at that point.

The average temperature values that were reached by the actuators are very close to the maximum, which indicates that most of the volume of the actuators is heated sufficiently. Meanwhile, the minimum temperature is recorded at the ends of the actuators, as presented in **Figure 6.3** (c), which has a minor effect on the deformation.

6.4   Experimental Results and Discussion

The results section consists of two parts, where the first encompasses the testing of the actuators across different voltages to test their activation criteria. These results are used to control the actuators, for specific voltages and timings. The second part is a proof-of-concept application of a Joule-heating-activated manipulator that can hold and displace a small object.

6.4.1   Voltage Control

In this work, different voltage values were used to activate the actuators. It was observed that voltage values below 40 V did not generate sufficient temperature to activate the shape memory effect (SME) of the CB/PLA. On the other hand, voltage values above 60 V caused the actuators to melt since the generated temperature was above the melting point of the CB/PLA. These values are determined based on the significance of the results, where they represent the voltages that induce noticeable changes in the final bending angles, allowing for meaningful distinctions to be made between different experimental conditions. Thus, the results discussed in this section are for voltage values of 40, 50 and 60 V. The results of the power calculation and the bending angle of the actuators are presented in **Figure 6.5**.

The measured results are of different time frames for each voltage, which are 120 s for the 40 V, 60 s for the 50 V and 30 s for the 60 V. The measurements were stopped when the actuator measurements stabilized or when the power in the actuators increased rapidly, thus melting them. When using 40 V to activate the actuator, the power stabilizes at about 0.46 W after about 30 s. On the other hand, when using 50 V and 60 V to activate the actuators, the power increased rapidly causing melting after around 55 s and 28 s, respectively, and was stopped.

As is seen in **Figure 6.5**, the bending angles of the three voltages peak at different times. The 40 V results show that a maximum angle of 63° was achieved after around 80 s of activations. Meanwhile, when using 50 V and 60 V for the activation, maximum angles of 74° and 78° were observed at around 28 s and 18 s, respectively. As is seen in **Figure 6.5** (b) and (c,) the power in the actuators starts rising rapidly after 55 s and 27 s when using 50 V and 60 V, respectively.
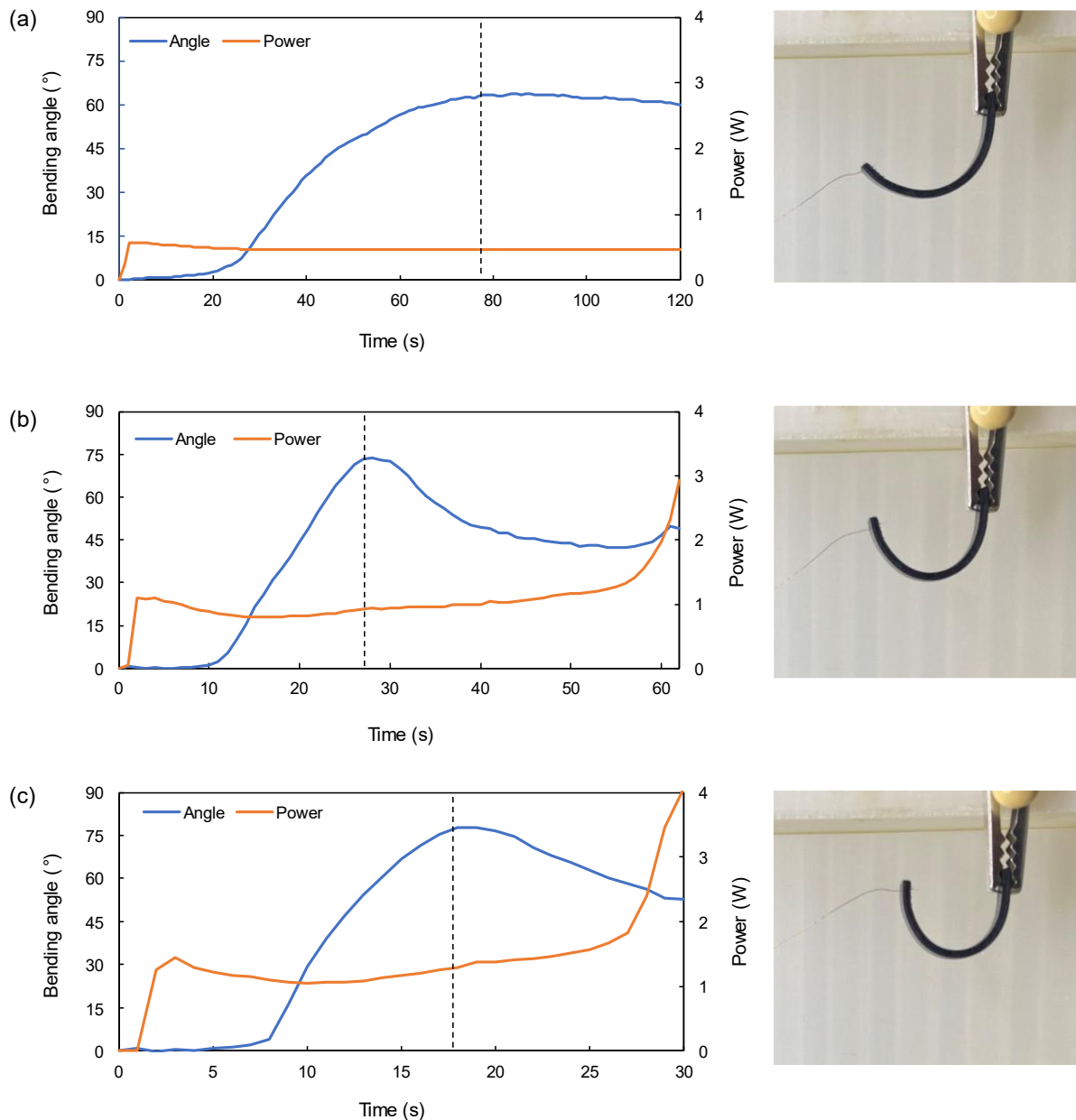

Figure 6.5. Electro-mechanical experimental results of the actuators at the three different voltage values. (a) 40 V. (b) 50 V. (c) 60 V. Left: Supplied power and the resultant bending angle vs. time. Right: Maximum deformation achieved by the actuator when activated using the corresponding voltage value.

This behaviour is accompanied by variation in the bending angle as well, which is caused by the overheating of the actuators. The current starts rising rapidly in the actuators as their temperature reaches very high values. The deformation that happens beyond is not due to the SME in the actuators; it is caused by melting due to excessively high temperatures. The start of deformation seems to also vary with the voltage since increasing the voltage causes the temperature to rise quickly, which consequently affects the deformation.

The activation voltage influences the force generated by the actuators as well. As presented in **Figure 6.6**, the force of the three activation voltages is shown with the actuator surface temperature. The force rises when the activation starts at the same time as the initial shape change, which is clearly presented in the figure. This behaviour is observed in all three tested voltages.

The shape change in the 40 V actuators starts at about 15 seconds after activation, at which a rapid rise in the recorded force is seen. The force increased up to 16 mN and then reduced, which is expected of this material since at a lower temperature since the actuator is still semi-rigid generating higher forces on the force sensor. This force is generated as the temperature rises until the material gets softer, where the force then slowly declines until it reaches the zero point (not shown in the figure).

The temperature in the 40 V actuator stabilizes early in the actuation process, with minor fluctuations in the recording. This might be caused by the thermal capture due to the deformation, which shifts the point of temperature readings. The other two actuators' temperatures rise in a semi-linear manner, but the activation was stopped to prevent melting the actuators. The highest temperatures recorded for the 50 V and 60 V actuators are about 118 °C and 129 °C.

The force generated by the actuators depends directly on the activation voltage, where the higher the voltage, the higher the force. The maximum measured force values were 16 mN, 17 mN, and 18 mN when respectively using 40 V, 50 V, and 60 V to activate the actuators. In addition, the duration of the activation was varied with the supplied voltage as the force returned to 0 mN faster when a higher voltage value was used. The 40 V actuator reached 0 N at 180 seconds (not shown in **Figure 6.6** (a)), while the 50 V and 60 V actuators reached 0 N at 42 s 30 s, respectively.
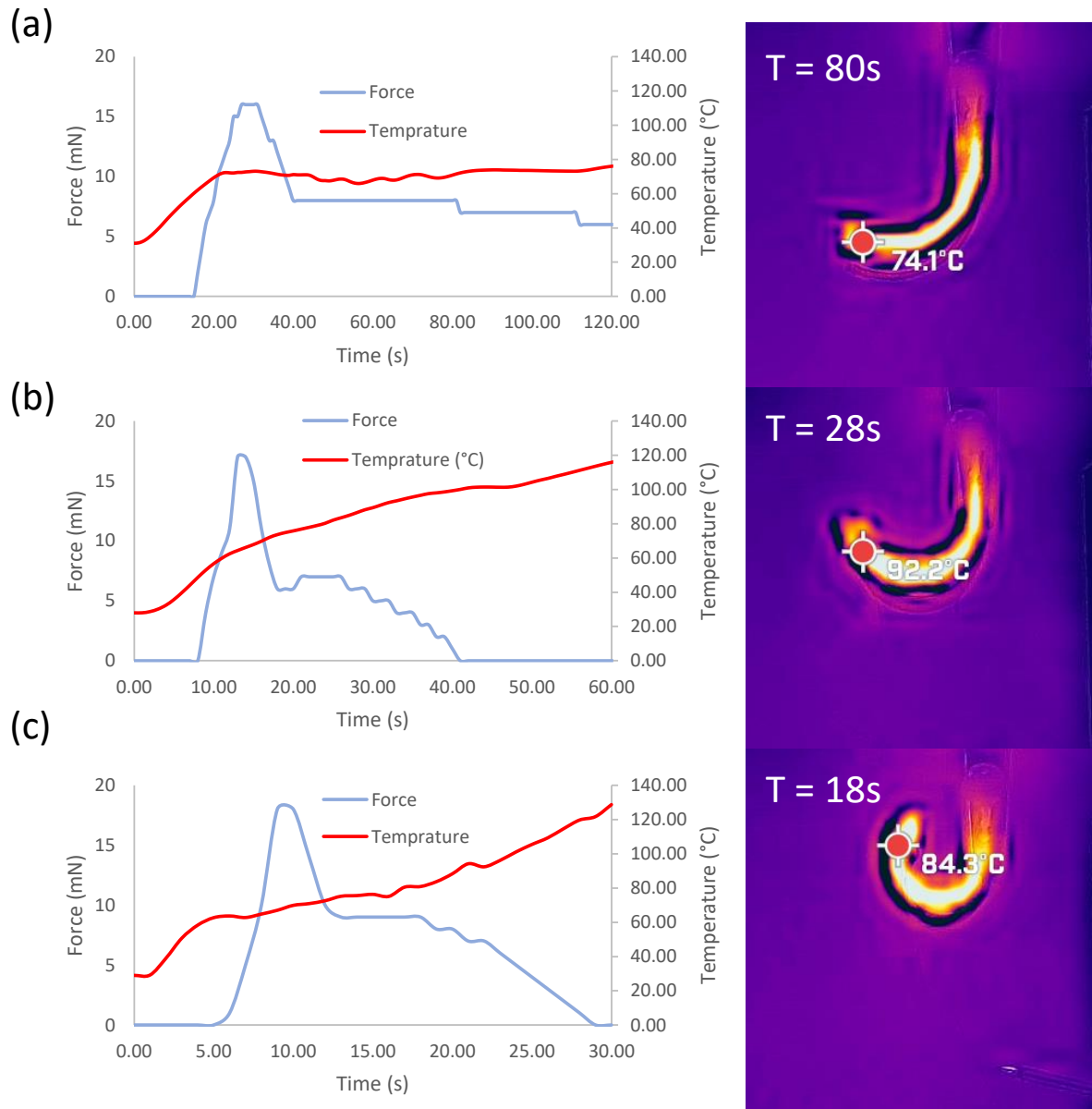
Figure 6.6. Thermo-mechanical experimental results of the actuators at the three different voltage values. (a) 40 V. (b) 50 V. (c) 60 V. Left: The Joule heating temperature and the resultant generated force by the actuator vs. time. Right: Maximum temperature achieved at maximum deformation by the actuator when activated using the corresponding voltage value.

The force standard deviation is less than 1 mN, which indicates the repeatability of the test, thus meaning that the force is caused by the voltage applied. This mechanism and the understanding of the force generated by the actuators can be used and controlled based on the application needed. Precise control of the electric stimuli can be used with a high degree of

144

freedom to manipulate the actuators. The deformation of the actuators can also be seen as a product of the temperature that is reached by the actuator.

The experiments showed repeatable results with standard deviation values below 3°. There are factors that can contribute to the slight variation of these tests, including the placement of the activation wire and contact with the alligator clip. In addition, the imperfections in the printing process cause the printed actuators to be unidentical. These factors might alter the flow of current through the actuator since the current flows through the path with less resistance. The resistance of the actuator also varies as the actuator gets heated up, this is reported in the literature to increase with the temperature [234], although is it concluded that this is not overall resistance, but the dominant path resistance. The overall resistance is then obtained by Ohm's law. Although this is the case, the current flow is increasing as the temperature rises, this could indicate a decrease in the overall resistance in the actuators.

The results of the deformation in each of the actuators are recorded and tracked in terms of *x*- and *y*-displacements of the actuator tip. These graphs are presented in **Figure 6.7**, where each activation temperature of 40 V, 50 V, and 60 V are presented separately in **Figure 6.7** (a), (b), and (c), respectively. The images of the actuators at each important point during the shape change are displayed under the graphs. The numbers in the graphs are displayed visually in the pictures under each graph. When the results in **Figure 6.7** are compared to the force measurements in **Figure 6.6**, it can be seen that the force is generated slightly after the deformation starting point. This should always be taken into account since some of the force profiles might not match the expected force generated because of the deformation of the actuators. This behaviour might be caused by many reasons, but most notably, the high temperature of the actuators, making them very rubbery. These observations agree well with the results presented in **Figure 6.6**. Thus, if the actuators are used in a device that requires applying force to manipulate or move an object, then the generated temperature should be limited to be below 100 °C since the generated force degrades beyond that point.
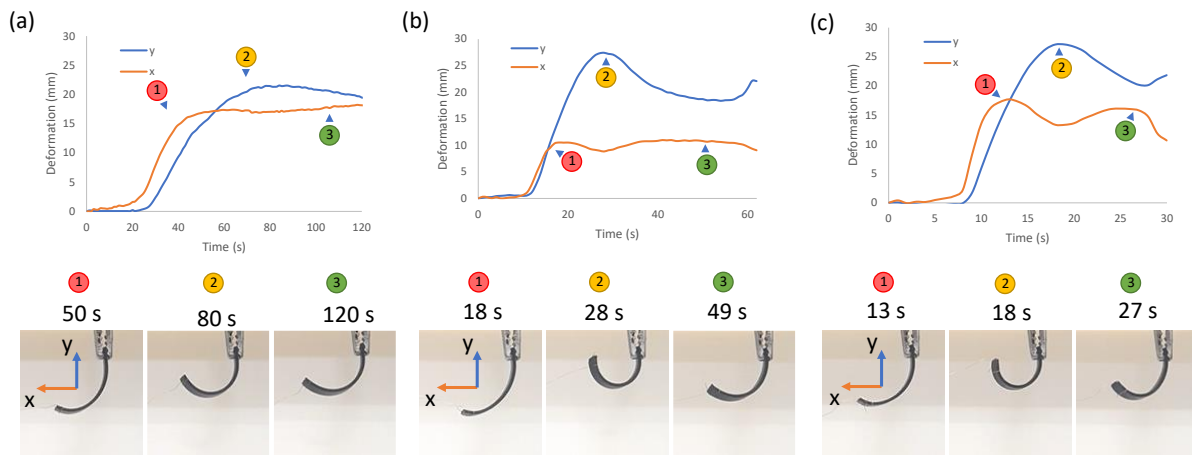
Figure 6.7. Deformation assessment of the actuators at activation voltages of (a) 40 V, (b) 50 V, and (c) 60 V. Top: The tracking results of deformation in the *x*- and *y*-directions. Bottom: Snapshots of the actuators during the deformation at selected timestamps.

The three points marked in the figure are the first peak of the *x*-direction, the peak of the *y*-direction, and the second peak of the *x*-direction. The first peak of the actuators is midway through the full deformation. This is the point at which the actuator is at its furthest distance to the side of deformation, which might offer advantages for certain applications. This point is marked with the red ①, which is the case for all three actuators. the distances ranged from 10 to 18 mm. The second point which is marked with the yellow ② is the highest distance in the *y*-direction, which is the closest point to the base of the actuator. It is also observed that for the tested actuators, it is at the peak of bending too. This might not be the case for stronger strain actuators, since they curl and reduce the *y*-displacement, which reached up to 27 mm.

The last point is the green ③, which is the point where the displacement is reduced because of the high temperature. The summary of the results of the tested actuators is summarized in **Table 6.3**. The compares different terms, where V_S is the activation voltage, P_{max} is the maximum power recorded before melting, T_{max} is the maximum temperature reached by the actuators, x_{max} and y_{max} are the largest *x*- and *y*-directions displacements. Moreover, θ_{max} is the largest achieved bending angle, and t_θ, P_θ, T_θ are respectively the time, power, and temperature at which the largest angle is achieved. Furthermore, F_{max} is the largest force recorded, and t_F and P_F are the time and power at which the largest force is achieved.

146

Table 6.3. Summary of the experimental results using different activation voltages.

V_S (V)	P_{max} (W)	T_{max} (°C)	x_{max} (mm)	y_{max} (mm)	θ_{max} (°)	t_θ (s)	P_θ (W)	T_θ (°C)	F_{max} (mN)	t_F (s)	P_F (W)
40	0.47	76.25	18.24	21.56	63.76	87.00	0.47	73.66	16.00	27.00	0.48
50	2.93	117.68	11.00	27.43	73.78	28.00	0.95	86.51	17.00	13.00	0.82
60	4.06	128.74	17.71	27.11	77.76	18.00	1.29	80.89	18.00	9.00	1.06

Upon evaluating all three activation voltages, it becomes evident that the maximum power recorded before reaching the melting point is closely related to the activation voltage, although the relationship appears to be nonlinear. At 40 V, the strain release occurs more gradually, leading to activation at a significantly lower power level, approximately eight times less than what is achieved at 60 V. When comparing the 50 V and 60 V actuators, both of which can cause the actuator to melt if left running, the higher voltage actuator exhibits greater power output without undergoing melting. This discrepancy could be attributed to the time it takes for the actuators to reach the melting point, allowing the higher voltage actuator to generate more power before this critical point is reached.
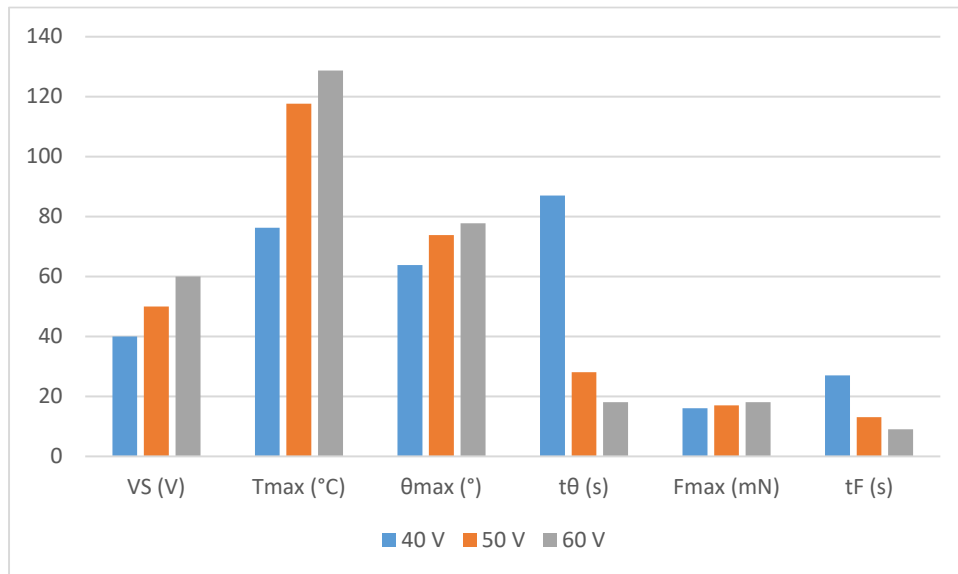
Figure 6.8. Summary of the Joule heating experiment results

The same trend is observed in the recorded temperature data. Which can be observed in **Figure 6.8**. A faster strain release results in a higher bending angle and greater force, potentially influenced by the time taken to release the strain. The higher rigidity during the initial activation phase and the speed at which bending occurs may contribute to the higher force output, as the same amount of strain is accommodated within a shorter time frame. This

effect is particularly noticeable in the time of maximum force, where the shortest duration is three times faster than the slowest one.

6.4.2 Joule-Heating Activated Manipulator

The actuators developed in this study were used to create a manipulator that is used to grip and move a small object along the *x*- and *y*-axes, as presented in **Figure 6.9**. The manipulator consists of three independent CB/PLA parts, a gripper made of two small fingers that are activated simultaneously, and two independent arms that deform in opposite directions along the *x*-axis. The fingers and arms are connected at both ends to copper wires using a 3D printing pen. The wires are connected to a DC power supply so that the desired arm or fingers can be activated independently. The manipulator is assembled by inserting the conductive parts into slots on links printed using PLA. Then, the manipulator is suspended vertically by fixing its top link to a test rig.
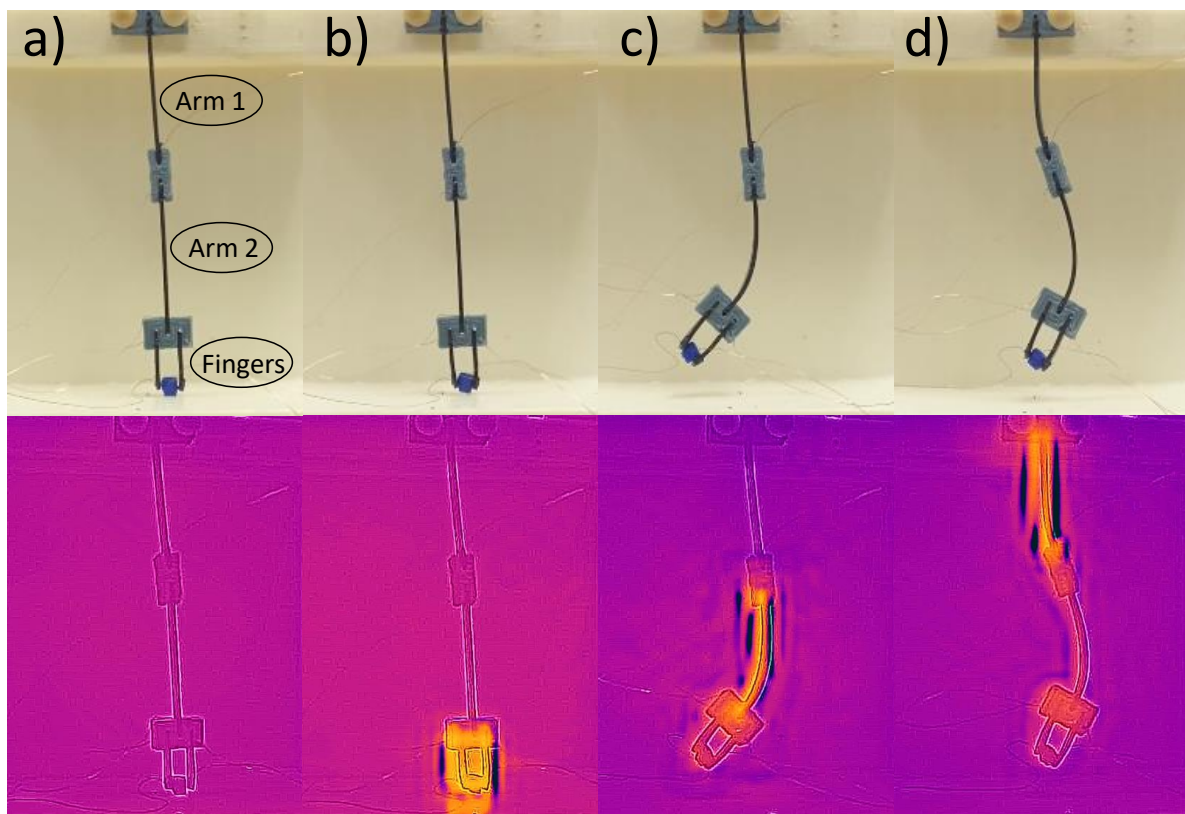
Figure 6.9. Optical and thermal results showing the sequential activation of the parts of the manipulator using Joule heating. (a) Initial shape before activation. (b) Activation of the fingers of the gripper. (c) Activation of Arm 2. (d) Activation of Arm 1.

Figure 6.9 (a) – (d) shows the activation of the manipulator at three different activation points, which are Arm 1, Arm 2, and the fingers. These points are marked as such in the undeformed manipulator shown in **Figure 6.9** (a), shown in both optical and thermal imaging. The voltage for each arm was fixed to achieve maximum deformation without burning. This was chosen to be 60 V for each of the arms, and 30 V for the fingers. **Figure 6.9** (b), shows the manipulator with the fingers activated to grasp a small object, the fingers are activated and left for a few seconds after activation without heating to cool down and grasp the object. As the fingers are soft and mendable when heated and might drop the object. **Figure 6.9** (c) and (d) present the activation of the directional arms, which are activated in the same process of heating and them allowing to cool. The arms and fingers can be activated simultaneously, but a separate actuation was done to assess the effect of each deformation on the carried object.

The bottom images in **Figure 6.9** show the same manipulator in activation in thermal imaging of the sequential activation of each of the sections of the manipulator. Between every activation, the arms are allowed to cool down. This is done to prevent any deformation caused by the movements of other arms which may cause unwanted deformation in the soft hot material. When comparing thermal and video pictures, the effect of each activation is seen very clearly, as the heating of each actuator is isolated. The heating in the fingers does not leak into the arm above it, and so on between the two arms. This is a good indication of the usability of this technique in local activation.

The deformations of the manipulator are very controllable, and based on previous testing of the actuators, different activation voltages can be used to control many aspects of the manipulator. Certain factors, such as the speed at which the actuators activate can be controlled by the activation voltage. This means that the force is controlled as well. Because of the weight that each arm is moving, their behaviour changes, such as the bending angle possible and the amount of force generated in a certain direction. This explains why the deformations in the actuator's arms are smaller than when they were tested without any weight on them.

The force in the fingers is measured to have a peak of 6 mN, while the lower arm (marked Arm 2) peaks at 5 mN, and the upper arm (marked Arm 1) had a peak force of only 3 mN. This is a much smaller force generated by the actuator in one direction, this seems to be because of the weight that each arm carried. The highest force is recorded by the small

gripper, The measured 6 mN is expected as these grippers are much smaller than the other actuators. The two long arms which change the position of the gripper head seem to be dependent on the weight they are moving, the more the weight the lower the force. As Arm 2 carries the weight of the gripper head, which consists of the gripper arms and their holder, lowering the force that is produced in the bending direction. Arm 1 carries Arm 2 along and the holder between them, alongside the rest of the manipulator, rendering its directional force the lowest.

The activation displacement of the manipulator is assessed by the three sections for each actuator, as displayed in **Figure 6.10**, which is a plot of the displacements recorded at the top of each section. The purpose of tracking each actuator is to divide the effects of the stimuli on each section, thus tracking each arm throughout the process. This also allows for the recording of the collective manipulation of the carried object.
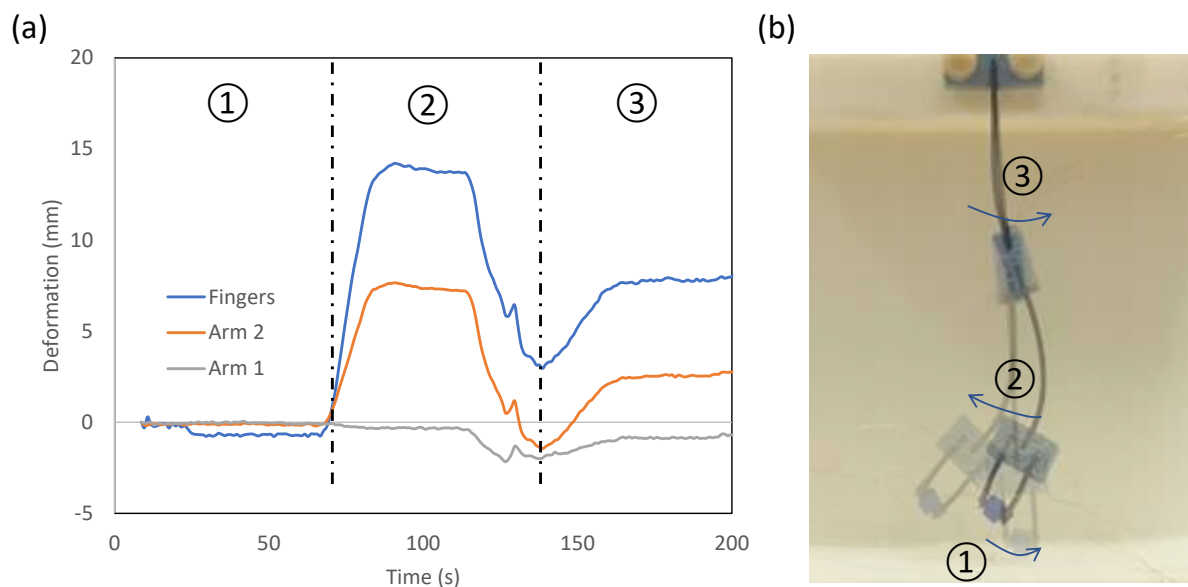
Figure 6.10. Deformation of the fingers of the gripper and the arms in the *x*- and *y*-directions. (a) Deformation vs. time with three main regions showing the activation of each part of the manipulator. (b) Stacked photographs showing the final displacement of each sequential activation that is presented in (a).

The displacement measurement in **Figure 6.10** (a), which is marked in blue, was made following one of the fingers that is carrying the small object to demonstrate the effect that the gripper imposes on whatever it manipulates. As seen in the figure, the object is gripped by the arms, shown in **Figure 6.10** (b), which is indicated by ① in the graph and

picture. At this point, the object is not moved, but it is grasped by the arms, the force generated is measured by 6 mN on each side.

The is a slight displacement in the fingers in the negative *x*-direction, which indicates the grasping mechanism, which is experienced on both fingers in opposing directions. The gripper is allowed to cool down for 20 seconds by removing the voltage supply to the arms. The arm that holds the gripper holder (Arm 2) is activated based on the timing of the actuators as tested in the previous section, the displacement of the holder is clearly seen to have moved about 7.5 mm in the positive *x*-direction, which translates to a displacement of the gripper fingers by about 14 mm. This is much smaller than the displacement experienced on the actuator when free of weight which was about 18 mm in the *x*-direction. The arm again is allowed to cool down for 20 s, before activating the third and final arm. The activation of the third arm caused a larger displacement in the fingers, although it deforms at a much smaller rate than the arm before it, but this is because the distance of the object is further from the actuator thus experiencing a larger displacement.

6.5   Development of Printing Speed Controlled Actuators

During the printing process, the passive layers were printed at a speed of 10 mm/s, while the active layers were printed at four different speeds: 20 mm/s, 40 mm/s, 60 mm/s, and 80 mm/s, yielding four distinct actuators. To facilitate the printing process, the nozzle temperature was set at 180 °C, and the bed temperature was maintained at 50 °C. Activation of the printed actuators was accomplished through Joule heating. Each sample was connected to a DC power supply with a voltage rating of 30 V and a current of 130 mA, using thin wires. This method of activation highlights the efficiency of these actuators in terms of power consumption when compared to alternative actuators like SMA actuators. The current was gradually increased until it reached its maximum value of 130 mA. Once the temperature reached 80 °C, the power supply was promptly turned off

The printing speed of the active layer has been shown to have a significant impact on the bending performance of 4D-printed actuators. Higher printing speeds for the active layer result in greater strain being stored within the actuators. In this study, C-PLA was employed to print actuators at varying printing speeds to achieve different bending angles. Specifically, the active layers of the actuators were printed at speeds of 20 mm/s, 40 mm/s, 60 mm/s, and 80 mm/s, while the passive layers were printed at a consistent speed of 10 mm/s.

The heating process was conducted rapidly, considering the resistivity of the material used, and the current was limited to 130 mA. The samples took approximately 71 seconds to heat up from 29.5 °C to 80.7 °C, allowing for the analysis of bending over a short period of time. The thermal camera was employed to record the actuator during activation, enabling the assessment of temperature changes as the actuator underwent deformation. Importantly, this approach allows for the examination of actuation occurring at temperatures below Tg for further analysis.

The gradual heating of the actuator is shown in **Figure 6.11** with the time stamp and temperature values. In this figure, the active layers of the actuator were printed at the highest speed of 80 mm/s, to demonstrate the largest bending angle possible in such an actuator. Full deformation was observed at the maximum temperature after 71 seconds. Visible deformation started at 14 seconds from current input, at a temperature of about 62°C, which is at T_b.
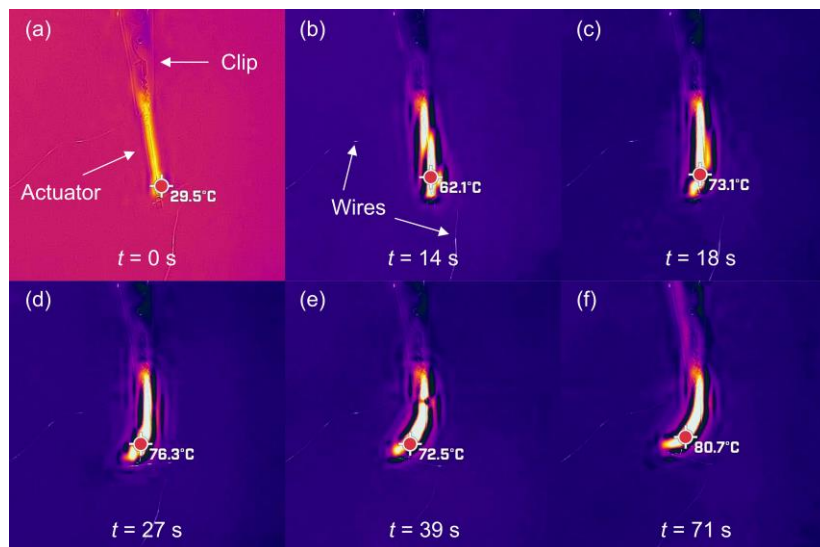
Figure 6.11. Thermal images of the Joule heating results of C-PLA actuators at different timestamps. The active layers of the actuator were printed at a speed of 80 mm/s

Approximately 39 seconds after activation, a slight decrease in temperature was observed, despite maintaining a constant supply current and voltages. These fluctuations could be attributed to various factors, including potential issues with the contact between the conductive wires and the actuator. As the actuator's shape changes due to the SME, there may be instances where the wires lose some contact, resulting in a temperature drop.

Furthermore, the FDM process used for printing may introduce slight variations in material distribution. This can occur due to factors like the quality of the filament used or minor deviations in the printed lines, often stemming from machine inaccuracies or vibrations

during the printing process. These combined factors can contribute to temperature irregularities during actuation. In **Figure 6.11**, it can be seen that the drop in temperature stopped after a few seconds and stabilized at about 80 °C. The bending of the actuator reached a steady state at that level, as shown in **Figure 6.11**(f).

The Joule heating process was repeated for all the samples, using the same steps. The results of activating the actuators printed using the four-printing speed are presented in **Figure 6.12**. The figure clearly illustrates that the bending of the actuators is directly proportional to the printing speed. Specifically, when employing printing speeds of 20, 40, 60, and 80 mm/s for the active layers, the resulting bending angles of the activated actuators were 13°, 19°, 26°, and 32°, respectively. This outcome aligns with the observed impact of printing speed on actuator behavior, consistent with findings in other studies. The actuators in **Figure 6.12**(a) – (c) are smooth transitions in bending, but there is a slight twisting in the actuator in **Figure 6.12**(d). Despite the twist observed in the last actuator, it is noteworthy that the overall bending angle behavior still follows the expected trend, increasing with higher printing speeds. This suggests that while there may be irregularities in the actuation, the fundamental relationship between printing speed and bending angle remains consistent.

(a)   (b)   (c)   (d)
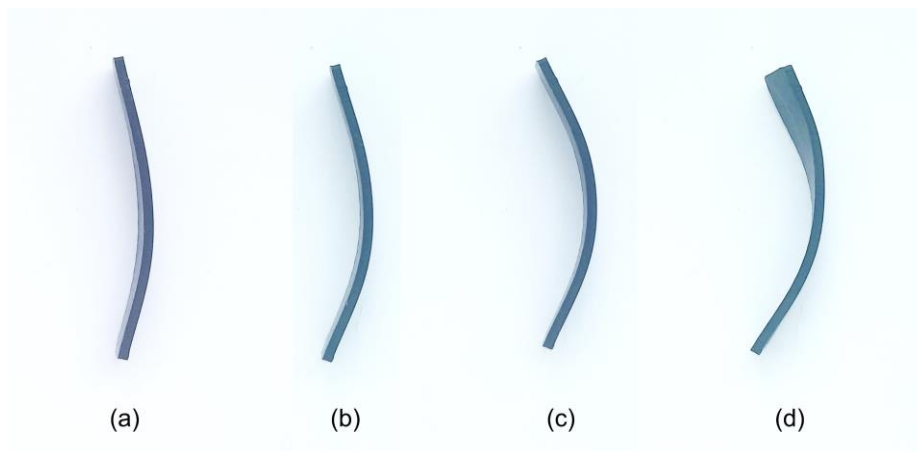
Figure 6.12. Activated actuators that were printed at different printing speeds for the active layers. (a) 20 mm/s. (b) 40 mm/s. (c) 60 mm/s. (d) 80 mm/s

Table 6.4. Printing parameters and actuation results

Actuator	S_{pp} (mm/s)	S_{pa} (mm/s)	θ (°)	t_s (s)
1	10	20	13	85
2	10	40	19	82
3	10	60	26	69
4	10	80	32	71

The actuation results of each actuator are summarized in **Table 6.4**. The table presents the printing speeds used to print the layers of the actuators, where S_{pp} and S_{pa} are the printing speeds of the passive and active layers, respectively. In addition, the corresponding bending angle (θ) and settling time (t_s), which is the time required to reach a steady-state temperature, are summarized in the table. As previously mentioned, it is evident that the bending angle increases in correlation with the printing speed of the active layers. Additionally, it is worth noting that the actuators exhibit a shorter settling time as the printing speed of the active layers increases, with the exception of the 80 mm/s speed.

The reduction in settling time may be attributed to the increased strain induced by stretching the filament as the printing speed rises. This strain leads to a minor change in the diameter of the extruded filament, thereby increasing resistance. Consequently, the effect of Joule heating becomes more pronounced. Moreover, the strain causes a re-orientation of carbon black particles within the filament, altering the conductive network and influencing the filament's conductivity. However, the behavior of the last actuator differs from the others. Its slight delamination of the active layers may have resulted in a non-uniform flow of current within the actuator, contributing to this distinct behavior.

As previously discussed, the activation of most Shape Memory Polymers (SMP) typically occurs in a heated liquid environment due to its ease of activation. However, utilizing electrical current for heating offers several advantages, bringing prototypes closer to practical applications. With Joule heating, it becomes possible to achieve local activation of the actuators without the necessity of a specific environmental setup. Additionally, Joule heating allows for precise control of the actuator's temperature, enabling the creation of controlled actuators that can be employed in various designs and applications. Examples include grippers, moving micro-stages, and a wide range of engineering and medical applications.

6.6   Summary

The response of Joule heated actuators is tested and analyzed in this study, this is done by electrical analysis, simulation, and video tracking of the actuators. The actuators show a direct relation between the activation voltage and the peak bending angle with a controllable bending angle between 63° to 80° using the tested activation voltages, controllable by adjusting activation time. The activation time for each actuator is limited as

the current increases exponentially beyond a certain temperature, causing the actuators to burn.

The force of each activation voltage varies too, increasing from 16 mN to 18 mN, this means that the voltage can be used to control the force generated and can be used for certain applications where force limiting is needed. The experimental tests were also validated by simulation of the thermal response of the actuators to the stimuli, to test for the Joule heating effect, temperature rise of the actuators, and deformation.

The simulation data tallies with the practical tests in terms of time-dependent temperature due to Joule heating. The tested designs are used to create a three-section manipulator which grips an object and can displace it according to the order of activation in the sections. This manipulator, much like the actuator, is controllable with a displacement range of up to 14 mm and up to 10 mm in the reversed direction. Further work into Joule heating should explore the ability of these actuators to reverse their shape change, which will be more helpful in the field of robotics and multi-use actuators.

Further control of the actuators can be made to provide better capabilities for designs. Further structural changes can be made to allow non-linear movements of deformations, which help in non-uniform shape change requirements. Furthermore, more than one shape change can be made into a single actuator, this can be made by many means. Certain design criteria can be made to induce multiple shapes into one actuator, which can be achieved at different activation temperatures.

Chapter 7: Testing Concepts in Structure Manipulation and Thermal Dependence

7.1   Introduction

This chapter presents work on further concepts in 4D printing, the first being a section on the twisting behaviour of actuators, and the second is on thermal-dependant actuation. The use of the actuator as a testing application allows for the recording of the print setting and its effect, which in turn ensures more accurate measurements of the predicting process of the SME. The use of more complex structures and applications can prove to be difficult for the purpose of testing and measuring the stimuli response. Such complexity makes it hard to replicate in simulations, making it a challenging task.

In the first section of this study, the testing of the effects of printing direction on the deformation of PLA actuators after heating to activate their SME is done. The actuators are all printed at the same parameters such as printing speed, temperature, and layer height. Then, a gripper was developed based on these actuators. The results show that the gripper provides the ability to grip an object with a cylindrical shape. The second section is on multi-shape actuation in a single material, The section presents multi-shape actuation using printing parameters and temperature-dependent activation of single-material actuators. The contributions of this chapter for both sections are as such:

- Twisting behaviour control in actuators by manipulating the angle of the printed lines, producing twisting control.
- A novel temperature-dependent method for multi-shape actuation in a single-material structure.
- Development of layer sandwiching printing method which isolated deformation in different bending directions

7.2   Twisting via Print Direction

This section presents a method of inducing twisting behaviour in the actuators, with a high degree of control in the required twisting rate. The results are analysed and presented, with a proof-of-concepts design for a gripper that uses this twisting behaviour.

7.2.1 Design and Working Principle

The actuators were designed with dimensions of 30 mm × 8 mm × 1 mm for the length, width, and height, respectively. The printing settings used in this chapter are summarized in **Table 7.1**. The difference in the printing speeds between the first layer and the other layers provides a higher strain in the actuator between the layers, allowing higher deformation angles. This is presented in many supporting works [42], [43], [44].

In addition, the use of a low printing speed for the first layer also helps with the adhesion of the PLA to the glass bed that it is printed on. The angle of the print was varied from 0° to 90°, measured parallel to the length of the actuator. The angle was varied at a rate of 15°, thus presenting 7 different printing angles (PAs). Each printing angle was printed and tested 3 times for repeatability measurements, thus measured data was recorded as the mean and standard deviation of 3 samples.

Table 7.1. Printing parameters of the actuators

Parameter	Values
Number of layers	10 layers
Layer height	0.1 mm
Printing speed of layer 1	10 mm/s
Printing speed of layers 2 – 10	60 mm/s
Printing temperature	200 °C

The assessment of the degree of deformation of actuators is usually made by the bending angle (φ) of the actuator after activation. However, since the actuators twist in a helical manner, the helix angle (α) was also used to assess the degree of SME in each actuator, as shown in **Figure 7.1**. The helix angle is found using the following formula:

$$\alpha = tan^{-1}(L/C) \tag{7.1}$$

where L is the lead of the helix or the vertical distance that is achieved by a full rotation of the helix, while C is the circumference of the helix. These parameters can be calculated from the shapes formed by the actuators after twisting, as shown in the following equations:

$$L = (360/\theta) \times H \tag{7.2}$$

$$C = (360/\theta) \times L_{arc} \tag{7.3}$$

where H is the distance of deformation of one edge of the actuator as compared to its original position, and L_{arc} is the arc length, which can be found using the radius of bending (R) and the angle formed by the arc of the actuator (θ).
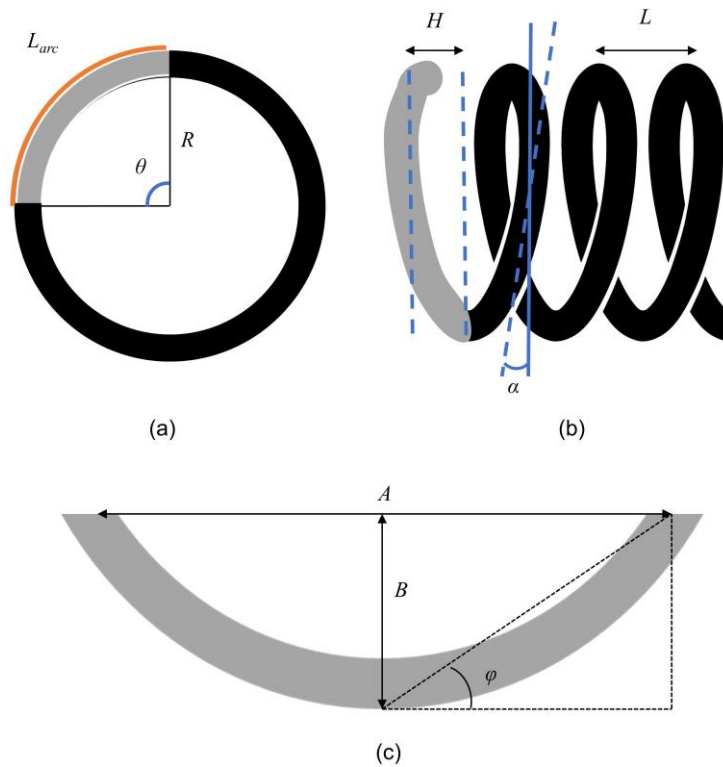
Figure 7.1. Bending and twisting measurements. (a) Top view of a helix shape. (b) Side view of the helix with the lead of helix. (c) The measurements taken from the tested actuators

7.2.2 Fabrication and Characterization

In this work, the filament used is PLA with a standard density of 1.24 g/cm³ (1.75 mm, 1.0 kg Gray, Flashforge 3D Technology Co., Ltd., Zhejiang, China). The 3D printer used is an FDM printer (Ender-3 V2, Creality 3D Technology Co., Ltd., Shenzhen City, China). Thermal analysis of the material was carried out to assess its activation.

The experimental setup used in this chapter is the same as that presented in **Figure 3.1** (a). The 3D designs were transferred to a 3D printing software (Simplify3D). All the parameters were set in the software. Then, the files were transferred to the printer to start printing. After completing the printing process, the actuators were then left to cool down to room temperature. After that, they were placed in a heated water medium of 85 °C until full

deformation was achieved. The actuators were then taken out and left to cool down to perform measurements using a digital caliper according to **Figure 7.1**.

7.2.3   Results and Discussion

The tested actuators are shown in **Figure 7.2**, where the actuators are presented in three views for each printing setting. In each case, the original undeformed actuator as printed, and the top and side views of the activated actuator are shown. As can be seen in **Figure 7.2**, the twisting effect seems to rise with the increasing printing angles, and peaks at a printing angle of 45°. The twisting rate reduces as the angle approaches 90°. Thus, the twisting is maximized in a diagonal direction where the strain-release forces are equal in the *x*- and *y*-directions.
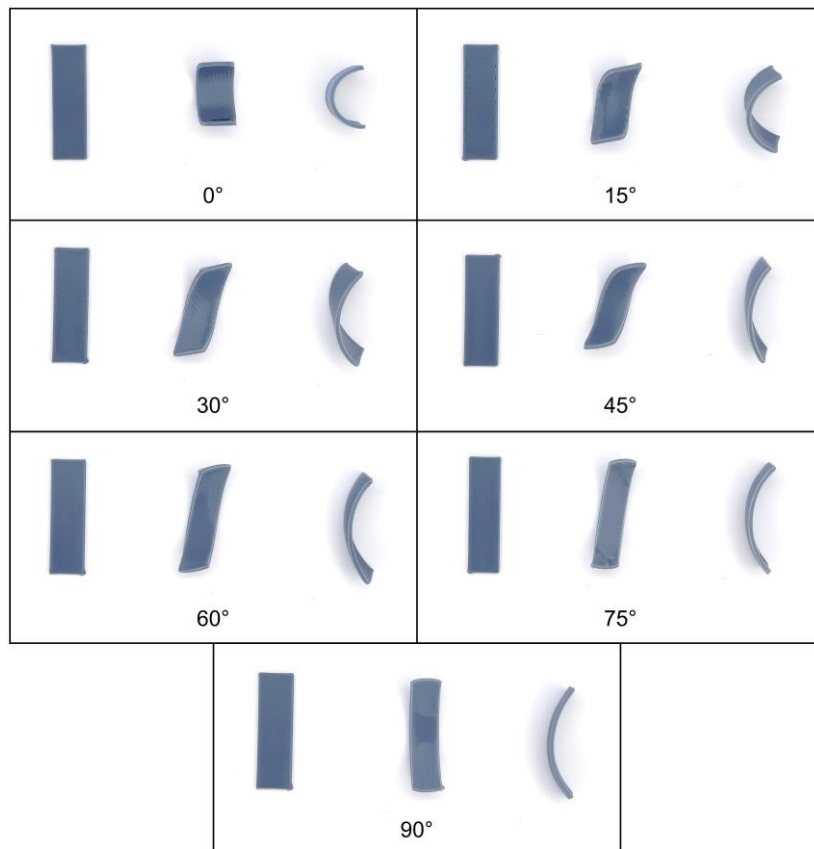
Figure 7.2. Printed and activated actuators using different line angles ranging from 0° – 90°. Left to right: printed top view, activated top view, and activated side view

Table 7.2. Measured parameters of the actuators.

PA (°)	*A* (mm)	*B* (mm)	*T* (mm)	*H* (mm)
0	16.02±0.25	7.65±0.12	9.19±0.27	0.00±0.00
15	17.84±0.07	6.57±0.05	8.39±0.05	6.23±0.07
30	20.88±0.04	4.68±0.12	7.73±0.11	7.67±0.17
45	24.51±0.07	4.78±0.05	7.05±0.06	11.22±0.08
60	25.79±0.05	5.97±0.11	6.79±0.07	7.93±0.03
75	26.83±0.03	6.60±0.06	6.60±0.06	5.09±0.03
90	27.49±0.19	7.16±0.06	6.27±0.07	0.00±0.00

The data measured are presented in **Table 7.2**, including the measurements of parameters *A* and *B*, which were presented in **Figure 7.1** (c). These parameters are utilized to calculate the radius of rotation and bending angles used in assessing the twisting angles. The thickness (*T*) of the actuators reduces as the angles increase. At 0°, the thickness of the actuator has expanded slightly, as compared to the undeformed actuators. This increase in thickness is caused by the expansion in the *y*-direction as the *x*-direction shrinks, which is seen clearly in **Figure 7.2** at 0°.

The shrinking of the actuator is parallel to the printed lines, while the expansion is perpendicular to the printing lines. This is shown clearly in the 0° actuator since the lines are across the whole length of the actuator, but it can be assumed that it is acting in each line. This means that expansion in the lines happens perpendicular to the lines of print in all actuators. This might not be observable since the lines are at an angle that is not affecting the length or width directly.

On the other hand, this behaviour is observed in the 90° actuator. This actuator is the thinnest of all angles, which aligns with the behaviour as the lines are printed perpendicular to the length. Moreover, the *H* parameter (see **Figure 7.1**) can be used to assess the degree of twist in the actuator by finding the lead of the helix. The parameters measured in **Table 7.2** are used to assess the twisting rate of each printing angle, as shown in **Table 7.3**.

Table 7.3. Calculations used in the assessment of the degree of twisting in the actuators.

PA (°)	φ (°)	L_{arc} (mm)	θ (°)	C (mm)	L (mm)	α (°)
0	43.68	24.45	174.70	50.37	0.00	0.00
15	36.39	23.72	145.55	58.68	15.41	14.71
30	24.16	23.58	96.62	87.86	28.56	18.01
45	21.32	26.93	85.30	113.64	47.37	22.63
60	24.86	29.33	99.43	106.20	28.71	15.13
75	26.20	30.97	104.80	106.38	17.49	9.33
90	27.53	32.20	110.12	105.34	0.00	0.00

The bending angle shows how tight the ending circle is, thus indicating a stronger deformation in the actuator. This is used widely to assess the SME of the materials or prints and is an indication of the strength of the direction strain in the materials [88]. The helix angle is the final parameter that is used to assess the twisting rate. As presented in **Figure 7.2**, the actuator with a printing angle of 45° has the highest helix angle, or the highest twisting rate. Using these parameters and measurements above, specific designs that might benefit from twisting can be made.

Figure 7.3 (a) shows that the thickness decreases linearly when varying the printing angle. This happens as the printing lines are perpendicular to the length of the actuator, causing shrinking across them. The arc of the helix shown in **Figure 7.3** (a) is affected by both the length of the actuator after deformation and the helix angle as larger ones will make it smaller, but as seen in the graph, the arc keeps increasing beyond 30°. This is because the effect of the shrinking is being reduced, coupled with smaller helix angles.

As is seen in **Figure 7.3** (b) the helix angle increases as the direction approaches 45° and then reduces. This influences the circle of the helix, as the higher the angle the smaller the circle appears since they are limited in length. Despite that, as the angle approaches 90°, there seems to be a smaller effect on the circumference of the helix. This is because those actuators maintained their length better, with limited shrinking.
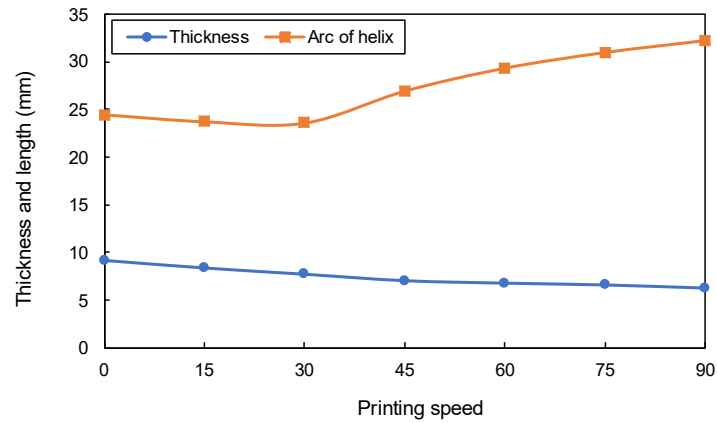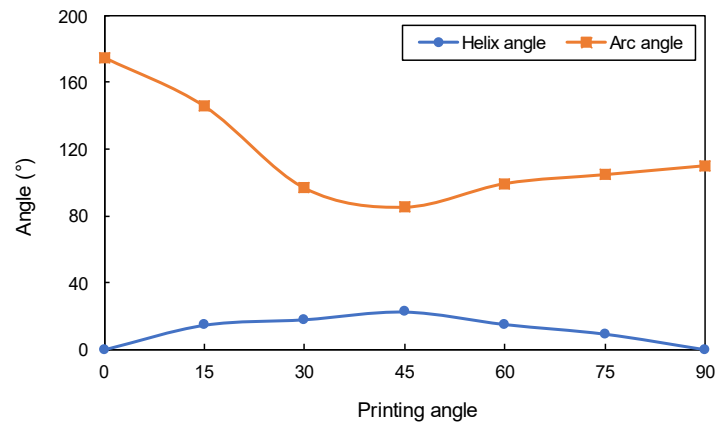
Figure 7.3. Graphical representation of notable characteristics that are influenced by the printing direction angles (a) Thickness and arc length. (b) Helix and arc angle

The actuator with a print angle of 45° was used to create a gripper as a proof-of-concept design for using the twisting mechanisms. The gripper presented in **Figure 7.4** (a) is the gripper before and after deformation. To make the gripper grasp a cylindrical shape, it must twist in opposite directions, thus the actuator directions are flipped but kept at a 45° printing angle. In addition, the twisted gripper arms are shown in **Figure 7.3** (a) without grasping any object to show the full deformation of the gripper.
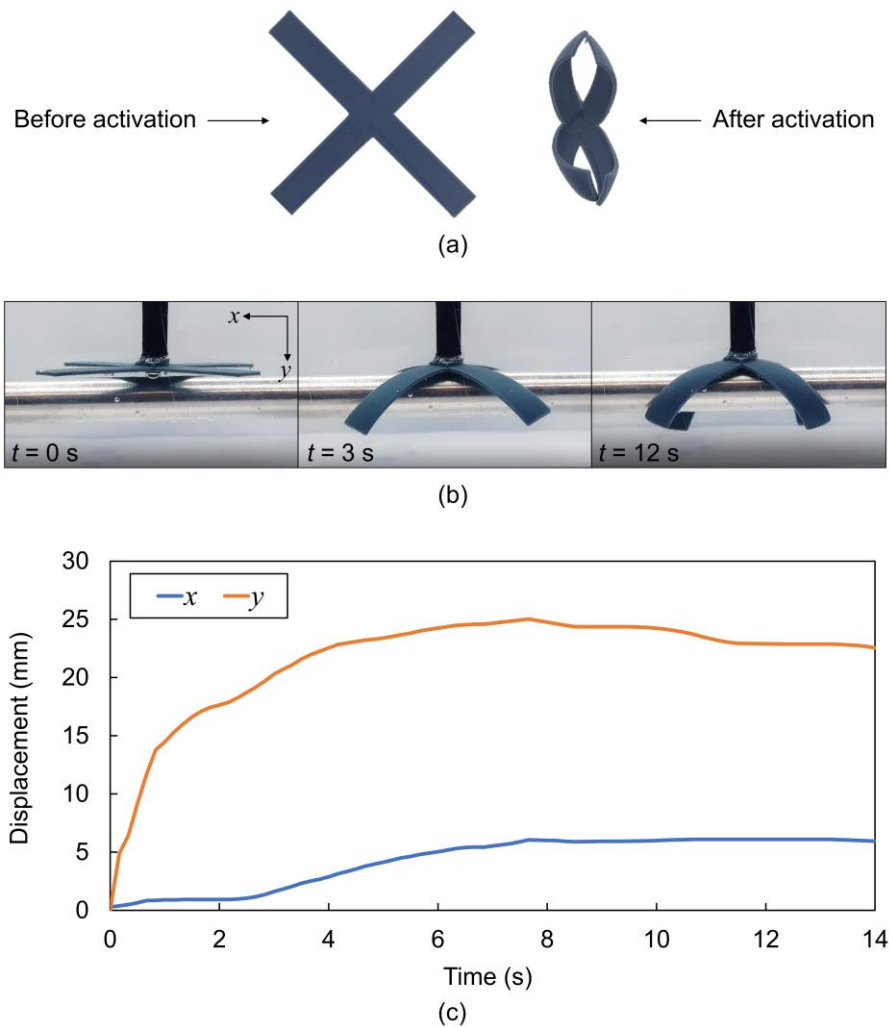
Figure 7.4. A gripper designed with four 45° actuators. (a) The gripper before and after activation. (b) The gripper used to twist around a metal cylinder to grip it. (c) The tracking of the movement of the arm of the gripper in the *x*- and *y*-directions.

The images in **Figure 7.4** (b) show the gripper used to twist around the metal cylinder. This grasping mechanism cannot be achieved when printing at 0° since the arms would fold in one direction not being able to hold the cylinder. It can be seen in **Figure 7.4** (b) that the arms appear to move upward slightly due to the twisting around the cylinder, causing the peak in the graph shown in **Figure 7.4** (c).

The full deformation of the gripper took around 12 seconds, while 89.30% of the deformation took place in the first 3 seconds. This can be seen clearly in **Figure 7.4** (c), which shows the tracking of the gripper in action. This was done as displacement in the *x*- and *y*-directions tracked from the side using a camera and a motion-analysis software (Kinovea). The arms moved around 5 mm in the *x*-direction as most of their movement is twisting. In the *y*-

direction, the gripper arms move about 25 mm before fully grasping the metallic cylinder and reaching a steady-state value of 22.60 mm. This can be seen at around 8 seconds, where the *y*-direction displacement has reduced. This is due to the arms moving around the cylinder to twist and grab it, thus seemingly moving upward from the side view.

The results presented in this chapter prove that the proposed concept is suitable for robotics applications, especially those that involve gripping cylindrical objects underwater. In addition, the gripper can also be activated using hot air sources, making it usable in various applications where other types of grippers cannot operate due to temperature constraints. The performance of the gripper can be further improved by using different materials, such as graphene-PLA. This will consequently allow activating the gripper using electricity based on the Joule heating concept [81]. Therefore, the application environment can be further expanded using this approach since the gripper will not need hot water to be activated.

7.3   Thermal Dependent Actuation

This section presents a novel method of achieving sequential shape change in a single-material actuator. The actuators are activated gradually, and different layers of the actuator affect the shape of the SME at different temperatures. The actuators are made with layers printed in horizontal lines sandwiched by layers printed in vertical lines. These can be observed when each of the horizontal or vertical layers is activated since they deform in different directions. This shape change is observed on either the x-axis or the y-axis, as each layer can only act on one axis. This effect is also further analyzed by increasing the ratio of horizontal line layers to vertical line layers to assess the activation temperatures of each layer.

7.3.1   Materials and Methods

PLA filament (1.75 mm, 1.0 kg Gray, Flashforge, Flashforge 3D Technology, Co., Ltd.) was used in this study. The thermal properties of this material were tested using a dynamic mechanical analysis (DMA) machine (DMA 8000, Perkin Elmer). The results of the thermal testing are shown in **Figure 7.5** (a). The glass transition temperature appears to be between 52 °C and 90 °C, and peaks at around 74.12 °C, where deformation of the materials upon activation can happen along this range.
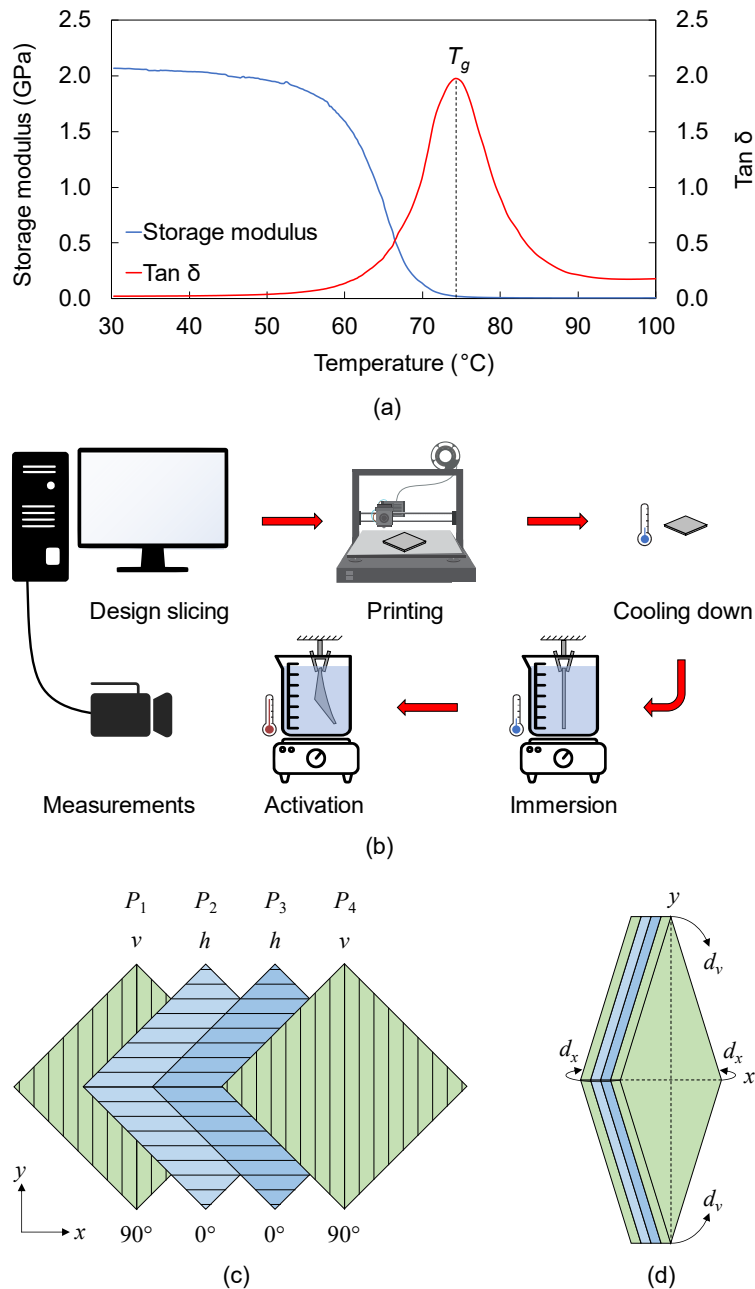
Figure 7.5. (a) DMA results of the PLA. (b) Fabrication process and experimental setup. (c) Exploded top view of the parts of the actuator. (d) Isometric view of the actuator.

The experimental setup used in this section is shown in **Figure 7.5** (b). The actuators were designed and sliced using Smiplify3D before being transferred to the printer. The printed actuators were removed and heated gradually in water from 25 °C to 85 °C for 840 s at a rate of 4.29 °C/min. The temperature was measured using a temperature sensor, and the deformation was recorded using a digital camera. The videos were then analysed using Kinovea software to track the deformation.

The actuators consist of four parts ($P_1 - P_4$ in **Figure 7.5** (c)) that were printed using different raster angles (*RA*). The raster angle refers to the direction of the printed lines, whether in the X or Y direction. The actuators comprise four distinct sections, designated as the bottom and top parts, printed with a 90° raster angle to create vertical-line layers (*VLL*), and the middle sections, printed with a 0° raster angle to produce horizontal-line layers (*HLL*). Both the bottom and top parts consist of an equal number of layers (v), while the middle parts consist of an equal number of layers (h).

All components were printed with a 100% infill ratio, a 0.1 mm layer height, a nozzle temperature of 190 °C, and a printing speed of 70 mm/s. However, an exception was made for P3, which was printed at a slower speed of 20 mm/s. This adjustment aimed to minimize strain in P3 compared to P2, ensuring that the horizontal deformation (d_x) predominantly occurs toward the bottom portion of the actuator. Simultaneously, the reheating process of the layers directs the vertical deformation (d_y) towards the top part of the actuator, progressively leading to higher induced strain values in the upper layers compared to the lower layers [235].

The difference in the *RA* ensures that *VLL* and *HLL* have orthogonal deformations, where the deformations along the *x*- and *y*-axes (d_x and d_y) are mainly caused by *HLL* and *VLL*, respectively, as shown in **Figure 7.5** (d). Furthermore, this approach allows the observation of the exact temperature at which the *HLL* and *VLL* are being activated.

Three actuators with dimensions of 30 mm × 30 mm × 1.6 mm were printed using the aforementioned printing parameters. However, each actuator was printed using a different ratio of sandwiched *HLL* to *VLL*. Since each pair of P_1 and P_4, and P_2 and P_3 have an equal number of layers, then the ratio of layers in P_1:P_2:P_3:P_4 or *v*:2*h*:*v* can be varied while maintaining a total of 16 layers in each actuator. Actuators 1 – 3 were printed with ratios of 3:10:3, 4:8:4, and 5:6:5, respectively.

7.3.2 Results and Discussion

The deformations of Actuators 1 – 3 along the *x*- and *y*-axes are presented in **Figure 7.6** (a) – (c), respectively. In all actuators, the deformation caused by *VLL* (marked ①) starts at 288 s, while there is a delay in the deformation caused by *HLL* (marked ②). This delay increases when increasing the number of *VLL* since more time is required for the inner *HLL* to reach the glass-transition range.

In addition, a higher number of *VLL* means that a lower number of *HLL* is releasing the induced strain, which increases the delay in the deformation. The value of d_x reaches its first peak at a timestamp ③ and then to its maximum value at a timestamp ④. Similar to the previous observation, it can be noted that these peaks require more time to be reached when increasing the number of *VLL*. On the contrary, the maximum d_y value (timestamp ⑤) is observed to occur earlier when increasing the number of *VLL* since a higher number of *VLL* is contributing to the overall deformation. Negative d_y values were observed in Actuator 1 between timestamps ② and ③, as shown in **Figure 7.6** (a). This is caused by the rapid increment in the d_x value between those timestamps, which pulls the actuators towards the opposite direction.
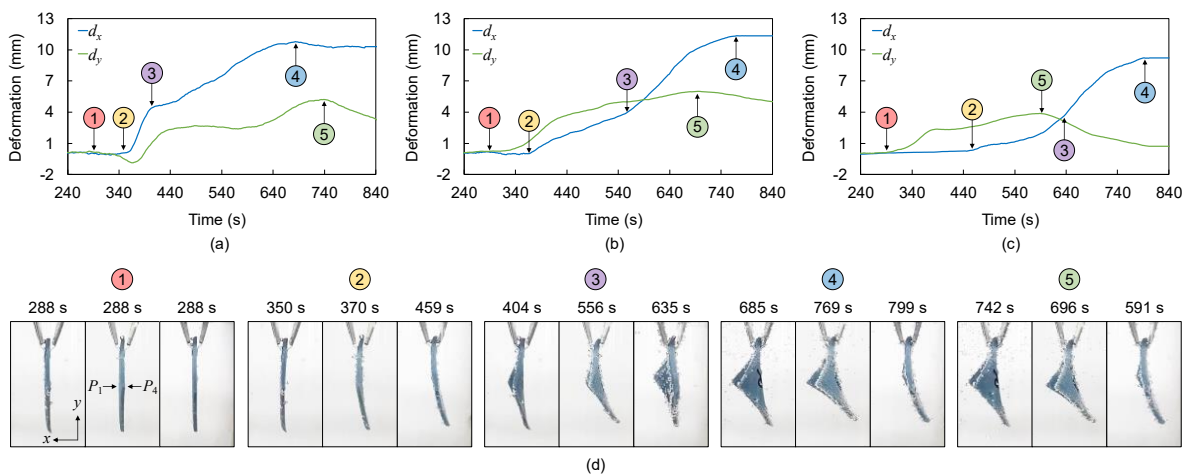
Figure 7.6. Temperature-dependent actuation results starting from 240 s. (a) – (c) d_x and d_y values during the experiments. (d) Snapshots of Actuators 1 – 3 (from left to right) at timestamps ① – ⑤.

Maximum deformations occur when the number of *HLL* and *VLL* is equal (Actuator 2), which allows *HLL* and *VLL* to have balanced effects on the deformation. Moreover, it can be seen that d_x values are higher than d_y values in all actuators. This is caused by the higher difference in the induced strain between P_2 and P_3 compared to the overall difference between P_1 and P_4. This higher difference is caused by the printing parameters stated in Section 2. **Figure 7.6** (d) shows snapshots of Actuators 1 – 3 at timestamps ① – ⑤. The actuation video is available in the Supplementary Information.

The aforementioned timestamps occur at temperature values that are summarised in **Figure 7.7** (a). The behaviour reported in **Figure 7.7** (a) matches the one presented in **Figure**

7.6 since the relationship between the temperature and time is almost linear. The effect of the temperature on the magnitude of the deformation ($|\sigma|$) is illustrated in **Figure 7.7** (b).

The results show that Actuator 2 achieved the highest $|\sigma|$ while Actuator 3 achieved the lowest $|\sigma|$. Moreover, Actuator 1 showed a reduction in $|\sigma|$ starting from 78.44 °C, which is caused by the drop in d_y value in **Figure 7.6** (a). These observations can be linked to the activation of *VLL* and *HLL*, as presented in **Figure 7.7** (a). The actuators follow a temperature-dependent actuation throughout all their timestamps.

The trajectory paths taken by the actuators starting from their initial shapes until their fully activated shapes are presented in **Figure 7.7** (c). The results demonstrate a nonlinear relationship between the *x*- and *y*-positions of the actuators, particularly noticeable in Actuator 1. This nonlinearity can be attributed to several factors, including the delay introduced by the temperature-dependent sequential activation of the layers and the mutual influence of d_x and dy on each other. There is also a reversal of direction that can be seen in (c) marked by the end of the blue line.
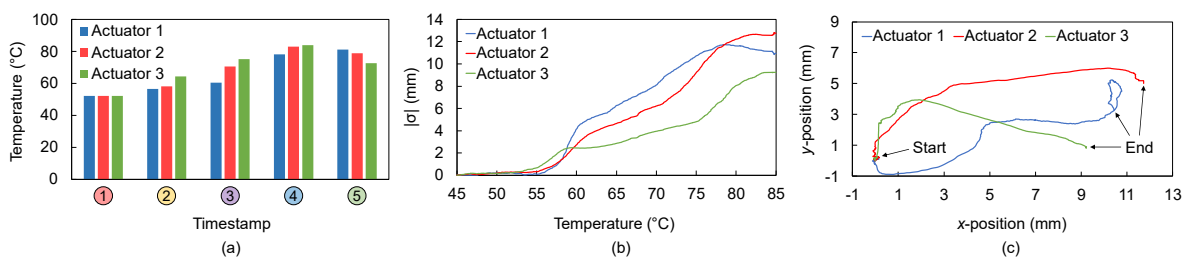
Figure 7.7. Actuation performance of Actuators 1 – 3. (a) Comparison between the temperature values that correspond to timestamps ① – ⑤. (b) Deformation magnitude starting from 45 °C. (c) Trajectory paths starting from the initial shapes to the fully activated shapes.

This effect of changing the ratio of the number of layers is indicative of their direct relation to the activation temperature. The experiment is designed so that, a total isolation of deformation is done when observed on each corner of the actuator. This allows for precise timing and temperature readings as to when the released strain in either the horizontal or vertical lines is strong enough to cause a deformation. Although there could be many factors affecting the activation temperature, or the temperature at which the force is strong enough to deform the actuator, it is controlled by the number of layers that act in each direction. This effect sheds light on how the force is released in actuators at gradual heating, allowing for

control over activating certain layers more than others. But may also reflect the behaviour that is undergone by the actuators when activated at a high temperature. Although this effect is different, the mechanisms that cause it are still in place.

Beyond the number of layers in each section of the actuator it should be taken into account that not all layers are the same, even when printed at the same printing parameters. There are several differences in the layers that may contribute to the amount of strain that is stored in each layer by the printing process based on the layer's location in the print. Some of these effects are, but are not limited to, the first layers, the top layers, and layers printed above a layer with a different printing direction.

The first layer is printed on the print bed; thus, no melting and fusing is undergone by that layer, except for the layer printed above it, it is also being reheated with the layers printed above it. As for the top layer, the layer is printed and fused with the layer below it, but there is no reheating since it is the last layer printed. This layer also has the fastest cooling time since there is no reheating or layers above it, so it is exposed to the colder environment air. As for the middle layers, theoretically, there is a range of heating and cooling rates along the layers from bottom to top, since they reheat the layers above them, and have fewer layers printed above them. Mutli-shape, or temperature-dependent actuation is reported in the literature when using multiple materials [236], composites [237], and manual shape programming [238]. The work in this section provided a novel approach toward single-material multi-shape actuation.

7.4   Summary

This chapter explores various parameters for controlling the deformation shape of actuators, encompassing both setting-related and structural factors. One innovative approach involves manipulating the printing direction of lines in Fused Deposition Modeling (FDM) to induce twisting in 4D printed PLA actuators, allowing precise control over the twisting angle through the printing angle. This twisting capability empowers 4D-printed actuators to execute helix movements in three-dimensional space, expanding design possibilities significantly. Remarkably, a helix angle as high as 22.63° was achieved using a printing angle of 45°, with deviations from this angle resulting in reduced twisting angles.

Moreover, the thickness of the actuators was influenced by the printing angles, shrinking parallel to the lines and slightly expanding perpendicular to them. Leveraging this

concept, a 4D-printed gripper with twisting arms was developed, enabling the gripping of cylindrical objects effectively. The gripper demonstrated complete gripping functionality within a mere 12 seconds.

The chapter's second section introduces an innovative approach utilizing temperature-dependent sequential layers activation to achieve multi-shape actuation. PLA actuators were printed with parts having 0° raster angles, sandwiched between 90° parts to observe deformations along the x- and y-axes. Actuators with different sandwiching ratios were characterized, revealing that increasing the percentage of outer layers from 37.5% to 50% and then to 62.5% led to delayed activation of inner layers, occurring after 62 s, 82 s, and 171 s, respectively. This concept facilitates multi-shape actuation in single-material 4D-printed actuators without necessitating manual shape-programming, presenting an innovative advancement in the field.

Chapter 8: Conclusion

8.1   Conclusion

The research focused on the shape programming mechanism of SMP actuators, using multiple methods to control and activate the induced strain in the structures. The research started with a comprehensive literature review on 4D printing discussing most aspects of the field. Four results chapters are presented on printing parameters control, variable stiffness actuation, and Joule heating actuation, with the final chapter on twisting behaviour and thermal-dependant multi-actuation.

Chapter 2 presented an extensive literature review focusing on 4D printing of SMP since they show favourable characteristics over other materials. The research was done on the main sections of the shape memory effect, the stimulus, printing techniques, and shape programming of 4D printed structures. Through the literature, there seemed to be a lack of predictive models for the shape memory effect of the SMPs, which can be used to develop application-oriented 4D printed structures. These models aid in many aspects of 4D printing ranging from design to simulations. The lack of simulation work of SMPs is also a big hurdle for the field, with early stages in development. Following the literature review, chapter 3 is the methodology used for this research. This chapter presented the general methods used to assess, test, and validate the results of the research. Brief details of the assessment of the results chapters are presented, with a detailed flowchart of the research.

Chapter 3 investigated how the enhancements in actuator shape programming were described. It began with material analysis, which was crucial for thermal and mechanical assessments. Unique experimental setups, tailored for specific criteria, utilized sensors for detailed analysis. Individual and collective effects of printing parameters were studied, with a focus on internal strain and shape memory effect. Various printing patterns were explored, and Joule heating was employed for different stimuli. The evaluation centered on shape alteration during and after actuation, serving as a basis for strain release analysis. Meticulous modeling and simulations, including static deformation and thermal analyses, were conducted. Challenges were encountered in simulating shape memory polymers due to their unique behavior.

Chapter 4 of the thesis presented the effect of the printing parameters on the shape change of the structures since it is a fundamental step in printing structures with precise control over the shape change. Five printing parameters were identified and tested which were the printing speed, the passive-to-active ratio, the printing temperature, the layer height of the prints, and the thickness of the actuators, these were assessed based on the deformation shape change they caused after activation.

It was concluded that the higher the printing speed, the higher the shape change. The printing temperature reduces the shape change as temperature increases in a linear manner, while the ratio of passive-to-active layers increases the shape change up to a ratio of 50%. Then, beyond that, the effects reverse with the shape change rate decreasing up to the 100% ratio point. The layer height has a high effect on the deformation as they increase it when the layers' height reduces, this effect increases exponentially as the layers height gets smaller. The thickness of the structure reduced the deformation as it increased since more force is needed to deform larger structures. These parameters produced an accurate control over the deformation with the actuators forming bending angles ranging from 0° to 90°, which is the full deformation.

The results of the parameters were used to create a mathematical model that is based on thermal expansion to replicate the shape change in the models. The model has a very high accuracy, with an R^2 value of up to 98%, in predicting the bending in the actuator based on their parameters. The model was also linked with simulations for replicating the effect of the printing parameter that is based on manipulating the CTE of the materials, with the same accuracy as the mathematical model. The control of shape change through the parameters was used to create a very reliable and highly controllable gripper, which can be controlled to deform to a very specific degree.

Chapter 5 used variable stiffness in actuators to induce controllable shape change. The designs were based on geometric shapes forming patterns, while printed with the same dimensions. These designs were bio-inspired by natural forming patterns based on *Volvox carteri* (circles), *Haloquadratum walsbyi* (squares), honeycombs (hexagons), *Sapium sebiferum* (rhombuses), and *Oxalis triangularis* (triangles). Printing of the same models with different patterns has a wide range of control over the deformation degree and behaviour of the polymer, as they can be used to program structures with varying shape changes. The results were divided into three sections. The first section is on actuators printed with one

pattern, the second is actuators made up of the same pattern shapes with different sizes, and the third is made up of different mixed patterns. The various designs allow for shape change with bending angles ranging from 0° to 31°. The work in the chapter provided a method of controlling the shape-changing without changing the printing parameters. The data obtained from this chapter is used to create a unique gripper which can be programmed by the patterns to hold objects at different grip sizes, allowing customizable actuation for delicate objects. This method is advantageous as it preserves the printing parameters while changing the shape change in the design.

Chapter 6, which used a different stimulus for activating the actuators, presented Joule heating activation of conductive filament prints. The developed actuators use the heat generated by the current flowing through it to heat up and activate the SME, with a high degree of control. Different voltages of activation have produced higher deformation angles on activation, in shorter activation times even though all actuators reach about the same temperature thus going through full deformation. The control and local activation that Joule heating allows means that larger and more complex structures can be activated by signals, allowing for separate actuation of sections of the structure. This also takes the actuators out of a controlled actuation environment, allowing for better observation of the activation and analysis. This was used in assessing the force generated by each actuator at the activation temperature, with the highest voltage producing the highest force. The force is highest at the first deformation mainly due to the rigidity of the material at that temperature, lowering beyond that point. The unit actuators were used to create a multi-segment manipulator which grabs and moves objects by activating certain parts of it at different timings, controlled by a power source. This design allows for full control of timed actuation for manually switching the local actuators within the body of the structure.

Chapter 7, which is the final results chapter, presented further concepts in 4D printing, made up of two separate and distinct sections. The first is a section on inducing twisting behaviour into actuators by manipulating the printing direction, or raster angle. This design allows for complete control of the helical angle formed by the actuators on activation. The twisting was assessed by the helix angle formed by the actuators post-activation, with a helix angle varying from 0° to about 22.6°. The second and final part is a section on thermal-dependent actuation, which is a method of controlling the activation temperature of the actuators. the experiment is designed to observe the activation of certain parts of the actuators in an isolated fashion and manipulate the structures to control the activation of those sections

at different temperatures. A novel method of isolating the deformation in a certain direction depending on the active layer was developed by sandwiching layers, this is carried by gradually heating up the water environment of the actuators. This allowed for the observation of the layers active at different activation temperatures. This proved that by controlling the ratio of sandwiched layers to surface layers, the activation temperature in different directions is controlled.

Through the thesis, the fulfilment of the objectives has been completed successfully. The effects of the printing parameters were tested and analysed, with very high accuracy. This was then used to create a mathematical model for bending angle prediction, which is also applied to the simulation work. Beyond the parameters, the use of geometrical shapes for patterns was investigated with the creation of pattern-driven actuators. For a better understanding of the activation mechanism in SMPs, local activation was used in conductive materials, along with an analysis of the performance. Lastly, a novel approach to single-material multi-shape actuation was achieved by creating a layer sandwich printing method. These novel approaches in 4D printing can be applied in many fields. Most notably, they delicately handle intricate tasks and irregular objects, defining new possibilities in soft robotics and automation. Moreover, healthcare may benefit from their precision in minimally invasive surgeries and targeted drug deliveries. Furthermore, aerospace and automotive sectors can potentially rely on them for maintenance and assembling intricate components.

8.2   Future Work

Future work may involve four main areas, including performing advanced simulation, tensile and thermal testing of the SMP materials for better parameters, the printing of complex structures with functional parts, and testing passive SMP devices.

The simulation work is currently in its early stages, requiring significant improvements to the existing model. At present, the simulation is based on thermal expansion, a factor that can replicate aspects of the SME but falls short of fully representing its complexities. One crucial limitation is the absence of SME deformation characteristics in the simulation, a component essential for an accurate portrayal of SME. Despite the lack of this crucial data in existing literature, incorporating SME deformation characteristics into the simulation is vital to capturing the true essence of the phenomenon.

To enhance the simulation accuracy, extensive material testing is essential. Identifying specific characteristics within materials is key to facilitating their simulation, enabling the design of intricate and precise SME structures. However, one of the fundamental challenges in 4D printing persists the absence of comprehensive SME simulation. The integration of material testing, particularly in analyzing strain release concerning storage modulus and glass transition, holds promise in bridging this gap. These tests can provide essential data, creating a genuine representation of the intricate mechanisms underlying SME.

Additionally, the field demands more tunable composites, especially those with lower and more precise activation temperature ranges. Such materials are critical as they bring thermal 4D printing closer to practical biomedical applications, where stringent temperature requirements are non-negotiable. Furthermore, as applications become more complex, the need for intricate designs becomes apparent. These advanced designs may require better-equipped facilities and more capable 3D printers. While the complexity of building smaller devices increases, these micro-manipulators hold the potential to revolutionize various industries.

In sectors like medical implants and drug delivery, where thermal limitations are strict, 4D printed SMPs offer promising solutions. These SMPs can provide passive devices that aid in various applications. However, to unlock their full potential, better control over activation temperatures is imperative, ensuring these innovative solutions are not just theoretical but practical and effective in real-world applications.

References

[1] P. Wu, J. Wang, and X. Wang, "A critical review of the use of 3-D printing in the construction industry," *Automation in Construction*, vol. 68. Elsevier B.V., pp. 21–31, Aug. 01, 2016. doi: 10.1016/j.autcon.2016.04.005.

[2] Z. Sun and S. Y. Lee, "A systematic review of 3-D printing in cardiovascular and cerebrovascular diseases," *Anatol. J. Cardiol.*, vol. 17, no. 6, pp. 423–435, 2017, doi: 10.14744/AnatolJCardiol.2017.7464.

[3] X. Chen *et al.*, "Harnessing 4D Printing Bioscaffolds for Advanced Orthopedics," *Small*, vol. 18, no. 36, p. 2106824, Sep. 2022, doi: 10.1002/smll.202106824.

[4] Y. W. D. Tay, B. Panda, S. C. Paul, N. A. Noor Mohamed, M. J. Tan, and K. F. Leong, "3D printing trends in building and construction industry: a review," *Virtual and Physical Prototyping*, vol. 12, no. 3. Taylor and Francis Ltd., pp. 261–276, Jul. 03, 2017. doi: 10.1080/17452759.2017.1326724.

[5] X. Wang, M. Jiang, Z. Zhou, J. Gou, and D. Hui, "3D printing of polymer matrix composites: A review and prospective," *Composites Part B: Engineering*, vol. 110. Elsevier Ltd, pp. 442–458, Feb. 01, 2017. doi: 10.1016/j.compositesb.2016.11.034.

[6] M. Bodaghi, A. R. Damanpack, and W. H. Liao, "Self-expanding/shrinking structures by 4D printing," *Smart Mater. Struct.*, vol. 25, no. 10, p. 105034, Sep. 2016, doi: 10.1088/0964-1726/25/10/105034.

[7] J. H. Na *et al.*, "Programming reversibly self-folding origami with micropatterned photo-crosslinkable polymer trilayers," *Adv. Mater.*, vol. 27, no. 1, pp. 79–85, Oct. 2015, doi: 10.1002/adma.201403510.

[8] S. Tibbits, "4D printing: Multi-material shape change," *Archit. Des.*, vol. 84, no. 1, pp. 116–121, Jan. 2014, doi: 10.1002/ad.1710.

[9] Q. Ge, H. J. Qi, and M. L. Dunn, "Active materials by four-dimension printing," *Appl. Phys. Lett.*, vol. 103, no. 13, p. 131901, Sep. 2013, doi: 10.1063/1.4819837.

[10] M. López-Valdeolivas, D. Liu, D. J. Broer, and C. Sánchez-Somolinos, "4D Printed Actuators with Soft-Robotic Functions," *Macromol. Rapid Commun.*, vol. 39, no. 5, p. 1700710, Mar. 2018, doi: 10.1002/marc.201700710.

[11] Z. Ding, O. Weeger, H. J. Qi, and M. L. Dunn, "4D rods: 3D structures via programmable 1D composite rods," *Mater. Des.*, vol. 137, pp. 256–265, Jan. 2018, doi: 10.1016/j.matdes.2017.10.004.

[12] D. Kashyap, P. Kishore Kumar, and S. Kanagaraj, "4D printed porous radiopaque shape memory polyurethane for endovascular embolization," *Addit. Manuf.*, vol. 24, pp. 687–695, Dec. 2018, doi: 10.1016/j.addma.2018.04.009.

[13] W. Zhao, F. Zhang, J. Leng, and Y. Liu, "Personalized 4D printing of bioinspired tracheal scaffold concept based on magnetic stimulated shape memory composites," *Compos. Sci. Technol.*, vol. 184, p. 107866, Nov. 2019, doi: 10.1016/j.compscitech.2019.107866.

[14] D. E. Hagaman, S. Leist, J. Zhou, and H. F. Ji, "Photoactivated Polymeric Bilayer

Actuators Fabricated via 3D Printing," *ACS Appl. Mater. Interfaces*, vol. 10, no. 32, pp. 27308–27315, Aug. 2018, doi: 10.1021/acsami.8b08503.

[15] H. Cui *et al.*, "A novel near-infrared light responsive 4D printed nanoarchitecture with dynamically and remotely controllable transformation," *Nano Res.*, vol. 12, no. 6, pp. 1381–1388, 2019, doi: 10.1007/s12274-019-2340-9.

[16] M. Bodaghi, A. Serjouei, A. Zolfagharian, M. Fotouhi, H. Rahman, and D. Durand, "Reversible energy absorbing meta-sandwiches by FDM 4D printing," *Int. J. Mech. Sci.*, vol. 173, p. 105451, May 2020, doi: 10.1016/j.ijmecsci.2020.105451.

[17] W. Liu, N. Wu, and K. Pochiraju, "Shape recovery characteristics of SiC/C/PLA composite filaments and 3D printed parts," *Compos. Part A Appl. Sci. Manuf.*, vol. 108, pp. 1–11, May 2018, doi: 10.1016/j.compositesa.2018.02.017.

[18] T. D. Ngo, A. Kashani, G. Imbalzano, K. T. Q. Nguyen, and D. Hui, "Additive manufacturing (3D printing): A review of materials, methods, applications and challenges," *Composites Part B: Engineering*, vol. 143. Elsevier Ltd, pp. 172–196, Jun. 15, 2018. doi: 10.1016/j.compositesb.2018.02.012.

[19] Y. Pyo *et al.*, "Design of a shape memory composite(SMC) using 4D printing technology," *Sensors Actuators, A Phys.*, vol. 283, pp. 187–195, Nov. 2018, doi: 10.1016/j.sna.2018.08.049.

[20] M. Herath, M. Islam, J. Epaarachchi, F. Zhang, and J. Leng, "4D printed shape memory polymer composite structures for deployable small spacecrafts," in *ASME 2019 Conference on Smart Materials, Adaptive Structures and Intelligent Systems, SMASIS 2019*, American Society of Mechanical Engineers (ASME), Dec. 2019. doi: 10.1115/SMASIS2019-5583.

[21] S. T. Ly and J. Y. Kim, "4D printing – fused deposition modeling printing with thermal-responsive shape memory polymers," *Int. J. Precis. Eng. Manuf. - Green Technol.*, vol. 4, no. 3, pp. 267–272, Jul. 2017, doi: 10.1007/s40684-017-0032-z.

[22] F. Momeni, S. M.Mehdi Hassani.N, X. Liu, and J. Ni, "A review of 4D printing," *Mater. Des.*, vol. 122, pp. 42–79, May 2017, doi: 10.1016/j.matdes.2017.02.068.

[23] A. Mitchell, U. Lafont, M. Hołyńska, and C. Semprimoschnig, "Additive manufacturing — A review of 4D printing and future applications," *Addit. Manuf.*, vol. 24, pp. 606–626, Dec. 2018, doi: 10.1016/j.addma.2018.10.038.

[24] C. Cui *et al.*, "Reconfigurable 4D Printing of Reprocessable and Mechanically Strong Polythiourethane Covalent Adaptable Networks," *Adv. Funct. Mater.*, vol. 32, no. 29, p. 2203720, Jul. 2022, doi: 10.1002/adfm.202203720.

[25] L. K. Rivera-Tarazona, T. Shukla, K. A. Singh, A. K. Gaharwar, Z. T. Campbell, and T. H. Ware, "4D Printing of Engineered Living Materials," *Adv. Funct. Mater.*, vol. 32, no. 4, p. 2106843, Jan. 2022, doi: 10.1002/adfm.202106843.

[26] Y. Wang, H. Cui, T. Esworthy, D. Mei, Y. Wang, and L. G. Zhang, "Emerging 4D Printing Strategies for Next-Generation Tissue Regeneration and Medical Devices," *Adv. Mater.*, vol. 34, no. 20, p. 2109198, May 2022, doi: 10.1002/adma.202109198.

[27] S. L. Buffington, J. E. Paul, M. M. Ali, M. M. Macios, P. T. Mather, and J. H. Henderson, "Enzymatically triggered shape memory polymers," *Acta Biomater.*, vol. 84, pp. 88–97, Jan. 2019, doi: 10.1016/j.actbio.2018.11.031.

[28] M. Zarek, M. Layani, I. Cooperstein, E. Sachyani, D. Cohn, and S. Magdassi, "3D Printing of Shape Memory Polymers for Flexible Electronic Devices," *Adv. Mater.*, vol. 28, no. 22, pp. 4449–4454, Jun. 2016, doi: 10.1002/adma.201503132.

[29] M. Bodaghi, A. R. Damanpack, and W. H. Liao, "Adaptive metamaterials by functionally graded 4D printing," *Mater. Des.*, vol. 135, pp. 26–36, Dec. 2017, doi: 10.1016/j.matdes.2017.08.069.

[30] W. Zhao, C. Yue, L. Liu, J. Leng, and Y. Liu, "Mechanical behavior analyses of 4D printed metamaterials structures with excellent energy absorption ability," *Compos. Struct.*, vol. 304, p. 116360, Jan. 2023, doi: 10.1016/j.compstruct.2022.116360.

[31] X. Wan, F. Zhang, Y. Liu, and J. Leng, "CNT-based electro-responsive shape memory functionalized 3D printed nanocomposites for liquid sensors," *Carbon N. Y.*, vol. 155, pp. 77–87, Dec. 2019, doi: 10.1016/j.carbon.2019.08.047.

[32] M. Zarek, N. Mansour, S. Shapira, and D. Cohn, "4D Printing of Shape Memory-Based Personalized Endoluminal Medical Devices," *Macromol. Rapid Commun.*, vol. 38, no. 2, p. 1600628, Jan. 2017, doi: 10.1002/marc.201600628.

[33] M. Carlson and Y. Li, "Development and kinetic evaluation of a low-cost temperature-sensitive shape memory polymer for 4-dimensional printing," *Int. J. Adv. Manuf. Technol.*, vol. 106, no. 9–10, pp. 4263–4279, Feb. 2020, doi: 10.1007/s00170-020-04927-5.

[34] S. Van Hoa, "Development of composite springs using 4D printing method," *Compos. Struct.*, vol. 210, pp. 869–876, Feb. 2019, doi: 10.1016/j.compstruct.2018.12.003.

[35] Q. Ge, C. K. Dunn, H. J. Qi, and M. L. Dunn, "Active origami by 4D printing," *Smart Mater. Struct.*, vol. 23, no. 9, p. 094007, Aug. 2014, doi: 10.1088/0964-1726/23/9/094007.

[36] S. Akbari *et al.*, "Enhanced multimaterial 4D printing with active hinges," *Smart Mater. Struct.*, vol. 27, no. 6, p. 065027, May 2018, doi: 10.1088/1361-665X/aabe63.

[37] Z. Zhang, K. G. Demir, and G. X. Gu, "Developments in 4D-printing: a review on current smart materials, technologies, and applications," *Int. J. Smart Nano Mater.*, vol. 10, no. 3, pp. 205–224, Jul. 2019, doi: 10.1080/19475411.2019.1591541.

[38] A. Subash and B. Kandasubramanian, "4D printing of shape memory polymers," *European Polymer Journal*, vol. 134. Elsevier Ltd, p. 109771, Jul. 05, 2020. doi: 10.1016/j.eurpolymj.2020.109771.

[39] X. Kuang *et al.*, "Advances in 4D Printing: Materials and Applications," *Advanced Functional Materials*, vol. 29, no. 2. Wiley-VCH Verlag, Jan. 10, 2019. doi: 10.1002/adfm.201805290.

[40] A. Nikoobin and M. Hassani Niaki, "Deriving and analyzing the effective parameters in microgrippers performance," *Sci. Iran.*, vol. 19, no. 6, pp. 1554–1563, Dec. 2012, doi: 10.1016/j.scient.2012.10.020.

[41] M. Hosseinzadeh, M. Ghoreishi, and K. Narooei, "4D printing of shape memory polylactic acid beams: An experimental investigation into FDM additive manufacturing process parameters, mathematical modeling, and optimization," *J. Manuf. Process.*, vol. 85, pp. 774–782, Jan. 2023, doi: 10.1016/j.jmapro.2022.12.006.

[42] J. Wang, Z. Wang, Z. Song, L. Ren, Q. Liu, and L. Ren, "Programming Multistage Shape Memory and Variable Recovery Force with 4D Printing Parameters," *Adv. Mater. Technol.*, vol. 4, no. 11, p. 1900535, Nov. 2019, doi: 10.1002/admt.201900535.

[43] L. Kačergis, R. Mitkus, and M. Sinapius, "Influence of fused deposition modeling process parameters on the transformation of 4D printed morphing structures," *Smart Mater. Struct.*, vol. 28, no. 10, p. 105042, Sep. 2019, doi: 10.1088/1361-665X/ab3d18.

[44] M. Barletta, A. Gisario, and M. Mehrpouya, "4D printing of shape memory polylactic acid (PLA) components: Investigating the role of the operational parameters in fused deposition modelling (FDM)," *J. Manuf. Process.*, vol. 61, pp. 473–480, Jan. 2021, doi: 10.1016/j.jmapro.2020.11.036.

[45] T. Han, S. Kundu, A. Nag, and Y. Xu, "3D printed sensors for biomedical applications: A review," *Sensors (Switzerland)*, vol. 19, no. 7. MDPI AG, p. 1706, Apr. 10, 2019. doi: 10.3390/s19071706.

[46] M. Y. Shie *et al.*, "Review of polymeric materials in 4D printing biomedical applications," *Polymers (Basel).*, vol. 11, no. 11, p. 1864, Nov. 2019, doi: 10.3390/polym11111864.

[47] X. Li, J. Shang, and Z. Wang, "Intelligent materials: A review of applications in 4D printing," *Assem. Autom.*, vol. 37, no. 2, pp. 170–185, 2017, doi: 10.1108/AA-11-2015-093.

[48] Y. Liu, H. Lv, X. Lan, J. Leng, and S. Du, "Review of electro-active shape-memory polymer composite," *Compos. Sci. Technol.*, vol. 69, no. 13, pp. 2064–2068, Oct. 2009, doi: 10.1016/j.compscitech.2008.08.016.

[49] M. H. Ali, A. Abilgaziyev, and D. Adair, "4D printing: a critical review of current developments, and future prospects," *Int. J. Adv. Manuf. Technol.*, vol. 105, no. 1–4, pp. 701–717, Nov. 2019, doi: 10.1007/s00170-019-04258-0.

[50] Y. J. Li, F. H. Zhang, Y. J. Liu, and J. S. Leng, "4D printed shape memory polymers and their structures for biomedical applications," *Science China Technological Sciences*, vol. 63, no. 4. Springer Verlag, pp. 545–560, Apr. 01, 2020. doi: 10.1007/s11431-019-1494-0.

[51] S. Joshi *et al.*, "4D printing of materials for the future: Opportunities and challenges," *Appl. Mater. Today*, vol. 18, p. 100490, Mar. 2020, doi: 10.1016/j.apmt.2019.100490.

[52] T. Zhao *et al.*, "4D printing of shape memory polyurethane via stereolithography," *Eur. Polym. J.*, vol. 101, pp. 120–126, Apr. 2018, doi: 10.1016/j.eurpolymj.2018.02.021.

[53] V. A. Gorodtsov and D. S. Lisovenko, "Extreme values of Young's modulus and Poisson's ratio of hexagonal crystals," *Mech. Mater.*, vol. 134, pp. 1–8, Jul. 2019, doi: 10.1016/j.mechmat.2019.03.017.

[54] Y. C. Sun, Y. Wan, R. Nam, M. Chu, and H. E. Naguib, "4D-printed hybrids with localized shape memory behaviour: Implementation in a functionally graded structure," *Sci. Rep.*, vol. 9, no. 1, pp. 1–13, Dec. 2019, doi: 10.1038/s41598-019-55298-1.

[55] K. K. Westbrook, P. H. Kao, F. Castro, Y. Ding, and H. Jerry Qi, "A 3D finite deformation constitutive model for amorphous shape memory polymers: A multi-

branch modeling approach for nonequilibrium relaxation processes," *Mech. Mater.*, vol. 43, no. 12, pp. 853–869, Dec. 2011, doi: 10.1016/j.mechmat.2011.09.004.

[56] H. Wu, P. Chen, C. Yan, C. Cai, and Y. Shi, "Four-dimensional printing of a novel acrylate-based shape memory polymer using digital light processing," *Mater. Des.*, vol. 171, p. 107704, Jun. 2019, doi: 10.1016/j.matdes.2019.107704.

[57] Y. S. Alshebly, M. Nafea, H. A. F. Almurib, M. Sultan Mohamed Ali, A. A. Mohd Faudzi, and M. T. T. Tan, "Development of 4D Printed PLA Actuators with an Induced Internal Strain upon Printing," *2021 IEEE Int. Conf. Autom. Control Intell. Syst. I2CACIS 2021 - Proc.*, pp. 41–45, Jun. 2021, doi: 10.1109/I2CACIS52118.2021.9495898.

[58] F. Zhang, L. Wang, Z. Zheng, Y. Liu, and J. Leng, "Magnetic programming of 4D printed shape memory composite structures," *Compos. Part A Appl. Sci. Manuf.*, vol. 125, p. 105571, Oct. 2019, doi: 10.1016/j.compositesa.2019.105571.

[59] L. Chen *et al.*, "Color-Changeable Four-Dimensional Printing Enabled with Ultraviolet-Curable and Thermochromic Shape Memory Polymers," *ACS Appl. Mater. Interfaces*, vol. 13, no. 15, pp. 18120–18127, 2021, doi: 10.1021/acsami.1c02656.

[60] X. Xin, L. Liu, Y. Liu, and J. Leng, "Origami-inspired self-deployment 4D printed honeycomb sandwich structure with large shape transformation," *Smart Mater. Struct.*, vol. 29, no. 6, p. 065015, May 2020, doi: 10.1088/1361-665X/ab85a4.

[61] C. Y. Cheng *et al.*, "4D printing of shape memory aliphatic copolyester via UV-assisted FDM strategy for medical protective devices," *Chem. Eng. J.*, vol. 396, p. 125242, Sep. 2020, doi: 10.1016/j.cej.2020.125242.

[62] S. Yamamura and E. Iwase, "Hybrid hinge structure with elastic hinge on self-folding of 4D printing using a fused deposition modeling 3D printer," *Mater. Des.*, vol. 203, p. 109605, May 2021, doi: 10.1016/j.matdes.2021.109605.

[63] Z. Song *et al.*, "Biomimetic Nonuniform, Dual-Stimuli Self-Morphing Enabled by Gradient Four-Dimensional Printing," *ACS Appl. Mater. Interfaces*, vol. 12, no. 5, pp. 6351–6361, 2020, doi: 10.1021/acsami.9b17577.

[64] C. Yuan, F. Wang, B. Qi, Z. Ding, D. W. Rosen, and Q. Ge, "3D printing of multi-material composites with tunable shape memory behavior," *Mater. Des.*, vol. 193, p. 108785, May 2020, doi: 10.1016/j.matdes.2020.108785.

[65] J. W. Su *et al.*, "4D printing of polyurethane paint-based composites," *Int. J. Smart Nano Mater.*, vol. 10, no. 3, pp. 237–248, Jul. 2019, doi: 10.1080/19475411.2019.1618409.

[66] C. A. Garcia Rosales *et al.*, "Characterization of shape memory polymer parts fabricated using material extrusion 3D printing technique," *Rapid Prototyp. J.*, vol. 25, no. 2, pp. 322–331, Mar. 2019, doi: 10.1108/RPJ-08-2017-0157.

[67] T. L. Tseng *et al.*, "3D printing of shape memory polymer (SMP)/carbon black (CB) nanocomposites with electro-responsive toughness enhancement," *Mater. Res. Express*, vol. 5, no. 6, 2018, doi: 10.1088/2053-1591/aacd53.

[68] M. Bodaghi, A. R. Damanpack, and W. H. Liao, "Triple shape memory polymers by 4D printing," *Smart Mater. Struct.*, vol. 27, no. 6, p. 065010, May 2018, doi: 10.1088/1361-665X/aabc2a.

[69]   R. Xiao, J. Guo, D. L. Safranski, and T. D. Nguyen, "Solvent-driven temperature memory and multiple shape memory effects," *Soft Matter*, vol. 11, no. 20, pp. 3977–3985, May 2015, doi: 10.1039/c5sm00543d.

[70]   T. Mu, L. Liu, X. Lan, Y. Liu, and J. Leng, "Shape memory polymers for composites," *Composites Science and Technology*, vol. 160. Elsevier Ltd, pp. 169–198, May 26, 2018. doi: 10.1016/j.compscitech.2018.03.018.

[71]   Y. Liu *et al.*, "Microstructural design for enhanced shape memory behavior of 4D printed composites based on carbon nanotube/polylactic acid filament," *Compos. Sci. Technol.*, vol. 181, p. 107692, Sep. 2019, doi: 10.1016/j.compscitech.2019.107692.

[72]   J. Wang, Z. Wang, Z. Song, L. Ren, Q. Liu, and L. Ren, "Biomimetic Shape–Color Double-Responsive 4D Printing," *Adv. Mater. Technol.*, vol. 4, no. 9, p. 1900293, Sep. 2019, doi: 10.1002/admt.201900293.

[73]   E. S. Keneth, R. Lieberman, M. Rednor, G. Scalet, F. Auricchio, and S. Magdassi, "Multi-material 3D printed shape memory polymer with tunable melting and glass transition temperature activated by heat or light," *Polymers (Basel).*, vol. 12, no. 3, p. 710, Mar. 2020, doi: 10.3390/polym12030710.

[74]   T. Chen and K. Shea, "An autonomous programmable actuator and shape reconfigurable structures using bistability and shape memory polymers," *3D Print. Addit. Manuf.*, vol. 5, no. 2, pp. 91–101, Jun. 2018, doi: 10.1089/3dp.2017.0118.

[75]   J. Wu *et al.*, "Multi-shape active composites by 3D printing of digital shape memory polymers," *Sci. Rep.*, vol. 6, no. 1, pp. 1–11, Apr. 2016, doi: 10.1038/srep24224.

[76]   X. Hu, Z. Ge, X. Wang, N. Jiao, S. Tung, and L. Liu, "Multifunctional thermo-magnetically actuated hybrid soft millirobot based on 4D printing," *Compos. Part B Eng.*, vol. 228, p. 109451, Jan. 2022, doi: 10.1016/j.compositesb.2021.109451.

[77]   X. Dong, F. Zhang, L. Wang, Y. Liu, and J. Leng, "4D printing of electroactive shape-changing composite structures and their programmable behaviors," *Compos. Part A Appl. Sci. Manuf.*, vol. 157, p. 106925, Jun. 2022, doi: 10.1016/j.compositesa.2022.106925.

[78]   Y. Y. C. Choong, S. Maleksaeedi, H. Eng, J. Wei, and P. C. Su, "4D printing of high performance shape memory polymer using stereolithography," *Mater. Des.*, vol. 126, pp. 219–225, Jul. 2017, doi: 10.1016/j.matdes.2017.04.049.

[79]   J. W. Su *et al.*, "4D printing of a self-morphing polymer driven by a swellable guest medium," *Soft Matter*, vol. 14, no. 5, pp. 765–772, Jan. 2018, doi: 10.1039/c7sm01796k.

[80]   L. H. Shao, B. Zhao, Q. Zhang, Y. Xing, and K. Zhang, "4D printing composite with electrically controlled local deformation," *Extrem. Mech. Lett.*, vol. 39, p. 100793, May 2020, doi: 10.1016/j.eml.2020.100793.

[81]   Y. C. Lee, Y. S. Alshebly, and M. Nafea, "Joule Heating Activation of 4D Printed Conductive PLA Actuators," *2022 IEEE Int. Conf. Autom. Control Intell. Syst. I2CACIS 2022 - Proc.*, pp. 221–225, 2022, doi: 10.1109/I2CACIS54679.2022.9815495.

[82]   M. Lalegani Dezaki and M. Bodaghi, "Magnetorheological elastomer-based 4D printed electroactive composite actuators," *Sensors Actuators A Phys.*, vol. 349, p.

114063, Jan. 2023, doi: 10.1016/j.sna.2022.114063.

[83]	H. Zhang *et al.*, "4D Printing of Ag Nanowire-Embedded Shape Memory Composites with Stable and Controllable Electrical Responsivity: Implications for Flexible Actuators," *ACS Appl. Nano Mater.*, vol. 5, no. 5, pp. 6221–6231, May 2022, doi: 10.1021/acsanm.2c00264.

[84]	M. Y. Razzaq *et al.*, "4D Printing of Electroactive Triple-Shape Composites," *Polymers (Basel).*, vol. 15, no. 4, p. 832, Feb. 2023, doi: 10.3390/polym15040832.

[85]	D. J. Roach, X. Kuang, C. Yuan, K. Chen, and H. J. Qi, "Novel ink for ambient condition printing of liquid crystal elastomers for 4D printing," *Smart Mater. Struct.*, vol. 27, no. 12, p. 125011, Nov. 2018, doi: 10.1088/1361-665X/aae96f.

[86]	F. Long, G. Xu, J. Wang, Y. Ren, and Y. Cheng, "Variable Stiffness Conductive Composites by 4D Printing Dual Materials Alternately," *Micromachines*, vol. 13, no. 8, p. 1343, Aug. 2022, doi: 10.3390/mi13081343.

[87]	L. Ren *et al.*, "Stiffness-tunable and self-sensing integrated soft machines based on 4D printed conductive shape memory composites," *Mater. Des.*, vol. 228, p. 111851, Apr. 2023, doi: 10.1016/j.matdes.2023.111851.

[88]	A. Zolfagharian, A. Kaynak, S. Y. Khoo, and A. Kouzani, "Pattern-driven 4D printing," *Sensors Actuators, A Phys.*, vol. 274, pp. 231–243, May 2018, doi: 10.1016/j.sna.2018.03.034.

[89]	J. Tang, Y. Zhou, L. Wan, and F. Huang, "Automatically Programmable Shape-Memory Polymers Based on Asymmetric Swelling of Bilayer Structures," *Macromol. Rapid Commun.*, vol. 39, no. 9, p. 1800039, May 2018, doi: 10.1002/marc.201800039.

[90]	A. J. Boyle, A. C. Weems, S. M. Hasan, L. D. Nash, M. B. B. Monroe, and D. J. Maitland, "Solvent stimulated actuation of polyurethane-based shape memory polymer foams using dimethyl sulfoxide and ethanol," *Smart Mater. Struct.*, vol. 25, no. 7, p. 075014, May 2016, doi: 10.1088/0964-1726/25/7/075014.

[91]	A. V. Salvekar *et al.*, "Water-Responsive Shape Recovery Induced Buckling in Biodegradable Photo-Cross-Linked Poly(ethylene glycol) (PEG) Hydrogel," *Acc. Chem. Res.*, vol. 50, no. 2, pp. 141–150, Feb. 2017, doi: 10.1021/acs.accounts.6b00539.

[92]	H. Luo *et al.*, "Multi-stimuli responsive carbon nanotube-shape memory polymeric composites," *Mater. Lett.*, vol. 137, pp. 385–388, Dec. 2014, doi: 10.1016/j.matlet.2014.09.054.

[93]	G. D. Soto, C. Meiorin, D. Actis, P. Mendoza Zélis, M. A. Mosiewicki, and N. E. Marcovich, "Nanocomposites with shape memory behavior based on a segmented polyurethane and magnetic nanostructures," *Polym. Test.*, vol. 65, pp. 360–368, Feb. 2018, doi: 10.1016/j.polymertesting.2017.12.012.

[94]	Y. Wang and X. Li, "4D printing reversible actuator with strain self-sensing function via structural design," *Compos. Part B Eng.*, vol. 211, p. 108644, Apr. 2021, doi: 10.1016/j.compositesb.2021.108644.

[95]	L. F. Fan, Y. N. Huang, M. Z. Rong, and M. Q. Zhang, "A simple and universal strategy for preparing external stress-free two-way shape memory polymers by making use of the chemical crosslinkages derived from peroxide initiator," *Express Polym.*

Lett., vol. 14, no. 4, pp. 295–308, Apr. 2020, doi: 10.3144/expresspolymlett.2020.26.

[96] A. Y. Lee, J. An, C. K. Chua, and Y. Zhang, "Preliminary Investigation of the Reversible 4D Printing of a Dual-Layer Component," *Engineering*, vol. 5, no. 6, pp. 1159–1170, Dec. 2019, doi: 10.1016/j.eng.2019.09.007.

[97] Y. N. Huang, L. F. Fan, M. Z. Rong, M. Q. Zhang, and Y. M. Gao, "External Stress-Free Reversible Multiple Shape Memory Polymers," *ACS Appl. Mater. Interfaces*, vol. 11, no. 34, pp. 31346–31355, Aug. 2019, doi: 10.1021/acsami.9b10052.

[98] B. Jin, H. Song, R. Jiang, J. Song, Q. Zhao, and T. Xie, "Programming a crystalline shape memory polymer network with thermo- and photo-reversible bonds toward a single-component soft robot," *Sci. Adv.*, vol. 4, no. 1, p. eaao3865, Jan. 2018, doi: 10.1126/sciadv.aao3865.

[99] Y. Mao *et al.*, "3D Printed Reversible Shape Changing Components with Stimuli Responsive Materials," *Sci. Rep.*, vol. 6, no. 1, pp. 1–13, Apr. 2016, doi: 10.1038/srep24761.

[100] Y. Liu *et al.*, "Programmable responsive shaping behavior induced by visible multi-dimensional gradients of magnetic nanoparticles," *Soft Matter*, vol. 8, no. 12, pp. 3295–3299, Mar. 2012, doi: 10.1039/c2sm07206h.

[101] S. K. Leist and J. Zhou, "Current status of 4D printing technology and the potential of light-reactive smart materials as 4D printable materials," *Virtual and Physical Prototyping*, vol. 11, no. 4. Taylor and Francis Ltd., pp. 249–262, Oct. 01, 2016. doi: 10.1080/17452759.2016.1198630.

[102] A. Y. Lee, A. Zhou, J. An, C. K. Chua, and Y. Zhang, "Contactless reversible 4D-printing for 3D-to-3D shape morphing," *Virtual Phys. Prototyp.*, vol. 15, no. 4, pp. 481–495, Oct. 2020, doi: 10.1080/17452759.2020.1822189.

[103] M. Q. Zafar and H. Zhao, "4D Printing: Future Insight in Additive Manufacturing," *Metals and Materials International*, vol. 26, no. 5. pp. 564–585, 2020. doi: 10.1007/s12540-019-00441-w.

[104] P. Rastogi and B. Kandasubramanian, "Breakthrough in the printing tactics for stimuli-responsive materials: 4D printing," *Chemical Engineering Journal*, vol. 366. Elsevier B.V., pp. 264–304, Jun. 15, 2019. doi: 10.1016/j.cej.2019.02.085.

[105] Y. S. Lui, W. T. Sow, L. P. Tan, Y. Wu, Y. Lai, and H. Li, "4D printing and stimuli-responsive materials in biomedical aspects," *Acta Biomaterialia*, vol. 92. Acta Materialia Inc, pp. 19–36, Jul. 01, 2019. doi: 10.1016/j.actbio.2019.05.005.

[106] J. J. Wu, L. M. Huang, Q. Zhao, and T. Xie, "4D Printing: History and Recent Progress," *Chinese Journal of Polymer Science (English Edition)*, vol. 36, no. 5. pp. 563–575, 2018. doi: 10.1007/s10118-018-2089-8.

[107] X. Peng *et al.*, "Shape memory effect of three-dimensional printed products based on polypropylene/nylon 6 alloy," *J. Mater. Sci.*, vol. 54, no. 12, pp. 9235–9246, Jun. 2019, doi: 10.1007/s10853-019-03366-2.

[108] F. Wang, C. Yuan, D. Wang, D. W. Rosen, and Q. Ge, "A phase evolution based constitutive model for shape memory polymer and its application in 4D printing," *Smart Mater. Struct.*, vol. 29, no. 5, p. 055016, Mar. 2020, doi: 10.1088/1361-665X/ab7ab0.

[109] E. Maniruzzaman, Mohammed, *3D and 4D Printing in Biomedical Applications*. 2019. doi: 10.1002/9783527813704.

[110] R. Singh, "Process capability study of polyjet printing for plastic components," *Evol. Ecol.*, vol. 25, no. 4, pp. 1011–1015, Jul. 2011, doi: 10.1007/s12206-011-0203-8.

[111] R. Udroiu and I. C. Braga, "Polyjet technology applications for rapid tooling," in *MATEC Web of Conferences*, EDP Sciences, 2017, p. 03011. doi: 10.1051/matecconf/201711203011.

[112] K. Yu, A. Ritchie, Y. Mao, M. L. Dunn, and H. J. Qi, "Controlled Sequential Shape Changing Components by 3D Printing of Shape Memory Polymer Multimaterials," *Procedia IUTAM*, vol. 12, pp. 193–203, Jan. 2015, doi: 10.1016/j.piutam.2014.12.021.

[113] Y. Mao, K. Yu, M. S. Isakov, J. Wu, M. L. Dunn, and H. Jerry Qi, "Sequential Self-Folding Structures by 3D Printed Digital Shape Memory Polymers," *Sci. Rep.*, vol. 5, no. 1, pp. 1–12, Sep. 2015, doi: 10.1038/srep13616.

[114] C. A. Mandon, L. J. Blum, and C. A. Marquette, "3D-4D printed objects: New bioactive material opportunities," *Micromachines*, vol. 8, no. 4, p. 102, Mar. 2017, doi: 10.3390/mi8040102.

[115] C. D. Devillard, C. A. Mandon, S. A. Lambert, L. J. Blum, and C. A. Marquette, "Bioinspired Multi-Activities 4D Printing Objects: A New Approach Toward Complex Tissue Engineering," *Biotechnol. J.*, vol. 13, no. 12, p. 1800098, Dec. 2018, doi: 10.1002/biot.201800098.

[116] M. Invernizzi, S. Turri, M. Levi, and R. Suriano, "4D printed thermally activated self-healing and shape memory polycaprolactone-based polymers," *Eur. Polym. J.*, vol. 101, pp. 169–176, Apr. 2018, doi: 10.1016/j.eurpolymj.2018.02.023.

[117] J. T. Miao *et al.*, "Dynamic Imine Bond-Based Shape Memory Polymers with Permanent Shape Reconfigurability for 4D Printing," *ACS Appl. Mater. Interfaces*, vol. 11, no. 43, pp. 40642–40651, Oct. 2019, doi: 10.1021/acsami.9b14145.

[118] X. Li *et al.*, "Dual-method molding of 4D shape memory polyimide ink," *Mater. Des.*, vol. 191, p. 108606, Jun. 2020, doi: 10.1016/j.matdes.2020.108606.

[119] B. Zhang *et al.*, "Mechanically Robust and UV-Curable Shape-Memory Polymers for Digital Light Processing Based 4D Printing," *Adv. Mater.*, vol. 33, no. 27, p. 2101298, 2021, doi: 10.1002/adma.202101298.

[120] Q. Mu, C. K. Dunn, L. Wang, M. L. Dunn, H. J. Qi, and T. Wang, "Thermal cure effects on electromechanical properties of conductive wires by direct ink write for 4D printing and soft machines," *Smart Mater. Struct.*, vol. 26, no. 4, p. 045008, Feb. 2017, doi: 10.1088/1361-665X/aa5cca.

[121] S. A. Khan and I. Lazoglu, "Development of additively manufacturable and electrically conductive graphite–polymer composites," *Prog. Addit. Manuf.*, vol. 5, no. 2, pp. 153–162, Jun. 2020, doi: 10.1007/s40964-019-00102-9.

[122] H. Wei, Q. Zhang, Y. Yao, L. Liu, Y. Liu, and J. Leng, "Direct-write fabrication of 4D active shape-changing structures based on a shape memory polymer and its nanocomposite," *ACS Appl. Mater. Interfaces*, vol. 9, no. 1, pp. 876–883, 2017, doi: 10.1021/acsami.6b12824.

[123] X. Kuang, K. Chen, C. K. Dunn, J. Wu, V. C. F. Li, and H. J. Qi, "3D Printing of Highly Stretchable, Shape-Memory, and Self-Healing Elastomer toward Novel 4D Printing," *ACS Appl. Mater. Interfaces*, vol. 10, no. 8, pp. 7381–7388, Feb. 2018, doi: 10.1021/acsami.7b18265.

[124] C. P. Ambulo, J. J. Burroughs, J. M. Boothby, H. Kim, M. R. Shankar, and T. H. Ware, "Four-dimensional Printing of Liquid Crystal Elastomers," *ACS Appl. Mater. Interfaces*, vol. 9, no. 42, pp. 37332–37339, Oct. 2017, doi: 10.1021/acsami.7b11851.

[125] M. C. Mulakkal, R. S. Trask, and A. M. Seddon, "Smart cellulose-hydrogel composites for 4D printing," *8th Conference on Smart Structures and Materials, SMART 2017 and 6th International Conference on Smart Materials and Nanotechnology in Engineering, SMN 2017*, vol. 2017-Janua. International Center for Numerical Methods in Engineering, pp. 511–524, 2017. Accessed: Jun. 26, 2020. [Online]. Available: https://researchportal.bath.ac.uk/en/publications/smart-cellulose-hydrogel-composites-for-4d-printing

[126] R. S. Jordan and Y. Wang, "3D printing of conjugated polymers," *J. Polym. Sci. Part B Polym. Phys.*, vol. 57, no. 23, pp. 1592–1605, Dec. 2019, doi: 10.1002/polb.24893.

[127] C. M. González-Henríquez, M. A. Sarabia-Vallejos, and J. Rodriguez-Hernandez, "Polymers for additive manufacturing and 4D-printing: Materials, methodologies, and biomedical applications," *Progress in Polymer Science*, vol. 94. Elsevier Ltd, pp. 57–116, Jul. 01, 2019. doi: 10.1016/j.progpolymsci.2019.03.001.

[128] A. Davoudinejad *et al.*, "Geometrical and feature of size design effect on direct stereolithography micro additively manufactured components," in *Procedia Structural Integrity*, Elsevier B.V., Jan. 2018, pp. 1250–1255. doi: 10.1016/j.prostr.2018.12.256.

[129] Y. Y. C. Choong, S. Maleksaeedi, H. Eng, S. Yu, J. Wei, and P. C. Su, "High speed 4D printing of shape memory polymers with nanosilica," *Appl. Mater. Today*, vol. 18, p. 100515, Mar. 2020, doi: 10.1016/j.apmt.2019.100515.

[130] Q. Ge, A. H. Sakhaei, H. Lee, C. K. Dunn, N. X. Fang, and M. L. Dunn, "Multimaterial 4D Printing with Tailorable Shape Memory Polymers," *Sci. Rep.*, vol. 6, no. 1, pp. 1–11, Aug. 2016, doi: 10.1038/srep31110.

[131] R. Noroozi, M. Bodaghi, H. Jafari, A. Zolfagharian, and M. Fotouhi, "Shape-adaptive metastructures with variable bandgap regions by 4D printing," *Polymers (Basel).*, vol. 12, no. 3, p. 519, Mar. 2020, doi: 10.3390/polym12030519.

[132] X. Sun *et al.*, "Machine Learning-Evolutionary Algorithm Enabled Design for 4D-Printed Active Composite Structures," *Adv. Funct. Mater.*, vol. 32, no. 10, p. 2109805, Mar. 2022, doi: 10.1002/adfm.202109805.

[133] S. K. Leist, D. Gao, R. Chiou, and J. Zhou, "Investigating the shape memory properties of 4D printed polylactic acid (PLA) and the concept of 4D printing onto nylon fabrics for the creation of smart textiles," *Virtual Phys. Prototyp.*, vol. 12, no. 4, pp. 290–300, Oct. 2017, doi: 10.1080/17452759.2017.1341815.

[134] J. E. M. Teoh, Y. Zhao, J. An, C. K. Chua, and Y. Liu, "Multi-stage responsive 4D printed smart structure through varying geometric thickness of shape memory polymer," *Smart Mater. Struct.*, vol. 26, no. 12, p. 125001, Oct. 2017, doi: 10.1088/1361-665X/aa908a.

[135] M. Bodaghi and W. H. Liao, "4D printed tunable mechanical metamaterials with shape memory operations," *Smart Mater. Struct.*, vol. 28, no. 4, p. 045019, Mar. 2019, doi: 10.1088/1361-665X/ab0b6b.

[136] A. Nojiri, E. Iwase, and M. Hashimoto, "Self-Assembly of Shape Memory Polymer Printed by Fused Deposition Modeling," in *Proceedings of the IEEE International Conference on Micro Electro Mechanical Systems (MEMS)*, Institute of Electrical and Electronics Engineers Inc., Jan. 2019, pp. 380–383. doi: 10.1109/MEMSYS.2019.8870849.

[137] Q. Zhang *et al.*, "Rapid Volatilization Induced Mechanically Robust Shape-Morphing Structures toward 4D Printing," *ACS Appl. Mater. Interfaces*, vol. 12, no. 15, pp. 17979–17987, Mar. 2020, doi: 10.1021/acsami.0c02038.

[138] A. Gopinath, M. Subaraja, and A. Sultan Nasar, "Fluorescent shape-memory hyperbranched polyurethanes: Synthesis, characterization and evaluation of cytotoxicity," *Eur. Polym. J.*, vol. 108, pp. 517–528, Nov. 2018, doi: 10.1016/j.eurpolymj.2018.09.037.

[139] C. Lin, L. J. Zhang, Y. J. Liu, L. W. Liu, and J. S. Leng, "4D printing of personalized shape memory polymer vascular stents with negative Poisson's ratio structure: A preliminary study," *Sci. China Technol. Sci.*, vol. 63, no. 4, pp. 578–588, Apr. 2020, doi: 10.1007/s11431-019-1468-2.

[140] A. Melocchi *et al.*, "Expandable drug delivery system for gastric retention based on shape memory polymers: Development via 4D printing and extrusion," *Int. J. Pharm.*, vol. 571, p. 118700, Nov. 2019, doi: 10.1016/j.ijpharm.2019.118700.

[141] A. Li, A. Challapalli, and G. Li, "4D Printing of Recyclable Lightweight Architectures Using High Recovery Stress Shape Memory Polymer," *Sci. Rep.*, vol. 9, no. 1, pp. 1–13, Dec. 2019, doi: 10.1038/s41598-019-44110-9.

[142] C. Yuan, T. Wang, M. L. Dunn, and H. J. Qi, "3D printed active origami with complicated folding patterns," *Int. J. Precis. Eng. Manuf. - Green Technol.*, vol. 4, no. 3, pp. 281–289, Jul. 2017, doi: 10.1007/s40684-017-0034-x.

[143] H. Y. Jeong, E. Lee, S. Ha, N. Kim, and Y. C. Jun, "Multistable Thermal Actuators Via Multimaterial 4D Printing," *Adv. Mater. Technol.*, vol. 4, no. 3, p. 1800495, Mar. 2019, doi: 10.1002/admt.201800495.

[144] H. Y. Jeong, B. H. Woo, N. Kim, and Y. C. Jun, "Multicolor 4D printing of shape-memory polymers for light-induced selective heating and remote actuation," *Sci. Rep.*, vol. 10, no. 1, pp. 1–11, Dec. 2020, doi: 10.1038/s41598-020-63020-9.

[145] D. Schmelzeisen, H. Koch, C. Pastore, and T. Gries, "4D textiles: Hybrid textile structures that can change structural form with time by 3D printing," in *Narrow and Smart Textiles*, Springer International Publishing, 2017, pp. 189–201. doi: 10.1007/978-3-319-69050-6_17.

[146] W. Wang, C. Y. Yu, P. A. Abrego Serrano, and S. H. Ahn, "Soft grasping mechanisms composed of shape memory polymer based self-bending units," *Compos. Part B Eng.*, vol. 164, pp. 198–204, May 2019, doi: 10.1016/j.compositesb.2018.10.081.

[147] W. Zhao, N. Li, L. Liu, J. Leng, and Y. Liu, "Origami derived self-assembly stents fabricated via 4D printing," *Compos. Struct.*, vol. 293, p. 115669, Aug. 2022, doi:

10.1016/j.compstruct.2022.115669.

[148] L. Xu, T. C. Shyu, and N. A. Kotov, "Origami and Kirigami Nanocomposites," *ACS Nano*, vol. 11, no. 8. American Chemical Society, pp. 7587–7599, Aug. 22, 2017. doi: 10.1021/acsnano.7b03287.

[149] T. Langford, A. Mohammed, K. Essa, A. Elshaer, and H. Hassanin, "4D Printing of Origami Structures for Minimally Invasive Surgeries Using Functional Scaffold," *Appl. Sci.*, vol. 11, no. 1, pp. 1–13, Jan. 2021, doi: 10.3390/app11010332.

[150] X. Zhou *et al.*, "Mechanochemical Regulated Origami with Tough Hydrogels by Ion Transfer Printing," *ACS Appl. Mater. Interfaces*, vol. 10, no. 10, pp. 9077–9084, Mar. 2018, doi: 10.1021/acsami.8b01610.

[151] J. E. M. Teoh, J. An, X. Feng, Y. Zhao, C. K. Chua, and Y. Liu, "Design and 4D printing of cross-folded origami structures: A preliminary investigation," *Materials (Basel).*, vol. 11, no. 3, p. 376, Mar. 2018, doi: 10.3390/ma11030376.

[152] Y. Liu *et al.*, "Shape memory behavior and recovery force of 4D printed laminated Miura-origami structures subjected to compressive loading," *Compos. Part B Eng.*, vol. 153, pp. 233–242, Nov. 2018, doi: 10.1016/j.compositesb.2018.07.053.

[153] W. Yang, Z. Wang, X. Wang, T. Yu, S. Xie, and Z. Ge, "3D printing of bioinspired hydrogel microstructures with programmable and complex shape deformations based on a digital micro-mirror device," *Opt. Laser Technol.*, vol. 157, p. 108759, Jan. 2023, doi: 10.1016/j.optlastec.2022.108759.

[154] J. A. Faber, A. F. Arrieta, and A. R. Studart, "Bioinspired spring origami," *Science (80-.).*, vol. 359, no. 6382, pp. 1386–1391, Mar. 2018, doi: 10.1126/science.aap7753.

[155] T. H. Kwok, C. C. L. Wang, D. Deng, Y. Zhang, and Y. Chen, "Four-Dimensional Printing for Freeform Surfaces: Design Optimization of Origami and Kirigami Structures," *J. Mech. Des. Trans. ASME*, vol. 137, no. 11, Nov. 2015, doi: 10.1115/1.4031023.

[156] Z. Zhao, J. Wu, X. Mu, H. Chen, H. J. Qi, and D. Fang, "Origami by frontal photopolymerization," *Sci. Adv.*, vol. 3, no. 4, p. e1602326, Apr. 2017, doi: 10.1126/sciadv.1602326.

[157] C. Yuan *et al.*, "3D printed reversible shape changing soft actuators assisted by liquid crystal elastomers," *Soft Matter*, vol. 13, no. 33, pp. 5558–5568, Aug. 2017, doi: 10.1039/c7sm00759k.

[158] A. Velasco-Hogan, J. Xu, and M. A. Meyers, "Additive Manufacturing as a Method to Design and Optimize Bioinspired Structures," *Adv. Mater.*, vol. 30, no. 52, p. 1800940, Dec. 2018, doi: 10.1002/adma.201800940.

[159] W. P. Ryan-Johnson, L. C. Wolfe, C. R. Byron, J. K. Nagel, and H. Zhang, "A systems approach of topology optimization for bioinspired material structures design using additive manufacturing," *Sustain.*, vol. 13, no. 14, p. 8013, Jul. 2021, doi: 10.3390/su13148013.

[160] Y. L. Tee and P. Tran, "On bioinspired 4d printing: materials, design and potential applications," *Aust. J. Mech. Eng.*, vol. 19, no. 5, pp. 642–652, 2021, doi: 10.1080/14484846.2021.1988434.

[161] C. De Maria *et al.*, "Biomimetic Tendrils by Four Dimensional Printing Bimorph Springs with Torsion and Contraction Properties Based on Bio-Compatible Graphene/Silk Fibroin and Poly(3-Hydroxybutyrate-co-3-Hydroxyvalerate)," *Adv. Funct. Mater.*, vol. 31, no. 52, p. 2105665, Dec. 2021, doi: 10.1002/adfm.202105665.

[162] J. Liu *et al.*, "Dual-Gel 4D Printing of Bioinspired Tubes," *ACS Appl. Mater. Interfaces*, vol. 11, no. 8, pp. 8492–8498, Feb. 2019, doi: 10.1021/acsami.8b17218.

[163] J. M. McCracken, B. M. Rauzan, J. C. E. Kjellman, H. Su, S. A. Rogers, and R. G. Nuzzo, "Ionic Hydrogels with Biomimetic 4D-Printed Mechanical Gradients: Models for Soft-Bodied Aquatic Organisms," *Adv. Funct. Mater.*, vol. 29, no. 28, p. 1806723, Jul. 2019, doi: 10.1002/adfm.201806723.

[164] A. Sydney Gladman, E. A. Matsumoto, R. G. Nuzzo, L. Mahadevan, and J. A. Lewis, "Biomimetic 4D printing," *Nat. Mater.*, vol. 15, no. 4, pp. 413–418, Jan. 2016, doi: 10.1038/nmat4544.

[165] D. Correa *et al.*, "4D pine scale: Biomimetic 4D printed autonomous scale and flap structures capable of multi-phase movement," *Philos. Trans. R. Soc. A Math. Phys. Eng. Sci.*, vol. 378, no. 2167, Mar. 2020, doi: 10.1098/rsta.2019.0445.

[166] W. Peng *et al.*, "Light-Coded Digital Crystallinity Patterns Toward Bioinspired 4D Transformation of Shape-Memory Polymers," *Adv. Funct. Mater.*, vol. 30, no. 19, p. 2000522, May 2020, doi: 10.1002/adfm.202000522.

[167] T. Cheng *et al.*, "Bio-Inspired Motion Mechanisms: Computational Design and Material Programming of Self-Adjusting 4D-Printed Wearable Systems," *Adv. Sci.*, vol. 8, no. 13, p. 2100411, Jul. 2021, doi: 10.1002/advs.202100411.

[168] S. Zeng, Y. Feng, Y. Gao, H. Zheng, and J. Tan, "Layout design and application of 4D-printing bio-inspired structures with programmable actuators," *Bio-Design Manuf.*, vol. 5, no. 1, pp. 189–200, Jul. 2022, doi: 10.1007/s42242-021-00146-3.

[169] S. Mallakpour, F. Tabesh, and C. M. Hussain, "3D and 4D printing: From innovation to evolution," *Adv. Colloid Interface Sci.*, vol. 294, p. 102482, 2021, doi: 10.1016/j.cis.2021.102482.

[170] Y. Xia, Y. He, F. Zhang, Y. Liu, and J. Leng, "A Review of Shape Memory Polymers and Composites: Mechanisms, Materials, and Applications," *Adv. Mater.*, vol. 33, no. 6, p. 2000713, Feb. 2021, doi: 10.1002/adma.202000713.

[171] X. Teng, M. Zhang, and A. S. Mujumdar, "4D printing: Recent advances and proposals in the food sector," *Trends in Food Science and Technology*, vol. 110. Elsevier Ltd, pp. 349–363, Apr. 01, 2021. doi: 10.1016/j.tifs.2021.01.076.

[172] L. B. Huang *et al.*, "4D-printed self-recovered triboelectric nanogenerator for energy harvesting and self-powered sensor," *Nano Energy*, vol. 84, p. 105873, Jun. 2021, doi: 10.1016/j.nanoen.2021.105873.

[173] L. Wang, F. Zhang, Y. Liu, and J. Leng, "Shape Memory Polymer Fibers: Materials, Structures, and Applications," *Adv. Fiber Mater.*, vol. 4, no. 1, pp. 5–23, Apr. 2022, doi: 10.1007/s42765-021-00073-z.

[174] S. Basak, "Redesigning the modern applied medical sciences and engineering with shape memory polymers," *Adv. Compos. Hybrid Mater.*, vol. 4, no. 2, pp. 223–234, Jun. 2021, doi: 10.1007/s42114-021-00216-1.

[175] A. Melocchi *et al.*, "Shape memory materials and 4D printing in pharmaceutics," *Advanced Drug Delivery Reviews*, vol. 173. Elsevier B.V., pp. 216–237, Jun. 01, 2021. doi: 10.1016/j.addr.2021.03.013.

[176] R. Xiao and W. M. Huang, "Heating/Solvent Responsive Shape-Memory Polymers for Implant Biomedical Devices in Minimally Invasive Surgery: Current Status and Challenge," *Macromol. Biosci.*, vol. 20, no. 8, p. 2000108, Aug. 2020, doi: 10.1002/mabi.202000108.

[177] S. Miao, W. Zhu, N. J. Castro, J. Leng, and L. G. Zhang, "Four-Dimensional Printing Hierarchy Scaffolds with Highly Biocompatible Smart Polymers for Tissue Engineering Applications," *Tissue Eng. - Part C Methods*, vol. 22, no. 10, pp. 952–963, Oct. 2016, doi: 10.1089/ten.tec.2015.0542.

[178] R. Xiao and T. D. Nguyen, "Modeling the solvent-induced shape-memory behavior of glassy polymers," *Soft Matter*, vol. 9, no. 39, pp. 9455–9464, Sep. 2013, doi: 10.1039/c3sm51210j.

[179] C. Lin, L. Liu, Y. Liu, and J. Leng, "4D Printing of Bioinspired Absorbable Left Atrial Appendage Occluders: A Proof-of-Concept Study," *ACS Appl. Mater. Interfaces*, vol. 13, no. 11, pp. 12668–12678, Mar. 2021, doi: 10.1021/acsami.0c17192.

[180] C. Zhang *et al.*, "4D Printing of shape-memory polymeric scaffolds for adaptive biomedical implantation," *Acta Biomater.*, vol. 122, pp. 101–110, Mar. 2021, doi: 10.1016/j.actbio.2020.12.042.

[181] M. Nafea, A. Nawabjan, and M. S. Mohamed Ali, "A wirelessly-controlled piezoelectric microvalve for regulated drug delivery," *Sensors Actuators, A Phys.*, vol. 279, pp. 191–203, Aug. 2018, doi: 10.1016/j.sna.2018.06.020.

[182] T. Rehman, M. Nafea, A. A. Faudzi, T. Saleh, and M. S. M. Ali, "PDMS-based dual-channel pneumatic micro-actuator," *Smart Mater. Struct.*, vol. 28, no. 11, p. 115044, Oct. 2019, doi: 10.1088/1361-665X/ab4ac1.

[183] W. Zhang *et al.*, "Structural multi-colour invisible inks with submicron 4D printing of shape memory polymers," *Nat. Commun.*, vol. 12, no. 1, pp. 1–8, Dec. 2021, doi: 10.1038/s41467-020-20300-2.

[184] S. Wolf *et al.*, "Variable Stiffness Actuators: Review on Design and Components," *IEEE/ASME Transactions on Mechatronics*, vol. 21, no. 5. Institute of Electrical and Electronics Engineers Inc., pp. 2418–2430, Oct. 2016. doi: 10.1109/TMECH.2015.2501019.

[185] M. Xie, M. Zhu, Z. Yang, S. Okada, and S. Kawamura, "Flexible self-powered multifunctional sensor for stiffness-tunable soft robotic gripper by multimaterial 3D printing," *Nano Energy*, vol. 79, p. 105438, Jan. 2021, doi: 10.1016/j.nanoen.2020.105438.

[186] T. T. Hoang, J. J. S. Quek, M. T. Thai, P. T. Phan, N. H. Lovell, and T. N. Do, "Soft robotic fabric gripper with gecko adhesion and variable stiffness," *Sensors Actuators, A Phys.*, vol. 323, p. 112673, Jun. 2021, doi: 10.1016/j.sna.2021.112673.

[187] J. Luo, S. Wang, Y. Zhao, and Y. Fu, "Variable stiffness control of series elastic actuated biped locomotion," *Intell. Serv. Robot.*, vol. 11, no. 3, pp. 225–235, Jul. 2018, doi: 10.1007/s11370-018-0248-y.

[188] S. Liu, X. Tang, D. Zhou, and Y. Liu, "Fascicular module of nylon twisted actuators with large force and variable stiffness," *Sensors Actuators, A Phys.*, vol. 315, p. 112292, Nov. 2020, doi: 10.1016/j.sna.2020.112292.

[189] T. Sun, Y. Chen, T. Han, C. Jiao, B. Lian, and Y. Song, "A soft gripper with variable stiffness inspired by pangolin scales, toothed pneumatic actuator and autonomous controller," *Robot. Comput. Integr. Manuf.*, vol. 61, p. 101848, Feb. 2020, doi: 10.1016/j.rcim.2019.101848.

[190] Y. J. Park, T. M. Huh, D. Park, and K. J. Cho, "Design of a variable-stiffness flapping mechanism for maximizing the thrust of a bio-inspired underwater robot," *Bioinspiration and Biomimetics*, vol. 9, no. 3, p. 036002, Mar. 2014, doi: 10.1088/1748-3182/9/3/036002.

[191] F. Momeni and J. Ni, "Nature-inspired smart solar concentrators by 4D printing," *Renew. Energy*, vol. 122, pp. 35–44, Jul. 2018, doi: 10.1016/j.renene.2018.01.062.

[192] Y. F. Zhang *et al.*, "Fractal-Based Stretchable Circuits via Electric-Field-Driven Microscale 3D Printing for Localized Heating of Shape Memory Polymers in 4D Printing," *ACS Applied Materials and Interfaces*, vol. 13, no. 35. American Chemical Society, pp. 41414–41423, 2021. doi: 10.1021/acsami.1c03572.

[193] M. Bodaghi, R. Noroozi, A. Zolfagharian, M. Fotouhi, and S. Norouzi, "4D Printing Self-Morphing Structures," vol. 12, no. 8, p. 1353, Apr. 2019, Accessed: Apr. 17, 2023. [Online]. Available: https://www.mdpi.com/1996-1944/12/8/1353/htm

[194] C. M. Hamel, D. J. Roach, K. N. Long, F. Demoly, M. L. Dunn, and H. J. Qi, "Machine-learning based design of active composite structures for 4D printing," *Smart Mater. Struct.*, vol. 28, no. 6, p. 065005, May 2019, doi: 10.1088/1361-665X/ab1439.

[195] Y. Zou, Z. Huang, X. Li, and P. Lv, "4D Printing Pre-Strained Structures for Fast Thermal Actuation," *Front. Mater.*, vol. 8, p. 122, Apr. 2021, doi: 10.3389/fmats.2021.661999.

[196] Y. Wang and X. Li, "An accurate finite element approach for programming 4D-printed self-morphing structures produced by fused deposition modeling," *Mech. Mater.*, vol. 151, p. 103628, Dec. 2020, doi: 10.1016/j.mechmat.2020.103628.

[197] A. Zolfagharian, L. Durran, S. Gharaie, B. Rolfe, A. Kaynak, and M. Bodaghi, "4D printing soft robots guided by machine learning and finite element models," *Sensors Actuators, A Phys.*, vol. 328, p. 112774, Sep. 2021, doi: 10.1016/j.sna.2021.112774.

[198] D. Maulud and A. M. Abdulazeez, "A Review on Linear Regression Comprehensive in Machine Learning," *J. Appl. Sci. Technol. Trends*, vol. 1, no. 4, pp. 140–147, Dec. 2020, doi: 10.38094/jastt1457.

[199] Z. Hashemi Aslani, B. Omidvar, and A. Karbassi, "Integrated model for land-use transformation analysis based on multi-layer perception neural network and agent-based model," *Environ. Sci. Pollut. Res.*, vol. 29, no. 39, pp. 59770–59783, Aug. 2022, doi: 10.1007/s11356-022-19392-8.

[200] A. Rana, A. S. Rawat, A. Bijalwan, and H. Bahuguna, "Application of Multi Layer (Perceptron) Artificial Neural Network in the Diagnosis System: A Systematic Review," *Proc. 2018 3rd IEEE Int. Conf. Res. Intell. Comput. Eng. RICE 2018*, Oct. 2018, doi: 10.1109/RICE.2018.8509069.

[201] H. Li *et al.*, "Prediction of the optical properties in photonic crystal fiber using support vector machine based on radial basis functions," *Optik (Stuttg).*, vol. 275, p. 170603, Mar. 2023, doi: 10.1016/j.ijleo.2023.170603.

[202] J. Cervantes, F. Garcia-Lamont, L. Rodríguez-Mazahua, and A. Lopez, "A comprehensive survey on support vector machine classification: Applications, challenges and trends," *Neurocomputing*, vol. 408, pp. 189–215, Sep. 2020, doi: 10.1016/j.neucom.2019.10.118.

[203] J. G. Eisenhauer, "Regression through the origin," *Teach. Stat.*, vol. 25, no. 3, pp. 76–80, Sep. 2003, doi: 10.1111/1467-9639.00136.

[204] J. M. Álvarez-Alvarado, J. G. Ríos-Moreno, S. A. Obregón-Biosca, G. Ronquillo-Lomelí, E. Ventura-Ramos, and M. Trejo-Perea, "Hybrid techniques to predict solar radiation using support vector machine and search optimization algorithms: A review," *Applied Sciences (Switzerland)*, vol. 11, no. 3. Multidisciplinary Digital Publishing Institute, pp. 1–17, Jan. 24, 2021. doi: 10.3390/app11031044.

[205] A. Zolfagharian *et al.*, "Silicon-based soft parallel robots 4D printing and multiphysics analysis," *Smart Mater. Struct.*, vol. 31, no. 11, p. 115030, Nov. 2022, doi: 10.1088/1361-665X/ac976c.

[206] Y. Yu *et al.*, "Material characterization and precise finite element analysis of fiber reinforced thermoplastic composites for 4D printing," *CAD Comput. Aided Des.*, vol. 122, p. 102817, May 2020, doi: 10.1016/j.cad.2020.102817.

[207] F. Momeni and J. Ni, "Laws of 4D Printing," *Engineering*, vol. 6, no. 9, pp. 1035–1055, Sep. 2020, doi: 10.1016/j.eng.2020.01.015.

[208] J. Odent *et al.*, "Hierarchical chemomechanical encoding of multi-responsive hydrogel actuators: Via 3D printing," *J. Mater. Chem. A*, vol. 7, no. 25, pp. 15395–15403, Jun. 2019, doi: 10.1039/c9ta03547h.

[209] J. E. M. Teoh, J. An, C. K. Chua, M. Lv, V. Krishnasamy, and Y. Liu, "Hierarchically self-morphing structure through 4D printing," *Virtual Phys. Prototyp.*, vol. 12, no. 1, pp. 61–68, Jan. 2017, doi: 10.1080/17452759.2016.1272174.

[210] D. Deng and Y. Chen, "Origami-Based Self-Folding Structure Design and Fabrication Using Projection Based Stereolithography," *J. Mech. Des. Trans. ASME*, vol. 137, no. 2, Feb. 2015, doi: 10.1115/1.4029066.

[211] D. Raviv *et al.*, "Active printed materials for complex self-evolving deformations," *Sci. Rep.*, vol. 4, 2014, doi: 10.1038/srep07422.

[212] T. H. Kwok and Y. Chen, "GDFE: Geometry-Driven Finite Element for Four-Dimensional Printing," *J. Manuf. Sci. Eng. Trans. ASME*, vol. 139, no. 11, Nov. 2017, doi: 10.1115/1.4037429/383961.

[213] Q. Zhang, K. Zhang, and G. Hu, "Smart three-dimensional lightweight structure triggered from a thin composite sheet via 3D printing technique," *Sci. Rep.*, vol. 6, pp. 1–8, Feb. 2016, doi: 10.1038/srep22431.

[214] R. Nuzzo, "Biomimetic 4D Printing," 2015, Accessed: Apr. 22, 2023. [Online]. Available: https://www.ideals.illinois.edu/items/93995

[215] M. S. Singhvi, S. S. Zinjarde, and D. V. Gokhale, "Polylactic acid: synthesis and

biomedical applications," *J. Appl. Microbiol.*, vol. 127, no. 6, pp. 1612–1626, Dec. 2019, doi: 10.1111/jam.14290.

[216] M. Hosseinzadeh, M. Ghoreishi, and K. Narooei, "An investigation into the effect of thermal variables on the 3D printed shape memory polymer structures with different geometries," *J. Intell. Mater. Syst. Struct.*, vol. 33, no. 5, pp. 715–726, Aug. 2022, doi: 10.1177/1045389X211028286.

[217] D. S. Cheah, Y. S. Alshebly, M. S. Mohamed Ali, and M. Nafea, "Development of 4D-printed shape memory polymer large-stroke XY micropositioning stages," *J. Micromechanics Microengineering*, vol. 32, no. 6, p. 065006, May 2022, doi: 10.1088/1361-6439/ac68ca.

[218] M. Gouge, P. Michaleris, E. Denlinger, and J. Irwin, "The Finite Element Method for the Thermo-Mechanical Modeling of Additive Manufacturing Processes," *Thermo-Mechanical Model. Addit. Manuf.*, pp. 19–38, Jan. 2017, doi: 10.1016/B978-0-12-811820-7.00003-3.

[219] L. Zhao, M. Zhang, B. Chitrakar, and B. Adhikari, "Recent advances in functional 3D printing of foods: a review of functions of ingredients and internal structures," *Critical Reviews in Food Science and Nutrition*, vol. 61, no. 21. Taylor & Francis, pp. 3489–3503, 2021. doi: 10.1080/10408398.2020.1799327.

[220] S. Shinde, R. Mane, A. Vardikar, A. Dhumal, and A. Rajput, "4D printing: From emergence to innovation over 3D printing," *European Polymer Journal*, vol. 197. Pergamon, p. 112356, Oct. 10, 2023. doi: 10.1016/j.eurpolymj.2023.112356.

[221] G. Nematollahi, A. Kianianmomeni, and A. Hallmann, "Quantitative analysis of cell-type specific gene expression in the green alga Volvox carteri," *BMC Genomics*, vol. 7, no. 1, pp. 1–19, Dec. 2006, doi: 10.1186/1471-2164-7-321.

[222] A. Oren, "The function of gas vesicles in halophilic archaea and bacteria: Theories and experimental evidence," *Life*, vol. 3, no. 1, pp. 1–20, Dec. 2012, doi: 10.3390/life3010001.

[223] D. Goss *et al.*, "Bioinspired honeycomb core design: An experimental study of the role of corner radius, coping and interface," *Biomimetics*, vol. 5, no. 4, pp. 1–24, Nov. 2020, doi: 10.3390/biomimetics5040059.

[224] D. Peng, B. Zhou, Y. Jiang, X. F. Tan, D. Y. Yuan, and L. Zhang, "Enhancing freezing tolerance of Brassica napus L. by overexpression of a stearoyl-acyl carrier protein desaturase gene (SAD) from Sapium sebiferum (L.) Roxb.," *Plant Sci.*, vol. 272, pp. 32–41, Jul. 2018, doi: 10.1016/j.plantsci.2018.03.028.

[225] R. M. Taha, N. Mahmad, J. S. Yaacob, N. Abdullah, and S. Mohajer, "Synthetic Seeds Production and Regeneration of Oxalis triangularis for Mass Propagation and Conservation," *Int. J. Environ. Sci. Dev.*, pp. 461–464, 2013, doi: 10.7763/ijesd.2013.v4.394.

[226] M. Mehrpouya, H. Vahabi, S. Janbaz, A. Darafsheh, T. R. Mazur, and S. Ramakrishna, "4D printing of shape memory polylactic acid (PLA)," *Polymer (Guildf).*, vol. 230, p. 124080, Sep. 2021, doi: 10.1016/j.polymer.2021.124080.

[227] C. Lin, L. Liu, Y. Liu, and J. Leng, "4D printing of shape memory polybutylene succinate/polylactic acid (PBS/PLA) and its potential applications," *Compos. Struct.*,

vol. 279, p. 114729, Jan. 2022, doi: 10.1016/j.compstruct.2021.114729.

[228] A. Abuzaiter, M. Nafea, and M. S. Mohamed Ali, "Development of a shape-memory-alloy micromanipulator based on integrated bimorph microactuators," *Mechatronics*, vol. 38, pp. 16–28, Sep. 2016, doi: 10.1016/j.mechatronics.2016.05.009.

[229] J. M. Ferri, O. Fenollar, A. Jorda-Vilaplana, D. García-Sanoguera, and R. Balart, "Effect of miscibility on mechanical and thermal properties of poly(lactic acid)/ polycaprolactone blends," *Polym. Int.*, vol. 65, no. 4, pp. 453–463, Apr. 2016, doi: 10.1002/pi.5079.

[230] J. Beauson, G. Schillani, L. Van der Schueren, and S. Goutianos, "The effect of processing conditions and polymer crystallinity on the mechanical properties of unidirectional self-reinforced PLA composites," *Compos. Part A Appl. Sci. Manuf.*, vol. 152, p. 106668, Jan. 2022, doi: 10.1016/j.compositesa.2021.106668.

[231] O. Zmeskal, L. Marackova, T. Lapcikova, P. Mencik, and R. Prikryl, "Thermal properties of samples prepared from polylactic acid by 3D printing," *AIP Conf. Proc.*, vol. 2305, no. 1, p. 20022, Nov. 2020, doi: 10.1063/5.0033857.

[232] I. Blanco, G. Cicala, G. Recca, and C. Tosto, "Specific Heat Capacity and Thermal Conductivity Measurements of PLA-Based 3D-Printed Parts with Milled Carbon Fiber Reinforcement," *Entropy*, vol. 24, no. 5, p. 654, May 2022, doi: 10.3390/e24050654.

[233] H. Gao and N. A. Meisel, "Exploring the manufacturability and resistivity of conductive filament used in material extrusion additive manufacturing," in *Solid Freeform Fabrication 2017: Proceedings of the 28th Annual International Solid Freeform Fabrication Symposium - An Additive Manufacturing Conference, SFF 2017*, 2020, pp. 1612–1626.

[234] I. Tirado-Garcia *et al.*, "Conductive 3D printed PLA composites: On the interplay of mechanical, electrical and thermal behaviours," *Compos. Struct.*, vol. 265, p. 113744, Jun. 2021, doi: 10.1016/j.compstruct.2021.113744.

[235] Y. S. Alshebly *et al.*, "Bioinspired Pattern-Driven Single-Material 4D Printing for Self-Morphing Actuators," *Sustain.*, vol. 14, no. 16, p. 10141, Aug. 2022, doi: 10.3390/su141610141.

[236] G. Scalet, "Two-way and multiple-way shape memory polymers for soft robotics: An overview," *Actuators*, vol. 9, no. 1, p. 10, Feb. 2020, doi: 10.3390/act9010010.

[237] D. J. Roach, X. Sun, X. Peng, F. Demoly, K. Zhou, and H. J. Qi, "4D Printed Multifunctional Composites with Cooling-Rate Mediated Tunable Shape Morphing," *Adv. Funct. Mater.*, vol. 32, no. 36, p. 2203236, Sep. 2022, doi: 10.1002/adfm.202203236.

[238] Y. Liu, F. Zhang, J. Leng, and T. W. Chou, "Microstructural design of 4D printed angle-ply laminated strips with tunable shape memory properties," *Mater. Lett.*, vol. 285, p. 129197, Feb. 2021, doi: 10.1016/j.matlet.2020.129197.

Appendix A – FESEM Report

PLA

Sample: PLA
Type: Default
ID:

Label :   Spectrum 1
Collected :   13-Oct-2022 12:21 PM
Livetime (s) :   40.07
Real time (s) :   41.55
Detector :   X-Max
Window :   SATW

Tilt (deg) :   0.0
Elevation (deg) :   35.0
Azimuth (deg) :   0.0

Magnification :   300 X
Accelerating voltage (kV) :   20.00
Process time :   5

Spectrum processing :
Peak possibly omitted : 2.060 keV

Processing option : All elements analyzed
(Normalised)
Number of iterations = 3

Standard :
C   CaCO3   1-Jun-1999 12:00 AM
O   SiO2   1-Jun-1999 12:00 AM
Na   Albite   1-Jun-1999 12:00 AM
Cl   KCl   1-Jun-1999 12:00 AM

Element	Weight%	Atomic%
C K	55.55	62.61
O K	43.85	37.11
Na K	0.27	0.16
Cl K	0.33	0.13
Totals	100.00	
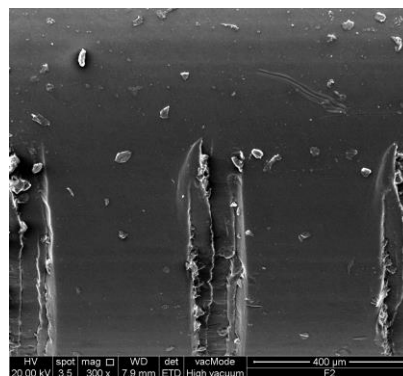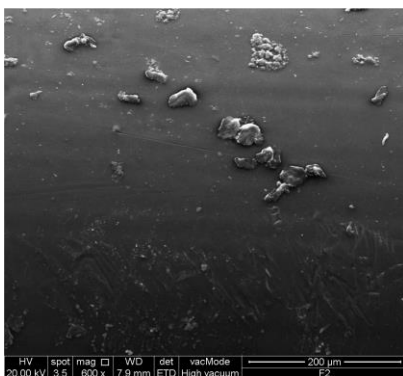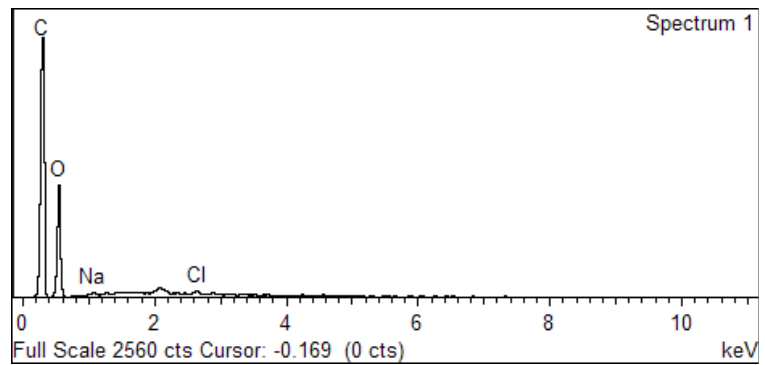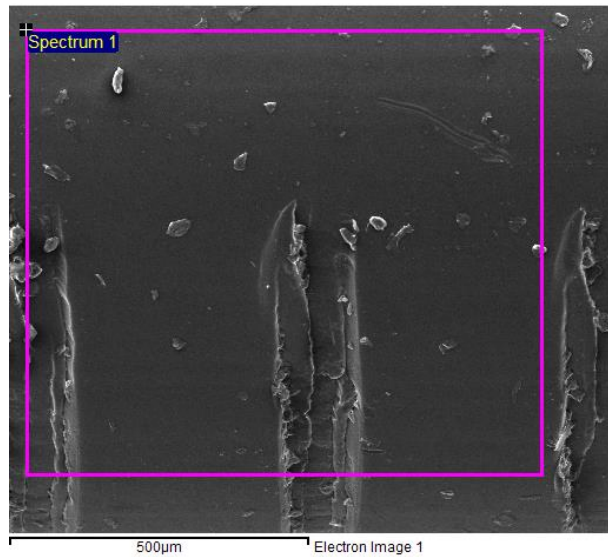
Conductive PLA

Sample: Conductive PLA
Type: Default
ID:

Label :   Spectrum 1
Collected :   13-Oct-2022 12:07 PM
Livetime (s) :   40.08
Real time (s) :   42.60
Detector :   X-Max
Window :   SATW

Tilt (deg) :   0.0
Elevation (deg) :   35.0
Azimuth (deg) :   0.0

Magnification :   20000 X
Accelerating voltage (kV) :   20.00
Process time :   5

Spectrum processing :
Peak possibly omitted : 2.049 keV

Processing option : All elements analyzed
(Normalised)
Number of iterations = 4

Standard :
C   CaCO3   1-Jun-1999 12:00 AM
O   SiO2   1-Jun-1999 12:00 AM

Element	Weight%	Atomic%
C K	82.77	86.48
O K	17.23	13.52
Totals	100.00	

Electron Image 1

Spectrum 1

Full Scale 6217 cts Cursor: -0.046 (131 cts)   keV
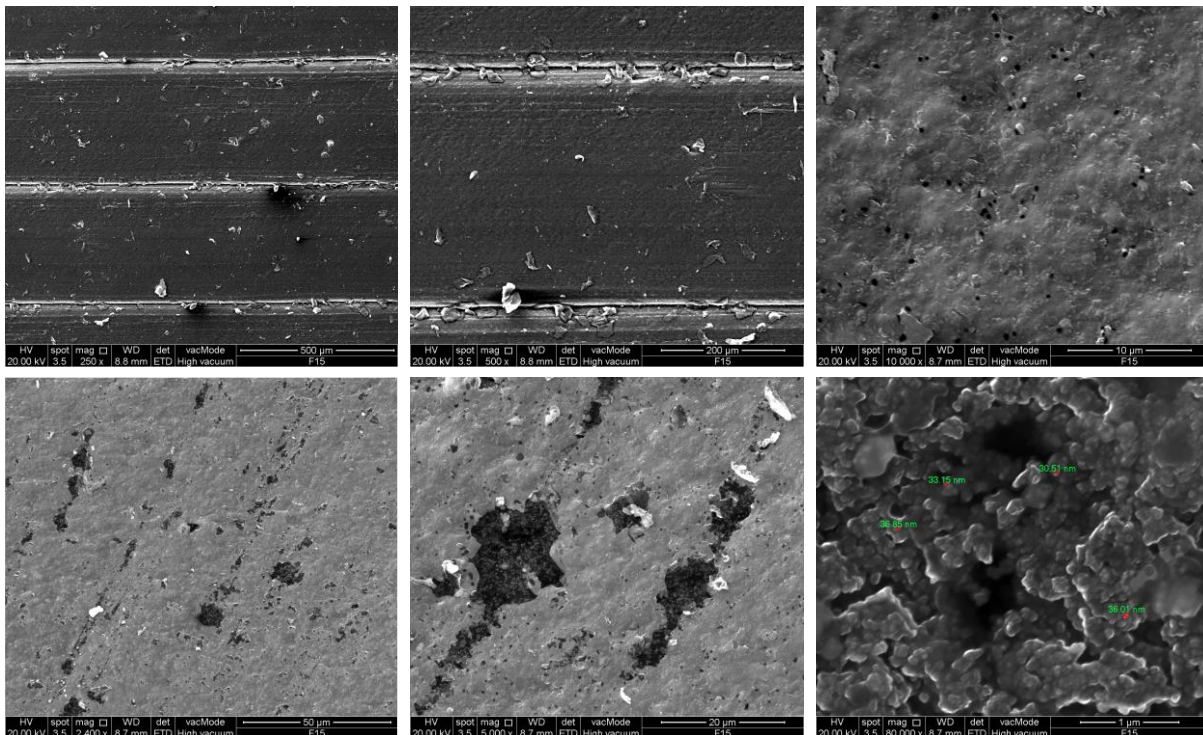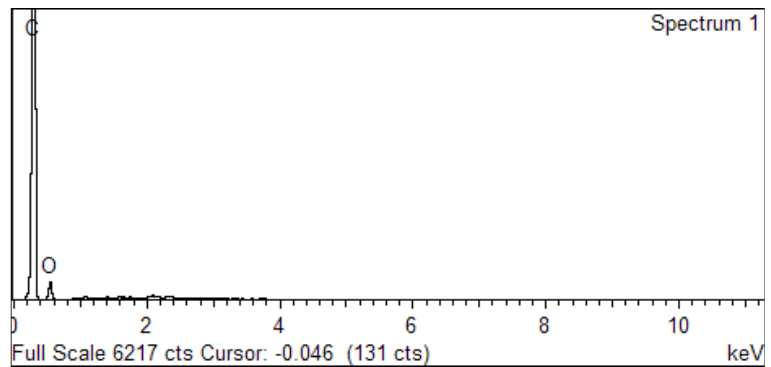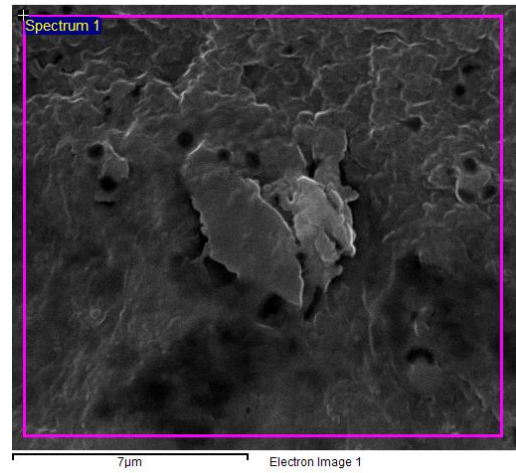
Appendix B – Figure Resuse Permission

Figure 2-2

JOHN WILEY AND SONS LICENSE
TERMS AND CONDITIONS
May 01, 2023

License Number	5540160013985
License date	May 01, 2023
Licensed Content Publisher	John Wiley and Sons
Licensed Content Publication	Advanced Materials Technologies
Licensed Content Title	Biomimetic Shape–Color Double-Responsive 4D Printing
Licensed Content Author	Lei Ren, Qingping Liu, Luquan Ren, et al
Licensed Content Date	Jun 17, 2019
Licensed Content Volume	4
Licensed Content Issue	9
Licensed Content Pages	10
Type of use	Dissertation/Thesis
Requestor type	University/Academic
Format	Print and electronic
Portion	Figure/table
Number of figures/tables	1
Will you be translating?	No
Title	Development of 4D-Printed Shape Memory Polymer Actuators
Institution name	University of Nottingham Malaysia
Expected presentation date	May 2023
Order reference number	1
Portions	Figure 9
Requestor Location	Mr. Yousif Alshebly Ascotte boulevard B-19-16, jalan Bandar kajang, Selangor 43500 Malaysia Attn: Mr. Yousif Alshebly
Publisher Tax ID	EU826007151
Total	0.00 USD

Figure 2-3

Figure 2-4

Figure 2-5

Figure 2-6

4D printing of polyurethane paint-based composites

Jheng-Wun Su, Wenxin Gao, Khoinguyen Trinh, Stuart M. Kenderes, Ezgi Tekin Pulatsu, Cheng Zhang, ...show all

📄 Full Article   🖼 Figures & data   📙 References   66 Citations   📊 Metrics   © Licensing   🖨 Reprints & Permissions

Reprints and Permissions

Relate

People
read

Develop
current
applicat

Figure 2-7

	Multimaterial 4D Printing with Tailorable Shape Memory Polymers
SPRINGER NATURE	**Author:** Qi Ge et al
	Publication: Scientific Reports
	Publisher: Springer Nature
	Date: Aug 8, 2016
	Copyright © 2016, The Author(s)

Figure 2-10

Figure 2-12